

UNCOVERING STEREOCOMPLEMENTARITY IN TWO ALKENE REDUCTASES OF  
THE OLD YELLOW ENZYME FAMILY AND THE DIFFERENT FATES OF  
ELECTRONS IN THE SECOND HALF-REACTION OF DIHYDROOROTATE  
DEHYDROGENASE 1B

By

YURI ALEXEY ANDREIW POMPEU

A DISSERTATION PRESENTED TO THE GRADUATE SCHOOL  
OF THE UNIVERSITY OF FLORIDA IN PARTIAL FULFILLMENT  
OF THE REQUIREMENTS FOR THE DEGREE OF  
DOCTOR OF PHILOSOPHY

UNIVERSITY OF FLORIDA

2013

© 2013 Yuri Alexey Andreiw Pompeu

To my mom, Elosavete Andreiv, who moved from our native Brazil just to be closer to me and has always supported my decisions no matter how absurd they may seem. I also dedicate this to my Father, Marcus Pompeu, whom I have gotten closer to every year of my life despite the 4,337 miles separating us.

## ACKNOWLEDGMENTS

First, I express my sincere gratitude to my advisor Professor Jon Stewart for his unique ability of subtly leading me toward the “right way to do things” and away from the wrong paths. His approachability and guidance were invaluable to me and my career. I acknowledge the extreme patience and willingness to help of Professor Steve Bruner. He has always provided me with valuable insight and discussions from the moment I appeared in his office stating that I wished to learn protein crystallography. I must acknowledge Professor Rob McKenna who has always found the time not only to accommodate my experiments in his facilities, but also to answer questions, irrespective of their quality. I thank Professor David Ostrov, for bringing me into a very exciting project and trusting me with valuable data; I am truly honored. Finally, I thank Professors Valerie de Crecy-Lagard and Nicole Horenstein for being part of my advisory committee and for their helpful criticism throughout this process.

I must also acknowledge members of the Stewart group for many helpful discussions, in particular Dr. Bradford Sullivan, who participated directly in the studies of carvone reductions and Dr. Adam Walton who performed substrate screenings using OYE2.6 and the alkene reductase library of homologs.

## TABLE OF CONTENTS

	<u>page</u>
ACKNOWLEDGMENTS.....	4
LIST OF TABLES.....	8
LIST OF FIGURES.....	9
LIST OF ABBREVIATIONS.....	14
ABSTRACT.....	15
CHAPTER	
1 OYE1 AND BIOCATALYSIS.....	17
The Isolation and Discovery of OYE1.....	17
History of Purification and Spectral Characterization.....	18
The Structure of OYE1.....	21
Overall Structure.....	22
The FMN Binding Environment.....	24
The Active Site of OYE1.....	26
The Catalytic Cycle and Mechanism of OYE1.....	28
Aromatization of Cyclic Enones: A Dismutation Reaction in OYE1.....	31
Biocatalysis and the Potential of OYE1 as a Suitable Catalyst.....	33
Expectations and Limitations.....	33
OYEs as Biocatalysts.....	34
Earlier Studies of OYE1's Substrate Size and Stereocomplementarity.....	37
2 UNCOVERING STEREOCOMPLEMENTARITY IN <i>S. pastorianus</i> OYE1.....	42
Stereocomplementarity in OYE1: Accessing the "Other" Product.....	42
The "Other" Product and the Different Substrate Binding Modes.....	42
Discriminating Between ( <i>R</i> )-and ( <i>S</i> ): The Grounds for "Flipping".....	43
Addressing the Limitations: Experimental Design.....	44
The Problem.....	44
Experimental Approach and Techniques.....	45
Results and Discussion.....	46
Catalytic Studies of OYE1 Mutants.....	46
( <i>S</i> )-Carvone reductions.....	46
( <i>R</i> )-Carvone reductions.....	47
Probing the Active Site through Charge-Transfer Complex Formation	
Studies.....	49
Crystallography Studies.....	52
Structural overview.....	52
Wild-type.....	53

	Trp116Leu mutant.....	54
	Trp116Ile mutant.....	60
	Trp116Ala mutant .....	64
	Trp116Val mutant .....	68
	Trp116 Thr mutant .....	70
	Trp116 Gln mutant .....	73
	Conclusions and Future Work.....	76
	Experimental Procedures.....	81
	Enzymatic Reductions Screening (Catalytic Studies) .....	81
	Charge-Transfer Formation Assays .....	82
	GC-MS Analysis .....	82
	Site-Directed Mutagenesis .....	83
	Protein Expression and purification .....	84
	Crystallographic Studies.....	86
	Structure Solution.....	87
	Enzyme-substrate Complex Modeling.....	88
3	STRUCTURAL AND CATALYTIC CHARACTERIZATION OF <i>P. stipitis</i> OYE2.6, A USEFUL CATALYST FOR ALKENE REDUCTIONS.....	89
	Background and Motivation .....	89
	Results and Discussion.....	92
	Overall Fold .....	93
	Quaternary Structure.....	94
	Flavin Environment and Phenol Binding.....	97
	The Active Site and Ligand Binding.....	100
	Catalytic Characterization through Mutagenesis .....	107
	Conclusions and Future Direction .....	113
	Experimental Procedures.....	116
	Protein Purification .....	116
	Native Gel Filtration.....	117
	Crystallogenesis.....	118
	Structure Solution.....	120
	Phenol Binding Studies .....	121
4	CHARACTERIZATION OF <i>Lactococcus lactis</i> CV56 DIHYDROOROTATE DEHYDROGENASES IA AND IB .....	122
	Introduction and Rationale .....	122
	Background and Experimental Design.....	124
	DHODase Function .....	124
	Catalytic Cycle and Electron Acceptors.....	125
	Structural Similarities and Potential as an Alkene Reductase .....	127
	Results and Discussion.....	129
	<i>Lactococcus lactis</i> CV56 DHOD 1A Cloning, Expression and Purification .....	129
	<i>Lactococcus lactis</i> CV56 DHOD 1B .....	133
	Introduction .....	133

Cloning, expression and purification .....	134
Crystallization and Structure of <i>L. lactis</i> CV56 DHOD 1B.....	139
Substrate Specificity and Mutagenesis Targets.....	145
Characterization of Ile74Glu and Ile74Asp .....	147
Characterization of the G75N and I74E/G75N Mutants.....	148
Steady-state Kinetics and Catalytic Efficiency .....	149
Wild-type .....	150
Ile74Asp mutant .....	150
Ile74Glu mutant.....	151
Gly75Asn mutant .....	151
Ile74Glu/Gly75Asn mutant .....	151
Residues 74 and 75 can Disrupt Electron Transfer to the $\beta$ -subunit .....	152
Kinetic studies of oxidase reactions .....	152
Choosing between NAD <sup>+</sup> and oxygen: studies of uncoupling .....	156
Conclusion and Future Directions .....	161
Experimental Procedures.....	167
Site-Directed Mutagenesis .....	167
Protein Expression and Purification.....	168
Crystallographic Studies.....	170
Structure Solution.....	171
Steady-State Kinetics .....	171

## APPENDIX

A SELECTED GC-MS DATA .....	173
B PLASMID CONSTRUCTS USED .....	176
C PURIFIED OYE1 SDS-PAGE ANALYSIS.....	179
D GEL FILTRATION OF PROTEIN LADDER AND LINEAR REGRESSION .....	180
LIST OF REFERENCES .....	181
BIOGRAPHICAL SKETCH.....	190

## LIST OF TABLES

<u>Table</u>	<u>page</u>
1-1 Reductions of 2 and 3-alkyl-substituted 2-cyclohexenones .....	38
2-1 X-ray Crystallographic Data Collection and Refinement Statistics.....	59
2-2 X-ray Crystallographic Data Collection and Refinement Statistics.....	61
2-3 X-ray Crystallographic Data Collection and Refinement Statistics.....	67
2-4 X-ray Crystallographic Data Collection and Refinement Statistics.....	69
2-5 X-ray Crystallographic Data Collection and Refinement Statistics.....	71
2-6 X-ray Crystallographic Data Collection and Refinement Statistics.....	75
2-7 Mutagenic primers utilized for constructing the enzymes used for X-ray crystallography. ....	83
3-1 X-ray Crystallographic Data Collection and Refinement Statistics.....	106
4-1 X-ray Crystallographic Data Collection and Refinement Statistics.....	144
4-2 Steady-state parameters of wild-type and mutant DHOD 1B enzymes .....	149
4-3 Steady-state parameters of wild-type and mutant DHOD 1B enzymes .....	154
4-4 Catalytic Properties of WT and DHOD 1B mutants. ....	162
4-5 Mutagenic primers utilized for constructing the mutant enzymes. ....	167

## LIST OF FIGURES

<u>Figure</u>	<u>page</u>
1-1	Respiratory chain described by Warburg and Christian..... 18
1-2	Spectra of free oxidized and complexed OYE1.. ..... 20
1-3	The overall structure of OYE1. .... 23
1-4	The FMN environment and direct hydrogen-bonding network..... 25
1-5	The active site of OYE1 and interactions with the ligand <i>p</i> -HBA.. ..... 27
1-6	The catalytic cycle of OYE1 shows the reductive and oxidative half- reactions..... 28
1-7	The kinetic mechanism of OYE1. $S_{ox}$ is oxidized substrate and $S_{red}$ reduced. ... 29
1-8	The simplified chemical mechanism of OYE1..... 30
1-9	Observed dismutation reaction products of ODE and 2-cyclohexenone..... 31
1-10	Dismutation reaction..... 32
1-11	2 and 3-alkyl-substituted 2-cyclohexenones tested in OYE1 reductions. .... 37
1-12	Stereo-view of the modeled pseudo-Michaelis complex of 3-ethyl-2- cyclohexenone and OYE1. .... 39
1-13	The unexpected stereochemical outcomes of OYE1-mediated reductions of ( <i>R</i> )-and ( <i>S</i> )-carvone..... 41
2-1	The alternative binding mode hypothesis. .... 42
2-2	Stereocomplementarity in OYE1 variants..... 45
2-3	The results of ( <i>S</i> )-carvone reductions..... 47
2-4	The results of ( <i>R</i> )-carvone reductions.. ..... 48
2-5	This scheme shows the geometric constraints for ( <i>S</i> )-and ( <i>R</i> )-carvone oxidation in the reductive half-reaction ..... 50
2-6	Charge-transfer complex formation activities of Trp116 with ( <i>S</i> )-carvone (light bars) and ( <i>R</i> )-carvone (dark bars). .... 51
2-7	Panels A and B show results from OYE1 and ligands co-crystallization..... 53

2-8	Yellow and green crystal forms.....	55
2-9	The normal binding mode.....	56
2-10	OYE1 Trp116Leu.....	57
2-11	OYE1 Trp116Ile.....	62
2-12	Detailed view of Trp116Ile.....	63
2-13	OYE1 Trp116Ala.....	65
2-14	Schematic representation of ( <i>R</i> )-carvone formation from (+)-dihydrocarvone, via an enzymatic oxidation (dehydrogenation). ....	66
2-15	OYE1 Trp116Val.....	68
2-16	Crystal Structure of the Trp116Thr mutant.....	70
2-17	OYE1 Trp116Gln.....	74
2-18	Alignment of all four binding modes.....	77
2-19	The correlation between the ligand's C8-116 side chain distance and the fraction of flipped product.....	78
2-20	Hydrophobic pockets created in OYE1.....	80
2-21	Temperature program for GC-MS analysis on DB-17 cloumn.....	82
3-1	Reductions of Baylis-Hillman Adducts by Alkene Reductases.....	90
3-2	Partial sequence conservation in seven OYE family representatives.....	91
3-3	Comparison of OYE1 and OYE2.6 stereoselectivity.....	91
3-4	Superposition of the structures of OYE2.6 (cyan) and OYE1 (orange).....	93
3-5	The proposed OYE2.6 dimer. The 2-fold molecular axis is indicated by a dashed line.....	95
3-6	OYE2.6 crystal lattice.....	96
3-7	OYE1 crystal lattice.....	97
3-8	The FMN biding environment and direct interactions. Hydrogen-bonds are shown as black dashes.....	98
3-9	Complex formation between OYE2.6 and <i>p</i> -CP.....	99

3-10	Complex formation with <i>p</i> -HBA.....	100
3-11	The active site comparison of OYE2.6 and OYE1.....	101
3-12	OYE2.6-malonate complex.....	102
3-13	OYE2.6-nicotinamide complex. ....	103
3-14	Crystal structure of OYE2.6 in complex with <i>p</i> -chlorophenol.....	105
3-15	Structures of the three Baylis-Hillman adducts tested. ....	107
3-16	Mutations of positions 188 and 191.....	109
3-17	Effects of mutations of amino acid Thr35. ....	110
3-18	Mutations of positions 113 and 116.....	111
3-19	Comparison of OYE 2.6 and <i>S. pastorianus</i> OYE1 complexes. ....	114
3-20	Elution profile of OYE2.6.. ....	118
3-21	X-ray diffraction images of crystals.....	119
4-1	The pyrimidine <i>de novo</i> biosynthesis.....	125
4-2	The catalytic cycle of DHOD.....	126
4-3	Active site alignment of OYE1 and DHOD 1A.. ....	129
4-4	The primers utilized to clone the <i>pydA</i> gene from <i>L. lactis</i> CV56.....	130
4-5	SDS-PAGE analysis of <i>E. coli</i> cells carrying pYAP-3.. ....	131
4-6	Region of <i>L. lactis</i> CV56 genome containing the <i>pyrZ</i> and <i>pyrD</i> genes.....	135
4-7	Absorption spectrum of DHOD 1A.....	136
4-8	Elution profile of the purified DHOD 1B. The enzyme elutes at 11.4 mL primarily.....	137
4-9	The absorption spectrum of the purified DHOD 1B. ....	138
4-10	Wild-type DHOD 1B crystal optimization .....	140
4-11	X-ray diffraction pattern at different temperatures. ....	141
4-12	The biological heterotetramer of DHOD 1B.....	142
4-13	The conformational changes in the active site loop.....	143

4-14	Potential substrates for DHOD 1B that would complement the substrate range in our existing library of OYE-like alkene reductases. ....	145
4-15	Active site comparison of DPD and DHOD 1B. ....	147
4-16	Concentration dependence of measured initial velocities $V_o$ for w.t. ....	150
4-17	Concentration dependence of measured initial velocities $V_o$ for the I74D mutant. ....	150
4-18	Concentration dependence of measured initial velocities $V_o$ for the G75N mutant. ....	151
4-19	Concentration dependence of measured initial velocities $V_o$ for the I74E/G75N double mutant. ....	152
4-20	The possible fates of electrons in DHOD 1B.. ....	153
4-21	Concentration dependence of measured initial velocities $V_o$ for wild-type DHOD1B. ....	154
4-22	Concentration dependence of measured initial velocities $V_o$ for the I74D mutant. ....	155
4-23	Concentration dependence of measured initial velocities $V_o$ for the I74E mutant. ....	155
4-24	Concentration dependence of measured initial velocities $V_o$ for the G75N mutant. ....	156
4-25	Uncoupling by wild-type DHOD 1B.....	157
4-26	Uncoupling by I74E DHOD 1B.....	158
4-27	Uncoupling by I74D DHOD 1B.. ....	159
4-28	Uncoupling by G75N DHOD 1B.....	160
4-29	Uncoupling by I74E/G75N DHOD 1B.. ....	160
4-30	Absorption spectra of the five DHOD 1B enzymes studied.. ....	163
4-32	SDS-PAGE analysis of all DHOD 1B enzymes purified in this study.....	170
A-1	Authentic standard (Acros) of (+)-dihydrocarvone containing a mixture of isomers.....	173
A-2	Chromatogram of authentic sample of ( <i>R</i> )-carvone (Acros Organics).....	173

A-3	GC-MS analysis of OYE1 catalyzed ( <i>R</i> )-carvone reduction.. .....	174
A-4	GC-MS analysis of W116A-OYE1 catalyzed ( <i>R</i> )-carvone reduction.....	174
A-5	GC-MS analysis of OYE1 catalyzed ( <i>S</i> )-carvone reduction.....	175
A-6	GC-MS analysis of W116I- OYE1 catalyzed ( <i>S</i> )-carvone reduction.. .....	175
B-1	Plasmid map of all pET-OYE-W116X used for structural studies. ....	176
B-2	Plasmid construct of pYAP-7. DHOD 1A with C-terminal His-tag.....	176
B-3	pYAP-5 encodes pyrD with C-terminal His-tag. ....	177
B-4	pYAP-6 encodes pyrZ with N-terminal His-tag. ....	177
B-5	Basic plasmid construct for pYAP-8, pYAP-9, pYAP-12 and pYAP-13. Each mutant was created using primers listed in Table 4-4.....	178
C-1	Typical purity of OYE1 enzymes used for X-ray crystallography.. .....	179
D-1	Elution profile of the protein standards used for calibration. ....	180
D-2	The linear fit of the molecular weight (log M.W.) versus the relative elution volumes plot. ....	180

## LIST OF ABBREVIATIONS

Abs	Absorbance
DHO	Dihydroorotate
DHOD	Dihydroorotate dehydrogenase
DHOD	Dihydroorotate dehydrogenase
DPD	Dihydropyrimidine dehydrogenase
FAD	Oxidized flavin adenine dinucleotide
FADH <sub>2</sub>	Reduced flavin adenine dinucleotide
FMN	Oxidized flavin mononucleotide
FMNH <sub>2</sub>	Reduced flavin mononucleotide
GC-MS	Gas chromatography-mass spectrometry
GDH	Glucose dehydrogenase
M	Mole/liter
NAD(P) <sup>+</sup>	Oxidized nicotinamide adenine dinucleotide
NAD(P)H	Reduced nicotinamide adenine dinucleotide
OYE	Old yellow enzyme
<i>p</i> -HBA	<i>para</i> -Hydroxybenzaldehyde
UV-Vis	Ultra-violet and visible light

Abstract of Dissertation Presented to the Graduate School  
of the University of Florida in Partial Fulfillment of the  
Requirements for the Degree of Doctor of Philosophy

UNCOVERING STEREOCOMPLEMENTARITY IN TWO ALKENE REDUCTASES OF  
THE OLD YELLOW ENZYME FAMILY AND THE DIFFERENT FATES OF  
ELECTRONS IN THE SECOND HALF-REACTION OF DIHYDROOROTATE  
DEHYDROGENASE 1B

By

Yuri Alexey Andreiw Pompeu

August 2013

Chair: Jon D. Stewart  
Major: Chemistry

The first portion of this work reports the efforts towards uncovering the factors controlling stereoselectivity in two alkene reductases belonging to the Old Yellow Enzyme family. We demonstrate, through site-saturation mutagenesis the impact that each of the 20 amino acids has on the stereochemical outcome of OYE1 mediated carvone reductions. Furthermore, in order to explain the stereochemical diversity observed we investigated, at an atomic level, the most interesting OYE1 variants using high resolution single crystal X-ray crystallography. The structure elucidation of OYE2.6, an OYE1 homolog that displays desirable physical and catalytic properties, is also presented. In addition to the determination of its three-dimensional and quaternary structures, catalytic characterization was done by mutating key active-site residues. Taken together, these results provide significant insight for future protein engineering projects as well as some guidance towards understanding how, in some cases, minute changes can lead to big differences in the stereoselectivity of these alkene reductases.

The second part of this dissertation describes how, in an attempt to modify substrate specificity in the enzyme DHOD 1B, we uncovered the importance of two amino

acids, Ile74 and Gly75, to the electron transfer mechanism of the enzyme. The design, expression, kinetic characterization as well as the structural elucidation of the wild type enzyme is described in detail. In essence, our results suggest that modifications of positions 74 and 75 in the  $\alpha$ -subunit of *L. lactis* CV56 DHOD1B can impact the enzyme's dehydrogenase and oxidase activities to different extents. In one extreme example, mutation of Ile 74 to Glu completely abolished catalytic activity towards NAD<sup>+</sup> while retaining oxidase activity that was comparable to that of the wild-type enzyme.

## CHAPTER 1 OYE1 AND BIOCATALYSIS

### **The Isolation and Discovery of OYE1**

Old yellow enzyme (OYE, EC 1.6.99.1), was the first enzyme found to contain flavin as a prosthetic group required for catalysis and has served as a model for many flavin dependent oxidoreductases. In recent years the catalytic activity of this enzyme and an entire subset of related homologs have appeared in the literature as valuable catalysts with industrial applications<sup>1</sup>. Old Yellow Enzyme was first isolated from the brewers' bottom yeast *Saccharomyces carlsbergensis* (so named after the Danish brewery, Carlsberg, where it was first isolated and later reclassified as *Saccharomyces pastorianus*) by Warburg and Christian in 1932<sup>2</sup>. Their original aim was to elucidate the nature of biological oxidations in yeast. In the course of their work, a yellow protein was isolated from portions of yeast lysate termed "*gelbe ferment*" (yellow ferment). This yellow protein was present in appreciable amounts in the lysate and it was noted that addition of the yellow lysate would facilitate the oxidation of glucose-6-phosphate in the presence of a thermostable "coferment". The observations made by Warburg and Christian ultimately described a respiratory chain consisting of the oxidation of glucose-6-phosphate in the presence of NADP<sup>+</sup>/NADPH and glucose-6-phosphate dehydrogenase (Figure 1.1). In 1938, Haas independently reported the discovery of a new yellow protein homolog in yeast<sup>3</sup> which then led to the designation of Warburg and Christian's enzyme as "Old". The name has persisted and the original enzyme in the "*gelbe ferment*" is now called Old yellow enzyme, or simply OYE. Remarkably, despite the overabundance of kinetic and structural data about OYE1 and many other homologs

that has been accumulated in the last 80 years, the natural substrate and the exact function of OYEs remains a topic for debates among researchers.

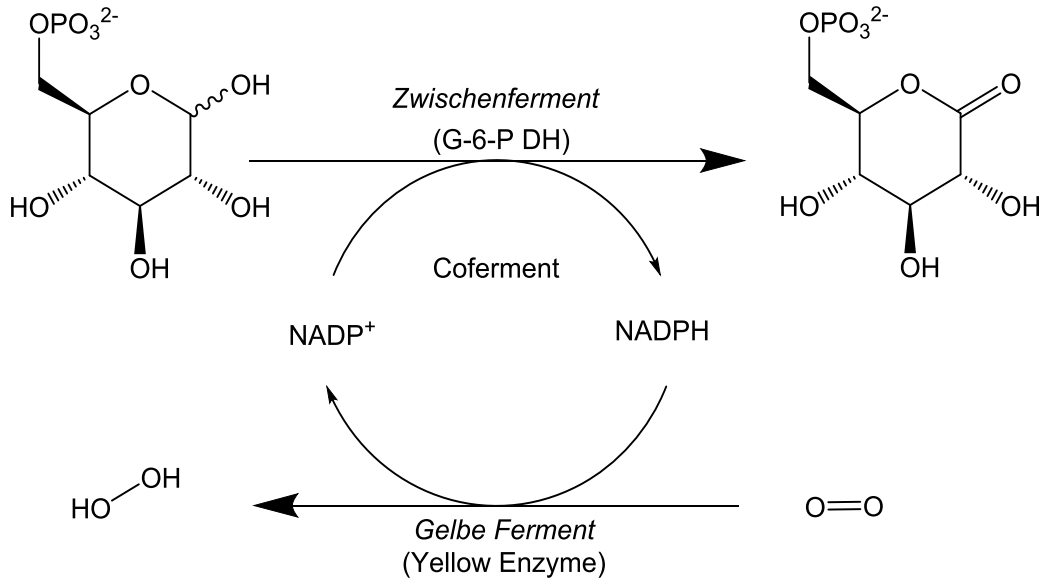


Figure 1-1. Respiratory chain described by Warburg and Christian. Glucose-6-phosphate is oxidized by glucose-6-phosphate dehydrogenase (zwischenferment) in the presence of NADP<sup>+</sup> (coferment). Old Yellow Enzyme (gelbe ferment) serves to regenerate NADP<sup>+</sup> by facilitating a 2-electron transfer from NADPH to molecular oxygen.

### History of Purification and Spectral Characterization

Following the work of Warburg and Christian, Theorell and Åkeson, developed a more robust isolation and purification method which allowed for more accurate and therefore conclusive studies of Old Yellow Enzyme <sup>4</sup>. Their procedure consisted of the lysis of dry yeast cells, followed by several precipitation steps using lead acetate, cold acetone, ethanol and ammonium sulfate and adsorption onto a 4% calcium phosphate gel. The eluted enzyme could be crystallized through dialysis using a buffer with gradually increasing amounts of ammonium sulfate. Through analysis of the crystalline OYE it was determined that the enzyme had a molecular weight of approximately

100,000 Da and 2 FMN molecules at a ratio of 1/50,000 Da, suggesting its existence as a functional dimer. The purity of this preparation was assessed using the enzyme's spectroscopic characteristics in the ultraviolet and visible range. It was reported that the enzyme had absorption maxima at 280, 383 and 464 nm. The ratio of  $A^{383}:A^{464}$  was 0.98 and the ratio of  $A^{280}:A^{464}$  was 11.5. The molar extinction coefficient  $\epsilon^{464}$  for the bound flavin mononucleotide had a reported value of  $10,600 \text{ M}^{-1} \text{ cm}^{-1}$ .

In 1969, expanding on the work of Theorell, Matthews and Massey were able to improve on the purification of the Old Yellow Enzyme and carried out an even more detailed characterization of the enzyme <sup>5</sup>. They made the observation that the enzyme preparation appeared green and that upon reduction using sodium dithionite the enzyme solution became colorless. Additionally, when the reduced enzyme was dialyzed extensively it would return to its native yellow color upon reoxidation. Remarkably, when the oxidized yellow enzyme was mixed with the dialysate it regained its green color. It was rationalized that a "green-forming compound" was bound to oxidized enzyme and that it had a diminished affinity for the reduced enzyme and could therefore be removed by dialysis. Several attempts were made to identify the "green forming" compound and it was concluded that the molecule was aromatic with an ionization behavior similar to that of a phenol hydroxyl group shown to be a substrate for xanthine oxidase, albeit a poor one. This change in color was apparent in the enzyme's UV-Vis spectrum as a broad absorption maximum in the 600-680 nm range and it was hypothesized that it was the result of the formation of a charge-transfer complex involving the enzyme's oxidized flavin mononucleotide and the phenolic ligand as it had been observed previously in other flavoproteins <sup>6</sup>. Figure 1.2 shows a typical spectrum of

oxidized Old Yellow Enzyme in its free form and in its charge-transfer complex (“green”) form.

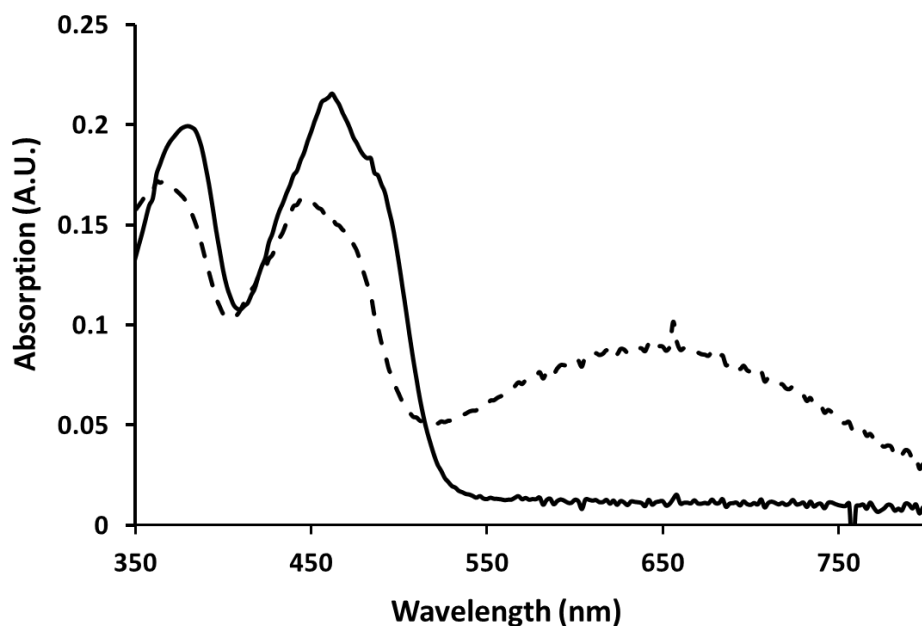


Figure 1-2. Spectra of free oxidized and complexed OYE1. The solid lined spectrum (—) is that of free oxidized OYE1. The dashed lined spectrum (- - -) is that of OYE1 in 80  $\mu$ M 4-chlorophenol, a charge-transfer complex forming ligand.

In a subsequent study, Matthews and Massey were able to isolate and unequivocally identify the “green forming” compound as *para*-hydroxybenzaldehyde. This led to the conclusion that the green appearance of the enzyme was indeed a result of the formation of a charge-transfer complex<sup>7</sup>. In such complex there are direct interactions between the  $\pi$ -systems of the electron rich ligand and the electron deficient oxidized flavin. It was also shown that this and other related phenols were capable of inhibiting Old Yellow Enzyme’s NADPH oxidase activity.

In 1975, Abramovitz and Massey undertook the identification and characterization of many ligands capable of forming charge-transfer complexes with Old Yellow Enzyme. This work showed that charge-transfer complexes had characteristic

absorption maxima in the range of 550-680 nm that varied depending on both the identity of the ligand and the redox potential of the bound flavin. Another important observation was the fact that the observed pH dependence of ligand dissociation strongly suggested that the phenolate form, rather than the conjugate acid form, was responsible for complexation <sup>8</sup>.

Shortly after, Abramovitz and Massey exploited phenol binding to develop an affinity purification technique using a phenol-functionalized resin for the sole chromatographic step <sup>9</sup>. This further facilitated a simpler and more effective isolation of the enzyme from its native host in greater yield. The method consisted of allowing the oxidized enzyme to bind to the phenol-resin followed by elution through the use of a reducing buffer. The reducing agent used was sodium dithionite which quickly reduces OYE's flavin mononucleotide. In the reduced form, OYE's affinity for the phenol resin is greatly diminished causing the enzyme to elute off the chromatographic column.

In 1991 the gene for Old Yellow Enzyme (now termed OYE1) was finally cloned and overexpressed in *Escherichia coli* <sup>10</sup>. Comparison of the overexpressed protein with non-recombinant enzyme preparations led to the discovery that several OYE isozymes were present in brewers' yeast <sup>11</sup>. The cloned gene also led to a homogenous source which allowed the enzyme's unambiguous characterization and later proved to be suitable for structural determination.

### **The Structure of OYE1**

Even though some structural information on OYE1 had been inferred based on extensive studies of the environment around the bound FMN <sup>12</sup>, the complete three-dimensional structure of the protein was highly anticipated. Previous attempts at obtaining OYE1 crystals suitable for structural investigation through X-ray

crystallography, had largely failed. The only crystal forms that could be obtained were of partially proteolytically cleaved enzyme. This was due to the fact that enzyme isolated directed from brewers' bottom yeast is a mixture of at least two different isozymes which formed mixtures of homo and heterodimers<sup>13</sup>. With the cloning of the gene encoding OYE1 by Saito *et al.*<sup>10</sup>, larger amounts of recombinant OYE1 that appeared electrophoretically homogenous could be purified from *E. coli* cells. Homogenous OYE1 preparations resulted in crystal forms that enabled the elucidation of the enzyme's three-dimensional structure<sup>14</sup>.

### **Overall Structure**

The protein contained a single domain consisting of a parallel, eight-stranded  $\alpha/\beta$ -barrel similar to that of triosephosphate isomerase (TIM)<sup>15</sup>. The largely hydrophobic active site is accessible to solvent via a deep cleft. This cleft is, in part, obscured by a flexible loop that has implications in the dynamic binding of the NADPH substrate. FMN binds to OYE1 at the carboxy-terminal end of the barrel in an extended conformation. The isoalloxazine ring lies perpendicular to the barrel axis with the phosphoryl group held between strand  $\beta 7$ , strand  $\beta 8$  and the amino terminus of helix D causing the flavin moiety being placed near the center of the barrel (Fig. 1-3). The FMN is mostly buried, surrounded by the carboxy-terminal loops which cover the end of the barrel and inhibit the access of solvent to the interior of the barrel.

Fox and Karplus also solved the crystal structure of OYE1 with bound *para*-hydroxybenzaldehyde and this structure shed light onto the physical nature of previously discovered charge-transfer interactions<sup>7</sup>. The 2 Å resolution was sufficient to confidently define the orientation of the ligand, and its electron density was quite clear after refinement.

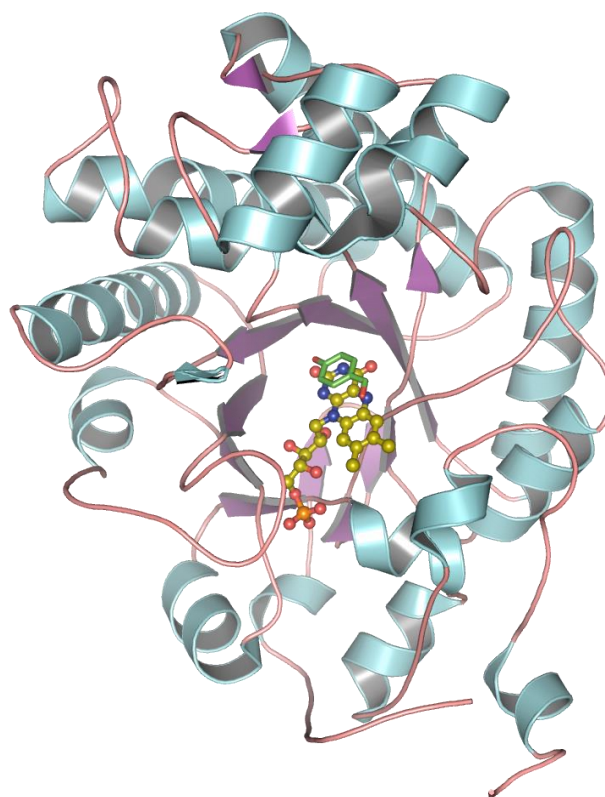


Figure 1-3. The overall structure of OYE1. A single protomer of OYE1 is depicted in cartoon representation, and the flavin mononucleotide cofactor is shown in ball-and-stick representation. The inhibitor *p*-hydroxybenzaldehyde is shown in stick representation. This Figure was generated using the atomic coordinates of PDB code 1OYB

The phenol ring displaces a chloride ion bound in the active site of free OYE1 and is stacked above the *si*-face of the flavin ring with the planes of the two rings approximately parallel. The orientation of the molecule places the phenolate oxygen above the C2 atom of the flavin, interacting with His191 and Asn194 and the aldehyde carbonyl hydrogen bonded to the hydroxyl of Tyr375. The close physical interaction between ligand and FMN, in addition to being geometrically positioned to participate in  $\pi$ - $\pi$  stacking interactions, helped explain the nature of charge-transfer complex formation in OYE1. The enzyme's binding to its substrate NADPH was also investigated through the soaking of OYE1 crystals in a solution containing an NADPH analog. It was

concluded that the binding mode of NADH and NADPH cofactors is largely dictated by the interactions of the nicotinamide's amide group with both His191 and Asn194 through hydrogen bonding. These interactions placed carbon *C4* of the nicotinamide directly above *N5* of the flavin, in a favorable position for a hydride transfer. The remaining portion of the cofactor appeared to be of less importance and this observation helped explain the fact that OYE1 can be reduced by both NADH and NADPH, although a preference for the phosphorylated cofactor is observed.

### **The FMN Binding Environment**

The tightly bound flavin mononucleotide interacts with amino acids that line the interior of the parallel 8 stranded barrel, many of which are highly conserved amongst members of the OYE family<sup>14, 16</sup>. The isoalloxazine moiety of the flavin is involved in direct hydrogen bonds with the side-chains of Thr37, Gln114, Arg243 and the main-chain nitrogen of Gly72. All of these interactions are suspected to have a direct impact on reactivity and or spectral properties of the FMN cofactor in OYE1 and other related flavoproteins<sup>17</sup>. Figure 1-4 illustrates the flavin environment in OYE1.

Xu *et al.*<sup>17c</sup> carried out a more detailed study on the role of Thr37 in flavin reactivity in OYE1. In the crystal structure, Thr37 is hydrogen bonded with the *C4* carbonyl oxygen of FMN through its side-chain hydroxyl group. Such hydrogen bonding is likely to play a role in controlling the properties of the enzyme flavin. To investigate the possible role of the hydrogen bond in catalysis, a Thr to Ala (T37A) mutation of OYE1 was constructed and expressed. The mutation had different effects on the two separate - oxidative and reductive- half-reactions of the enzyme catalytic cycle (this concept will be further explored in the following sections).

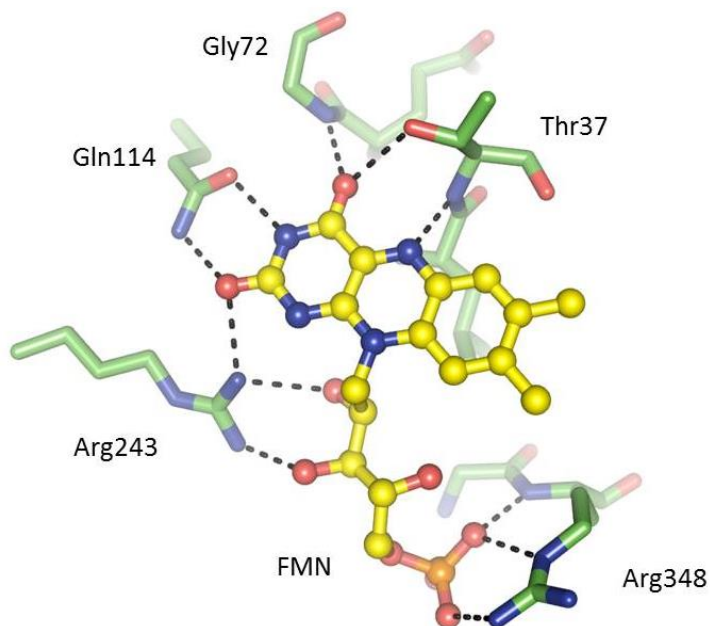


Figure 1-4. The FMN environment and direct hydrogen-bonding network. Figure was generated using the crystallographic model of OYE1 (PDB code 4GBU). Hydrogen bonds are indicated as dashed lines.

The properties of the mutant enzyme were examined in detail through direct measurement of redox potential, binding of phenolic ligands, rapid reaction studies of both the reductive and oxidative half-reactions, and catalytic turnover. The mutant enzyme has enhanced activity in the oxidative half-reaction (loss of electrons by  $\text{FMNH}_2$ ) but the reductive (gain of electrons by FMN) half-reaction is slowed down by more than one order of magnitude. The peaks of the absorption spectra for enzyme bound with phenolic compounds are shifted toward shorter wavelengths than those of wild-type OYE1, consistent with its lower redox potential. It is suggested that Thr37 in the wild-type OYE1 increases the redox potential of the enzyme by stabilizing the negative charge of the reduced flavin through hydrogen bonding with it.

## The active site of OYE1

The active site of OYE1 is situated directly above the *si*-face of the FMN. It is relatively small with a volume of approximately 460 Å<sup>3</sup> (calculated using the CASTp server<sup>18</sup>). It is connected to bulk solvent by a small channel that is roughly 8 Å wide and 10 Å deep. It is also a predominantly hydrophobic cavity as it is defined by amino acids Thr37, Tyr82, Trp116, Leu118, Phe123, Tyr196, Phe250, Pro295, Phe296 and Tyr375.

Two residues possessing more polar properties are found in the back wall of the active site, namely His191 and Asn194. Both side-chains of His191 and Asn194 are positioned directly above the pyrimidine portion of the flavin ring, and are hydrogen bond donors (with nearly ideal geometry) for carbonyl and or phenol(ate) groups of ligands. In fact, as observed in the crystal structure, the hydroxyl group of *p*-HBA is in excellent position to form hydrogen bonds with Nε2 of His191 and Nδ2 of Asn194 (Figure 1-5). These interactions help place the ligand's *meta* carbon directly above the N5 of flavin in a spatial arrangement favorable for a hydride transfer. These observations, along with the NADPH analog binding orientation (discussed above), led to the belief that this binding mode is also shared by other substrates of OYE1. Also evident in the crystal structure, the aldehyde group of *p*-HBA forms a hydrogen bond with the side-chain hydroxyl of Tyr375, which moved significantly in comparison to the unliganded OYE1 structure. Given their position in the active site and the evidence for direct interactions with ligands, His191 and Asn194 were thought to be of great relevance in the mechanism of OYE1.

In 1998, Brown *et al.* carried out studies specific OYE1 mutants in order to evaluate the roles played by these two amino acids.

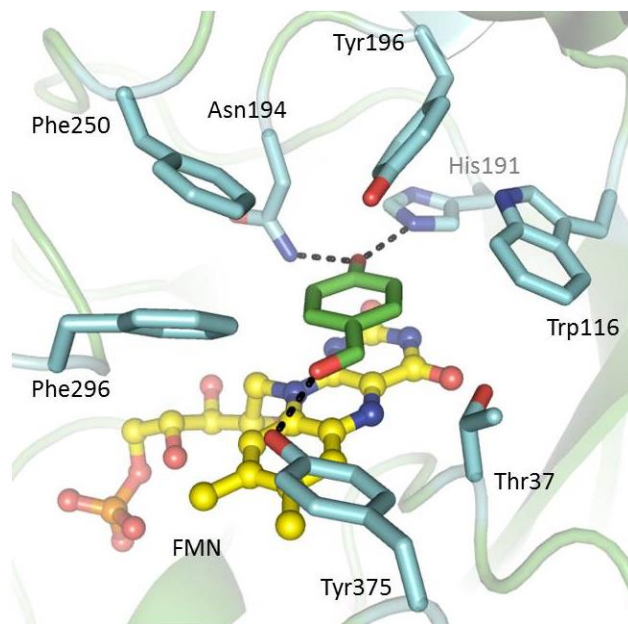


Figure 1-5. The active site of OYE1 and interactions with the ligand *p*-HBA. Hydrogen bonds are indicated by dashed lines. The FMN cofactor is shown in ball-and-stick, the amino acids and *p*-HBA as sticks. The Figure was generated using coordinates from PDB code 1OYB.

Mutations of His191 to Asn, Asn194 to His, and a double mutation, H191N/N194H, were made within OYE1. The N194H protein was expressed at very low levels and could not be purified. The H191N mutant and the H191N/N194H double mutant were successfully expressed and purified and their properties were evaluated. The two mutant forms had the expected effect on phenolic ligand binding, *i.e.* decreased binding affinity and decreased charge-transfer absorbance. In the case of *para*-chlorophenol, the  $K_D$  value increased from 1  $\mu\text{M}$  in the wild type to 2400  $\mu\text{M}$  in the H191N mutant. It had been previously established that the formation of charge-transfer complexes occur via the phenolate form of ligands<sup>8</sup>, thus it was concluded that the mutations caused a decreased stabilization of the phenolate anion. Reduction of the H191N mutant enzyme by NADPH was similar to that of OYE1, but the reduction rate constant for NADH was greatly decreased. The double mutant enzyme had an increased rate constant for

reduction by NADPH, but the reduction rate constant with NADH was lower by a factor of 15. The reactivity of OYE1 and the mutant enzymes with oxygen was similar, but the reactivity of 2-cyclohexenone was greatly decreased by all of the mutations. The crystal structures of the two mutant forms showed only minor changes from that of the wild type enzyme.

### The Catalytic Cycle and Mechanism of OYE1

Since its early discovery in 1932, OYE1 has been known to catalyze the oxidation of NADPH in the presence of molecular oxygen ( $O_2$ ) as an electron acceptor. The discovery of other substrates that could serve as electron acceptors, in addition to vast spectral knowledge, allowed for the conception of a clear model for the catalytic cycle of the enzyme (Figure 1-6)<sup>11, 19</sup>.

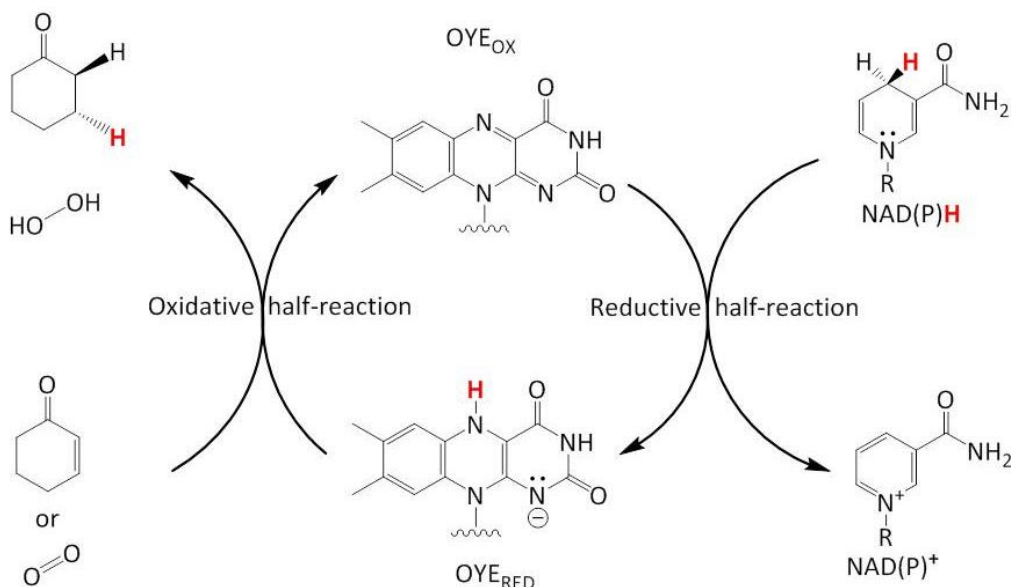


Figure 1-6. The catalytic cycle of OYE1 shows the reductive and oxidative half-reactions. Oxygen and the model substrate 2-cyclohexenone are shown as possible electron acceptors.

The accepted reaction cycle suggests a ping-pong mechanism. In fact, data for kinetic assays with different substrates have always been reported to yield sets of

parallel lines in double reciprocal plots. Additionally, the initial observation that the nicotinamide binds to the same site as substrate analogs do also served as substantiating evidence for a classic ping-pong mechanism (Figure 1-7).

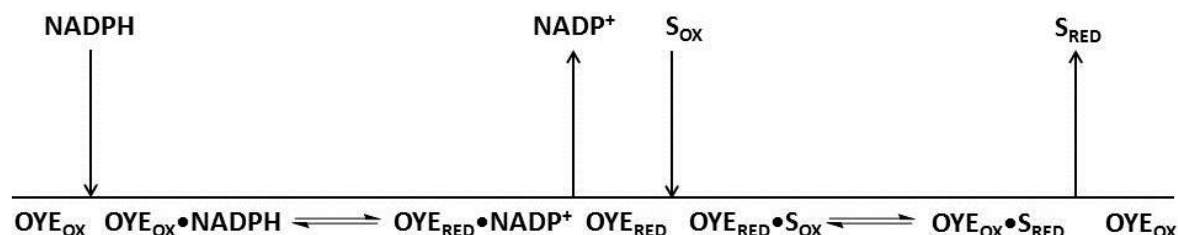


Figure 1-7. The kinetic mechanism of OYE1. S<sub>OX</sub> is oxidized substrate and S<sub>RED</sub> reduced.

By the mid 1990's, much was known about the roles of several of the residues forming the active site of OYE1. A surplus of kinetic and spectroscopic data derived not only from the wild type enzyme but also from several mutants had been reported as well. In a 1995 study Vaz et al. showed through deuterium labeling experiments that OYE1 catalyzed the net trans-addition of H<sub>2</sub> across the olefinic bond of an  $\alpha,\beta$ -unsaturated aldehyde, namely cinnamaldehyde<sup>19</sup>. These findings and the existence of an atomic model of the enzyme enabled the proposition of detailed chemical mechanism of the enzyme. In the reductive half-reaction, reduced nicotinamide cofactors bind OYE1. In the active site, two hydrogen bonds formed by His191, Asn194 and the nicotinamide amide carbonyl place its carbon C4 directly above N5 of the flavin favoring a hydride transfer. After completion of the reductive half-reaction, oxidized cofactor dissociates and oxidized substrates can enter the active site to react. Similarly, the substrate is properly oriented primarily through the hydrogen bonds formed by its carbonyl oxygen atom and the enzyme's His191 and Asn194. In addition to playing a key role in substrate orientation, the polar nature of these hydrogen bonds -

accentuated by His191's ability of carrying a positive charged - is thought to aid in stabilization of the enolate form of the substrate. This stabilization would activate the substrate by increasing the  $\beta$ -carbon's electron deficiency, making it more susceptible to a hydride attack from the flavin. A hydride attack to the  $\beta$ -carbon would build electron density in the  $\alpha$ -carbon and its protonation would complete the net *trans*-addition of  $H_2$ . Tyr196 is positioned directly above the substrate's  $\alpha$ -carbon at a distance of 3.41 Å, making it an obvious candidate for the protonation step. Results show that mutation of Tyr196 to Phe severely impairs the rate of the oxidative-half reaction in OYE1<sup>20</sup> with  $k_{cat}$  being decreased by nearly 6 orders of magnitude with 2-cyclohexenone. Figure 1-8 shows the chemical mechanism of the oxidative half reaction for OYE1.

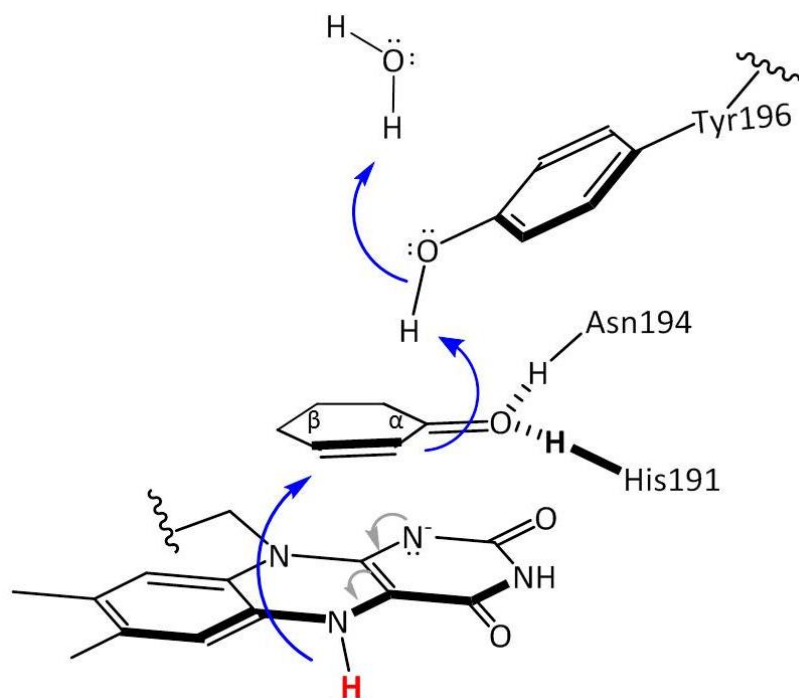


Figure 1-8. The simplified chemical mechanism of OYE1. The illustration shows the oxidative half-reaction, wherein fully reduced flavin ( $FMNH_2$ ) transfers a hydride to the  $\beta$ -carbon of 2-cyclohexenone and protonation of the  $\alpha$ -carbon occurs concomitantly.

## Aromatization of Cyclic Enones: A Dismutation Reaction in OYE1

With the discovery that  $\alpha,\beta$ -unsaturated ketones could be reduced by OYE1, the search for novel and more diverse substrates began. Curiously it was observed that when OYE1 was allowed to react with certain cyclic 2-ene-1-ones in the absence of an electron donor such as NADPH, a long wavelength absorption band developed in the UV-Vis spectrum of the enzyme. This band had absorption maxima values in the 550-680 nm range and it was a rather broad peak strongly resembling those previously seen in charge-transfer complex spectra. In 1995 Vaz *et al* carried out a more detailed investigation of this phenomenon and reported a new reaction pathway in OYE1<sup>19</sup>. Figure 1-9 shows two of the reactions observed in the study.

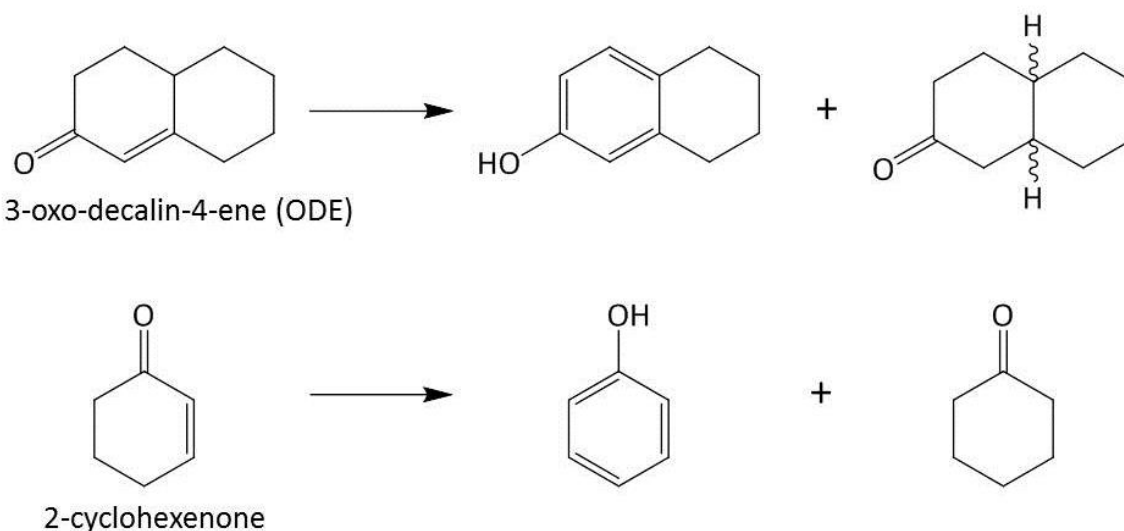


Figure 1-9. Observed dismutation reaction products of ODE and 2-cyclohexenone.

In this dismutation pathway, the reductive half-reaction is accomplished by abstracting electrons from the enone to generate FMNH<sub>2</sub>, the reduced form of the enzyme. This results in a two-electron oxidation of the enone creating a second C-C double bond. In the case of six-membered ring enones, the oxidized molecule is a 2,5-

diene-1-one that can undergo a thermodynamically favorable tautomerization to gain aromaticity and form a phenol (Figure 1-10 C). In the oxidative half-reaction, the enzyme can reduce a second molecule of substrate to return to its original oxidized state thus completing the catalytic cycle. One consequence of this proposed mechanism is that in each half-reaction the substrate must bind in different orientations in the active site, more specifically in different orientations relative to *N5* of the flavin. Figures 1-10 A,B show a rationalization of the different binding modes in the reductive and oxidative half-reactions.

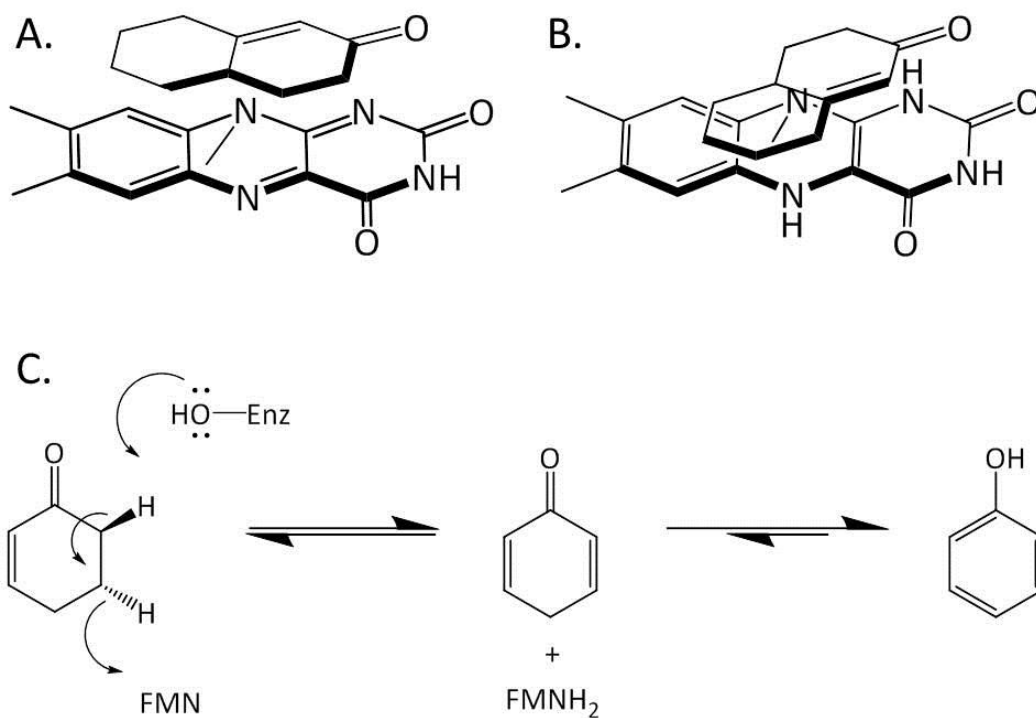


Figure 1-10. Dismutation reactions. Panels A and B illustrate the proposed binding modes of ODE in the reductive and oxidative half-reactions, respectively. Panel C shows the proposed simplified mechanism for the formation of the phenolic inhibitor from a cyclic enone.

## Biocatalysis and the Potential of OYE1 as a Suitable Catalyst

### Expectations and Limitations

Over the past few years the use of enzymes as biocatalysts for the preparation of enantiopure active compounds has become an established manufacturing process in the speciality (applied fine chemicals) and pharmaceutical industry. The employment of biocatalysts is attractive for synthetic organic chemists as a consequence of the controlled insertion of chirality and selectivity with regard to regio- and stereochemistry in molecules and the simple usage in technical production units. Thus many researchers are discovering the advantages in utilizing these natural catalysts for producing optically active, higher value molecules. In particular as multiple process steps can be circumvented or combined, the natural catalysts are contributing to more economic industrial processes. Natural evolution has provided a number of enzymes with high enantio and positional (regio) selectivities suitable for the synthesis of enantiomerically pure compounds with few byproducts<sup>21</sup>. making biocatalysis an attractive option in synthesis. In fact, enzymes have been exploited in organic chemistry for more than one hundred years with a number of notable industrial examples<sup>22</sup> and references therein. Therefore, the use of enzymes for the production of high value pharmaceuticals and fine chemicals is at the forefront of the quest for mild and ecologically sustainable processes<sup>23</sup>.

Biocatalysis has, however, traditionally suffered in many cases from limitations associated with narrow substrate scope, incomplete enantioselectivities and insufficient robustness. In reality, the range of chemical reactions open to biocatalysis is limited, due to the disadvantageous reaction conditions in an aqueous environment near physiological conditions and enzymes' usual limited reactivity towards more complex

larger chemical compounds. Nature has evolved a pool of catalysts which operate most effectively under physiological conditions and on a narrow range of natural substrates. While these characteristics are optimal for sustaining life, naturally occurring enzymes are often not suitable for biocatalytic processes without further tailoring or redesign. The pioneering work of Frances Arnold and Pim Stemmer on directed evolution set the ground for implementing evolution of enzymes for the synthesis of technological useful compounds<sup>24</sup>.

### **OYEs as Biocatalysts**

Asymmetric catalysis plays a pivotal role in modern synthetic organic chemistry and the increasing demand for optically pure building blocks has fueled interest in identifying and creating new stereoselective catalysts. In particular, the use of alkene reductases is regarded as an attractive option since the reduction of a C-C double bond generates two adjacent  $sp^3$  centers and opens the possibility for the creation of two distinct chiral centers in a single step. Existing synthetic methods of asymmetric hydrogenations currently involve the use of precious metals in conjunction with chiral phosphines. In addition, the organocatalytic hydrogenation of cyclic enones to allow the synthesis of a wider range of enantiomerically pure organic compounds has been developed as well<sup>25</sup>. However, enzymes continue to be competitive catalysts in asymmetric syntheses due to their low costs, ability to manipulate the substrate specificity through site-directed mutagenesis) and the need for typically mild operating conditions such as atmospheric pressure, mild temperatures and pH.

The Old Yellow Enzyme family is a classic example of enzymes able to catalyze the reduction of certain alkenes to produce many commercially useful substrates and synthons. Since the discovery of its first family member nearly 80 years ago, these

flavin dependent enzymes have been shown to catalyze the reduction of the C-C double bond of  $\alpha,\beta$ -unsaturated ketones, aldehydes, nitro alkenes, carboxylic acids and esters<sup>26, 27, 28, 29</sup>. The potential applicability of OYEs has also been tested in improving established synthetic processes such as reduction of  $\beta$ -nitro acrylates to produce  $\beta^2$ -amino acids<sup>30</sup>.

As mentioned before, there are some limitations on the applicability of enzymes for extensive organic synthesis and OYEs share many of these inadequacies. Firstly, most of the family members, including OYE1, display optimal pH values for activity near physiological values and the same trend is followed in their optimal temperature profile, which is around 37 °C. Two enzymes in this class, namely *Thermus scotoducts* SA-10 chromate reductase (CrS)<sup>31</sup> and *Thermoanaerobacter pseudoethanolicus* E39 TOYE<sup>32</sup>, have been reported to display higher tolerances towards elevated temperatures. Both enzymes maintained significant activities in temperatures near 60-65 °C. Perhaps not surprisingly, these values are close to the optimal growth temperature of their respective host organisms. Another aspect that can keep biocatalysts from being suitable for a synthetic route is the lack of denaturation resistance in the presence of organic solvents. It is often the case that solvent tolerance is related to temperature tolerance and researchers may turn to thermophilic organisms in search of a suitable biocatalyst. While it may be possible to find an enzyme that catalyzes the reaction of interest in a thermophilic organism which tolerates harsh solvents and gives the expected optically pure enantiomer, the reality is that, frequently, a biocatalyst has several inherent limitations that keep it from being ideal.

In the case of OYEs, and the majority of naturally occurring enzymes, the substrate range is rather narrow. Enzymes generally evolve to catalyze a specific reaction, it is therefore expected that a great preference towards a single substrate be observed. Even though OYEs have been shown to work on a variety of substrates, a more detailed analysis indicates that most of the substrates share some common features and have limited diversity as a whole. The substrates' alkenes must be activated and are usually conjugated to carbonyls of ketones, aldehydes, esters and to a lesser extent, acids. In addition, some nitro alkenes can serve as substrates<sup>26, 33</sup> and the reduction of nitrile containing alkenes by "enoate reductase" ERED has been reported although it is uncertain whether this enzyme is a true member of the OYE family<sup>34</sup>. Substrate size is another limitation in this class of enzymes. As described in previous sections, the active site of OYE1 is relatively small and secluded by a narrow opening which limits the nature and the number of substituents that can be found in substrates. This observation generally holds true for other members that have been structurally characterized to date. Another challenge encountered with OYEs is related to their stereoselectivity. Owing to the generally conserved active site architecture that is seen across several members of the family, OYEs tend to display little stereochemical diversity. The work of Bougioukou (PhD thesis and references therein) has shown that many OYE1 display nearly identical stereoselectivities towards a number of enones, enals and nitro alkenes. The lack of stereochemical diversity in OYE-mediated alkene reductions is a natural consequence of the multipoint binding of the alkene substrate and FMN along with the fixed location of the highly conserved proton donor Tyr196.

## Earlier Studies of OYE1's Substrate Size and Stereocomplementarity

Substrate size restriction in OYE1 is particularly apparent in the 3-alkyl-substituted 2-cyclohexenone class of substrates (Figure 1-11). In 2006, Swiderska and Stewart<sup>28</sup> conducted a systematic investigation that looked to shed some light on the enzyme active site restrictions. A series of 2 and 3-alkyl-substituted cyclohexenones were screened in OYE1 mediated reductions (Figure 1-11).

It was evident that that as the size of the alkyl substituents increased, their conversions efficiencies decreased. The general substrate preferences are: Me>Et>*n*-Pr>*i*-Pr>>*n*-Bu for enones substituted at position 3-, and a similar trend was seen for substitutions at position 2- (Me>Et). Under the experimental conditions, 100% of 3-methyl-2-cyclohexenone was reduced while no reaction was detected with the substrate 3-butyl-2-cyclohexenone (Table 1-1).

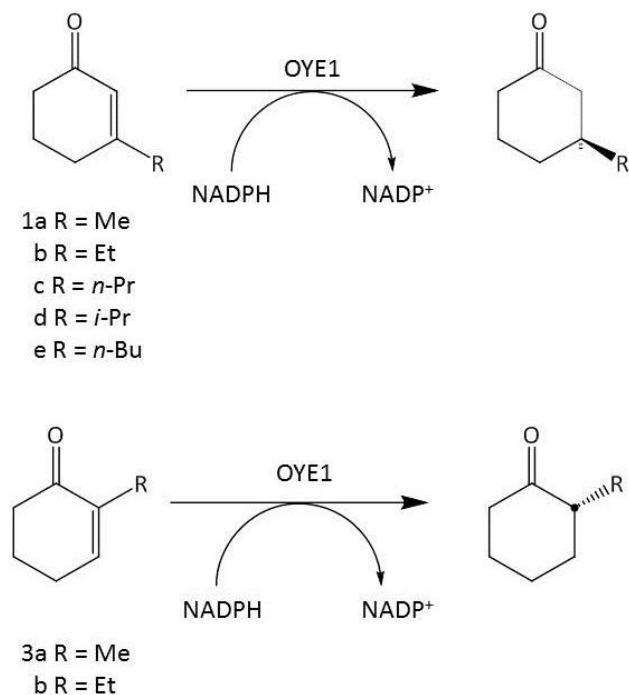


Figure 1-11. 2 and 3-alkyl-substituted 2-cyclohexenones tested in OYE1 reductions.

Since the generation of chiral centers from the starting alkene requires substitutions at positions 2 and 3, improvement upon size limitations could positively impact OYE1's applicability for a wider range of synthetic routes.

Table 1-1. Reductions of 2 and 3-alkyl-substituted 2-cyclohexenones

Ketone	R group	Conversion (%)	e.e. (%)	Configuration
1a	Me	100	94	S
1b	Et	76	94	S
1c	<i>n</i> -Pr	25	89	S
1d	<i>i</i> -Pr	18	90	S
1e	<i>n</i> -Bu	ND <sup>1</sup>	-	-
3a	Me	100	96	R
3b	Et	16	94	R

<sup>1</sup>ND. Not detected.

The results reported in this study provided some guidance for new investigations on the active site of OYE1. They also helped draw attention to a particular location in the active site architecture and its potential as a target for subsequent protein engineering studies.

In 2009, during their efforts to address the problem of low rates for larger substrates, Padhi *et al.* unexpectedly uncovered a solution to a different limitation that affects OYEs, namely the lack of stereochemical diversity in these enzymes<sup>35</sup>. Specifically, it was found that conservative changes to a single residue (Trp116) inverted the stereoselectivity of *S. pastorianus* OYE1 for one alkene substrate ((*S*)-carvone). This opened many possibilities for using this enzyme and related biocatalysts in asymmetric synthesis.

It was suspected that, diminished rates for OYE1-mediated reductions of substrates such as 3-ethyl-2-cyclohexenone were a consequence of unfavorable steric interactions with active site residues. The authors hypothesized that increasing the active site volume would alleviate these adverse contacts. To guide these efforts, they modeled a possible Michaelis complex of this substrate (Figure 1-12) and focused attention on residues within 5 Å of the bound substrate as candidates for replacement. Trp116 was selected since its side chain is closest to the 3-substituents of 2-cyclohexenones and changes at this position would be expected to have the largest effect on increasing the active site volume.

Site-saturation mutagenesis utilizing homologous recombination in yeast cells was performed and 200 random colonies had their activities screened for 3-methyl-2-cyclohexenone reduction. Only 19 colonies encoded mutants that sustained at least 50% of the activity seen in wild type. DNA sequencing revealed that six encoded Trp at position 116, six encoded Phe, three encoded Ile (on had an extra mutation), and there were single examples of Leu, Met, and Tyr.

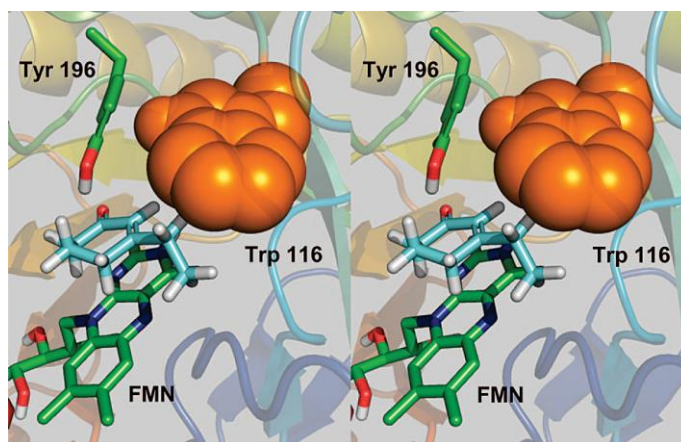


Figure 1-12. Stereo-view of the modeled pseudo-Michaelis complex of 3-ethyl-2-cyclohexenone and OYE1. Reprinted from *J. Am. Chem. Soc.* 2009, 131, 3271–3280. Copyright 2009 American Chemical Society.

Because Phe and Ile were found most commonly, these variants were chosen for further characterization and were purified as GST-fusion proteins. It was expected that OYE variants with smaller residues at position 116 would have higher reduction rates for 3-substituted-2-cyclohexenones; however, this was not observed. In fact, both the Phe and Ile OYE mutants had lower specific activities for both 3-methyl and 3-ethyl-2-cyclohexenone than the wild-type values, although the enantioselectivities were identical (>98% e.e. favoring the (*S*)-products).

Since the initial hypothesis relating improved reaction rates with the identity of the residue at position 116 proved incorrect, purified wild-type, W116F, and W116I OYE1 proteins were tested against a panel of representative enones and enals to see whether these mutations had other effects on OYE properties. The enantiomers of carvone provided a surprising result: while (*R*)-carvone was reduced by all three proteins to the same *trans*-product with very high diastereoselectivity, the fate of the (*S*)-antipode depended on the identity of the residue at position 116 (Figure 1-13).

The wild-type and W116F reduced (*S*)-carvone to *cis*-(2*R*,5*S*)-dihydrocarvone. By contrast, the W116I mutant afforded *trans*-(2*S*,5*S*)-dihydrocarvone. The origin of the altered stereoselectivity displayed by the W116I OYE variant was probed by using (4*R*)-NADPD as the cofactor for reducing (*S*)-carvone. MS analysis of the *trans*-product revealed incorporation of a single deuterium atom, as expected (76% of the total product). The <sup>1</sup>H NMR spectrum showed that the C3 axial proton (*H*<sub>3ax</sub>) of *trans*-(2*S*,5*S*)-dihydrocarvone had been deuterated. This assignment was supported by careful analysis of the coupling patterns

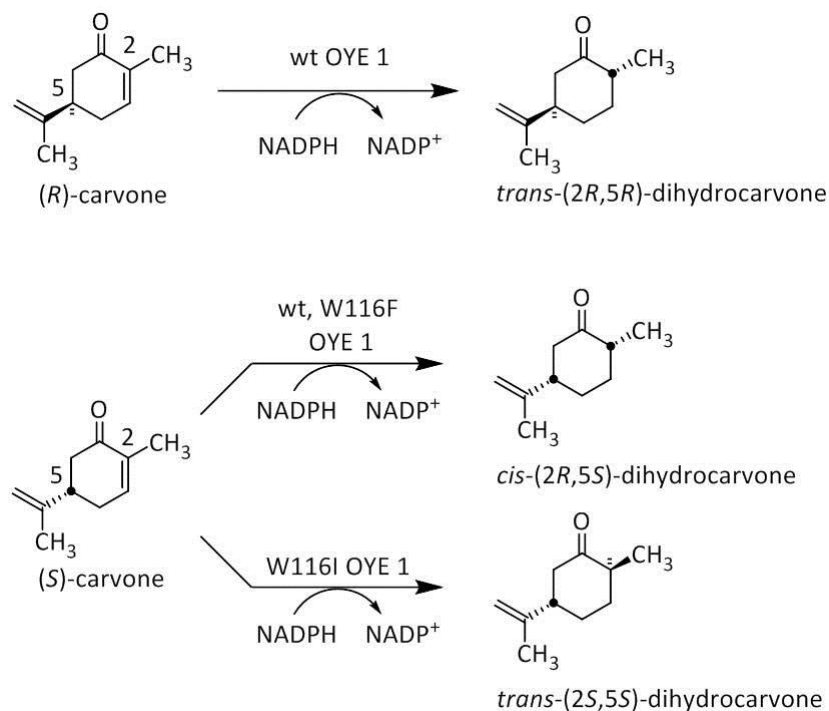


Figure 1-13. The unexpected setereochemical outcomes of OYE1-mediated reductions of *(R)*- and *(S)*-carvone. The Trp116Ile variant reduced *(S)*-carvone to yield a product that was different than that produced by the wild type enzyme.

Taken together, these data indicate that the W116I mutant carries out net *trans*-addition of H<sub>2</sub> across the double bond of *(S)*-carvone however, the substrate binds in a “flipped” orientation compared to that of *(R)*-carvone. This was the first report that an alternative substrate binding mode has been created by protein engineering for a member of the OYE family of alkene reductases.

CHAPTER 2  
UNCOVERING STEREOCOMPLEMENTARITY IN *S. pastorianus* OYE1

**Stereocomplementarity in OYE1: Accessing the “Other” Product**

**The “Other” Product and the Different Substrate Binding Modes**

The work of Padhi *et al.* provided clear evidence that it was possible to achieve stereocomplementary products by making changes in the active site of OYE1. As indicated by the  $^2\text{H}$  NMR studies, the Trp116Ile enzyme- like the wild type enzyme- catalyzed the net trans-addition of  $\text{H}_2$  to (*S*)-carvone. This result is not entirely unexpected considering the geometric constraints imposed by the spatial arrangement of Tyr196 and the FMN cofactor. This observation then suggested that the reversed stereoselectivity was a result of a binding orientation that placed the opposite face of the alkene above the *si*-face of the flavin ring. Alternative binding modes, similar to those proposed by Vaz *et al.*, would offer a plausible explanation for the observed stereochemical outcome. Furthermore, previous *in silico* studies had also suggested the feasibility of alternative Michaelis complexes<sup>35</sup>. The two hypothesized binding modes for (*S*)-carvone are illustrated in Figure 2-1.

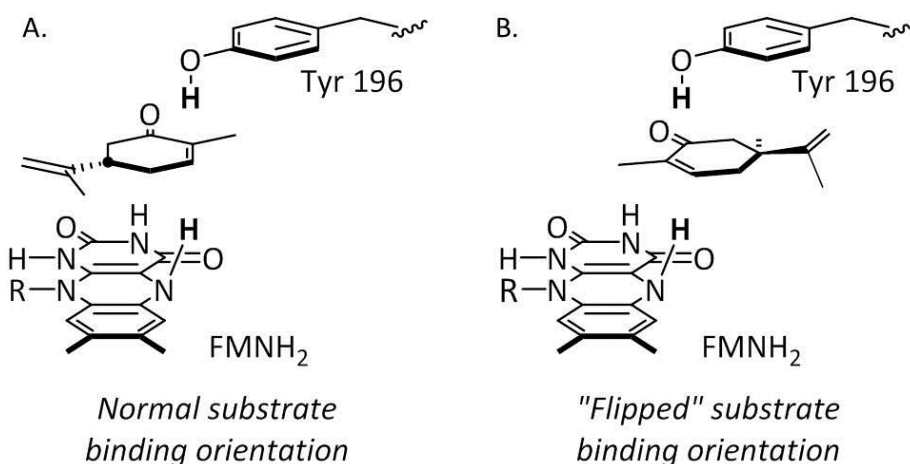


Figure 2-1. The alternative binding mode hypothesis. A. The normal binding mode. B. The flipped binding mode

## Discriminating Between (*R*)-and (*S*): The Grounds for “Flipping”

While the alternative binding mode hypothesis provides a clear explanation for the observed stereochemical diversity displayed by Trp116Ile, it does not offer much guidance in understanding the precise mechanism for a flipped binding mode. Neither does it explain how a particular enzyme variant can discriminate between flipping (*R*)- and (*S*)-carvone. At a first glance, one obvious explanation can be linked to the fact that tryptophan is much larger than isoleucine. A Trp side-chain has an approximate volume of  $169 \text{ \AA}^3$  while Ile is significantly smaller at  $108 \text{ \AA}^3$  (calculated from the values reported by Zamyatin<sup>36</sup>). A Trp to Ile mutation would, therefore, significantly increase the active site volume possibly allowing for an alternative substrate orientation. However, more careful deliberation raises an interesting question that cannot be answered on the bases of molecular volumes alone. How is it possible that the Trp116Ile mutant can lead to a reduction product of (*S*)-carvone that is opposite to that of wild-type while yielding an (*R*)-carvone reduction product that is the same as that of wild-type OYE1?

Another question worthy of asking is: What effect does each amino acid substitution at position 116 have on OYE1's stereochemical outcome? Given the way Padhi and co-workers carried out their original studies, it was unclear whether all 19 possible Trp116 variants were generated. Secondly, the screening procedure was designed to identify OYE1 variants that had high 3-methyl-2-cyclohexenone reductase activity, which could have led to the omission of many variants with other interesting properties. If an understanding of the precise factors that control stereoselectivity in OYE1 was to be achieved, a library of position 116 variants that is fully saturated was in order.

## Addressing the Limitations: Experimental Design

### The Problem

The ultimate goal of this project is to increase OYE1's value as a biocatalyst particularly in the area of asymmetric reductions. One challenge in developing biocatalytic methods for organic synthesis is that gaining access to both product enantiomers can be difficult, but also essential in achieving acceptance of these catalysts in preparative organic chemistry. OYEs are particularly challenging in this regard. Because of active-site spatial constraints as well as the geometric constraints of the FMN-mediated hydride transfer, these enzymes often show very high stereoselectivities and readily provide one product enantiomer in appreciable excess. However, obtaining the "other" stereoisomer can prove much more difficult making protein engineering an attractive strategy. With one exception (in (*S*)-carvone), we were unable to discover an enantiocomplementary OYE1 for any of the substrates we investigated and were therefore able to fulfill only few of our methodological goals. While our earlier studies had yielded one stereocomplementary OYE1 variant for (*S*)-carvone reduction, this was an isolated example, and an analogous solution for (*R*)-carvone was not found in the limited number of Trp116 replacements examined (Figure 2-2). To address this problem, a more systematic study of mutations in position 116 was undertaken. Moreover, while we had deduced that (*S*)-carvone should have bound in the "flipped" orientation in order to explain the observed stereochemistry, we had no direct experimental evidence to support this contention. We therefore gathered extensive structural data in order to not only validate our previous hypotheses but also to provide valuable guidance for protein engineering efforts.

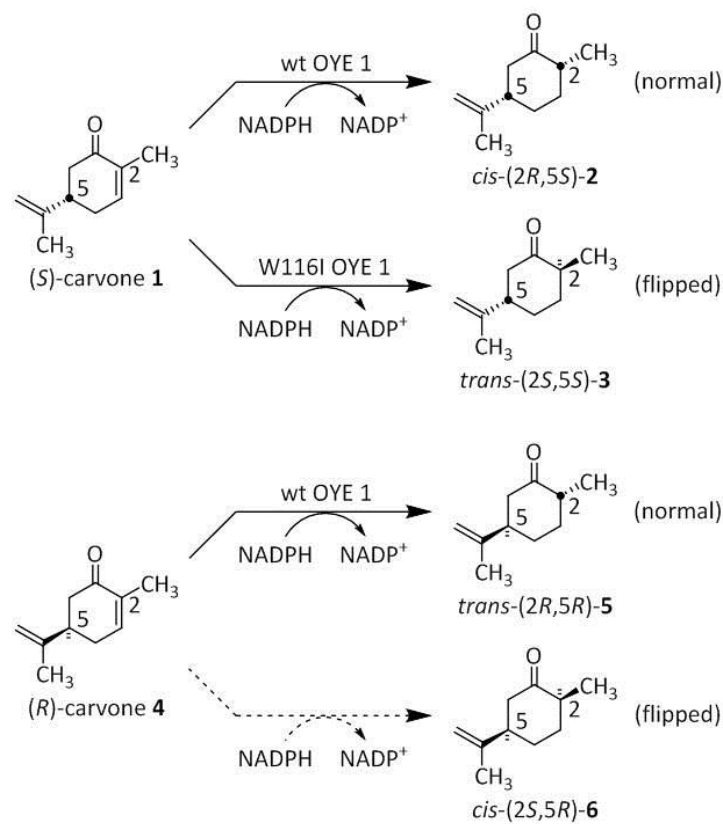


Figure 2-2. Stereocomplementarity in OYE1 variants. While both product diastereomers could be obtained for (*S*)-carvone, no variant could mimic this result for (*R*)-carvone.

### Experimental Approach and Techniques

Our goal was not only to solve this particular synthetic problem and gain access to all possible asymmetric reduction products, but also to discover general principles that might guide future efforts to adapt these versatile biocatalysts for even wider synthetic applications. Another aspect that we sought to fully explain was the precise mechanism for the observed stereochemical inversion and also we looked to corroborate our flipped binding mode hypothesis with experimental evidence.

In order to address the aforementioned concerns, a full library that contained a complete set of Trp116 amino acid replacements for OYE1 was constructed through

site-directed mutagenesis. Several Trp116 variants had been previously generated by Dr. W. Colin Conerly, and with the help of Dr. Bradford Sullivan, a library containing all 19 possible amino acid replacements was constructed. Each mutant had its properties evaluated with respect to carvone reductions and ability to carry out carvone dismutation. Additionally, in an attempt to gain an understanding of the mechanism for stereocomplementarity in this system at an atomic level, we turned to single crystal X-ray diffraction studies. Trp116 that exhibited the most interesting properties were overexpressed and purified to homogeneity for crystallization and structure determination.

## **Results and Discussion**

### **Catalytic Studies of OYE1 Mutants**

#### **(S)-Carvone reductions**

Replacements for Trp116 had significant impacts on both the efficiency and the stereoselectivity of (S)-carvone reductions. While most polar replacements – particularly those with charged side-chains – were highly detrimental, the majority of non-polar amino substitutions yielded functional OYE1 variants. The main exceptions were Asn and Gln, both of which gave good catalytic efficiencies and mainly the product expected to arise from “flipped” substrate binding. The most striking observation was that the Trp116Leu mutant afforded mostly the product derived from the normal substrate binding mode whereas the closely-related amino acids Ile and Val gave almost exclusively the diastereomer derived from the “flipped” orientation. In addition, Thr, which is nearly isosteric with Val, gave much lower catalytic efficiency. These were the first indications that substrate binding and catalytic activity could be altered by very subtle changes to the OYE1 active site structure. Figure 2-3 summarizes the results

obtained. The x-axis represents the conversion percentage while the y-axis lists the diastereomeric excess (d.e. %). The values for diastereomeric excesses were calculated as follows:

$$d.e. = \left| \frac{(d_1 - d_2)}{(d_1 + d_2)} \right| \times 100\%$$

Where  $d_1$  is the amount of diastereomer 1 (major product) and  $d_2$  the amount of diastereomer 2 (minor product) observed. The peaks were assigned through GC-MS analyses of authentic standards (Appendix A-1).

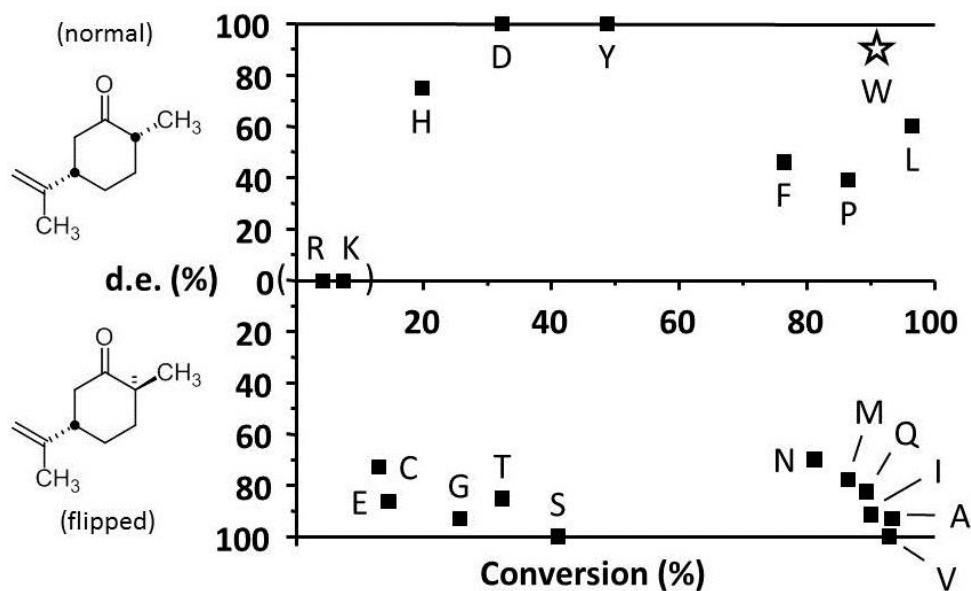


Figure 2-3. The results of (*S*)-carvone reductions. Each square (■) represents a single Trp116 replacement and has an associated conversion and d.e. percentage value. Wild-type (W) is indicated by a star.

### (*R*)-Carvone reductions

Trp116 substitution also had significant impacts on the outcomes of (*R*)-carvone reductions (Figure 2-4). As before, polar amino acids (except for Asn and Gln) dramatically decreased alkene reduction efficiency. Surprisingly, all variants except two

(Ala and Val) gave almost exclusively the product derived from the normal substrate binding mode. The behavior of the Val mutant is even more surprising since the closely-related Leu and Ile variants productively bound (*R*)-carvone only in the normal orientation. From a practical point of view, the Ala and Val variants are useful in completing the collection of diastereoselective alkene reductases that allow selective access to all four stereoisomeric products from (*S*)- and (*R*)-carvone (Figure 2-2).

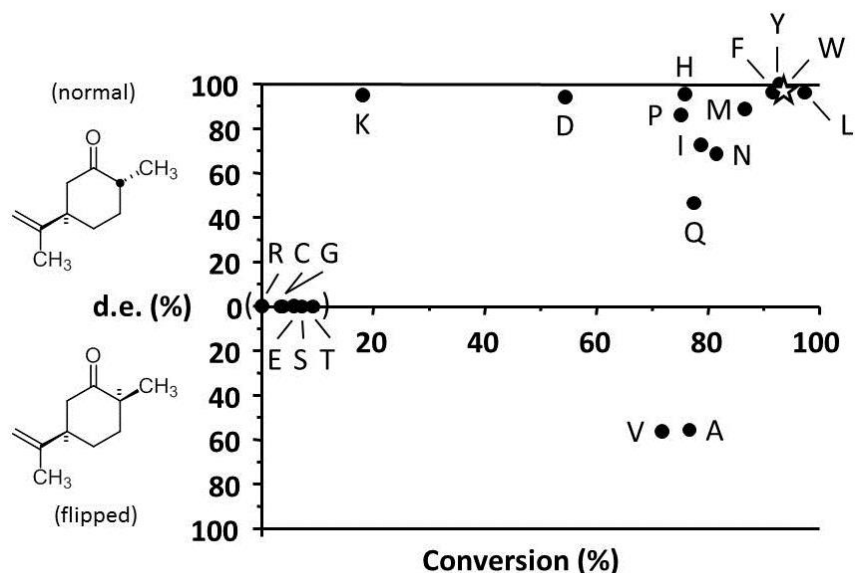


Figure 2-4. The results of (*R*)-carvone reductions. Each circle (●) represents a single Trp116 replacement and has an associated conversion and d.e. percentage value. Wild-type (W) is indicated by a star.

The results of carvone reduction by wild-type and Trp116 variants of OYE1 are summarized in Figure 2-3 and 2-4. Aside from those mutants with little or no catalytic activity, successful replacements for Trp116 can be divided into three categories: 1) those that productively bound both (*S*)- and (*R*)-carvone mainly in the normal orientation; 2) those that bound (*S*)-carvone in a “flipped” orientation, but (*R*)-carvone normally; 3) those that productively bound both (*S*)- and (*R*)-carvone in the “flipped” orientation.

## Probing the Active Site through Charge-Transfer Complex Formation Studies

In the absence of an external reductant such as NADPH, OYE1 catalyzes a dismutation reaction in which  $H_2$  is abstracted from one substrate molecule and transferred to a second <sup>19</sup>. In the case of 2-cyclohexenones, this process is essentially irreversible since the oxidation product is a cyclohexadienone that rapidly tautomerizes to the corresponding phenol. These phenols subsequently form high-affinity charge-transfer complexes with OYE1 that feature absorbance maxima at ca. 650 nm <sup>8</sup> that can be recognized visually by the change in enzyme color from bright yellow (oxidized FMN form) to green.

Carvone dismutation requires that the reacting hydrogens be oriented in a *trans*-diaxial arrangement (Figure 2-5). Because the location of the FMN is fixed within the protein environment, the substrate must be positioned so that its  $C_\beta$  hydrogen lies within the cofactor's cone of reactivity above  $N5$  <sup>37</sup>. In addition, the carbonyl oxygen must form hydrogen bonds to the side-chains of His191 and Asn 194 to facilitate the polar elimination of  $H_2$ . These requirements, in addition to avoiding steric conflict between the isopropenyl side-chain and the FMN cofactor, define the active site locations of (*S*)- and (*R*)-carvone to be those shown in Figure 2-5. While the ring carbons of (*S*)-carvone lie in the same locations as those of a phenol inhibitor, those of (*R*)-carvone must be shifted somewhat in order to maintain the proper locations of  $C_\beta$  and the carbonyl oxygen. This has the effect of moving the (*R*)-substrate into closer proximity to the side-chain of the amino acid at position 116 as compared to its (*S*)-counterpart. We used this approach to gain some information on the effective active volume created by Trp116 mutations. We would later use this information in an attempt to draw parallels between carvone "flipping" and charge-transfer complex formation.

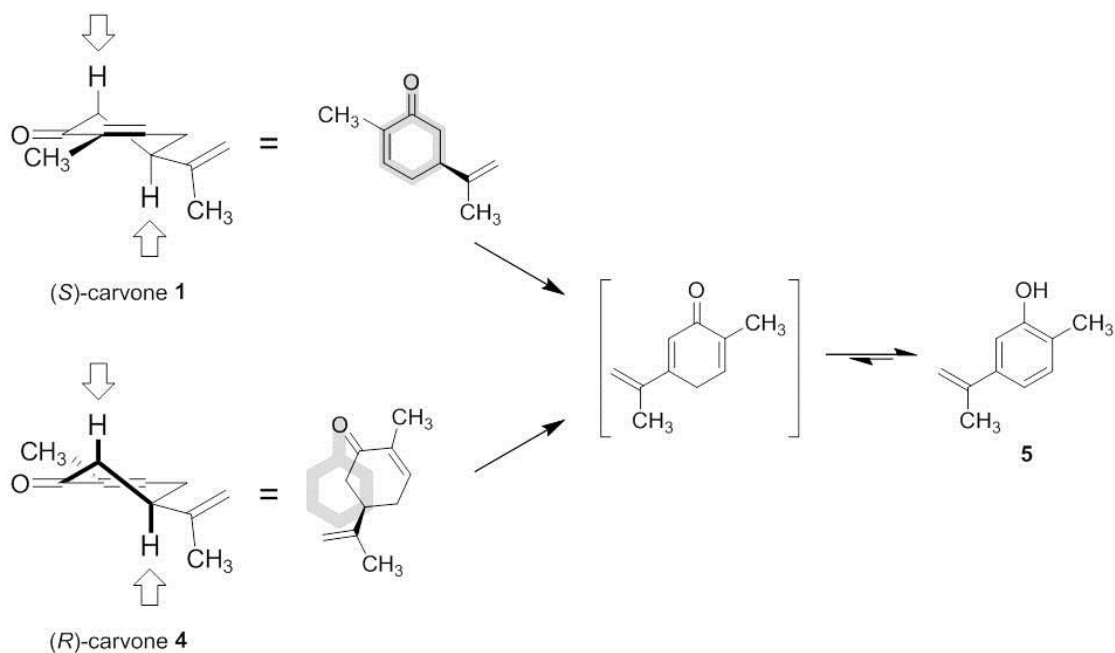


Figure 2-5. This scheme shows the geometric constraints for (*S*)- and (*R*)-carvone oxidation in the reductive half-reaction. In order to react, *trans*-diaxial hydrogens must be properly positioned. This implicates different orientations for (*R*)- and (*S*)-carvone.

The ability to form phenol **5** from both (*S*)- and (*R*)-carvone were determined spectrophotometrically for all catalytically active OYE1 Trp116 mutants (this criterion excluded the Glu, Arg, Cys, Lys, Thr and Gly variants since they showed less than 30% activity in NADPH-driven reductions). Because the oxidation product, phenol **5**, is a potent inhibitor of OYE1, progress curves for these reactions are inherently non-linear. We, therefore, chose a fixed reaction time (24 hrs.) and assessed the fraction of enzyme with bound phenol **5** at that time. This complexation generates a charge-transfer band centered at 648 nm, and we determined the fraction of OYE1 with bound **5** by measuring the  $A^{462} / A^{648}$  ratios both at the start of the reaction and after 24 hr. Values for  $A^{462} / A^{648}$  of completely saturated enzymes were determined by adding an excess of *p*-chlorophenol in separate experiments to determine the final  $A^{462} / A^{648}$  ratio of a completely saturated protein-phenol complex. Preliminary studies had shown that

the charge-transfer bands from *p*-chlorophenol were a good approximation for those formed by phenol **5**; the former was used here because it was commercially available. These data allowed the fractional saturation for each dismutation reaction to be calculated after 24 hr (Figure 2-6). Interestingly, both Gln and Asp replacements failed to show spectra typical of charge-transfer complexes and the results obtained were inconclusive.

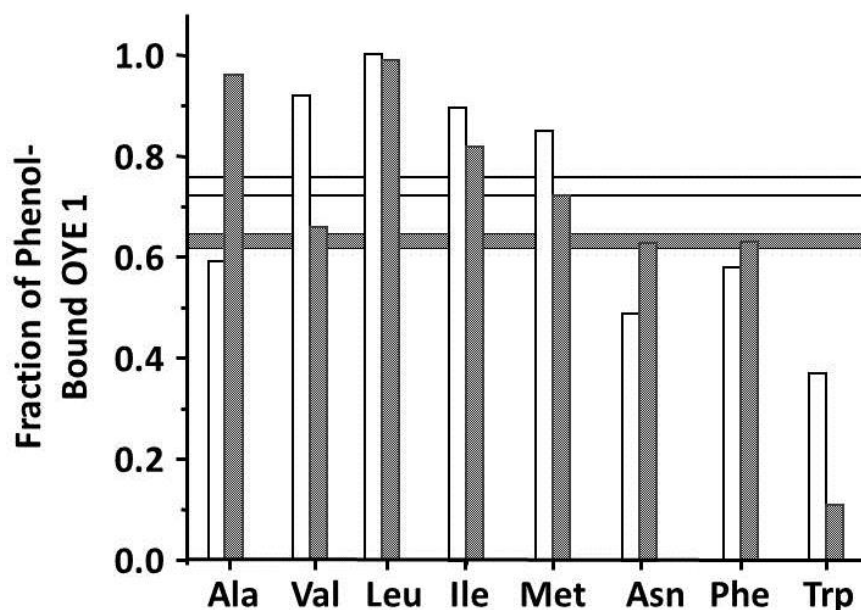


Figure 2-6. Charge-transfer complex formation activities of Trp116 with (*S*)-carvone (light bars) and (*R*)-carvone (dark bars). The horizontal bars represent the mean saturation percentage for each substrate.

In general, (*S*)-carvone was a better substrate than (*R*)-carvone at forming phenol **5**.

The mean value for (*S*)-carvone binding saturation is 73% in contrast to 65% for the *R* enantiomer. In the case of the wild-type enzyme the largest discrepancy in charge-transfer complex formation was observed. (*S*)-carvone reached nearly 40% saturation contrasting (*R*)-carvone's 9% saturation. This general trend is in fair agreement with the proposed model (*vide supra*).

## Crystallography Studies

### Structural overview

To help understand what molecular interactions controlled the orientation of substrate binding in wild-type OYE1 and its Trp116 replacements, we determined the three-dimensional structures for several key variants in the presence of substrates and / or other ligands. To avoid potential interference during crystallization, the GST fusion tag was deleted and proteins were purified by affinity chromatography on a phenol-containing resin followed by final polishing by gel filtration chromatography (see experimental section for full details). All variants crystallized in a hanging-drop vapor diffusion setup under very similar conditions and in the same space group as reported by Fox and Karplus for the wild-type enzyme ( $P 4_3 2_1 2$ )<sup>14</sup>. As expected, the overall structures for all mutants were nearly identical (RMSD 0.10 – 0.27 Å). The only exception was the extra-barrel helix B (residues 145 – 153), which exhibited greater deviation. This region usually exhibited higher B-factors and makes contacts with adjacent protein molecules in the crystal lattice. These variations usually seemed to correlate with small differences in unit cell dimensions and are likely to be caused by crystal packing restraints.

All structures were solved by molecular replacement using the wild-type OYE1 structure (PDB accession code 1OYA) or one of the first mutants determined during the course of this study (3RND). All of our structures showed a slightly different protein structure near the C-terminus than reported previously as well as an ordered  $Mg^{2+}$  ion. Aside from these minor differences, the overall structures reported here are highly similar to that of 1OYA. The positions of the mutant side-chains at position 116 were readily apparent from the high-resolution omit electron density difference maps  $mF_o -$

DF<sub>c</sub>. To obtain crystal structures of enzyme•ligand complexes, soaking experiments were carried out for all key variants by adding neat (*R*)- and (*S*)-carvone to pre-grown OYE1 crystals in the mother liquor prior to mounting. Attempts to obtain co-crystallize the usually resulted in no crystal growth or poorly diffracting crystals (figure2-7A,B). We also carried out some soaking experiments with (+)-dihydrocarvone, which was added to crystals of the Thr, Ala and Val OYE1 variants.

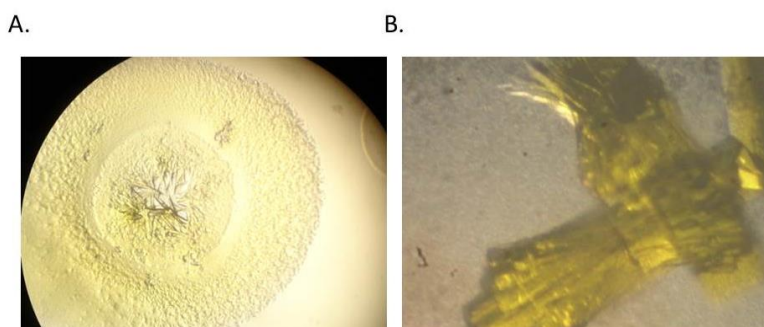


Figure 2-7. Panels A and B show results from OYE1 and ligands co-crystallization. These are not suitable for X-ray diffraction studies

All crystals initially exhibited the characteristic bright yellow color of oxidized flavin; however, after several days of soaking in the presence of carvone, some mutants gradually adopted a green color. This was particularly apparent in crystals of the Val and Ala replacements. By contrast, crystals of the Ile and Gln variants remained bright yellow, even after prolonged ligand soaking times. When ligands were observed in the active site, occupancies were generally very high ( $\geq 85\%$ ) and their locations were very well-defined by the electron density. Ligand atoms were added manually only after the protein and most water molecules had been refined to avoid model bias.

### Wild-type

Crystals of wild-type OYE1 were soaked individually with both (*S*)- and (*R*)-carvone and complete, high-resolution data sets were collected for both experiments.

No electron density that could be modeled as carvone was observed; instead, electron density that could be best interpreted as a chloride ion was found at the location occupied by a phenolate oxygen atom in charge-transfer complex structures. OYE1 is known to bind monovalent anions including chloride with a  $K_D$  of about 8 mM<sup>38</sup> and chloride is present in the crystallization buffer at approximately 400 mM. For these reasons, chloride ion is the “default” active site ligand found in the absence of additional ligand soaking. That it remained bound to the wild-type enzyme even in the presence of saturating carvone implies that the thermodynamic stability of these complexes was insufficient to displace even this weakly-bound active site chloride.

### **Trp116Leu mutant**

Based on the nature of the carvone reduction products obtained from this protein, we surmised that the Trp116Leu OYE1 variant must have bound both (*R*)- and (*S*)-carvone in the “normal” orientation. Numerous soaking experiments were carried out in an effort to observe the latter within the active site; unfortunately, only a spherical region of electron density best modeled as a chloride ion was found when (*S*)-carvone was used. By contrast, we were successful with (*R*)-carvone, although the nature of the active site ligand depended on the time between substrate addition and crystal cooling in liquid nitrogen. Initially yellow crystals soaked with (*R*)-carvone for two days at 4 °C gradually became green (Figure 2-8A, right panel). When the soaking time was decreased to 2.5 hr before cooling in liquid nitrogen, the crystals remained yellow (Figure 2-8A, left panel). We suspected that the green color was a result of a charge-transfer complex formation between the enzyme and a phenol resulting from a dismutation reaction during the soaking period (Figure 2-5). In order to validate this hypothesis we turned to *in crystallo* UV-Vis spectroscopy. In these experiments,

Trp116Leu single crystals that had been soaked in (*R*)-carvone for different time lengths were mounted, in typical manner, for X-ray data collection at 100 K. After determining the optimal crystal orientation, UV-Vis (350-800 nm) absorbance spectra were collected using a microspectrophotometer that is focused on the crystal rotation axis. Complete data sets were collected for both (yellow and green) crystal forms, which exhibited significantly different absorbance spectra in the 550 – 800 nm (Figure 2-8B).

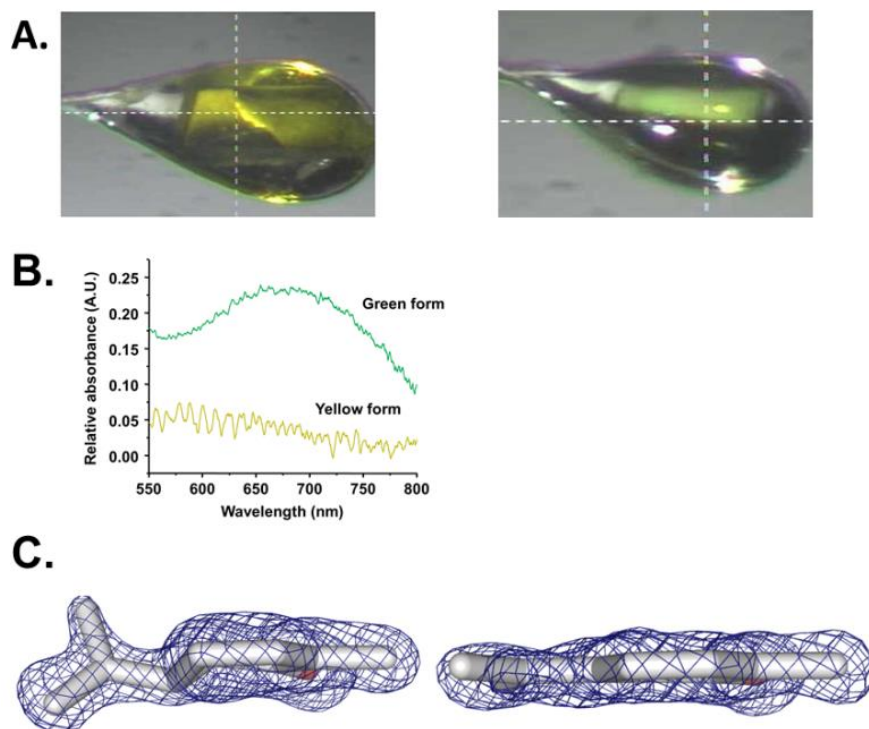


Figure 2-8. Yellow and green crystal forms. Panel A - photographs of the mounted Trp116Leu crystals. Crystals were soaked for 2.5 hrs. (left) or for 48 hrs. (right). Panel B shows the spectra collected for both crystal forms. C- Experimental electron density maps (omit mFo-DFc) for the ligands in the active site.

The spectra for the green crystal form were consistent with those of charge-transfer complexes between OYE and a phenolic inhibitor (see previous sections for discussion). Based on the  $\lambda_{\max}$  value of ca. 675 nm observed for the green crystals during X-ray data collection, we suspected that (*R*)-carvone had, in fact, undergone

dismutation and that the active site ligand was actually phenol **5**. Since no phenolic molecules were present during the purification procedure or in the crystallization buffer, we rationalized that phenolic ligand formation must have occurred post crystallization. This notion was supported by the ligand electron density maps, which was fit much better by phenol **5** than by the starting substrate (*R*)-carvone (Figure 2-8C).

As expected, the orientation of phenol **5** in the active site matched our expectations for the normal binding mode wherein the ligand is directly superimposed onto the *p*-hydroxybenzaldehyde inhibitor as initially reported by Fox and Karplus<sup>14</sup> (Figure 2-9).

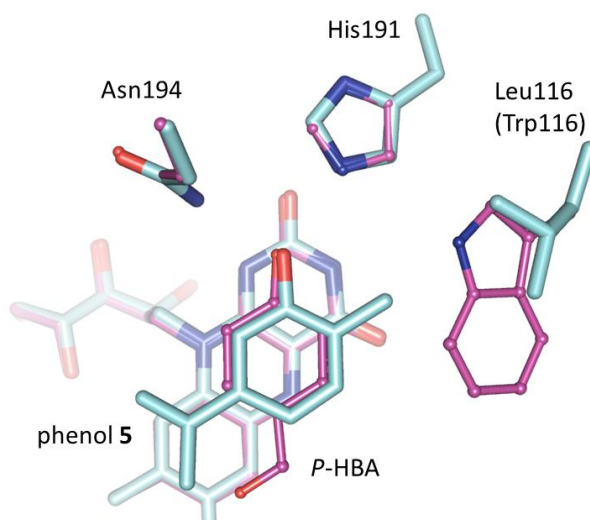


Figure 2-9. The normal binding mode. Superposition of phenol **5** and *p*-HBA. Trp116Leu atoms are shown as thick lines in cyan color. OYE1 wild-type is shown as thinner ball-and-stick representation.

The phenolic oxygen of phenol **5** is ideally positioned to hydrogen bond to His191 and Asn194 and its aromatic ring is directly above the *si*-face of the flavin mononucleotide ring. As highlighted in Figure 2-8, the phenolic ligand ring displays flat topology and is oriented parallel to the isoalloxazine rings of the flavin. This

conformation places the ligand's isopropenyl moiety very close to the side-chain of Phe 296 (closest approach of 3.20 Å); nevertheless, the phenyl side-chain predominantly occupied one well-defined conformation. Tyr375 is also in close proximity and has some evidence for multiple conformations although a major position could be deduced from its electron density. In addition, the Leu116 side-chain was also well-defined with no unduly close contacts between the methyl group of **5** and this protein residue (Figure 2-10A).

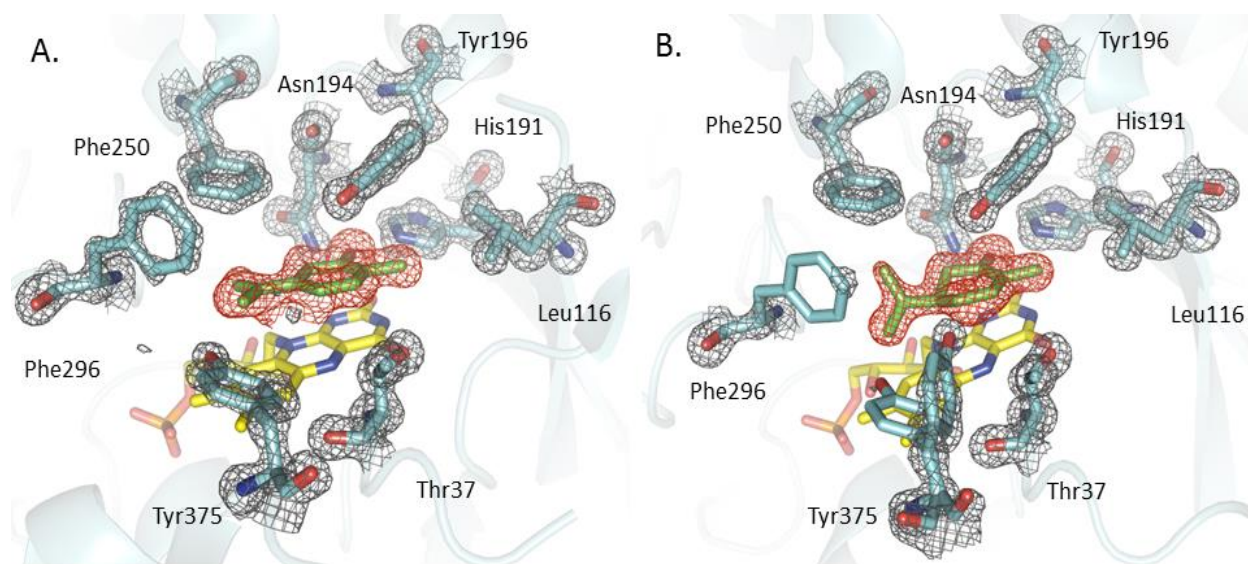


Figure 2-10. OYE1 Trp116Leu. A- Crystal structure of phenol **5** bound to Trp116Leu OYE1. 2mFo-DFc Electron density maps for relevant residues are shown at contour level 1.2  $\sigma$ . Protein residues are colored in cyan, FMN in yellow and the ligand in green. The red mesh is the omit difference (mFo-DFc) map of the ligand at contour level 3.0  $\sigma$ . PDB code 4GXM. B- Crystal structure of (*R*)-carvone **4** bound to Trp116Leu OYE1. Electron density maps are shown at contour level 1.2  $\sigma$  for relevant residues. Protein residues are colored in cyan, FMN in yellow and ligand in green. The red mesh is the omit difference (mFo-DFc) map of the ligand at contour level 3.0  $\sigma$ . PDB code 4GWE.

Both the ligand electron density from the yellow crystals of (*R*)-carvone soaked Trp116Leu OYE1 and the absence of an absorption band in the 500 – 800 nm range were consistent with unmodified substrate in the active site (Figure 2-10B). In fact, the

experimental 2mFo-DFc and mFo-DFc electron density maps made (*R*)-Carvone easily identifiable. As in the previous structure, the (*R*)-carvone ligand was found in the “normal” binding mode occupying a position similar to that of phenol **5** seen in the structure of the green crystal. The carbonyl oxygen of **4** was ideally positioned to form hydrogen bonds with both Nε2 of His191 and Nδ2 of Asn194. Its isopropenyl group pointed away from the side chain of Leu116 and made contacts with the side-chains of Phe250, Pro295 and Phe296. Minor adjustments were also observed in the side-chain positions of Phe 250 and Tyr 375, which appeared to populate multiple conformations. The C<sub>2</sub> methyl group of **4** makes hydrophobic contacts with Cδ1 and Cδ2 of Leu116. The distance and angle from the FMN N5 atom (3.75 Å and 105°, respectively) suggests that this complex mimics the catalytically productive Michaelis complex and also confirms that this substrate was indeed bound in the “normal” orientation by the Leu variant. One important difference between this intact (*R*)-carvone complex and that with dismutation product **5** was that the non-planar carvone provoked two key changes in the protein structure. First, the electron density for the side-chain of Phe296 was weak, and it was clear that several conformations were present in the ensemble of protein molecules within the crystal (Figure 2-10B). Likewise, the side-chain of Tyr375 was also found in at least two conformations. These observations suggest that additional changes at positions 296 and 375 that create additional space for substrate binding might yield even more catalytically efficiency OYE1 variants. The close approach of the isopropenyl group to the abovementioned protein residues may also explain why we were unable to observe a complex with (*S*)-carvone despite numerous soaking attempts.

Table 2-1. X-ray Crystallographic Data Collection and Refinement Statistics

PDB Accession code	4GXM	4GWE
Ligand Soaked	( <i>R</i> )-carvone	( <i>R</i> )-carvone
Observed active site ligand	Phenol 5	( <i>R</i> )-carvone
X-ray source	NLSL X26C	NLSL X26C
Space group	P 4 <sub>3</sub> 2 <sub>1</sub> 2	P 4 <sub>3</sub> 2 <sub>1</sub> 2
Unit cell dimensions		
a = b, c (Å)	141.12, 42.92	140.78, 42.76
Resolution (Å)	34.2 – 1.36 (1.41 – 1.36)	28.2 – 1.45 (1.49 – 1.44)
Unique reflections	87,060 (5,990)	70,039 (4,324)
Completeness (%)	93.78 (65.40)	90.83 (56.74)
Multiplicity	16.5 (7.5)	12.8 (11.7)
R <sub>sym</sub> <sup>[b]</sup>	0.062 (0.38)	0.044 (0.18)
I/σ (I)	39.89 (4.49)	48.82 (12.97)
R <sub>work</sub> <sup>[c]</sup> , R <sub>free</sub> <sup>[d]</sup>	0.108, 0.137	0.115, 0.145
Ramachandran statistics <sup>[e]</sup>		
Favored (%)	98	98
Allowed (%)	2	2
Outliers (%)	0	0
Number of protein, solvent and ligand atoms	3,287, 633, 100	3,255, 590, 65
Average B factors (Å <sup>2</sup> )		
Protein	11.5	13
Solvent	25.4	26.7
FMN	7.5	10.0
Ligand	18.1	19.1

<sup>[a]</sup>Values in parentheses denote data for the highest resolution bin.

<sup>[b]</sup> $R_{\text{merge}} = \frac{\sum hkl \sum i |I_i(hkl) - [I(hkl)]|}{\sum hkl \sum i I_i(hkl)}$ , where  $I_i(hkl)$  is the intensity of the  $i$ th observation of unique reflection  $hkl$ .

<sup>[c]</sup> $R_{\text{work}} = \frac{\sum |F_o(hkl) - |F_c(hkl)||}{\sum |F_o(hkl)|}$ .

<sup>[d]</sup> $R_{\text{free}}$  is calculated in the same manner as  $R_{\text{work}}$  using 10% of the reflection data not included during the refinement.

<sup>[e]</sup>Statistics generated using MOLPROBITY<sup>39</sup>

While the positions of the isopropenyl side-chains occupy similar locations in the two carvone enantiomers, their exact locations differ slightly and in cases where they are nearly in van der Waals contact with protein residues, very minor changes in the location of this moiety may have significant impacts. Both X-ray data sets of the Trp116Leu enzyme yielded high quality atomic models. The complete crystallographic parameters, data collection and refinement statistics can be found in Table 2-1.

### **Trp116Ile mutant**

This OYE1 mutant was of particular interest to us since it exhibited a unique behavior. Trp116Ile catalyzed the reduction of (*S*)-carvone with a nearly complete reversal of stereochemistry compared to the wild-type enzyme. Curiously, it showed the same stereochemistry as the wild-type enzyme in the reduction of (*R*)-carvone. We therefore attempted to obtain crystal structures of complexes formed between the enzyme and both (*R*)- and (*S*)-carvone.

Crystals soaked with (*R*)-carvone yielded active site electron density maps that were not consistent with the (*R*)-carvone substrate. Rather, the best interpretation was consistent with a chloride ion which is present in the crystallization buffer and known to bind to OYE1. One important aspect is that, in the high-resolution crystal structure (1.55 Å), the Ile116 side-chain showed very well-defined electron density for all of its atoms (Figure 2-12A). The side chains of Phe296 and Tyr375 showed indications of disorder having weak electron density and high B-factors. As anticipated, this substitution created a much larger pocket on the “eastern” side of the OYE1 active site just below Tyr196.

Table 2-2. X-ray Crystallographic Data Collection and Refinement Statistics

PDB Accession code	4H6K	4GE8
Ligand Soaked	( <i>R</i> )-carvone	( <i>S</i> )-carvone
Observed active site ligand	Chloride	( <i>S</i> )-carvone
X-ray source	NSLS X25	NSLS X25
Space group	P 4 <sub>3</sub> 2 <sub>1</sub> 2	P 4 <sub>3</sub> 2 <sub>1</sub> 2
Unit cell dimensions		
a = b, c (Å)	140.93, 42.46	140,93, 42.48
Resolution (Å)	31.5 – 1.55 (1.60 – 1.55)	24.2 – 1.5 (1.55 – 1.49)
Unique reflections	62,517 (6,122)	68,916 (6,757)
Completeness (%)	99.94 (99.69)	99.75 (99.22)
Multiplicity	9.1 (8.7)	11.1 (10.4)
R <sub>sym</sub> <sup>[b]</sup>	0.080 (0.90)	0.048 (0.63)
I/σ (I)	14.22 (1.89)	29.40 (2.83)
R <sub>work</sub> <sup>[c]</sup> , R <sub>free</sub> <sup>[d]</sup>	0.182, 0.204	0.137, 0.170
Ramachandran statistics <sup>[e]</sup>		
Favored (%)	97	98
Allowed (%)	3	2
Outliers (%)	0	0
Number of protein, solvent and ligand atoms	3,216, 313, 56	3,256, 465, 91
Average B factors (Å <sup>2</sup> )		
Protein	29.6	21.2
Solvent	38	38.0
FMN	19.5	13.7
Ligand	-	23.9

<sup>[a]</sup>Values in parentheses denote data for the highest resolution bin.

<sup>[b]</sup>Rmerge =  $\frac{\sum_{hkl} \sum_i |I_i(hkl) - [I(hkl)]|}{\sum_{hkl} \sum_i I_i(hkl)}$ , where  $I_i(hkl)$  is the intensity of the  $i$ th observation of unique reflection  $hkl$ .

<sup>[c]</sup>R<sub>work</sub> =  $\frac{\sum | |F_o(hkl)| - |F_c(hkl)| |}{\sum |F_o(hkl)|}$ .

<sup>[d]</sup>R<sub>free</sub> is calculated in the same manner as R<sub>work</sub> using 10% of the reflection data not included during the refinement.

<sup>[e]</sup>Statistics generated using MOLPROBITY<sup>39</sup>

Addition of (*S*)-carvone to these crystals yielded a *pseudo*-Michaelis complex that demonstrated directly – for the first time – that carvone could be accommodated in the active site of *S. pastorianus* OYE1 in a “flipped” orientation (Figure 2-11B). The side-chain of Tyr196 moves significantly to bind the substrate. A  $\chi^2$  rotation of 80° and a slight backbone shift are observed in the crystal structure of the complex. (*S*)-Carvone was stacked above the FMN co-factor with its carbonyl oxygen atom positioned to form hydrogen bonds with both *N*ε2 of His191 and *N*δ2 of Asn 194. Its *iso*-propenyl group lies in a hydrophobic pocket directly above Thr37 and makes hydrophobic contacts with the side chain of the Ile introduced at position 116. The side chains of Tyr375 and Phe296 showed well defined electron density, contrasting what was seen in the crystal structure of the uncomplexed enzyme. The distance and angle from *N*5 of the FMN (3.70 Å and 89°, respectively) were within the range of values expected<sup>37</sup> for catalytically relevant complex.

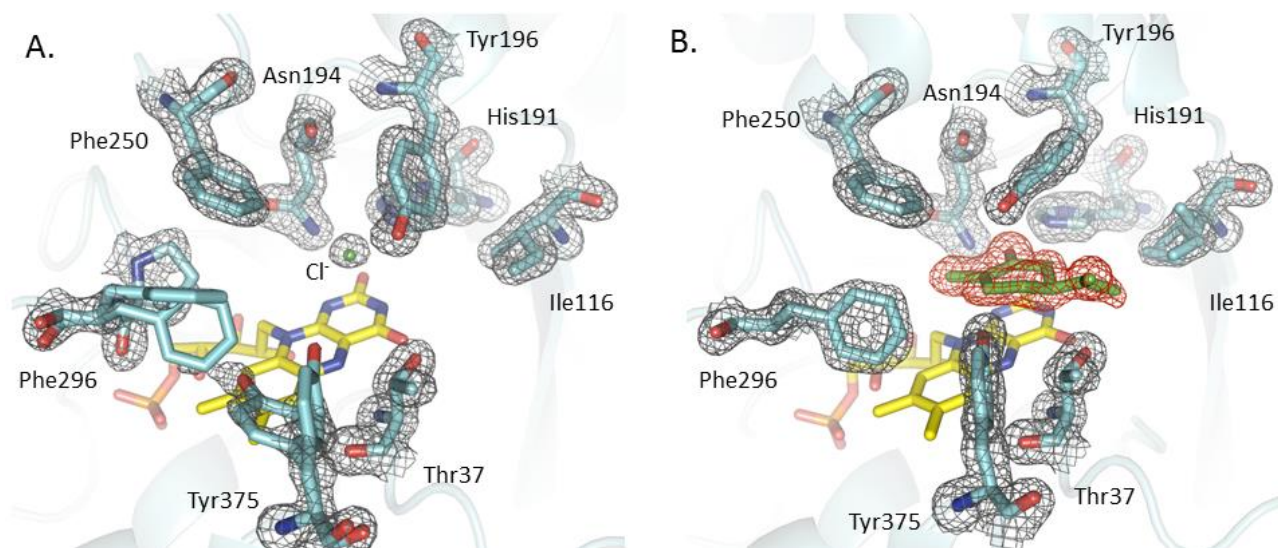


Figure 2-11. OYE1 Trp116Ile. A- The free enzyme structure. B- Complex of enzyme and (*S*)-carvone. The gray mesh represents 2mFo-DFc maps at 1.0 $\sigma$ . The red mesh in B represents the omit mFo-DFc map at contour level of 3 $\sigma$ . PDB codes 4H6K (A), 4GE8 (B). Protein residues are colored in cyan, FMN in yellow and the ligand in green

Interestingly, the side-chain of Ile116 was no longer well-defined at the methyl terminus in this pseudo-Michaelis complex; rather, disorder was observed at the point of closest approach to the bound substrate (Figure 2-12B). Moreover, the main conformer of Ile had rotated 180 ° about  $\chi_1$  to avoid clashing into the *iso*-propenyl group of carvone. This suggests that there may be some steric interference, even in a variant that allows (*S*)-carvone to bind in the “flipped” orientation. These steric clashes between the side-chain of Ile at position 116 and the *iso*-propenyl moiety of the substrate may also explain why the same mutant was unable to bind (*R*)-carvone in an analogous “flipped” orientation. The substituents in these substrate enantiomers occupy similar, but not identical, spatial positions. The complete crystallographic parameters, data collection and refinement statistics can be found in Table 2-2.

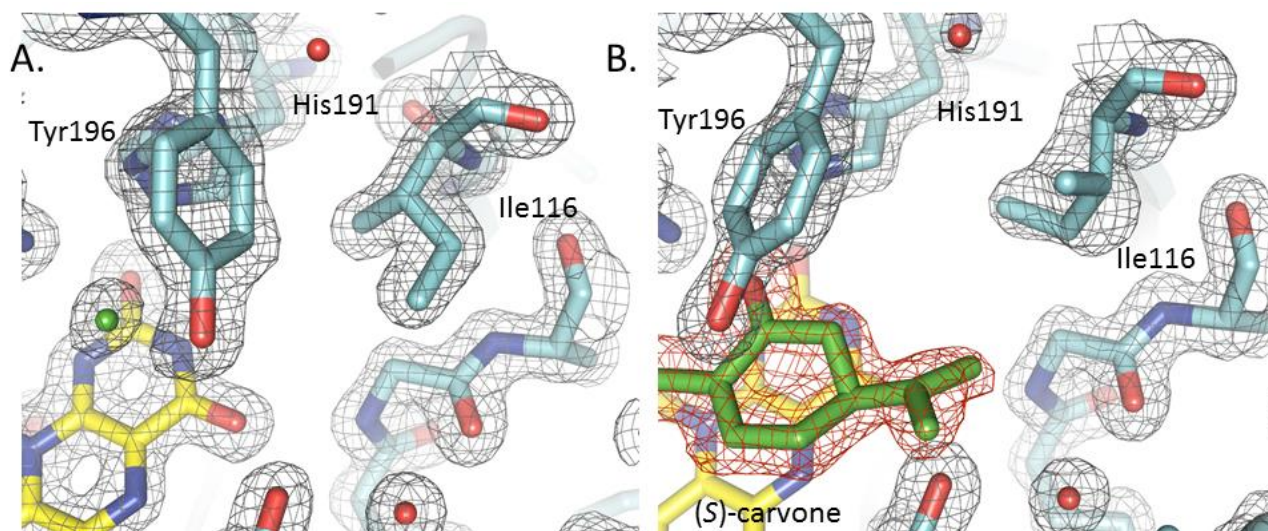


Figure 2-12. Detailed view of Trp116Ile. A- Electron density observed in the chloride structure. B- Electron density observed in the (*S*)-carvone complex structure. The gray mesh represents 2mFo-DFc maps at 1.0 $\sigma$ . The red mesh in B represents the omit mFo-DFc map at contour level of 3 $\sigma$ . The main conformations of Ile116 have rotated 180° apart. Protein residues are colored in cyan, FMN in yellow and the ligand in green.

## Trp116Ala mutant

Based on the alkene reduction products obtained, we deduced that the Trp116Ala mutant must have bound both (*S*)- and (*R*)-carvone primarily in “flipped” orientations. These predictions were borne out by the results of soaking experiments, which yielded electron density maps that were only consistent with the expected ligand binding orientation (Figure 2-13 B). Unfortunately, the high dismutation activity of this OYE1 variant toward both carvone enantiomers meant that only phenol **5** could be observed in the crystals) even after relatively short soaking times. The position of phenol **5** in both complexes was very similar to that observed for the (*S*)-carvone•Trp116Ile variant. The *iso*-propenyl group of **5** rests above the side chain of Thr37 and its phenolic oxygen makes short (2.71 and 2.77 Å) and well aligned hydrogen bonds with *Nε2* of His191 and *Nδ2* of Asn194, respectively.

As mentioned above, crystals soaked with (*S*)- and (*R*)-carvone solutions yielded electron density maps that were best fitted by phenol **5** (Figure 2-13D). The final models were essentially indistinguishable, independently of which enantiomer of carvone they had been exposed to. Curiously, soaking crystals of the Trp116Ala mutant with (+)-dihydrocarvone **6** overnight at 4 °C yielded active site electron density best fit by (*R*)-carvone **4** in the flipped orientation (Figure 2-13A, C). One possible route to the crystallographically observed complex is summarized in Figure 2-14. *Trans*-elimination of H<sub>2</sub> from **6** would most logically occur from a binding arrangement in which the substrate’s ring atoms matched those of the phenol inhibitor, thereby yielding reduced cofactor and (*R*)-carvone within the active site in the “normal” orientation. From this complex, the FMNH<sub>2</sub> can either transfer a pair of electrons to the alkene (back-reaction to re-form **6**) or reduce a different acceptor (likely O<sub>2</sub>) in an essentially irreversible step.

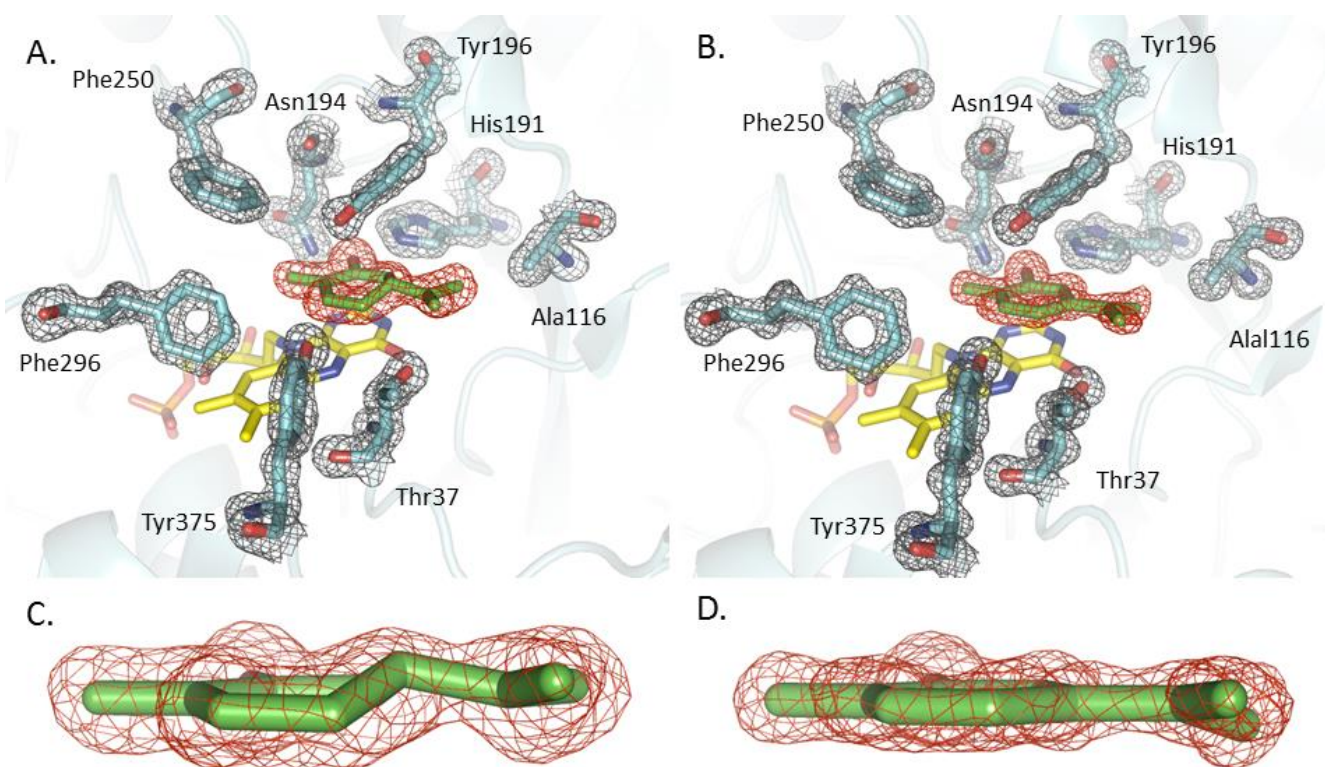


Figure 2-13. OYE1 Trp116Ala. A- Crystal structure of Trp116Ala in complex with (*R*)-carvone. B- Trp116Ala with phenol **5** bound in the active site. C- Omit mFo-DFc map of (*R*)-carvone at  $3\sigma$ . D- Omit mFo-DFc map of phenol **5** at  $4.5\sigma$ . Protein residues are colored in cyan, FMN in yellow and the ligand in green.

This would leave an oxidized substrate in the active site with an oxidized cofactor. In the absence of an external reductant as in the crystallization drop, this dead-end complex then isomerizes to the favored “flipped” binding orientation to yield the crystallographically-observed complex. Whether this change in substrate binding orientation involves dissociation and re-binding of (*R*)-carvone or occurs intramolecularly is unknown; however, the high external concentration of (+)-dihydrocarvone would diminish the chances of re-binding any (*R*)-carvone released to the bulk solution, suggesting that the latter pathway may be more likely. It is also possible that  $H_2$  is eliminated from the minor, *cis*-isomer of (+)-dihydrocarvone (present at 15% in the commercial reagent used). This would place (*R*)-carvone in the active site

in the same orientation as observed experimentally. One puzzling observation is that little or no further dismutation of (*R*)-carvone to phenol **5** was observed in the crystal structure, despite the demonstrated ability of this mutant to catalyze this reaction when (*R*)-carvone was the starting substrate. It is possible that the enzyme had insufficient time to carry out the second dismutation step prior to flash cooling in liquid nitrogen.

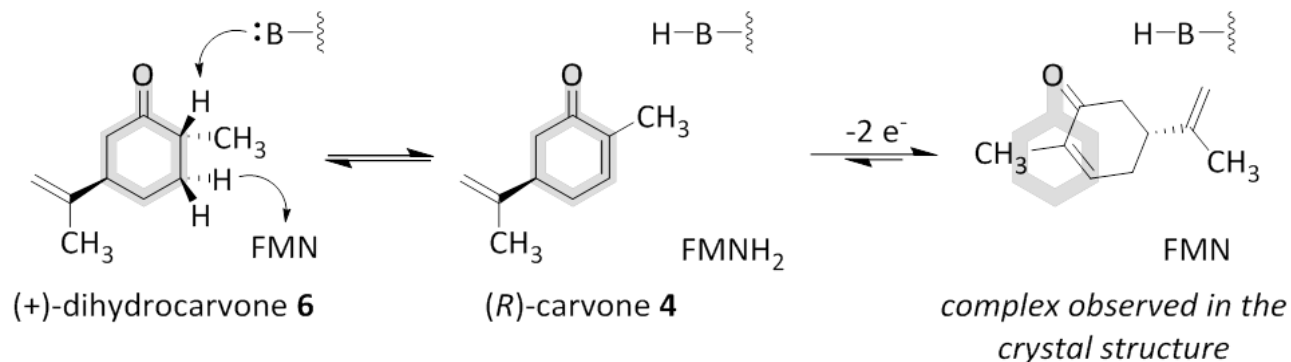


Figure 2-14. Schematic representation of (*R*)-carvone formation from (+)-dihydrocarvone, via an enzymatic oxidation (dehydrogenation).

Regardless of the precise mechanism by which the “flipped” (*R*)-carvone complex with the Trp116Ala mutant was formed, this structure provided valuable information. The initial dehydrogenation step most likely involved the “normal” substrate binding mode, clearly demonstrating that this mutant is capable of interacting with substrate in this manner (Figure 2-14). That the final (*R*)-carvone complex involved the “flipped” orientation, however, showed that the latter arrangement is energetically preferred even when the alternative is accessible. This led us to hypothesize that OYE1 intrinsically prefers to bind carvone in the “flipped” orientation and only when this arrangement is sterically precluded by an amino acid side-chain at position 116 is the “normal” binding orientation utilized. This notion was further supported by studies of the Trp116Val mutant.

Table 2-3. X-ray Crystallographic Data Collection and Refinement Statistics

PDB Accession code	4GBU	4K7V
Ligand Soaked	(S)-carvone	(+)-dihydrocarvone
Observed active site ligand	Phenol 5	(R)-carvone
X-ray source	NSLS X6A	NSLS X6A
Space group	P 4 <sub>3</sub> 2 <sub>1</sub> 2	P 4 <sub>3</sub> 2 <sub>1</sub> 2
Unit cell dimensions a = b, c (Å)	141.12, 42.81	140.85, 42.84
Resolution (Å)	21.0 – 1.18 (1.22 – 1.17)	35.42 – 1.52 (1.57 – 1.516)
Unique reflections	141,261 (13,929)	66,315 (6,492)
Completeness (%)	99.71 (99.59)	98.52 (97.79)
Multiplicity	7.1 (6.6)	7.8 (7.2)
R <sub>sym</sub> <sup>[b]</sup>	0.076 (0.55)	0.093 (0.524)
I/σ (I)	15.10 (2.05)	22.67 (3.44)
R <sub>work</sub> <sup>[c]</sup> , R <sub>free</sub> <sup>[d]</sup>	0.100, 0.121	0.145, 0.183
Ramachandran statistics <sup>[e]</sup>		
Favored (%)	98	97
Allowed (%)	2	3
Outliers (%)	0	0
Number of protein, solvent and ligand atoms	3,281, 658, 107	3,205, 500, 62
Average B factors (Å <sup>2</sup> )		
Protein	11.5	18.5
Solvent	26.1	30.90
FMN	6.9	16.6
Ligand	16.3	25.3

<sup>[a]</sup>Values in parentheses denote data for the highest resolution bin.

<sup>[b]</sup>R<sub>merge</sub> =  $\sum_{hkl} \sum_i |I_i(hkl) - [I(hkl)]| / \sum_{hkl} \sum_i I_i(hkl)$ , where  $I_i(hkl)$  is the intensity of the  $i$ th observation of unique reflection  $hkl$ .

<sup>[c]</sup>R<sub>work</sub> =  $\sum | |F_o(hkl)| - |F_c(hkl)| | / \sum |F_o(hkl)|$ .

<sup>[d]</sup>R<sub>free</sub> is calculated in the same manner as R<sub>work</sub> using 10% of the reflection data not included during the refinement.

<sup>[e]</sup>Statistics generated using MOLPROBITY<sup>39</sup>

## Trp116Val mutant

As observed with the Ala variant, soaking crystals of the Trp116Val OYE1 mutant with either (*S*)- or (*R*)-carvone overnight at 4 °C gave complexes with dismutation product **5** in the “flipped” binding orientation (Figure 2-15 B). The ligand location was similar to that observed for the Ala structures, although C8 of the ligand was shifted by 0.64 Å in order to accommodate contacts with Cy1 and Cy2 of the Val at position 116. The phenolic oxygen remained at essentially the same position as seen earlier in the Trp116Ala complexes.

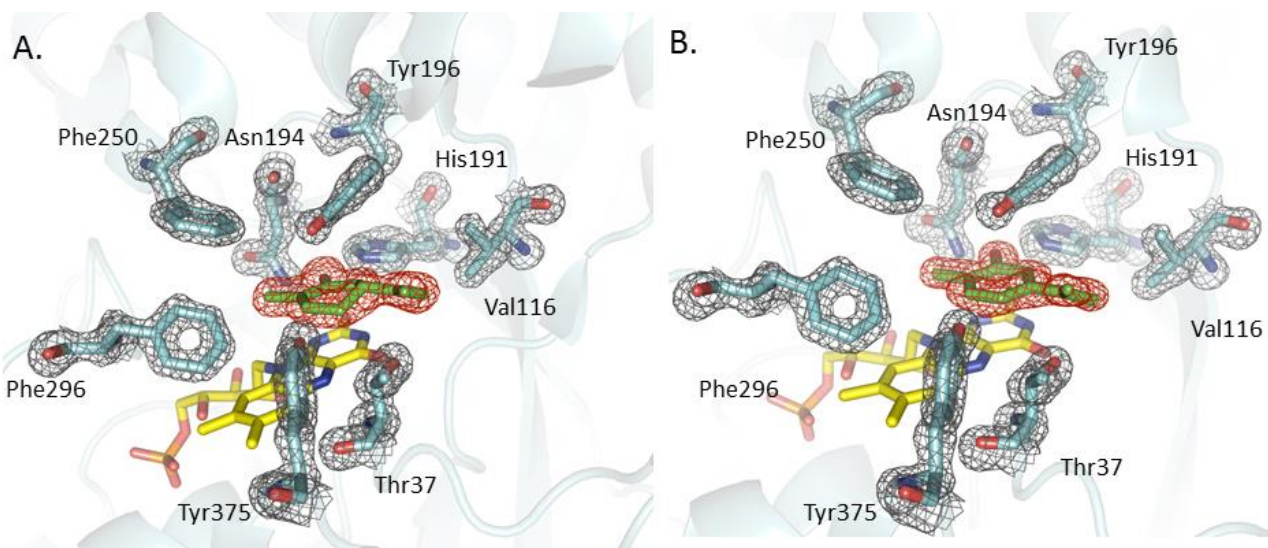


Figure 2-15. OYE1 Trp116Val. A- Crystal structure of Trp116Val in complex with (*R*)-carvone. B- Trp116Val with phenol **5** bound in the active site. Grey mesh is 2mFo-DFc electron density map contoured at 1.2  $\sigma$ . The red mesh is the omit mFo-DFc maps at 3  $\sigma$ . Protein residues are colored in cyan, FMN in yellow and the ligand in green.

Soaking the Trp116Val mutant with (+)-dihydrocarvone **6** yielded complex of (*R*)-carvone within the active site in the “flipped” binding orientation (Figure 2-15 A). This complex likely arises by the same mechanism as described above for the Ala case (Figure 2-14) and further underscores the notion that even when both ligand binding orientations are accessible, OYE1 prefers the “flipped” arrangement.

Table 2-4. X-ray Crystallographic Data Collection and Refinement Statistics

PDB Accession code	4H4I	4K8E	4K8H
Ligand Soaked	(S)-carvone	(R)-carvone	(+)-dihydrocarvone
Observed active site ligand	Phenol 5	Phenol 5	(R)-carvone
X-ray source	NSLS beamline X6A	NSLS X6A	NSLS beamline X6A
Space group	P 4 <sub>3</sub> 2 <sub>1</sub> 2	P 4 <sub>3</sub> 2 <sub>1</sub> 2	P 4 <sub>3</sub> 2 <sub>1</sub> 2
Unit cell dimensions		141.35, 42.85	141.443, 42.851
a = b, c (Å)	141.00, 42.82		
Resolution (Å)	23.6 – 1.25 (1.29 – 1.25)	24.2 – 1.27 (1.315 – 1.269)	35.48 – 1.55 (1.605 – 1.55)
Unique reflections	119,164 (11,776)	113,485 (11,067)	65,589 (6,247)
Completeness (%)	99.98 (99.95)	99.44 (98.44)	99.95 (99.57)
Multiplicity	10.2 (9.9)	9.9 (9.0)	12.2 (12.2)
R <sub>sym</sub> <sup>[b]</sup>	0.10 (0.55)	0.069 (0.547)	0.086 (0.676)
I/σ (I)	19.58 (3.07)	20.33 (2.46)	24.60 (3.79)
R <sub>work</sub> <sup>[c]</sup> , R <sub>free</sub> <sup>[d]</sup>	0.124, 0.146	0.107, 0.127	0.124, 0.162
Ramachandran statistics <sup>[e]</sup>			
Favored (%)	98	98	97
Allowed (%)	2	2	3
Outliers (%)	0	0	0
Number of protein, solvent and ligand atoms	3,286, 660, 108	3,325, 642, 97	3,320, 542, 72
Average B factors (Å <sup>2</sup> )			
Protein	9.8	11.7	15.00
Solvent	26.5	27.90	27.60
FMN	5.8	8.6	12.1
Ligands	14.7	16.6	19.3

## Trp116 Thr mutant

The Thr mutant was chosen for additional study because this residue, although very different in polarity, is nearly isosteric with Val. Our hypothesis was that if substrate binding orientation was controlled primarily by steric factors, the Thr and Val variants should show similar properties. In other words, the same inversion of stereoselectivity for both (*R*)- and (*S*)-carvone displayed by the Ala mutant was expected in the Thr mutant. However, this was not observed. Substituting Thr for Trp116 was highly detrimental for the catalytic efficiency of OYE1 and this mutant showed essentially no conversion for (*R*)-carvone and relatively poor conversion of (*S*)-carvone with reversed stereoselectivity. (Figures 2-3, 2-4).

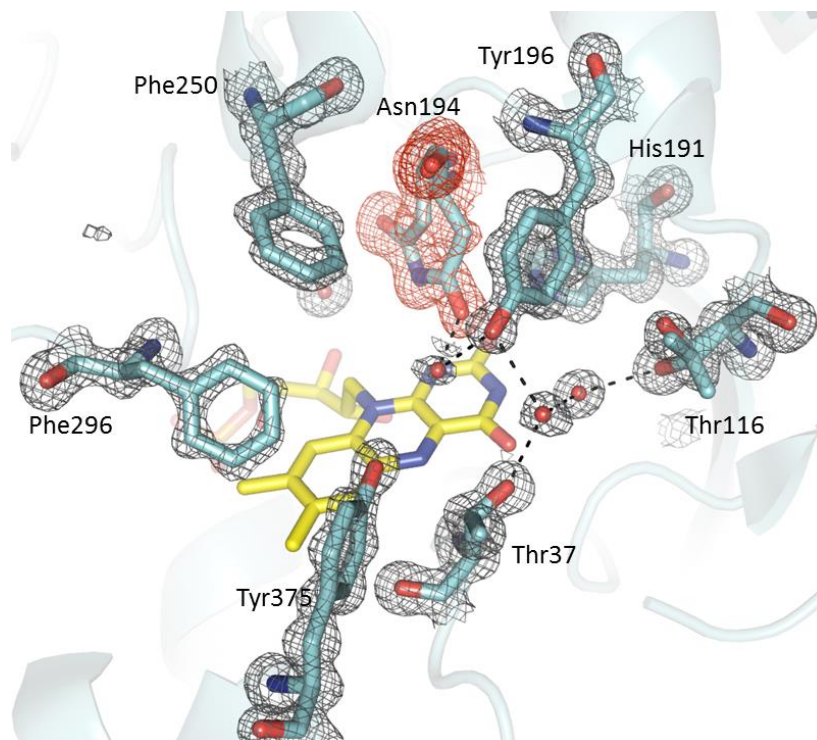


Figure 2-16. Crystal Structure of the Trp116Thr mutant. The grey mesh shows 2mFo-DFc electron density map contoured at 1.2  $\sigma$ . The red mesh is the omit mFo-DFc maps at 3  $\sigma$ . Protein residues are colored in cyan, FMN in yellow and the waters are shown as red spheres.

Table 2-5. X-ray Crystallographic Data Collection and Refinement Statistics

PDB Accession code	4K7Y
Ligand Soaked	( <i>R</i> )-carvone
Observed active site ligand	Chloride
X-ray source	NSLS X6A
Space group	P 4 <sub>3</sub> 2 <sub>1</sub> 2
Unit cell dimensions	
a = b, c (Å)	141.37, 42.83
Resolution (Å)	23.59 – 1.2 (1.242 – 1.199)
Unique reflections	135,136 (13,135)
Completeness (%)	99.80 (98.28)
Multiplicity	6.0 (5.6)
R <sub>sym</sub> <sup>[b]</sup>	0.067 (0.570)
I/σ (I)	14.34 (1.87)
R <sub>work</sub> <sup>[c]</sup> , R <sub>free</sub> <sup>[d]</sup>	0.1150, 0.1350
Ramachandran statistics <sup>[e]</sup>	
Favored (%)	97
Allowed (%)	3
Outliers (%)	0
Number of protein, solvent and ligand atoms	3,358, 666, 58
Average B factors (Å <sup>2</sup> )	
Protein	11.4
Solvent	26.40
FMN	8.3
Ligands	-

<sup>a)</sup>Values in parentheses denote data for the highest resolution bin.

<sup>[b]</sup>R<sub>merge</sub> =  $\frac{\sum_{hkl} \sum_i |I_i(hkl) - [I(hkl)]|}{\sum_{hkl} \sum_i I_i(hkl)}$ , where I<sub>i</sub>(hkl) is the intensity of the i<sup>th</sup> observation of unique reflection hkl.

<sup>[c]</sup>R<sub>work</sub> =  $\frac{\sum | |F_o(hkl)| - |F_c(hkl)| |}{\sum |F_o(hkl)|}$ .

<sup>[d]</sup>R<sub>free</sub> is calculated in the same manner as R<sub>work</sub> using 10% of the reflection data not included during the refinement.

<sup>[e]</sup>Statistics generated using MOLPROBITY<sup>39</sup>

We soaked crystals of the Thr variant individually with (*S*)- and (*R*)-carvone as well as (+)-dihydrocarvone and collected complete, high-resolution data sets for each. In all cases, no active site electron density beyond that of chloride (buffer component) was observed. The highest resolution structure (1.20 Å) was derived from soaking with (*R*)-carvone (4K7Y). Crystal soaked with (*R*)-carvone and (+)-dihydrocarvone were indistinguishable and were fully refined. Surprisingly, the side-chain of Asn194 appeared to occupy at least two different conformations in this structure with an approximate occupancy of 65 : 35 ratio. To the best of our knowledge, this phenomenon has not been observed in any other OYE1 structure (Figure 2-16).

While the major conformer of Asn194 was identical to that observed normally, the second placed the side-chain carbonyl above the FMN, occupying the same space normally filled by a chloride ion in an unliganded OYE1 structure. Modeling only the two conformations of Asn 194 led to a positive peak in the Fo-Fc difference map, which could be eliminated by adding a chloride ion whose occupancy mirrored that of the Asn 194 side-chain in its normal conformation. It is possible to model a hydrogen bond network between the side-chain of Thr116, water723 and the side-chain of Asn194 (in the second conformation) and these favorable interactions may partially explain the observed structural changes. It should be noted that locating the side-chain of Asn194 directly above the FMN would preclude substrate binding and this may be the reason that this Trp116 variant showed poor catalytic efficiency. The side of Thr116 also showed evidence for multiple conformations and participates directly in a hydrogen bond network with solvent molecules not previously observed in other structures. The change in hydrophobicity of the binding pocket coupled to the unusual movement of

Asn194 (residue known to be critical for substrate binding) may explain the lack of success in obtaining structures of the enzyme substrate complexes. The complete crystallographic parameters, data collection and refinement statistics can be found in Table 2-5.

### **Trp116 Gln mutant**

The final mutant selected for structural studies was the Trp116Gln variant since this protein showed good catalytic activity toward both (*R*)- and (*S*)-carvone with altered stereoselectivity for the latter (Figure 2-3, 2-4). In this regard, its properties closely resemble that of the Ile mutant. We were unable to determine a dismutation activity for the Gln mutant, either because it was unable to catalyze the reaction or it was unable to form a stable charge-transfer complex carvone dismutation product **5** under the experimental conditions.

Attempts to observe (*S*)-carvone within the active site of the Trp116Gln mutant by soaking with neat ligand were unsuccessful. Soaking experiments with (*R*)-carvone did afford a complex; however, there were several unusual features. Based on the stereochemistry of its reduction, we anticipated a “normal” substrate binding orientation similar to that seen for the Val and Ala variants. Instead, the substrate was observed in a “flipped” orientation, which would lead to the opposite stereoisomer (Figure 2-17 A).

Several features of this “flipped” complex argue that it does not represent a catalytically productive arrangement, however. First, the distances between the substrate’s carbonyl oxygen and  $N\epsilon 2$  of His191 and  $N\delta 2$  of Asn 194 were 3.7 and 4.5 Å, respectively. Such distances preclude hydrogen bonds, which are known to be essential for catalytic turnover by OYE1<sup>40</sup>. An analogous binding mode for phenols, lacking these hydrogen bonds, would also be consistent with our inability to observe a charge-transfer

complex in dismutation studies of the Gln mutant. In wild-type OYE1, a hydrogen bond between the phenol oxygen and the side-chain of His191 stabilizes the former in its electron-rich anionic form, allowing a charge-transfer complex with the electron-deficient FMN.

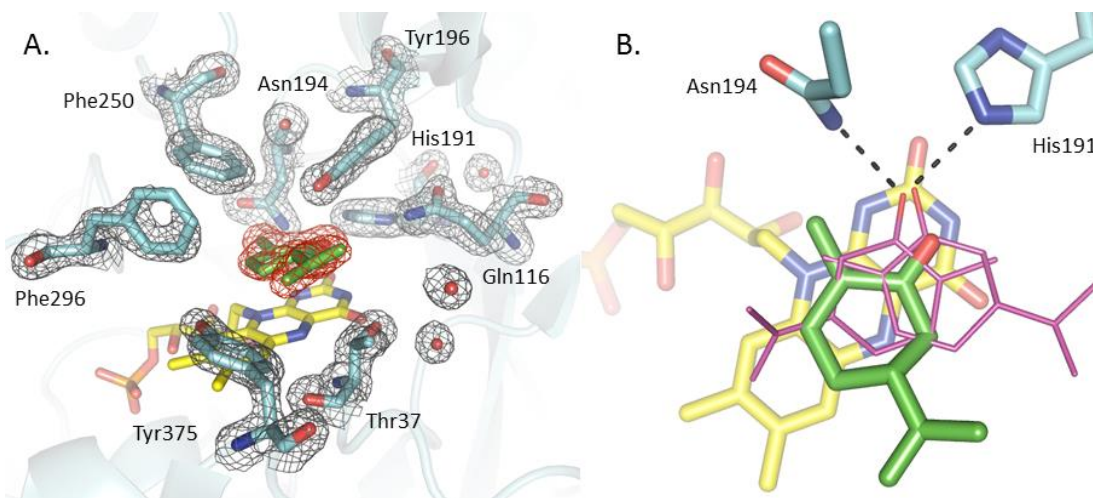


Figure 2-17. OYE1 Trp116Gln. A- The complex of Trp116Gln and (*R*)-carvone. The grey mesh shows 2mFo-DFc electron density map contoured at 1.2  $\sigma$ . The red mesh is the omit mFo-DFc maps at 3  $\sigma$ . B- Superposition of the all binding modes observed. The normal and flipped binding modes are shown in thin magenta lines, the non-canonical binding observed in the Gln116 variant is shown in thick green lines.

By mutating His191, Massey demonstrated that loss of this hydrogen bond eliminated charge-transfer complex formation; in our case, it is ligand re-positioning that eliminates the interaction. The geometric relationship between bound (*R*)-carvone and the FMN cofactor also argues against the catalytic relevance of the observed complex. In particular, the angle formed between  $C\beta$  of carvone and  $N5$  and  $N10$  of the FMN is  $66.5^\circ$  and the  $C\beta$ -to- $N5$  distance is 3.9 Å. Both of these values fall well outside the ranges observed by Fraaije in his survey of flavoproteins bound to their respective substrates and / or products, strongly suggesting that hydride transfer would be

Table 2-6. X-ray Crystallographic Data Collection and Refinement Statistics

PDB Accession code	3TXZ
Ligand Soaked	( <i>R</i> )-carvone
Observed active site ligand	( <i>R</i> )-carvone
X-ray source	X25
Space group	P 4 <sub>3</sub> 2 <sub>1</sub> 2
Unit cell dimensions	
a = b, c (Å)	141.36, 42.69
Resolution (Å)	45.0 – 1.7 (1.76 – 1.7)
Unique reflections	48,165 (4,726)
Completeness (%)	99.99 (99.96)
Multiplicity	9.5 (6.2)
R <sub>sym</sub> <sup>[b]</sup>	0.052 (0.58)
I/σ (I)	17.10 (2.22)
R <sub>work</sub> <sup>[c]</sup> , R <sub>free</sub> <sup>[d]</sup>	0.161, 0.186
Ramachandran statistics <sup>[e]</sup>	
Favored (%)	98
Allowed (%)	2
Outliers (%)	0
Number of protein, solvent and ligand atoms	3,244, 368, 43
Average B factors (Å <sup>2</sup> )	
Protein	23.5
Solvent	36.1
FMN	16.8
Ligands	25.6

<sup>a)</sup>Values in parentheses denote data for the highest resolution bin.

<sup>[b]</sup>Rmerge =  $\sum_{hkl} \sum_i |I_i(hkl) - [I(hkl)]| / \sum_{hkl} \sum_i I_i(hkl)$ , where  $I_i(hkl)$  is the intensity of the  $i$ th observation of unique reflection  $hkl$ .

<sup>[c]</sup>R<sub>work</sub> =  $\sum | |F_o(hkl)| - |F_c(hkl)| | / \sum |F_o(hkl)|$ .

<sup>[d]</sup>R<sub>free</sub> is calculated in the same manner as R<sub>work</sub> using 10% of the reflection data not included during the refinement.

<sup>[e]</sup>Statistics generated using MOLPROBITY<sup>39</sup>

impossible from this geometry. The isopropenyl group of (*R*)-carvone has moved away from the side chain of Gln116 and makes contacts primarily with Thr37 and Tyr375. The position of (*R*)-carvone is unlike those observed in either flipped or normal binding modes (Figure 2-17 B). The complete crystallographic parameters, data collection and refinement statistics can be found in Table 2-6.

### **Conclusions and Future Work**

The main goals of this work were to: a) engineer stereocomplementary OYE1 variants, therefore gaining access to all four possible diastereomers of dihydrocarvone; b) uncover the general principles by which the orientation of substrate binding is controlled in OYE1. We therefore combined data from catalytic studies (alkene reduction and dismutation activity) with X-ray crystallography. Given the hydrophobicity of carvone and the nature of OYE1's active site, which is also predominantly hydrophobic, we initially hypothesized that substrate binding is largely dictated by steric constraints.

The crystallographic studies provided experimental data for four possible types of OYE1-ligand complexes, namely: a) carvone bound in a normal orientation; b) carvone in a "flipped" orientation; c) dismutation product (phenol **5**) in normal orientation and d) "flipped" orientation. To obtain a comparative overview of substrate binding, we superimposed the crystal structures of each of the cases described. Structures were overlaid with respect to their FMN cofactor only. All four overlaid structures show that the oxygen atoms of the ligands - either a ketone carbonyl or a phenol hydroxyl- occupy essentially identical positions. Their location is ideal for forming hydrogen bonds with both His191 and Asn194, reinforcing the notion that this interaction is of high importance to ligand binding (Figure 2-18).

Interestingly, whether the ligand was aromatic or non-aromatic, the positions of the branch-point carbon C8 on the isopropenyl substituent were in very close agreement. While the positions of atom C8 are somewhat fixed, the atom of the methyl and methylene groups (C9 and C10) are able to move due to the facile rotation of the C5-C8 single bond.

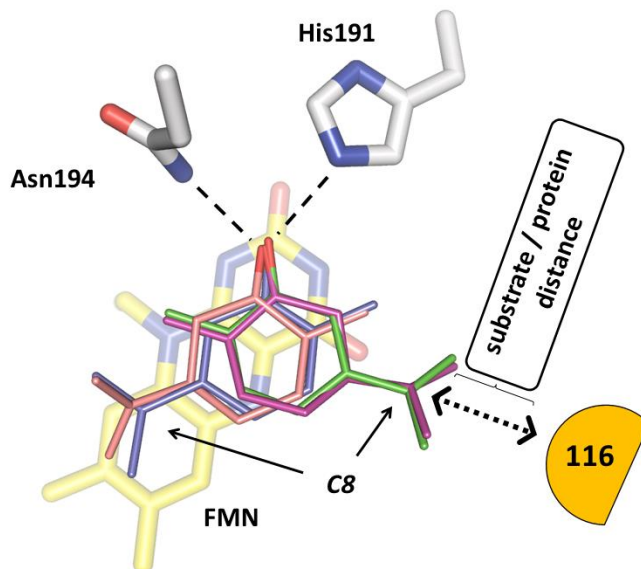


Figure 2-18. Alignment of all four binding modes. (*R*)-carvone in the normal orientation (pink), phenol **5** in the normal orientation (purple), (*R*)-carvone in the flipped orientation (magenta), phenol **5** in the flipped orientation (green).

We attempted to correlate the results of the catalytic assays with a variety of molecular distances and angles based on the crystal structures. The most informative geometric data turned out to be the distances between the ligand C8 position and the closest atom of the amino acid at position 116. For Trp116 variants that bound the ligand in a flipped orientation, the distances were measured directly from the X-ray crystal structures. In cases where no ligand in the flipped orientation was observed but the structures were known (w.t., Gln and Ile), phenol **5** was modeled in the active site based on alignment

as shown in Figure 2-18. Finally, for variants lacking crystal structures (Met, Asn, Phe, and Tyr) both the ligand and the side chains were modeled.

We found a good correlation between the interatomic distances from the ligand's C8 atom to the side chain of amino acid 116 of and the fraction of product derived from a supposedly "flipped" binding mode (Figure 2-19). In the case of (*S*)-carvone, the relationship was surprisingly consistent. If the ligand to protein distance was less than *ca.* 3.7 Å, the enzyme was essentially unable to productively bind the substrate in a flipped orientation (Figure 2-19). Given the C-C bond distances of C8, C9 and C10 in addition to the possible C5-C8 bond rotation, this critical distance likely reflects complexes where the protein-substrate distance would be smaller than their van der Waals contact limits. These data suggest that the "flipping event" is largely controlled by steric factors.

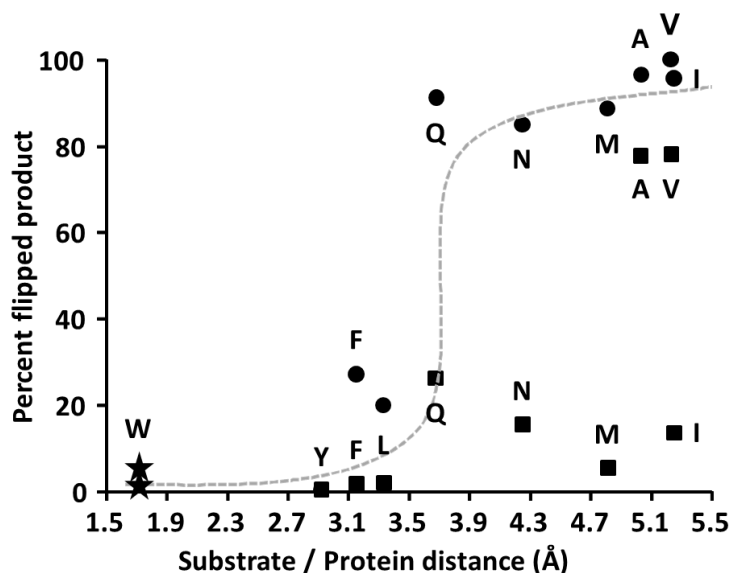


Figure 2-19. The correlation between the ligand's C8-116 side chain distance and the fraction of flipped product. The data are shown as circles (●) for (*S*)-carvone and as squares (■) for (*R*)-carvone.

Three Trp116 variants showed significant deviations from the predicted behavior for (*R*)-carvone, namely Asn, Ile and Met; in each of these cases additional factors, not accounted for in the modeling are likely to contribute. The crystallographic studies of Trp116Gln showed that this substitution provoked (*R*)-carvone to bind in an unusual manner. It is possible that the Asn side caused similar perturbations. In the case of the Trp116Ile enzyme, the crystal structure revealed that the isobutyryl side chain had undergone conformational rearrangements to accommodate the bound ligand. This observation suggested that some steric interference occurred and in this case very minute differences in substrate structure may dictate whether or not flipping would be observed. This hypothesis seems to offer a plausible explanation to the fact that Ile allowed for (*R*)-carvone flipping but not (*S*)-carvone. Minor steric interference coupled to facile  $\chi_1$ ,  $\chi_2$  and  $\chi_3$  rotations, resulting in several conformers, also offer a rationalization for the last amino acid substitution that escapes the overall trend, namely Met.

Perhaps the most striking conclusion of this study is the fact that, in OYE1, the preferred binding mode for carvone is the “flipped” orientation. For example, the wild-type enzyme (Trp116) reduces (*S*)-carvone to *cis*-(2*R*,5*S*)-dihydrocarvone with a diastereomeric excess of 90%. In contrast, the Trp116Ile variant nearly completely inverted the stereochemical outcome yielding a 90% d.e. of *trans*-(2*S*,5*S*)-dihydrocarvone. Why would an increase active site volume on one side cause “flipping” when clearly the wild-type enzyme was able to carry out catalysis with a “normal” binding mode? To a good approximation, “flipped” is the preferred binding orientation and only when this substrate orientation becomes precluded by a large amino acid side chain will the reduction product derive from a normal binding mode.

The obvious question will ask why, then, is flipped the preferred orientation? To address this, we decided to analyze the active site more carefully. We calculated the pockets and cavities present in the wild type enzyme as well as in the Trp116Val mutant since this variant was able to invert the stereochemistry of both (*R*)- and (*S*)-carvone reductions. It was evident that this substitution had created an extra pocket that very nicely accommodated the isopropenyl group of carvone (Figure 2-20 A). This pocket - absent in the wild type (Figure 2-20 B) - had a shape nearly complementary to carvone's side chain and was predominantly hydrophobic in nature.

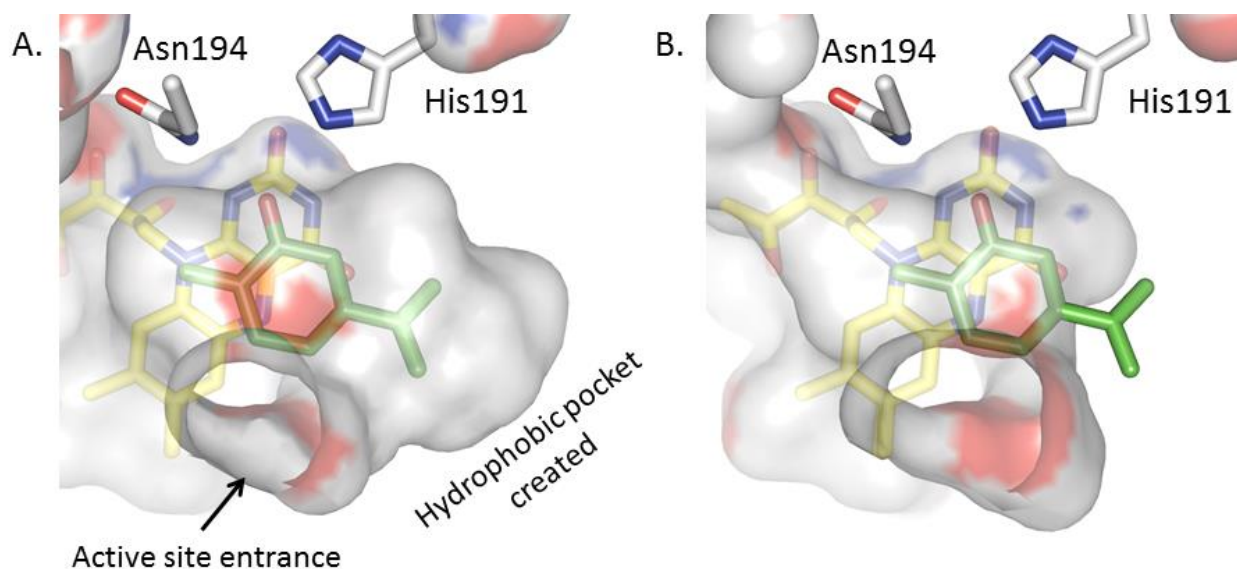


Figure 2-20. Hydrophobic pockets in OYE1. A- The active site pocket of Trp116Val. (*R*)-carvone is shown in green sticks. B- The active site pocket in wild-type OYE1. The isopropenyl group of (*R*)-carvone simply could not fit in this “flipped” orientation. The pockets are shown as semi-transparent surfaces.

As supported by the crystals structures, in a “normal” binding orientation, carvone's isopropenyl side-chain makes close contacts with Phe250, Pro295, Phe296 and Tyr375. In fact, both Tyr375 and Phe296 appear to move significantly in an attempt to accommodate this binding orientation with the latter being essentially disordered. In contrast, in an enzyme variant that allows for the “flipped” binding mode such as

Trp116Val, by simply replacing the large Trp residue with a smaller side-chain access to a new binding pocket is created. As noted previously, this pocket has the ideal characteristics for accommodating carvone. Its shape is nearly ideal to fit the isopropenyl group. Additionally, it is formed by the Thr37, Met39, Gly72, Phe74, Tyr82, Ala85, Leu118 and Val116 making it suited to interact with a hydrophobic substrate such as carvone. One final important observation is that upon substrate binding, no appreciable movement of any of the side chains that delineate this pocket is observed, further validating the idea of it being a more natural fit for this substrate.

This work has described the discovery of OYE1 variants that are fully stereocomplementary, giving access to all four diastereomers of dihydrocarvone. A rationalization based on the wealth of structural and catalytic data is also presented. The principles that govern substrate binding, and therefore stereoselectivity in OYE1, are likely to be shared by other members of this family. Hopefully the studies described herein can provide guidance and motivation for many protein engineering projects to come making this class of enzymes even more suitable for biocatalysis.

## **Experimental Procedures**

### **Enzymatic Reductions Screening (Catalytic Studies)**

Full library screen reactions were carried out aerobically in a 96-deepwell plate containing 10 mM substrate in 0.1 M  $\text{KPi}$  pH 7.0 in a total volume of 300  $\mu\text{L}$ . 0.3 mM NADPH was kept at a constant concentration via a regeneration system consisting of 200 mM glucose and 25 units/mL of GDH (glucose dehydrogenase). The catalyst loading was approximately 100  $\mu\text{grams}$ . Reactions were incubated at 22°C for 16 hours. The reactions were extracted by addition of 500  $\mu\text{L}$  of ethyl acetate followed by vigorous

mixing. The plate was then centrifuged at 3,000 × g for 10 minutes; finally 300 μL of the organic layer was collected and used for GC- MS analysis.

### Charge-Transfer Formation Assays

Each enzyme was added to final concentration *ca.* 15 μM in 0.1 M KPi pH 8.0. Substrate (either (*R*)- or (*S*)-carvone) was added to a final concentration of 2 mM from a 100 mM ethanol stock. The reactions were incubated for 24 hrs at room temperature (near 22 °C in a rotatory apparatus for mixing. The total reaction volume was 250 μL. All enzyme stocks had their concentrations estimated spectrophotometrically using an extinction coefficient  $\epsilon^{462} = 11,700 \text{ M}^{-1} \text{ cm}^{-1}$ . In separate experiments, each variant was incubated with 3 mM *p*-chlorophenol. This allowed us to estimate each variant's ability to form charge –transfer complexes as well as evaluate their spectrum at full binding saturation. This information was used to calculate the fractional charge-transfer complex formation with (*R*)- and (*S*)-carvone.

### GC-MS Analysis

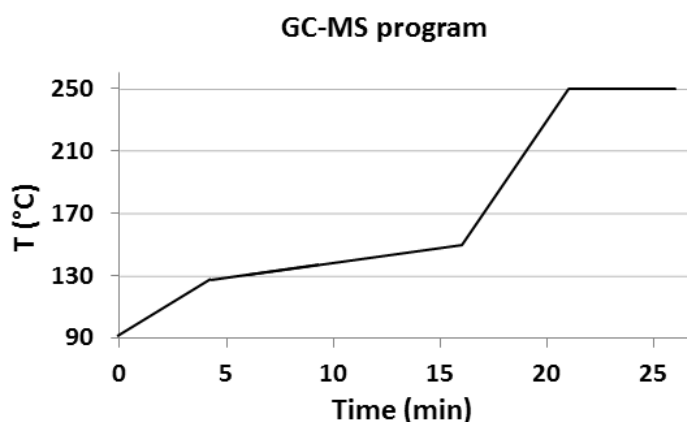


Figure 2-21. Temperature program for GC-MS analysis on DB-17 cloumn.

All samples were analyzed using DB-17 column (0.25 mm x 30 m) with the following temperature program: initial temperature of 90°C; followed by an increase of

10 °C/min up to 130 °C; increase rate of 2 °C/min up to 150 °C; increase rate of 20 °C/min up to 250 °C for 5 minutes (Figure 1-4). Typical retention times were 7.23 min for the trans-(2*R*,5*R*)-dihydrocarvone and trans-(2*S*,5*S*)-dihydrocarvone products, 7.62 min for cis-(2*S*,5*R*)-dihydrocarvone and cis-(2*R*,5*S*)-dihydrocarvone (Appendix A, Figure A-1) and 8.84 min for the substrates (*R*)-and (*S*)-carvone. (Appendix A, Figure A-2).

Appendix A shows results for typical analyses of the enzymatic reductions.

### Site-Directed Mutagenesis

All mutants used for were generated by PCR using primers with the desired mutation at position 116 in a modification of the method published by Zheng *et al.* <sup>41</sup>. Primers were designed as follows: 5'-GG GTT CAG TTA XXX GTT TTG GGT TGG GCT GCT TTC CCA GA-3' and 5'-CA ACC CAA AAC XXX TAA CTG AAC CCC AAA CGA ACG ATT TCT-3', where XXX represents the appropriate codon for each mutation.) Table 2-7 lists primers used in this study.

Table 2-7. Mutagenic primers utilized for constructing the enzymes used for X-ray crystallography.

Mutation	Primer Sequence
W116A <i>fwd</i>	5'-GG GTT CAG TTA GCT GTT TTG GGT TGG GCT GCT TTC CCA GA-3'
W116A <i>rev</i>	5'-CA ACC CAA AAC AGC TAA CTG AAC CCC AAA CGA ACG ATT TCT-3'
W116L <i>fwd</i>	5'-GG GTT CAG TTA TTG GTT TTG GGT TGG GCT GCT TTC CCA GA-3'
W116L <i>rev</i>	5'-CA ACC CAA AAC CAA TAA CTG AAC CCC AAA CGA ACG ATT TCT-3'
W116Q <i>fwd</i>	5'-GG GTT CAG TTA CAA GTT TTG GGT TGG GCT GCT TTC CCA GA-3'
W116Q <i>rev</i>	5'-CA ACC CAA AAC TTG TAA CTG AAC CCC AAA CGA ACG ATT TCT-3'
W116T <i>fwd</i>	5'-GG GTT CAG TTA ACC GTT TTG GGT TGG GCT GCT TTC CCA GA-3'
W116T <i>rev</i>	5'-CA ACC CAA AAC GGT TAA CTG AAC CCC AAA CGA ACG ATT TCT-3'
W116V <i>fwd</i>	5'-GG GTT CAG TTA GTT GTT TTG GGT TGG GCT GCT TTC CCA GA-3'
W116V <i>rev</i>	5'-CA ACC CAA AAC AAC TAA CTG AAC CCC AAA CGA ACG ATT TCT-3'

Each PCR reaction (total volume 100 µL) containing 5 × Phusion HF Buffer (20 µL), pET3b-OYE (Appendix B) (20 ng), forward and reverse primers (0.5 µM each), dNTPs (200 µM each), and Phusion Hot Start II High-Fidelity DNA Polymerase (1 U)

was subjected to an initial denaturation step of 98 °C (30 s) followed by 25 cycles of 98 °C (10 s) and 72 °C (4 min) followed by a final incubation at 72°C (7 min). Amplicons were purified by DNA spin columns, digested with DpnI at 37°C (10 U for 4 h followed by an additional 10 U for 4 h) then purified by an additional DNA spin column. Aliquots (5 µL) were used to transform *E. coli* JM109 (75 µL) by electroporation. SOC medium was added (600 µL), then the samples were incubated for 1 h at 37 °C prior to selection on LB medium supplemented with ampicillin. Plasmid DNA purified (spin columns) from randomly-chosen colonies was analyzed by DNA sequencing to identify the desired OYE1 variants.

The Trp116Ile mutant was constructed by digestion of pET3b-OYE and pSKP3-B30 (plasmid described in <sup>35</sup>) with Apal and KpnI. The resulting small fragment of pSKP3-B30 resulting from the digestion and contained the OYE1-W116I coding region was purified using a low melt agarose gel. Ligation was performed using this small fragment and the large fragment of the pET3b-OYE Apal/KpnI double digest which had also been purified by a low melt agarose gel. The ligation reaction used 1.75 µg of the pET3b-OYE fragment and 0.243 µg of pSKP3-B30 small fragment. 1 µL of the resulting ligation mixture was used to transform electro-competent *E. coli* JM109 cells (39 µL) by electroporation. SOC medium was added (600 µL), then the samples were incubated for 1 h at 37 °C prior to selection on LB medium supplemented with ampicillin. Plasmid DNA purified (spin columns) from randomly-chosen colonies was analyzed by DNA sequencing to identify the desired OYE1-W116I variant.

### **Protein Expression and purification**

Plasmids were transformed into *E. coli* BL21-Gold (DE3) cells and grown in LB broth supplemented with 0.1% glucose w/w, and 200 µg/mL ampicillin. Cultures were

induced by addition of 0.4 mM isopropyl- $\beta$ -thiogalactoside (IPTG) when the optical density at 600 nm reached 0.6. The temperature was decreased to 30°C during protein expression. Cells were harvested after 16 hours at a density of approximately 8 g/L. Cells were then pelleted by centrifugation at 5350 x g for 10 minutes and the pellet was resuspended to 1g/mL in 100mM Tris·HCl pH 8.0 containing 10 $\mu$ M phenylmethanesulfonyl fluoride (PMSF). All of the subsequent steps were performed at 4 °C. The resuspended cells were lysed at 15,000 psi in a French pressure cell using a Carver laboratory press. Lysed cells had debris removed by centrifugation at 20,000 x g for 1 hour. To remove nucleic acids, protamine sulfate (1 mg/mL) was added. Nucleic acids were centrifuged out at 10,000 x g for 15 min. The cell lysate had its pH adjusted to 8.5 by the addition of ammonium hydroxide. Solid ammonium sulfate was added to 78% saturation level and the lysate was centrifuged at 20,000 x g for 1 hour. The precipitate was resuspended in minimal amount of 100mM Tris·HCl, 100 mM ammonium sulfate, 10  $\mu$ M PMSF at pH 8.0, and dialyzed against the same buffer for 6 hours (buffer was exchanged after 3 hours). The lysate was then dialyzed against a new buffer of the same recipe containing an additional 10 mM sodium dithionite. This step served the purpose of removing any small phenolic type molecules that may be complexed with the enzyme. This step is also referred to as de-greening in allusion to the long wavelength charge-transfer complexes of OYE1. One last dialysis was performed to ensure removal of all of the sodium dithionite, and that the enzyme would return to its oxidized state before chromatography. The enzyme was purified by affinity chromatography using an N-(4-hydroxybenzoyl) aminoethyl agarose gel matrix. The column was packed with about 3 mL of the matrix and connected to a Pharmacia FPLC

system. The column was equilibrated with buffer containing 100mM Tris-HCl, 100 mM ammonium sulfate pH 8.0. Cell extract was loaded onto the column and it was washed with buffer until the absorbance at 280 nm became stable at approximately 0.2 A.U. For elution, the column was washed with 3 volumes of buffer supplemented with 6 mM sodium dithionite. The elution buffer was deoxygenated and flushed with nitrogen gas before addition of sodium dithionite. The enzyme eluted upon reduction by dithionite. Enzyme was collected in four 3 mL fractions. Fractions were pooled and concentrated by centrifugation using a 10,000 MWCO membrane. For regeneration of the affinity matrix, the column was washed with 3 volumes of buffer containing 6 M guanidine-HCl, 0.2 M sodium acetate at pH 5.0. Purified protein was then loaded onto a Superdex 200 HR 10-30 (Pharmacia) for further purification. The column was equilibrated with low ionic strength buffer, 50 mM Tris-HCl, 50 mM NaCl, 10  $\mu$ M PMSF. Only the major peak at 280 nm was collected. A typical run would consist of a 10 mg of protein loading and after this step the protein samples were homogenous as indicated by SDS-PAGE (Appendix C)

### **Crystallographic Studies**

Crystals were obtained using by a hanging drop vapor diffusion method at 4° C. The protein solution had approximately 40 mg/mL protein in 50mM Tris-HCl, 50mM NaCl, 10  $\mu$ M PMSF pH 7.5. The reservoir solution contained 35% PEG 400, 200 mM MgCl<sub>2</sub>, and 100 mM HEPES pH 8.3. Crystal usually formed in about 5 to 7 days and would grow for another 7 to 14 days. Crystals grew as yellow tetragonal rods typically diffracted to 2.0- 1.2 Å and measured on average 180  $\mu$ m x 180  $\mu$ m x 500  $\mu$ m. For substrate soaking experiments, the crystals were soaked in mother liquor with the

addition of saturating amounts of ligand for varying amount of time depending on the experiment. Data collection was performed under cryogenic conditions at 100 K in Brookhaven National Laboratory beamlines X25, X6A and X26C. Crystals were mounted on nylon loops and plunged into liquid nitrogen prior to data collection. The best results were obtained when no further cryo-protection protocol was employed. The mother proved suitable for cryogenic data collection. These crystals were also amenable to the “annealing” technique which consists of allowing a cryo-cooled crystal to warm up to room temperature followed by flash cooling. In many cases, this was an efficient way of minimizing ice rings seen on the diffraction pattern.

### **Structure Solution**

X-ray data were processed using HKL2000 or iMOSFLM<sup>42, 43</sup>. The structures were solved by molecular replacement using AUTOMR in the PHENIX suite<sup>44</sup>. The search used a high resolution model of OYE1 (PDB code 3RND). The initial search model was devoid of water molecules and any ligands. Additionally, residue 116 was initially modeled as alanine. Inspection of the electron density maps was followed by manual rebuilding, addition of ordered waters and refinement of each model's coordinates and temperature factors against the X-ray data. During refinement, inspection of the calculated 2mFo-DFc and mFo-DFc difference maps showed clear positive electron density for the side chain of residue 116 and above the isoalloxazine moiety of the bound FMN cofactor. This allowed for building of the correct residue 116 side chains and unambiguous placement of the carvone ligands. This process was performed iteratively until residuals errors  $R_{work}$  and  $R_{free}$  converged. The complete crystallographic parameters, data collection and refinement statistics can be found in Results and Discussion.

## Enzyme-substrate Complex Modeling

The complexes generated were W116F/M/N/P/Q/Y and OYE1 w.t. bound to inhibitor (phenol **5**, *vide supra*). The enzyme-inhibitor complexes were generated by manually building each side chain in COOT<sup>45</sup> and clashes were calculated using the built-in MOLPROBITY<sup>39</sup> utility. The initial position of the side chains were selected on the basis of: a) the likelihood of the rotamer; b) the similarity to an amino acid in an existing crystal structure model, e.g. phenylalanine was placed similarly to tryptophan. Because of the constraints regarding position of the ligand such as, hydrogen bonding to N194 N $\delta$ 2 and H191 N $\epsilon$ 2, distance to the FMN isoalloxazine ring and distance to the proton donor Y196, the ligand was manually placed in a position similar to the observed in the crystal structures. The resulting enzyme-inhibitor models were then subjected to geometry optimization/energy minimization using REFMAC5<sup>46</sup>. The resulting refined models were then inspected for validity. If shifts greater than 0.20 Å in the inhibitor final coordinates were observed, the model was not considered for the measurements as it would likely represent an unproductive complex. This was the case for the W116Y and w.t. enzymes and simple least squares superposition was used to estimate steric clashes. The model of W116P was not used for measurements at all as energy minimization could not be performed successfully. This likely comes from the fact that mutation to a P116 would cause major backbone rearrangement in the protein and energy minimization procedures failed to find suitable conformations.

CHAPTER 3  
STRUCTURAL AND CATALYTIC CHARACTERIZATION OF *P. stipitis* OYE2.6, A  
USEFUL CATALYST FOR ALKENE REDUCTIONS

**Background and Motivation**

Our group was highly interested in discovering OYE family enzymes that would offer enantioselectivity as achieving such goal can provide a solution to one of the key factors that limits the applicability of enzymes in synthetic processes. The previous chapter discusses how some of our earliest protein engineering studies revealed that replacing an active site Trp residue (position 116) with Ile radically changed the stereoselectivity of *S. pastorianus* OYE1. Initially, this observation seemed to be unique to the reduction of carvones, however further investigation showed it was not an isolated occurrence<sup>47</sup>. Our group tested the stereoselectivity of OYE1 Trp116 variants in the reduction of three substrates that are useful intermediates in a number of synthetic routes<sup>48, 49, 50</sup>. Once again, position 116 was able to influence the enzyme's enantioselectivity and the outcome depended on the nature of the Trp116 replacement (Figure 3-1).

Interestingly, Trp116 is a well conserved residue in the OYE1 family (Figure 3-2) and yet it can drastically influence the enzyme's stereoselectivity. We therefore pursued old yellow enzyme homologs possessing residues other than Trp at the position corresponding to 116 of *S. pastorianus* OYE1. This led to the cloning and overexpression of OYE2.6 from the xylose-fermenting yeast *Pichia stipitis* CBS 6054 (Bougioukou PhD thesis). Based on sequence alignment and computer modeling from the *S. pastorianus* OYE1 structure, Ile113 in OYE2.6 was expected to occupy a similar active site location as Trp116.

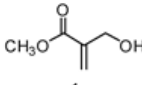
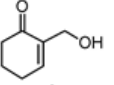
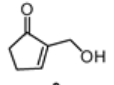
Protein	Substrate					
	 1		 2		 3	
	% conv	% ee <sup>a</sup>	% conv	% ee <sup>b</sup>	% conv	% ee <sup>c</sup>
<i>S. pastorianus</i> OYE1 mutants (116 residue)						
Trp (wt)	19	>98 (R)	≤5	N.D.	51	60 (R)
Ala	9	90 (R)	84	>98 (S)	>98	72 (S)
Val	52	86 (R)	84	>98 (S)	97	92 (S)
Tyr	68	76 (R)	>98	>98 (S)	>98	87 (S)
Phe	37	70 (R)	>98	>98 (S)	98	>98 (S)
Ser	13	46 (R)	84	>98 (S)	87	>98 (S)
Ile	50	9 (R)	>98	>98 (S)	>98	91 (S)
Arg	≤5	N.D.	≤5	N.D.	≤5	N.D.
Pro	≤5	N.D.	14	>98 (S)	16	77 (S)
Thr	≤5	N.D.	28	>98 (S)	44	>98 (S)
Cys	≤5	N.D.	31	>98 (S)	47	77 (S)
Lys	≤5	N.D.	60	>98 (S)	75	76 (S)
Glu	≤5	N.D.	93	90 (S)	96	88 (S)
Asp	≤5	N.D.	>98	91 (S)	95	77 (S)
Gly	14	16 (S)	98	>98 (S)	>98	86 (S)
Leu	>98	20 (S)	>98	>98 (S)	>98	57 (S)
Asn	>98	41 (S)	>98	>98 (S)	>98	89 (S)
Met	15	64 (S)	>98	>98 (S)	>98	86 (S)
His	67	97 (S)	>98	>98 (S)	>98	77 (S)
Gln	78	>98 (S)	>98	>98 (S)	>98	89 (S)

Figure 3-1. Reductions of Baylis-Hillman Adducts by Alkene Reductases

On this basis, we expected that the stereoselectivity of OYE2.6 would be analogous to that of the *S. pastorianus* OYE1 Trp116Ile mutant however, the reality proved more complex.

In general, OYE2.6 has proven to be a superior alkene reductase with regard to stereoselectivity, conversion rate and stability and was successfully employed in the reductions of citral<sup>51</sup>. In some cases, its stereoselectivity was opposite that of *S. pastorianus* OYE1, but this was not universally true. For example OYE1 reduces 2-hydroxymethylcyclopent-2-enone to the (*R*)- product mainly. In contrast, OYE2.6 afforded the (*S*)- enantiomer and this was in accord with our initial hypothesis. However,

curiously, OYE2.6 fails to display a similar inversion of stereochemistry in the reduction of (*S*)-carvone (Figure 3-3).

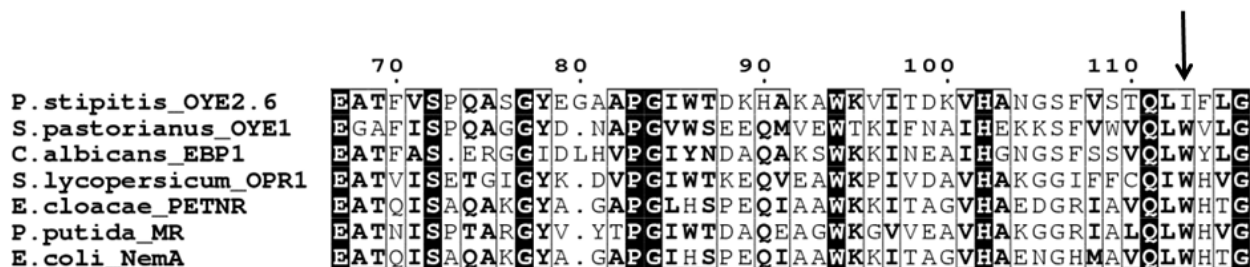


Figure 3-2. Partial sequence conservation in seven OYE family representatives. OYE2.6, OYE1, estrogen binding protein (EBP1), oxophytodienoate reductase (OPR1), pentaerythritol tetranitrate reductase (PETNR), morphinone reductase (MR) and N-ethylmaleimide reductase (NemA). Position 113 in OYE2.6 (116 in OYE1) is indicated by an arrow.

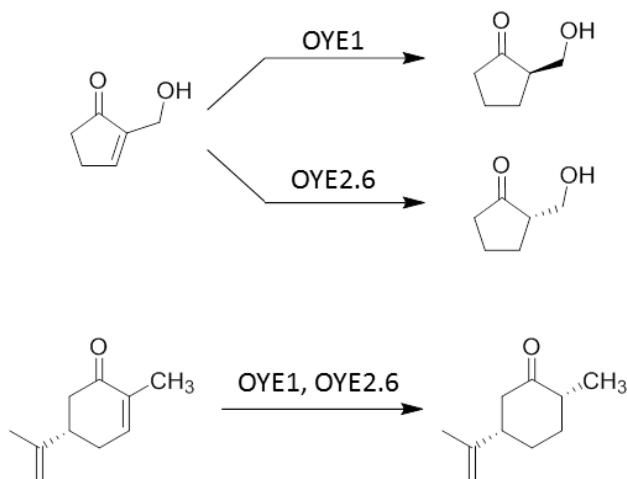


Figure 3-3. Comparison of OYE1 and OYE2.6 stereoselectivity.

Despite exhibiting superior and sometimes complementary catalytic properties, there are currently two impediments to the wider use of OYE2.6 in chemical synthesis: a relatively limited knowledge of substrate and stereoselectivity characteristics and an unknown three-dimensional structure. Because the latter is particularly critical for protein engineering studies of this enzyme, we undertook the elucidation of the X-ray

crystal structure of OYE2.6. In addition, the results of four site-saturation mutagenesis libraries that allow for meaningful comparisons with *S. pastorianus* OYE1 are presented. These will point the way toward future approaches to obtaining even more useful variants of OYE2.6.

## Results and Discussion

Native OYE2.6 was overexpressed in *E. coli* BL21-Gold (DE3) carrying the plasmid pBS3. The enzyme could be purified by ammonium sulfate fractionation followed by affinity and gel filtration chromatography. This afforded a preparation of the enzyme of >95% purity. After screening approximately 300 conditions, crystals were observed when organic salts were the main precipitants at near-neutral pH values. The most promising, obtained in 2.4 M sodium malonate, pH 7.0, diffracted to a maximum resolution of 2.0 Å using a Rigaku CuK $\alpha$  rotating anode X-ray source. Unfortunately, these proved unsuitable for crystallographic studies as they were not singular and yielded diffraction patterns that could not be indexed accurately. Because attempts at optimizing pH and salt concentrations proved unsuccessful, a further screening of 96 additives coupled with the original conditions (2.4 M sodium malonate, pH 7.0) was carried out. The best crystals were seen in the original conditions supplemented with 2% 2-propanol and formed from a ca. 40 mg/mL protein solution. After adequate cryoprotection the crystals diffracted to 1.4 Å using synchrotron source radiation at 100 K. The crystals belonged to space group P 6<sub>3</sub> 2 2 (number 182) and the unit cell measured 127.1 Å, 127.1 Å, 123.4 Å. The asymmetric unit consisted of one OYE2.6 molecule with a solvent content of 63% with a Matthews coefficient of 3.23 Å<sup>3</sup>/Da<sup>1/2</sup> <sup>52</sup> (See Experimental for more details).

## Overall Fold

The initial OYE2.6 structure was solved by molecular replacement using a modified version of *S. pastorianus* OYE1 as the search model (1OYA). The X-ray data yielded a high quality model that was refined to 1.5 Å resolution with final Rwork and Rfree values of 0.143 and 0.168, respectively (Table 3-1). The enzyme belongs to the TIM phosphate binding family and exhibits the eight-stranded  $\alpha/\beta$ -barrel fold characteristic of all OYEs first seen in triosephosphate isomerase (TIM)<sup>53</sup> and glycolate oxidase (GOX). The overall structure of OYE2.6 is similar to those of other old yellow enzyme homologs, particularly to that of *S. pastorianus* OYE1 (Figure 3-3). These share 43% sequence identity and also have closely related backbone positioning (aligning 325  $\alpha$ -carbons with a root mean square deviation of 0.92 Å).

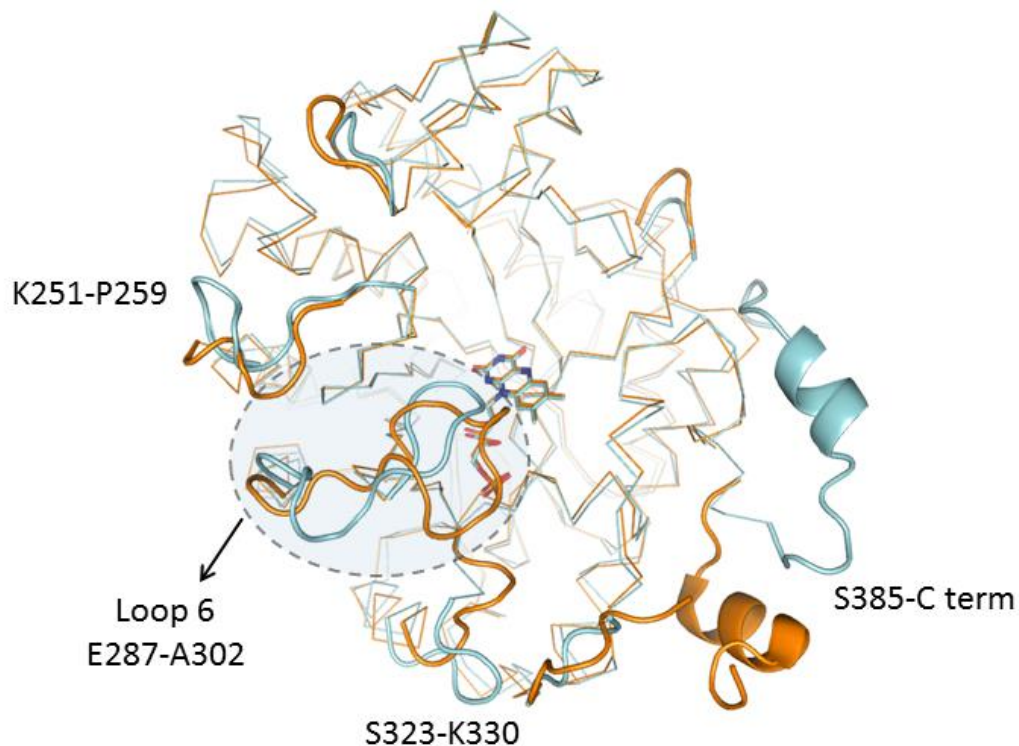


Figure 3-4. Superposition of the structures of OYE2.6 (cyan) and OYE1 (orange). The regions of highest dissimilarity are shown in cartoon representation and are labeled

The most important structural difference between *P. stipitis* OYE2.6 and *S. pastorianus* OYE1 is found in loop L6 (Glu287–Ala302) (Figure 3-4). Finally, the crystal structure also reveals that in OYE2.6, Ile113 is spatially equivalent to Trp116 in OYE1 as had been surmised initially.

In order to further gauge OYE2.6's place within the OYE family, we carried out structural comparisons to other members. After *S. pastorianus* OYE1, the next most similar structures are *Pseudomonas putida* morphinone reductase (MR, PDB code 1GWJ)<sup>16b</sup> (291 C $\alpha$  aligned, 1.26 Å r.m.s.d.), *Enterobacter cloacae* pentaerythritol tetranitrate reductase (PETNR, 1H50)<sup>16c</sup> (232 C $\alpha$  aligned, 1.38 Å r.m.s.d.), followed by *Bacillus subtilis* YqjM (1Z41)<sup>16d</sup> (191 C $\alpha$  aligned, 2.57 Å r.m.s.d.) (Appendix D). These results suggest that OYE2.6 and OYE1 can be grouped into the same class of OYE homologs.

### **Quaternary Structure**

Besides variations in active site residues and architecture, differences in quaternary structure are also an aspect that can help in the classification of OYE family enzymes. For instance, *S. pastorianus* OYE1 is dimeric while its plant homolog OPR1 is monomeric<sup>54</sup>. In contrast, the bacterial enzyme TOYE exists as an octamer and even higher oligomeric states<sup>32</sup>. In an attempt to unambiguously classify OYE2.6, we attempted to characterize its quaternary structure through native gel filtration and analysis of the molecular contacts in its crystalline form. Under our experimental conditions, homogenous recombinant OYE2.6 had an elution volume consistent with that of an 89 kDa assembly (Experimental Procedures). Given that OYE2.6 is a 407 amino acid protein with a theoretical molecular weight of 46.1 kDa this result strongly suggested that the protein is dimeric in solution. In order to evaluate OYE2.6's

oligomeric state in its crystal form we had to study the crystal contacts of each protomer since the crystallographic asymmetric unit consists of a single molecule.

One particular interaction buries the most surface area (total of 1520 Å<sup>2</sup>) and is composed of two protomers related by a two-fold crystallographic symmetry operator suggesting this could be the dimeric interface. This interface involves helix 4 (residues 212-216), helix 5 (252-260) and helix 6 (263-268, 271) in both molecules (Figure 3-5). As these helices are nearly perpendicular to the two-fold axis, each helix interacts with its symmetry mate and are the same helices as those seen in *S. pastorianus* OYE1 dimer<sup>14</sup>.

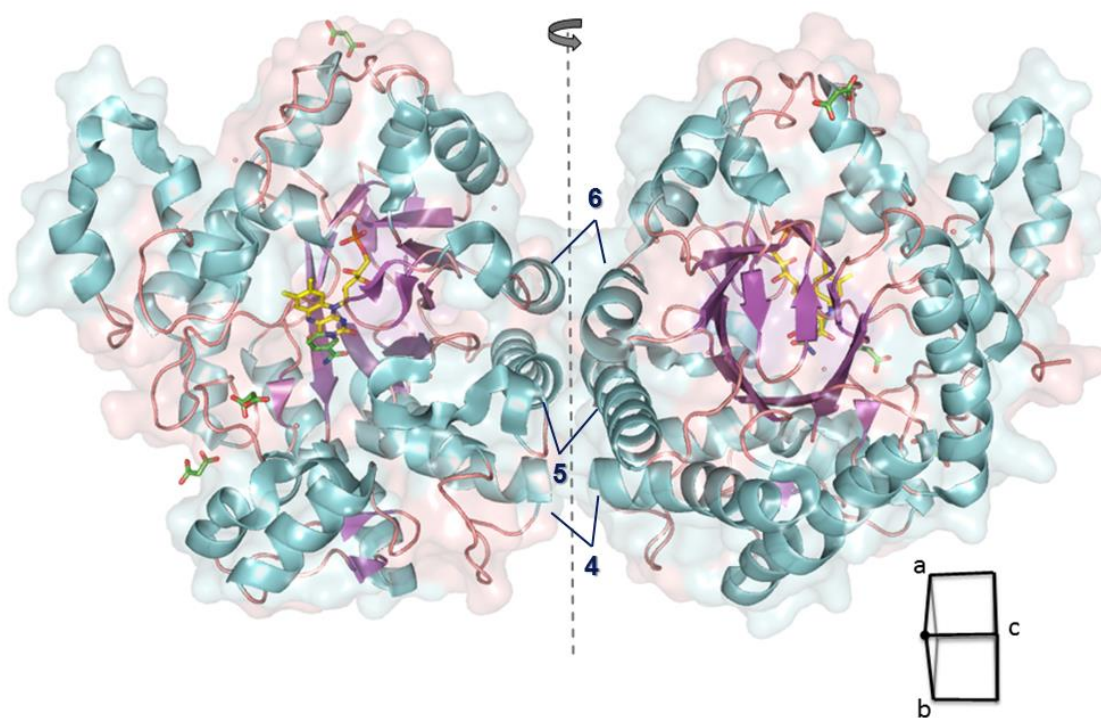


Figure 3-5. The proposed OYE2.6 dimer. The 2-fold molecular axis is indicated by a dashed line. Helices 4, 5 and 6 are label. The orientation of the crystallographic axes are shown for reference.

As previously noted by Fox and Karplus, the dimer interface area represents about 5% of the total surface area of an OYE monomer and is near the lower end of values

seen for dimeric proteins<sup>55</sup>. This may be one of the reasons why software prediction by PISA<sup>56</sup> results in a different dimeric interface although no single solution is heavily favored.

OYE2.6 crystallizes in space group  $P 6_3 2 2$  having 12 symmetry operators and each monomer makes contacts with five other symmetry mates (Figure 3-6 A). Dissimilarly, OYE1 crystallizes in  $P 4_3 2_1 2$  and makes contacts with seven symmetry mates (Figure 3-7 A).

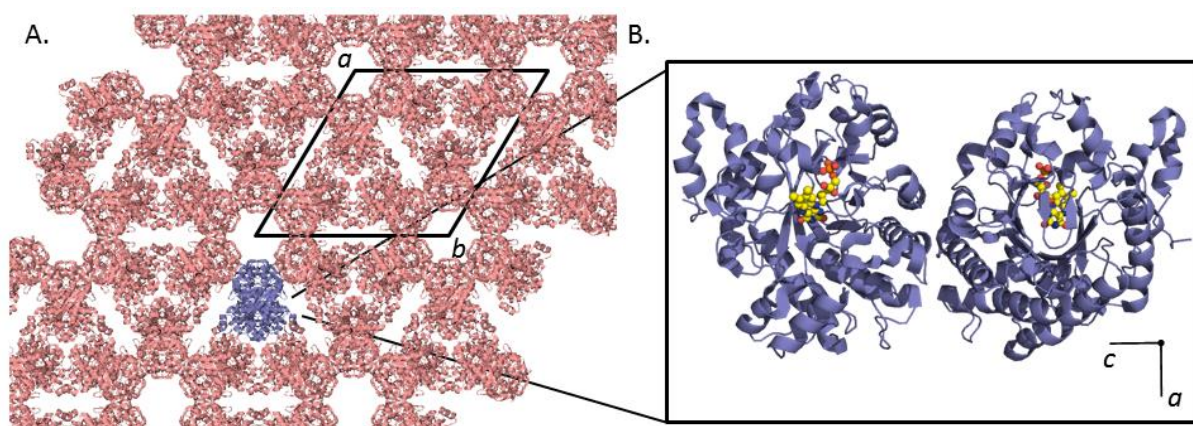


Figure 3-6. OYE2.6 crystal lattice. A- Crystal packing of OYE2.6 in  $P 6_3 2 2$ . viewed along the crystallographic  $c$ -axis. The unit cell is drawn as a black polygon and the dimer is shown in purple. B- Magnified view of the two molecules forming the homodimer.

Despite crystallizing in different space groups, the relative positions of the two monomers forming the dimers in OYE2.6 and OYE1 are nearly identical (figures 3-6 B and 3-7 B). The same helices, namely, helix 4, 5 and 6, interact with their symmetry mate equivalent in the crystal structure of both enzymes. This observation not only supports the structure of the dimeric assembly in OYE2.6 but also suggests that OYE2.6, like OYE1, has evolved these specific contacts to exist as a dimer. Taken together these results support the notion that OYE2.6 and OYE1 are indeed in the same class of fungal OYEs.

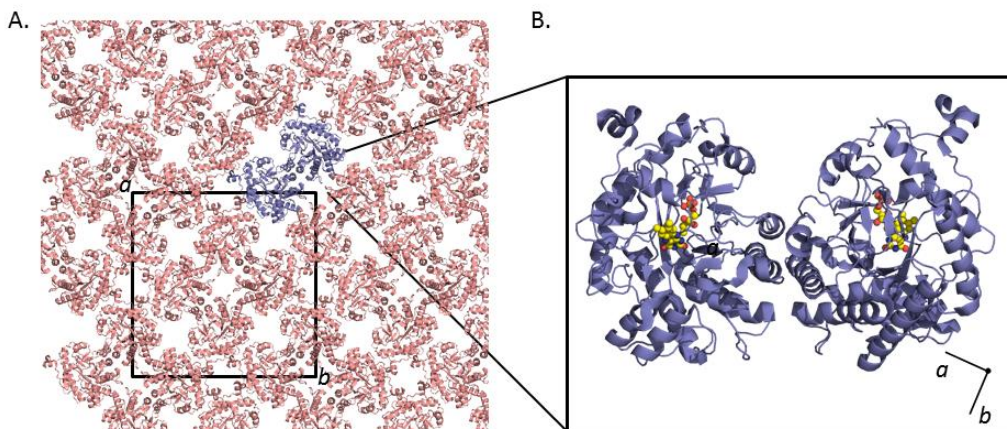


Figure 3-7. OYE1 crystal lattice. A- Crystal packing of OYE1 in  $P 4_3 2_1 2$  viewed along the crystallographic  $c$ -axis the dimer is shown in purple. The unit cell is drawn as a black polygon. B- Magnified view of the two molecules forming the homodimer.

### Flavin Environment and Phenol Binding

The flavin mononucleotide cofactor was readily apparent in the initial electron density maps. As anticipated, the FMN was well ordered and displayed well-defined electron density and low temperature factors *ca.*  $17 \text{ \AA}^2$  ( $22 \text{ \AA}^2$  for protein atoms) consistent with the  $K_D$  values near  $10^{-10} \text{ M}$  usually seen in OYE enzymes. The cofactor is bound in the center of the enzyme's 8-strand parallel  $\beta$ -barrel and makes extensive contacts with several highly conserved residues (Figure 3-8). The FMN's negatively charged phosphate group makes a salt bridge with Arg347. Oxygen O3' appears to hydrogen bond with both water 31 and Arg240, whose side chain also interacts indirectly with O2'. The dimethyl benzene moiety makes contacts with the aromatic residues Phe373 and Tyr374 and its isoalloxazine ring is positioned to form direct hydrogen bonds with Gln111, Thr35, Arg240 and the main chain nitrogen of Ala68. Gln111 is absolutely conserved in the OYE family and this side chain, along with that of Thr35, is implicated in regulating the FMN reactivity in *S. pastorianus* OYE1<sup>17c 17a</sup>.

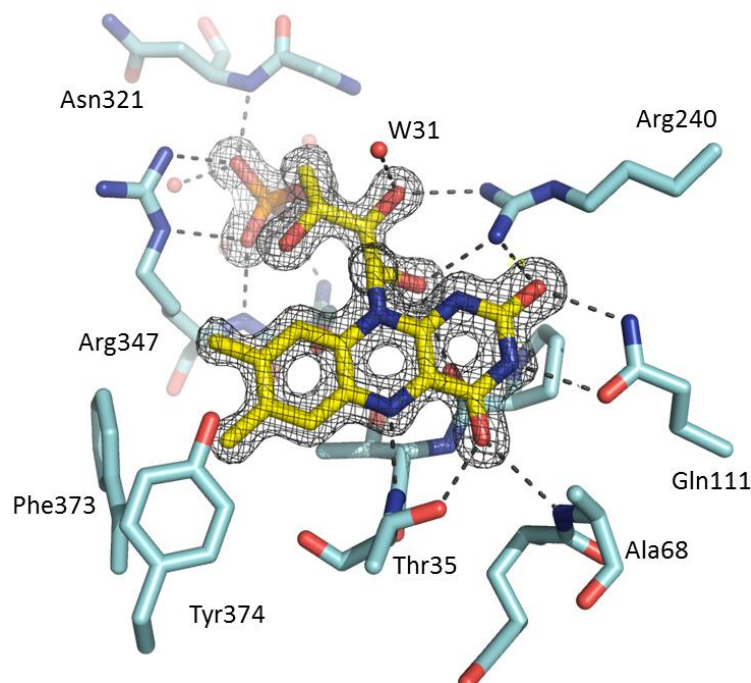


Figure 3-8. The FMN binding environment and direct interactions. Hydrogen-bonds are shown as black dashes.

We used spectral changes that accompany phenol binding to OYE2.6 to characterize its active site character and cofactor properties. OYE2.6 bound both *p*-chlorophenol and *p*-hydroxybenzaldehyde tightly and these complexes were accompanied by long wavelength charge transfer bands with  $\lambda_{\text{max}}$  at 600 and 555 nm, respectively. Massey determined that the positions of these charge transfer bands for *S. pastorianus* OYE1 depended upon both hydrogen bonding interactions with the phenol(ate) oxygen and the FMN reduction potential<sup>8</sup>. In OYE1, the phenolic oxygen interacts with the side chains of His191 and Asn194; by contrast, two histidines occupy these positions in OYE2.6 (His188 and 191). Compared with the corresponding values for *S. pastorianus* OYE1,  $\lambda_{\text{max}}$  values for both *p*-chlorophenol and *p*-

hydroxybenzaldehyde interacting with OYE2.6 are blue-shifted by 59 and 27 nm, respectively. Relatively small effects on charge-transfer  $\lambda_{\text{max}}$  values were observed from changing phenol(ate) hydrogen bonding partners in OYE1, whereas substituting the enzyme with FMN analogs possessing different reduction potentials led to more significant wavelength shifts<sup>57</sup>. Given the similarity in active site structures between OYE2.6 and OYE1, particularly in residues that interact directly with the flavin, the differences in charge-transfer  $\lambda_{\text{max}}$  values are therefore more likely to reflect small differences in flavin local environment rather than a significant redox potential difference. Using the nearly linear relationship between FMN  $E^{\circ}$  and  $\lambda_{\text{max}}$  values for *p*-chlorophenol and *p*-hydroxybenzaldehyde established for *S. pastorianus* OYE1, we estimated that the  $E^{\circ}$  value for OYE2.6 is ca. -248 mV. This is similar to that measured for wild-type OYE1 (-230 mV).

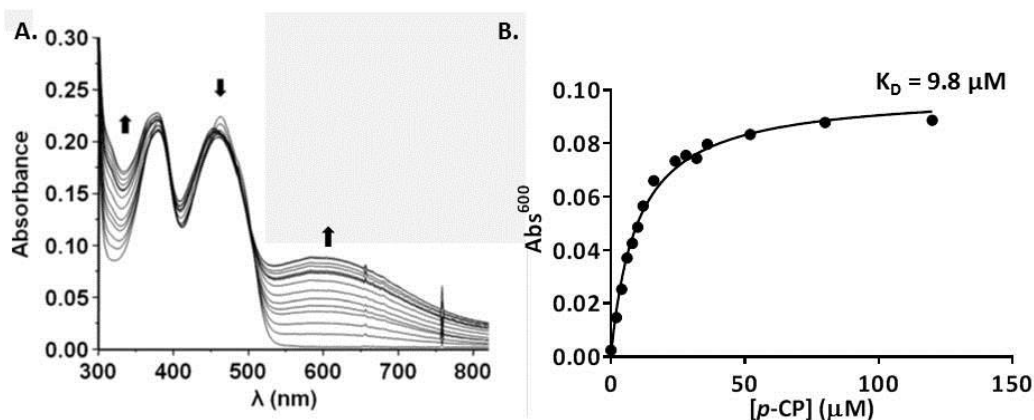


Figure 3-9. Complex formation between OYE2.6 and *p*-CP. A- The spectral changes in OYE2.6 upon ligand binding. The concentration of *p*-CP was increased from 0 to 120  $\mu$ M. B- Binding saturation curve and non-linear fit.

OYE2.6 bound *p*-chlorophenol with and the formation of the charge-transfer complex was measured at a  $\lambda_{\max}$  of 600 nm. The binding saturation could be fit using a specific-binding non-linear regression model (GraphPad). The estimated  $K_D$  is 9.8  $\mu\text{M}$  with an extinction coefficient  $\epsilon^{600}$  of 5170  $\text{M}^{-1}\text{cm}^{-1}$  (Figure 3-9). In contrast, OYE1 forms a charge-transfer complex with *p*-chlorophenol that shows  $\lambda_{\max}$  at 645 nm and  $\epsilon^{645}$  4400  $\text{M}^{-1}\text{cm}^{-1}$ <sup>40</sup>. In the case of *p*-hydroxybenzaldehyde, as expected, a charge-transfer complex formation was also observed. This complex had absorption maximum  $\lambda_{\max}$  at 555 nm and an extinction coefficient  $\epsilon^{555}$  of approximately 5400  $\text{M}^{-1}\text{cm}^{-1}$ . OYE2.6 titration with a solution of *p*-hydroxybenzaldehyde resulted in binding saturation behavior that was best interpreted as very tight binding with a  $K_D$  value being considerably smaller than the enzyme concentration of 24  $\mu\text{M}$  (Figure 3-10).

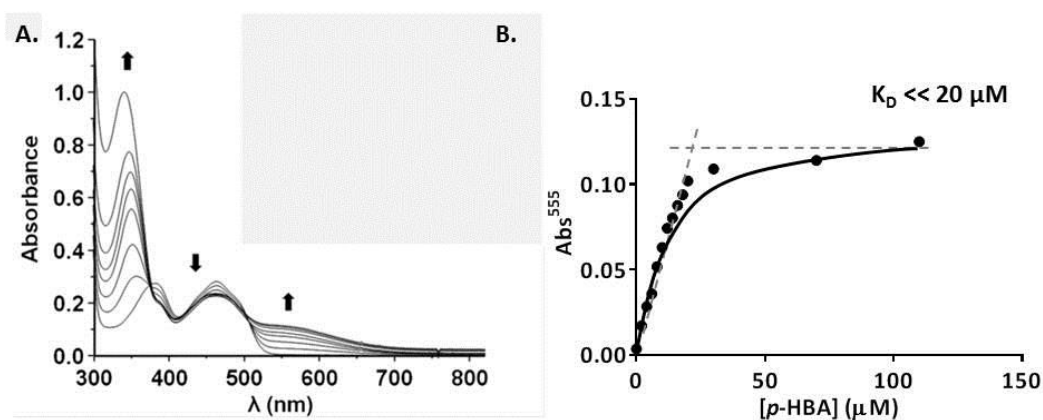


Figure 3-10. Complex formation with *p*-HBA. A- The spectral changes in OYE2.6 upon ligand binding. The concentration of *p*-HBA was increased from 0 to 120  $\mu\text{M}$ . B- Binding saturation curve and non-linear fit. The poor fit is due to an observed infinitely tight binding saturation.

### The Active Site and Ligand Binding

As mentioned before, the active site of OYE2.6 displays some significant differences relative to that of OYE1. First, the pair of hydrogen bond donors in the active site is composed of two histidine residues (188 and 191) instead of a histidine and an

asparagine. As had been predicted based on sequence alignment, an Ile (113) replaces a tryptophan and is very close to the bound ligands. Loop L6, which usually exhibits large plasticity across the OYE family, is also significantly different. The portion of the loop that defines the active site has an entirely different amino acid sequence. Interestingly, in OYE2.6 a glycine residue (292) replaces a proline (Pro295 in OYE1). Given their largely different physical characters, this substitution is very likely to be a factor in the substrate specificity differences between these two enzymes (Figure 3-11).

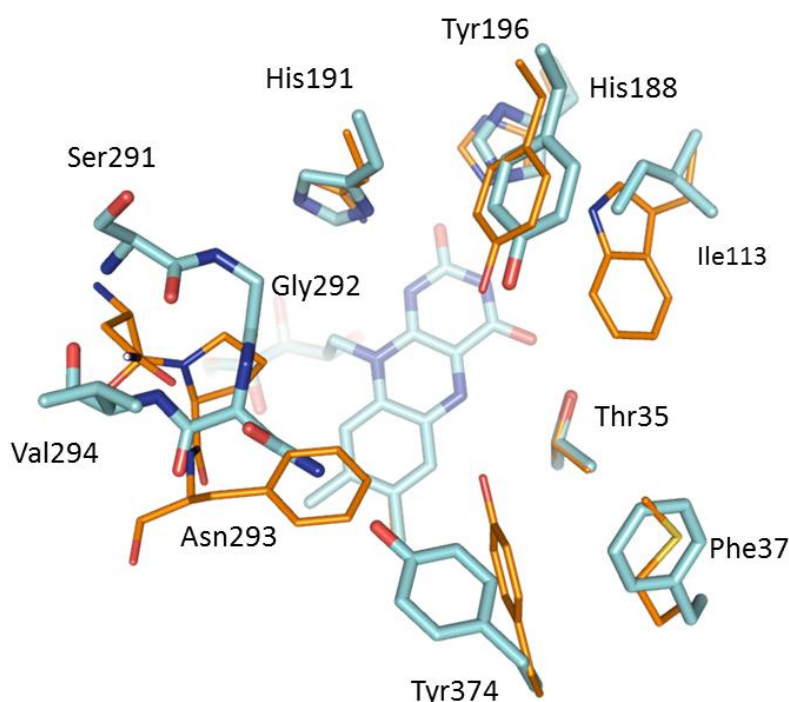


Figure 3-11. The active site comparison of OYE2.6 and OYE1. OYE2.6 residues are shown as thick lines and cyan carbons, while OYE1 residues are in thin lines with orange carbons. The labels indicate the residues in OYE2.6.

The initial OYE2.6 crystals displayed strong electron density peaks directly above the *si*-face of the FMN. This density region appeared symmetrical and had its strongest peak in optimal position to interact with His188 and 191. Since no ligands were

deliberately added throughout purification or crystallization steps, we turned our attention to buffer components. Malonate, present in the crystallization buffer at 2.4 M, was a near perfect fit for this density (Figure 3-12A). In this complex, one carboxylate oxygen is positioned to form hydrogen bonds with the side chains of histidines 188 and 191, which likely mimics their interactions with the carbonyl oxygens of conjugated alkene substrates as previously reported by us (previous chapter) and others.

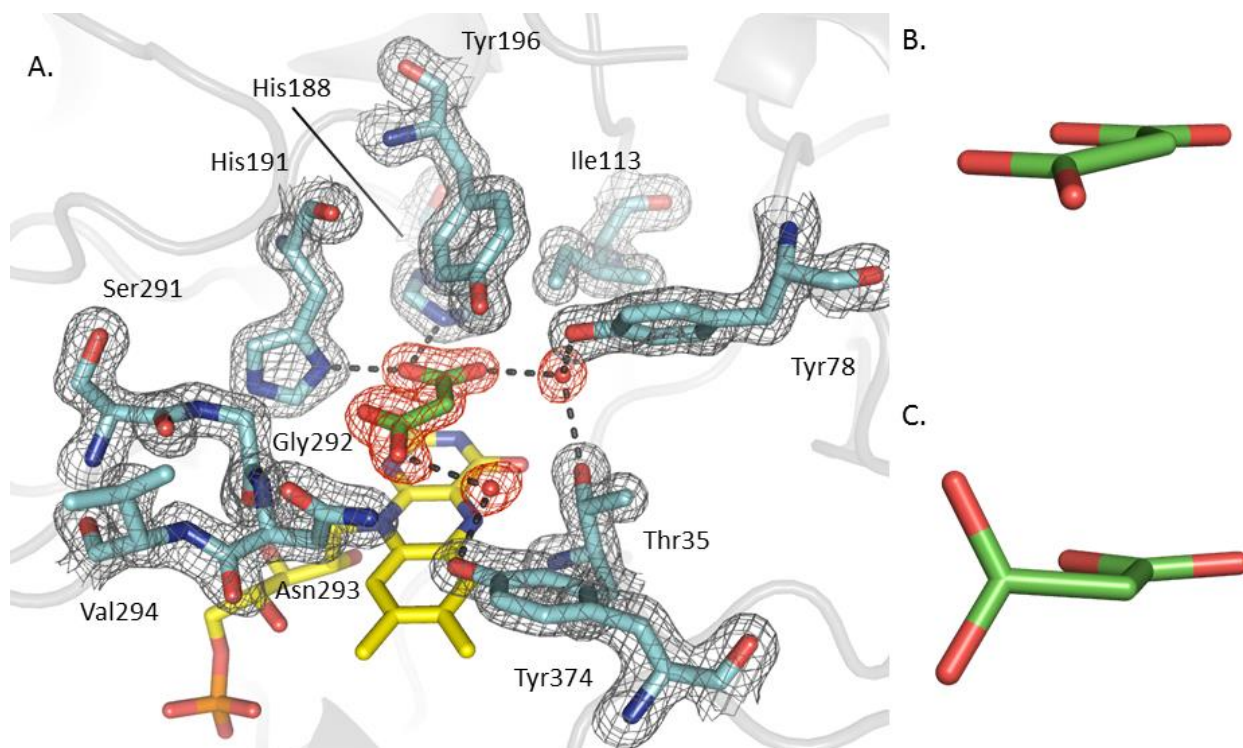


Figure 3-12. OYE2.6-malonate complex. A- Crystal structure of OYE2.6 in complex with malonate. B- The conformation of malonate bound in the active site. C- Conformation of malonates seen on the surface of protein. The omit mFo-DFc map of malonate contoured at  $3\sigma$  in red mesh. The 2mFo-DFc map of the active site residues is contoured at  $1.3\sigma$ . Protein residues are colored in cyan, FMN in yellow and the ligand in green.

The other carboxylate oxygen forms hydrogen bond with an ordered water molecule (WAT301) which in turn is hydrogen bonded to the side-chains of Tyr78 and Th35.

Curiously, while several well-ordered malonate molecules were observed in the surface

of the protein, only this active site malonate was found in the higher energy planar conformation (Figure 3-12B). The fact that the active site malonate appears in a higher energy conformation may be linked to interactions with the  $\pi$ -system of the flat flavin ring. All solvent-exposed malonate molecules were observed in the expected bent form (Figure 3-12C).

Crystals grown from a second preparation of OYE2.6 also showed additional electron density in the active site region; however, the shape differed significantly from that observed previously. This density suggested the species was a six-membered ring that appeared aromatic. Additionally, some extra density suggested that the molecule carried a three atom group with roughly trigonally planar geometry. These observations would be consistent with the shape of molecules such as benzoic acid, nitro-benzene, nicotinic acid and nicotinamide among others.

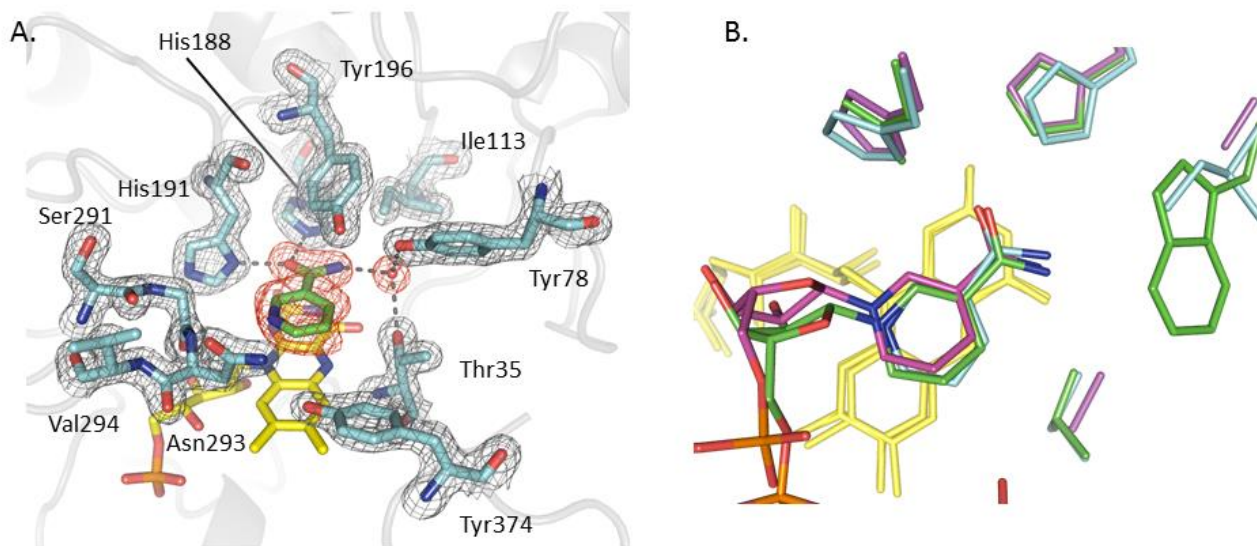


Figure 3-13. OYE2.6-nicotinamide complex. A- Crystal structure of OYE2.6 in complex with nicotinamide. The omit mFo-DFc map contoured at  $3\sigma$  as a red mesh. The  $2mFo$ -DFc map of the active site residues is contoured at  $1.3\sigma$ . Protein residues are colored in cyan, FMN in yellow and the ligand in green. B- Alignment of structures of OYE homologs containing nicotinamide derivatives.

Given that the identity of the ligand would be constrained by what molecules are likely to be present throughout the protein overexpression, isolation and crystallization processes, we deduced that it was free nicotinamide. This ligand could be successfully fit into the electron density and was refined to an occupancy of 95% (Figure 3-13 and Table 3-1). This fortuitous complex likely mirrors that between OYE2.6 and its natural substrate, NADPH. The amide carbonyl oxygen is located within hydrogen bond distances of the imidazole side chains of both His188 and His191 and the distance and angle between the nicotinamide C4 and the FMN are consistent with the geometry of hydride transfer (3.4 Å and 94°, respectively)<sup>37</sup>. This ligand conformation is also in agreement with that of a previously reported OYE1 complex with an NADP<sup>+</sup> analog<sup>58</sup>. Further supporting the notion that this arrangement mimics the productive NADPH/OYE2.6 Michaelis complex, the nicotinamide binding orientation within OYE2.6 is analogous to those observed for tetrahydronicotinamide within the active sites of *T. pseudethanolicus* TOYE<sup>32</sup> and morphinone reductase<sup>59</sup> (Figure 3-13B). Unfortunately, neither UV-Vis nor fluorescence spectroscopy yielded usable spectral changes for nicotinamide binding to OYE2.6, so its binding constant could not be measured by these methods.

To provide a model for how potential substrates might bind to the active site and for further comparison to its homolog OYE1, we attempted to obtain a crystal structure of the complex between OYE2.6 and *p*-chlorophenol by soaking crystalline enzyme in cryoprotectant buffer containing 2 mM. The OYE2.6 crystals were very sensitive to osmotic pressure and osmolality changes, which made soaking experiments very difficult. Long soaking times led to increased diffraction mosaicity and crystal cracking.

The best crystal used for data collection resulted from a short (ca. 2 seconds) soaking time. This crystal diffracted to a resolution of 2 Å and the electron density maps revealed the position of the *p*-chlorophenol inhibitor (Figure 3-14 and Table 3-1). The phenolic oxygen was positioned between the side chains of His188 and 191 and a *meta* ring carbon was 3.5 Å above the FMN *N5* atom.

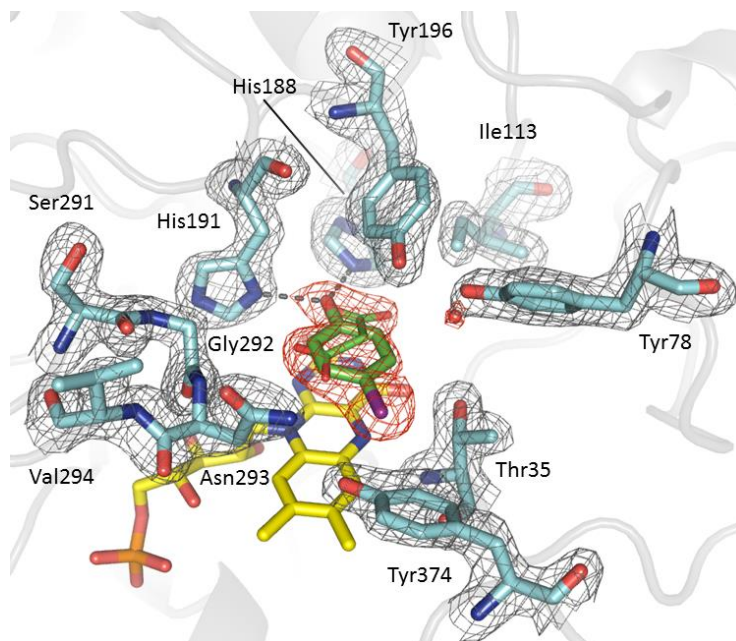


Figure 3-14. Crystal structure of OYE2.6 in complex with *p*-chlorophenol. The omit mFo-DFc map contoured at  $3\sigma$  as a red mesh. The 2mFo-DFc map of the active site residues is contoured at  $1.3\sigma$ . Protein residues are colored in cyan, FMN in yellow and the ligand in green.

The orientation of this carbon relative to the flavin ring is of particular interest since  $\beta$ -carbons of OYE2.6 substrates would be in an analogous location. The angle between this carbon and *N5* and *N10* of the FMN was  $105^\circ$ . These values are consistent with those expected for efficient hydride transfer to a cyclohexenone  $\beta$ -carbon. As the model neared completion, some areas of positive electron density remained and could be best

explained by a partially (near 35%) occupied malonate molecule. This is probably a result of the high concentration of malonate in the crystallization buffer and the short soaking times with *p*-chlorophenol.

Table 3-1. X-ray Crystallographic Data Collection and Refinement Statistics

Accession code	3TJL	3UPW	4DF2
Active site ligand	malonate	nicotinamide / malonate	<i>p</i> -chlorophenol
X-ray source	NSLS X25	NSLS X25	Rigaku CuK $\alpha$
Space group	P 6 <sub>3</sub> 2 2	P 6 <sub>3</sub> 2 2	P 6 <sub>3</sub> 2 2
Unit cell dimensions			
a=b, c (Å)	127.16, 122.45	127.30, 123.06	127.73, 123.64
$\alpha$ , $\beta$ , $\gamma$ (°)	90, 90, 120	90,90, 120	90, 90, 120
Resolution (Å)	44.10 - 1.50	44.24 - 1.78	24.86 - 2.02
Unique reflections	92,358 (2,365) <sup>1</sup>	56,484 (1,608)	38,149 (1,269)
Completeness (%)	99.07 (96.0)	99.76 (96.0)	96.70 (99.0)
Redundancy	7.6 (4.7)	10.5 (4.2)	7.2 (6.9)
R <sub>merge</sub> <sup>2</sup>	0.056 (0.60)	0.047 (0.55)	0.093 (0.70)
I/ $\sigma$ (I)	33.4 (2.0)	37.1 (2.1)	14.2 (2.1)
R <sub>work</sub> <sup>3</sup> , R <sub>free</sub> <sup>4</sup>	0.143, 0.168	0.157, 0.185	0.160, 0.198
Ramachandran statistics <sup>5</sup>			
Favored (%)	97.60	97.80	97.52
Allowed (%)	2.40	2.20	2.48
Outliers (%)	0	0	0
Number of protein, solvent and ligand atoms	3,238, 517, 52	3,211, 445, 65	3,218, 394, 53
Average B factors (Å <sup>2</sup> )			
Protein	22.21	23.20	31.40
Solvent	35.20	34.40	38.87
FMN	16.22	19.17	26.21
Ligands	33.30, 28.40, 23.10	34.90, 31.80, 38.0 (malonate); 21.70 (nicotinamide)	39.30, 26.20 (malonate); 27.01 ( <i>p</i> -chlorophenol)

<sup>a1</sup>Values in parentheses denote data for the highest resolution bin.

<sup>b1</sup>R<sub>merge</sub> =  $\frac{\sum hkl \sum i |I_i(hkl) - [I(hkl)]|}{\sum hkl \sum i I_i(hkl)}$ , where  $I_i(hkl)$  is the intensity of the *i*th observation of unique reflection *hkl*.

$$^{[c]}R_{\text{work}} = \sum | |F_o(hkl)| - |F_c(hkl)| | / \sum |F_o(hkl)|.$$

<sup>[d]</sup> $R_{\text{free}}$  is calculated in the same manner as  $R_{\text{work}}$  using 10% of the reflection data not included during the refinement.

<sup>[e]</sup>Statistics generated using MOLPROBITY <sup>39</sup>

### Catalytic Characterization through Mutagenesis

After structural characterization of OYE2.6 was completed, we turned our attention to probing its structure/function relationships with respect to alkene reductions. We chose three representative Baylis–Hillman adducts 1-3 for catalytic studies of OYE2.6 (Figure 3-15) since they possess additional functionality that makes them suitable for further useful chemical transformations following asymmetric alkene reductions <sup>48-50</sup>.

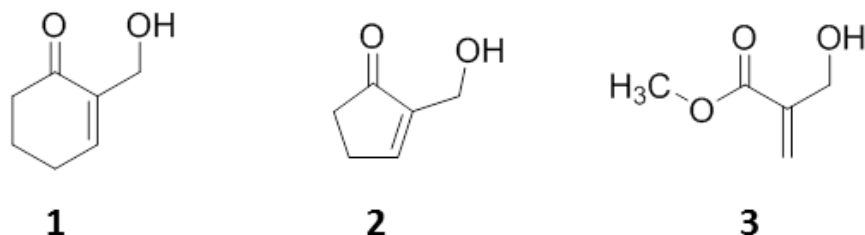


Figure 3-15. Structures of the three Baylis-Hillman adducts tested.

While a number of catalytic hydrogenation strategies for the asymmetric reduction of **3** has been reported <sup>60</sup> and references therein, we are not aware of similar catalysts being applied to cyclic enones **1** and **2**. In addition, we have previously used the same series for characterizing *S. pastorianus* OYE1 mutants, thereby facilitating direct comparison of their substrate conversions and stereoselectivity <sup>47</sup>. Four site-saturated mutagenesis libraries of OYE2.6 were created using a variation of the method published by Zheng and Reymond employing a reduced genetic alphabet (NNK) that contained 32 codons but still encompassed all twenty amino acids <sup>41</sup>. After extensive optimization by Drs. Adam Walton and Bradford Sullivan in our laboratory, libraries

routinely contained >16 amino acid replacements (usually 18 or 19). After verifying their diversity at the pooled plasmid DNA stage, this mixture was used to transform the *E. coli* expression host. In the case of the Ile113 library, simple site-directed mutagenesis methods were used to obtain the three missing codons so that a complete set of amino acid replacements could be screened. Enones 1–3 were reduced under whole-cell conditions in the presence of glucose for NADPH regeneration by host metabolic pathways.

In essence, His188 in OYE2.6 showed little tolerance toward amino acid substitutions and only the wild-type protein was highly active (Figure 3-16 A). The Ser, Gln and Asn variants reduced substrates **1** and **2** poorly and showed no detectable activity towards **3**. All variants that retained some catalytic activity showed the same (S)-stereoselectivity as seen in the wild-type enzyme. In *S. pastorianus* OYE1, the corresponding position (191) is also occupied by His and its function was probed by Brown and Massey. In their study, this residue was changed to Asn and, while the variant retained catalytic activity, the  $K_M$  value for 2-cyclohexenone increased significantly<sup>40</sup>. The differential response toward analogous substitutions highlights the subtle differences in active site architectures, even among highly similar alkene reductases as OYE family enzymes. Despite the lack of success in identifying functional histidine replacements in this particular case, others have found that site-saturation libraries can sometimes reveal unexpected results<sup>61</sup>. Scrutton mutated the corresponding His residue in *E. cloacae* PETNR (position 181) and found that this library had very low average catalytic activity when tested against carbonyl-conjugated

alkenes<sup>62</sup>. On the other hand, several useful replacements for this same PETNR variant were identified for certain nitroalkene substrates<sup>63</sup>.

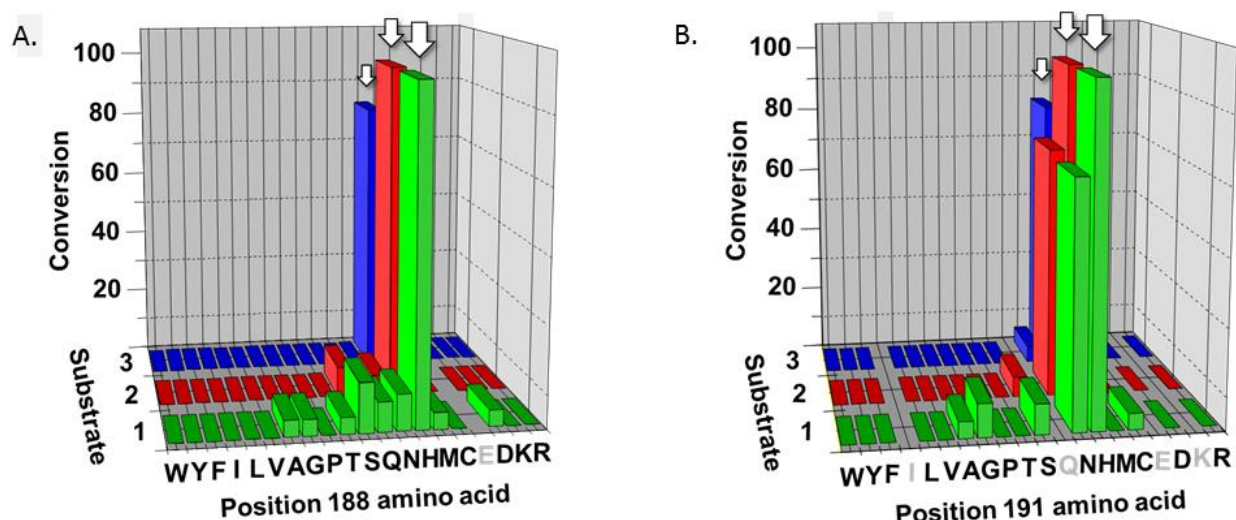


Figure 3-16. Mutations of positions 188 and 191. A- Effects of mutations of amino acid His188. B- Effects of mutations of position His191. The enone substrates **1**, **2** and **3** are colored in green, red and blue respectively. The wild-type enzyme is indicated by an arrow. Grey letters indicate substitutions that were missing in the library used for screening.

Position 191 in OYE2.6 was slightly more tolerant toward mutation, with both the native His and the Asn mutant proteins showing significant catalytic activity while no changes in enantioselectivity were observed for the three enones investigated here (Figure 3-16 B). As observed in the previous case, the catalytic activities of the mutant proteins were generally consistent across all three enone substrates. This underscores the point that the catalytic assays reveal general characteristics of the enzymes and suggests that similar behavior will apply to other potential substrates as well. The analogous position in *S. pastorianus* OYE1 (194) contains Asn and interestingly, attempts to prepare the single Asn194His mutant of *S. pastorianus* OYE1 were unsuccessful<sup>40</sup>. The analogous His in *E. cloacae* PETNR (position 184) also showed

limited tolerance for amino acid replacement, although the Asn mutant retained 20% of the wild-type activity for 2-cyclohexenone.

In both OYE2.6 and *S. pastorianus* OYE1, the side-chain of a key Thr residue forms a hydrogen bond with O4 of the bound FMN. For OYE1, loss of this interaction slowed the reductive half-reaction by an order of magnitude but increased the oxidative half-reaction in the Thr37Ala mutant. Other OYE family members contain Thr or Cys at the analogous position. Based on these precedents, we created and examined a systematic replacement library for Thr35 in OYE2.6 (Figure 3-17).

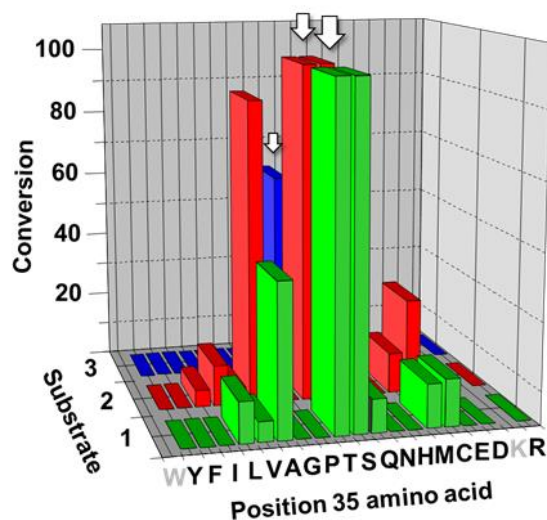


Figure 3-17. Effects of mutations of amino acid Thr35. The enone substrates 1, 2 and 3 are colored in green, red and blue respectively. The wild-type enzyme is indicated by an arrow. Grey letters indicate substitutions that were missing in the library used for screening.

For OYE2.6, the Ser replacement had essentially the same properties as the wild-type enzyme, consistent with the importance of hydrogen bonding with the FMN cofactor. The Ala variant also possessed activity, albeit diminished. The most surprising result was that several other residues (Cys, Leu, Met, Gln and Val) could also functionally replace Thr 35, though with lower efficiencies. No change in

stereoselectivity was found for any of the Thr 35 substitutions. The observed tolerance toward changes at this position bodes well for future work in active site remodeling.

Our previous studies of *S. pastorianus* OYE1 highlighted the key influence of Trp116 in controlling reactivity<sup>35, 47</sup> and similar observations have been made for both *E. cloacae* PETNR<sup>62</sup> and *B. subtilis* YqjM<sup>64</sup>. As noted above, the corresponding position in native OYE2.6 (113) is occupied by Ile. A number of amino acids replacements were tolerated by OYE2.6 at this position (Figure 3-18 A). Small-to-medium hydrophobic residues (Ala, Leu, Met, Phe and Val) as well as polar, uncharged amino acids (Asn, Cys, Gln, His, Ser and Thr) could replace the native Ile with good to excellent retention of catalytic activity.

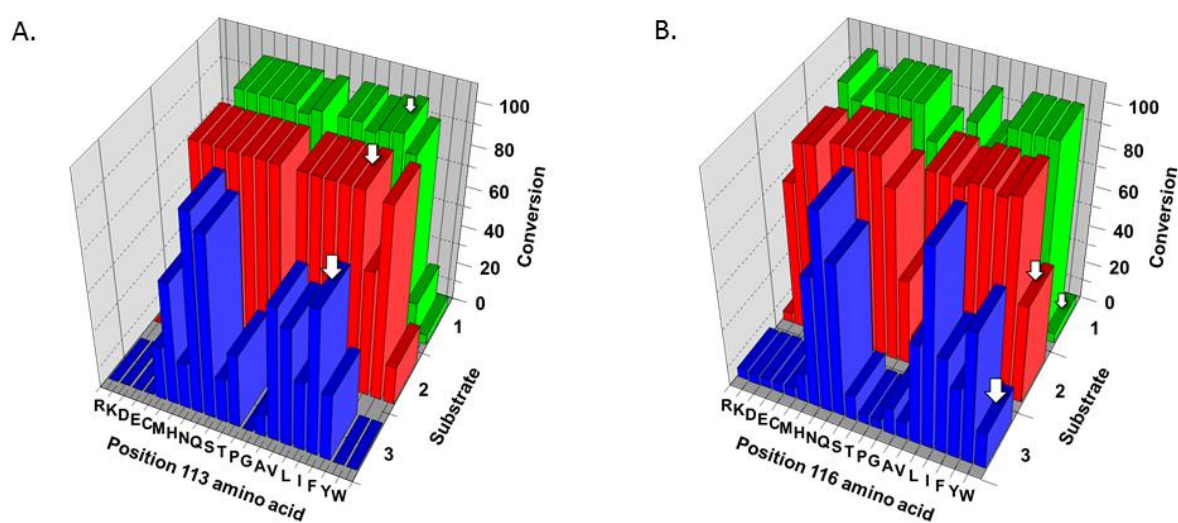


Figure 3-18. Mutations of positions 113 and 116. A- Effects of mutations of amino acid Ile113. B- Effects of mutations of position Trp116 in OYE1. The enone substrates 1, 2 and 3 are colored in green, red and blue respectively. The wild-type enzyme is indicated by an arrow.

On the other hand, charged amino acids, Pro and larger hydrophobic residues (Tyr and Trp) yielded inactive proteins toward the Baylis–Hillman adducts examined here. One difference between the position 113 mutants and the libraries described above is that

conversions differ significantly between the two cyclic enones and the acyclic Roche ester precursor. With regard to substrate conversion, the response of OYE2.6 toward amino acid substitutions at position 113 closely mirrors that of a Trp116 replacement library in *S. pastorianus* OYE1 (Figure 3-18 B) <sup>47</sup>.

Like OYE2.6, OYE1 prefers cyclic enones **1** and **2** over acyclic alkene **3** and similar ranges of residues at position 116 are acceptable substitutes for the native Trp. In some cases, this similarity extends to changes in stereoselectivity. For example, wild-type OYE1 (with Trp at position 116) reduces **2** with predominantly (*R*)-selectivity (60% e.e.); by contrast, the Trp116Ile mutant afforded 91% ee (*S*)-product <sup>47</sup>. For OYE2.6, wild-type (with Ile at position 113) reduced **2** with high (*S*)-selectivity (>90% ee) while the Ile113Trp mutant provided 11% ee favoring the (*R*)-enantiomer. However, one important difference between the behavior of OYE2.6 and *S. pastorianus* OYE1 mutants involves the acyclic Roche ester precursor **3**. Wild-type OYE2.6 and all of the Ile113 mutants that accept this substrate catalyze reductions with essentially complete (*S*)-selectivity, although some with relatively poor conversion. By contrast, mutating Trp116 in *S. pastorianus* OYE1 provides a range of stereoselectivities for this substrate, ranging from >98% ee (*R*)-(wild-type) to >98% ee (*S*)-(Trp116 Gln. These differences highlight the distributive nature of the substrate binding pocket within alkene reductases. While single amino substitutions can be sufficient to alter stereoselectivity in some favorable cases, multiple substitutions are more often required. Comparing the structures of OYE2.6 and *S. pastorianus* OYE1 in light of these mutagenesis data provides a much better roadmap for future protein engineering studies.

## Conclusions and Future Direction

A major motivation for determining the crystal structure of OYE2.6 was to understand its stereoselectivity, particularly why it is generally opposite to that of wild-type *S. pastorianus* OYE1 for Baylis–Hillman adducts **1–3**, but identical to that of the OYE1 Trp116Ile mutant. These observations in addition to the fact that the crystal structure revealed this enzyme possesses an Ile in place of a Trp for OYE1 would suggest that OYE2.6 is essentially a mimic of OYE1 Trp116Ile mutant. However, in catalyzing the reductions of certain substrates, such as (*S*)-carvone, this simplification proves incorrect and OYE2.6 does not share the stereoselectivity of OYE1 Trp116Ile. We were intrigued by this behavior and hoped that elucidation of its three-dimensional structure would enable us to rationalize these results.

We decided to directly compare the structures of OYE2.6 with that of OYE1 Trp113Ile with 2-hydroxymethyl-2-cyclopentenone **2** bound in the active site. Interestingly, in two of the three OYE2.6 structures solved, an ordered water molecule, which is absent in OYE1 structures, hydrogen bonds to the side-chains of Thr35 and Tyr78 (Figure 3-12 A and 3-13 A). When the flavin cofactors of the OYE2.6/malonate complex and the *S. pastorianus* W116I OYE1/enone **2** complex were overlaid, the hydroxyl group of **2** was in the same location as these ordered water molecules in OYE2.6 (Figure 3-19). Our previous results have argued that this protein-substrate interaction in *S. pastorianus* OYE1 plays a key role in determining which face of the alkene  $\pi$ -system will accept hydride from reduced FMN. It is therefore reasonable to suggest that an analogous hydrogen bond is also formed between OYE2.6 and the hydroxymethyl groups of **1–3** and this provides a structural rationale for the observed stereoselectivity. We carried out structural alignments of OYE2.6 with wild-type and the

Trp116Ile mutant *S. pastorianus* OYE1, *P. putida* morphinone reductase (MR), *E. cloacae* pentaerythritol tetranitrate reductase (PETNR), *B. subtilis* YqjM, *T. pseudethanolicus* E39 TOYE and tomato oxophytodienoate reductase OPR1 to determine whether these proteins also contain an analogous ordered water molecule.

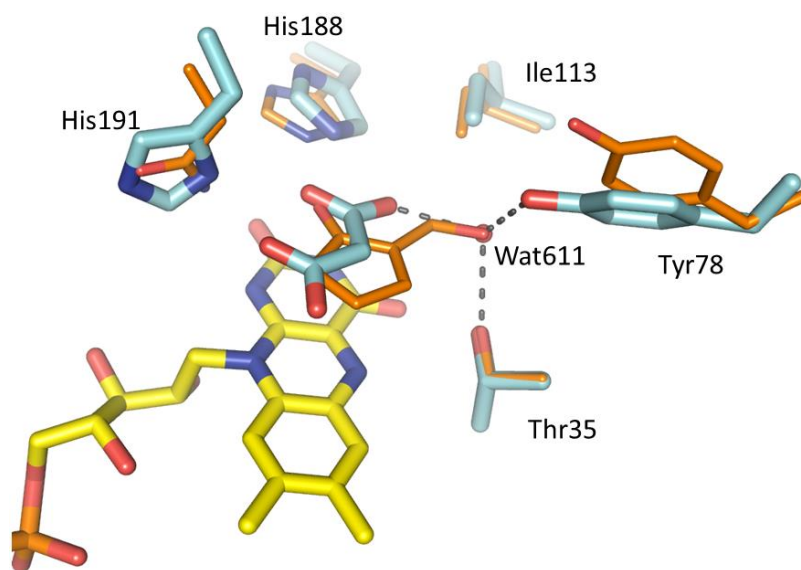


Figure 3-19. Comparison of OYE 2.6 and *S. pastorianus* OYE1 complexes. The structures of native OYE 2.6 with bound malonate (cyan) and the structure of the *S. pastorianus* W116I OYE1 mutant with enone **2** bound (orange) were overlaid using all FMN atoms (yellow carbons). Key side-chains and an ordered water molecule are shown. Numbers correspond to OYE2.6 sequence.

Interestingly, this water was only observed near the FMN in OYE2.6. In the case of OYE1, MR, PETNR and OPR1, a tryptophan residue fills this volume and eliminates the possibility of an ordered water molecule at this location. Both YqjM and TOYE possess Ala in this location that provides sufficient space; however, the two residues that form hydrogen bonds with the ordered water in OYE2.6 (Thr35 and Tyr78) either cannot form hydrogen bonds (Ile) or have a suitable residue (Cys), but in unfavorable orientations. Taken together, this may explain the absence of this critical ordered water

molecule in the other proteins. The positions of the active site Thr side-chains (positions 35 and 37 in OYE2.6 and *S. pastorianus* OYE1, respectively) are essentially indistinguishable. The same is true for the Ile side-chain (Ile113 in OYE2.6 and the W116I side-chain in *S. pastorianus* OYE1), with one important difference. In the OYE1 mutant, the Ile side-chain was observed in two conformations, only one of which allows productive substrate binding. Likewise, two binding orientations of enone 2 were observed in the complex with W116I *S. pastorianus* OYE1, one potentially relevant to catalysis and the other clearly incorrect. By contrast, the corresponding Ile side-chain in OYE2.6 (Ile113) was only found in a single conformation, which matched the productive arrangement in the W116I *S. pastorianus* OYE1 mutant (Figure 2-17). This singular conformation of Ile113 may be one reason that OYE2.6 is a more efficient catalyst when compared to the W116I mutant of *S. pastorianus* OYE1. Despite these similarities, there are also key differences between OYE2.6 and *S. pastorianus* OYE1 – even the OYE1 W116I mutant. For example, when reducing (*S*)-carvone, both wild-type *S. pastorianus* OYE1 and OYE2.6 share the same stereoselectivity, which is opposite that of the OYE1 W116I mutant. This not only points out the special nature of Baylis–Hillman substrate binding to alkene reductase active sites, but also underscores the fact OYE2.6 is not simply the same as the W116I mutant of *S. pastorianus* OYE1. Other active site residues of OYE2.6 must also influence the orientation of substrate binding.

In the previous chapter, the altered stereoselectivity observed by some Trp116 replacements of OYE1 was explained by the creation of a hydrophobic pocket that was capable of accommodating the isopropenyl chain of carvone. This would allow for a substrate flipping and therefore a different stereochemical outcome. In OYE2.6, an

analogous pocket seems to exist, however it is precluded by Tyr78 whose side chain occupies a slightly different position compared to its OYE1 counterpart (Tyr82).

Our group has used the structural knowledge gained throughout the course of this work and new amino acid positions are being targeted for mutagenesis. Future efforts will focus on expanding the substrate range for OYE2.6 as well as the identification of stereocomplementary variants. Another are currently being explored in our group is the increase in thermostability of the enzyme through combining directed evolution and rational design.

## **Experimental Procedures**

### **Protein Purification**

*E. coli* BL21 (DE3) harboring plasmid pBS3 (a derivative of pET-26b containing the OYE2.6 coding region flanked by NdeI and XhoI sites) was grown at 37 °C in LB medium supplemented with 50 µg/mL kanamycin. IPTG was added to a final concentration of 400 mM when the culture had reached an OD<sup>600</sup> value of 0.6 and shaking was continued at 30 °C for an additional 8–10 h. Cells were harvested by centrifugation at 5,000 x g, resuspended in 100 mM Tris-Cl, 10 mM PMSF, pH 8.0 at a concentration of 1 g/mL and lysed by a French pressure cell at 12,000 psi. All purification steps were carried out at 4 °C. Debris was removed by centrifugation (18,000 x g for 45–60 min). Solid ammonium sulfate was added to the supernatant to reach 78% saturation; insoluble material was then removed by centrifugation (18,000 x g for 30 min). The pellet was resuspended in a minimal volume of 100 mM Tris-Cl, 50 mM ammonium sulfate, pH 8.0, protamine sulfate was then added to a final concentration of 1 mg/mL and the resulting insoluble material was removed by centrifugation (15,000 g for 20 min). The dark yellow supernatant was dialyzed against

100 mM Tris-Cl, 50 mM ammonium sulfate, pH 8.0 for 8 hrs. This was replaced by additional dialysis buffer supplemented with 10 mM sodium dithionite for 6 h. In the final dialysis step (8 h), sodium dithionite was absent in the buffer, yielding a bright yellow dialysate. The crude protein sample was loaded onto an N-(4-hydroxybenzoyl) aminohexyl agarose affinity column[10] previously equilibrated with 100 mM Tris-Cl, 50 mM ammonium sulfate, pH 8.0. The column matrix became dark brown, indicating successful OYE2.6 binding. After loading, the column was washed with the starting buffer at a flow rate of 0.5 mL/min until the Abs<sup>280</sup> value of the flow-through solution was stabilized at ca. 0.2. OYE2.6 was eluted by washing the column with deoxygenated starting buffer supplemented with 4 mM sodium dithionite. The protein fractions with the most intense yellow color (after subsequent air oxidation) were pooled and concentrated by ultrafiltration to approximately 10 mg/mL. Final purification was achieved by gel filtration chromatography on a Superdex 200 column (Pharmacia) equilibrated with 30 mM Tris-Cl, 30 mM NaCl pH 7.5. The eluted protein was concentrated by ultrafiltration to ca. 40 mg/mL using a  $\epsilon^{280}$  value of 55,810 M<sup>-1</sup> cm<sup>-1</sup> as calculated by ExpASy [40] prior to crystallization studies.

### **Native Gel Filtration**

For gel filtration experiments, a Superdex 200 HR 10/30 (Pharmacia) column was equilibrated with five column volumes of 100 mM KP<sub>i</sub> pH 7.0 buffer at 4 °C and a flow rate of 0.5 mL/min. For calibration, 250  $\mu$ L of a protein mixture containing thyroglobulin, OYE1, BSA, ovalbumin, myoglobin at a concentration of 2-3 mg/mL each was injected. The elution volumes were recorded by monitoring the absorbance at 280 nm. The void volume was determined by injecting a 1 mg/mL sample of blue dextran. Appendix D shows the elution of the protein standards. The elution volumes were

plotted versus the logarithm of each protein molecular weight and fitted by a linear regression ( $R^2 = 0.9931$ ) (Appendix D, Figure D-2)

The elution volume for OYE2.6 (250  $\mu$ L at 10 mg/mL) was 13.6 mL at 4°C and a flow rate of 0.5 mL/min (Figure 3-20). This elution volume resulted in a calculated molecular of 88 kDa. The theoretical molecular based on amino acid sequence is 45 kDa which suggests OYE2.6 is a dimer.

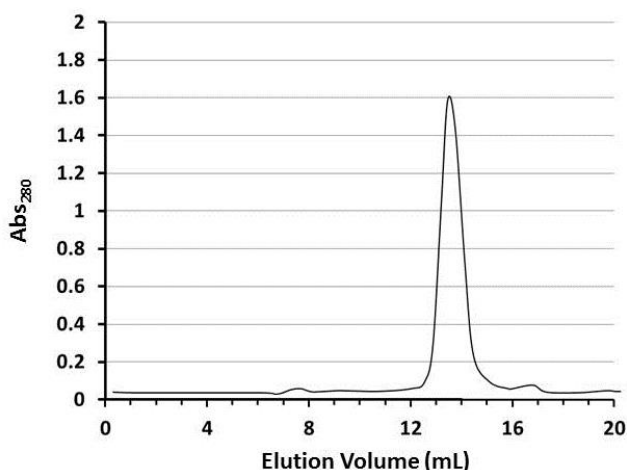


Figure 3-20. Elution profile of OYE2.6. The elution volume is consistent with that of a homodimer.

### Crystallogenesis

A protein solution of *ca.* 40 mg/mL OYE2.6 in 30 mM Tris HCl, 30 mM NaCl pH 7.5 was used in screening for crystallization conditions. In 96 well crystallization plates, 1  $\mu$ L of protein solution was mixed with an equal volume of 96 unique crystallization buffers (Classics II Suite, Qiagen). This procedure was repeated using a different set of crystallization conditions (Index, Hampton). The most promising results appeared in 2.4 M sodium malonate pH 7.0. A crystal was screened using a home-source CuK $\alpha$  rotating anode diffractometer (Rigaku) and diffraction to a maximum resolution of 2 Å was observed. Unfortunately these data could not be utilized for structure solution as they were highly mosaic and appeared to contain multiple, poorly defined lattices that could

not be indexed. As this condition proved recalcitrant to optimization, a screening kit containing 96 unique additives was used in combination with the original crystallization buffer. Finally, the best crystals were grown using the sitting drop vapor diffusion method on polystyrene microbridges from 2.4M sodium malonate, pH 7.0 buffer supplemented with 1–3% 2-propanol. These crystallization conditions were not ideal for cryo-crystallography and data collected at 100 K varied significantly in quality and an ideal cryo-protection protocol could not be readily indentified. A more systematic investigation showed that the best diffraction data were obtained when crystals were briefly washed in 3.0 M sodium malonate pH 7.0, 10% glycerol (Figure 3-21B)

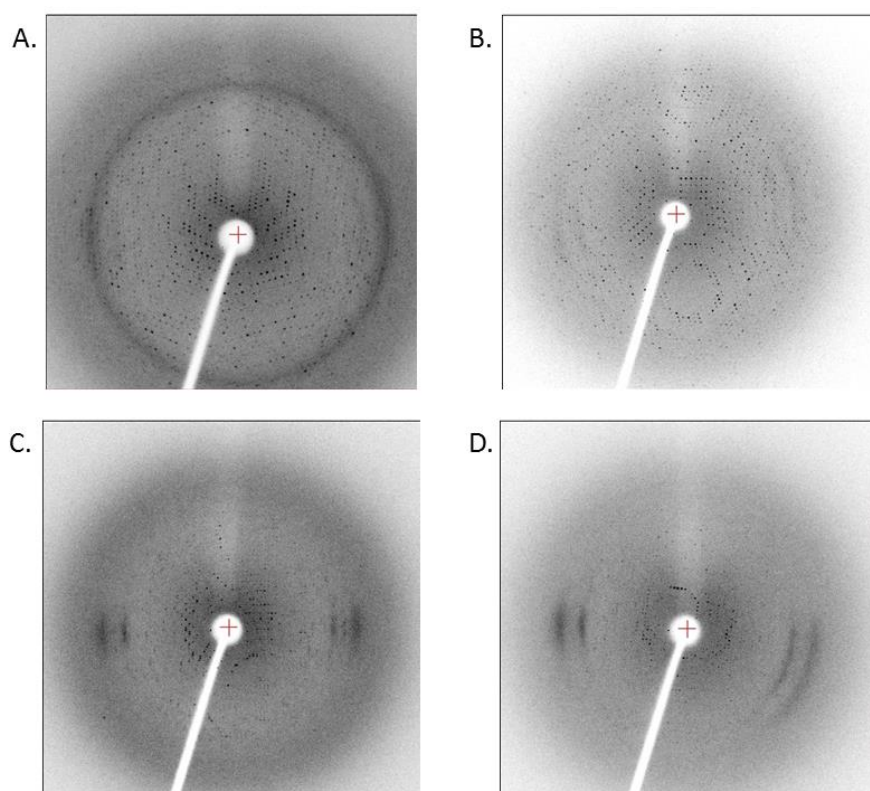


Figure 3-21. X-ray diffraction images of crystals that had been briefly washed in 3.0 M sodium malonate pH 7.0 and A- 5% glycerol; B- 10% glycerol; C- 15% glycerol and D- 20% glycerol v/v.

After growth, crystals were soaked in harvesting buffer (3.0 M sodium malonate, 10% v/v glycerol, pH 7.0) and flash cooled in liquid nitrogen for data collection. The crystals belonged to space group  $P 6_3 2 2$ . To prepare the *p*-chlorophenol complex, crystals were briefly soaked in harvesting buffer supplemented with 2 mM *p*-chlorophenol. Increasing soaking times increased mosaicity and decreased the resolution of the crystals. The best results (diffraction data to 2.02 Å) resulted from soaking for short periods of time (2- 5 seconds).

### Structure Solution

Reflection data were processed using the HKL3000 program suite<sup>42</sup>. Phases were obtained by molecular replacement using the AutoMR utility of PHENIX.<sup>44</sup> using a modification of *S. pastorianus* OYE1 (PDB code 1OYA) as the search model. All ligands, water molecules and non-identical side-chains were removed prior to molecular replacement. One solution was found in space group  $P 6_3 2 2$ . Moreover, the initially calculated 2mFo-DF and mFo-DFc maps showed electron density patterns that could be easily identified as FMN, further validating the molecular replacement solution. The initial model consisted of 385 amino acids (most devoid of side chains) and an  $R_{\text{free}}$  value of 0.33. After the initial simulated annealing refinement followed by refinement with individual xyz parameters and B-factors, the  $R_{\text{free}}$  dropped to 0.24. Inspection of the newly-phased electron density maps allowed placement of the missing residues and showed that some regions of the protein backbone required rebuilding. Refining the more complete model improved the phases and electron density maps clearly showed both ordered solvent molecules and amino acid side chains. Iterative cycles of model-building and refinement were continued to yield the final protein structures. Model building was carried out with COOT<sup>45</sup> and refinement was performed by PHENIX.

After the protein and cofactor modeling was completed, additional electron density lying above the FMN was apparent in both the  $2mF_o-F_c$  and  $F_o-F_c$  maps. Either malonate alone (3TJL) or nicotinamide (3UPW) completely accounted for this additional active site electron density. In the case of the *p*-chlorophenol soaked structure, the final electron density maps suggested only partial occupancy of this ligand (approximately 60%), this is consistent with the very short ligand soaking time. Additional electron density beyond that of *p*-chlorophenol was modeled as a malonate molecule in the same orientation as observed in the native structure. The deposited structure (4DF2) has both ligands in the model. All protein structure figures were created using PyMOL (Schrödinger, LLC)

### **Phenol Binding Studies**

Assays were performed at 20 °C in 100 mM  $KP_i$ , pH 7.0 in a total volume of 1 mL. Purified OYE2.6 was added to a final concentration of *ca.* 20  $\mu$ M. The actual protein concentration present during each experiment was calculated from the initial value of  $A^{460}$  using  $\epsilon^{460}=10,600$ . Aliquots of the appropriate phenol (*p*-chlorophenol or *p*-hydroxybenzaldehyde; 4.0 mM stocks in EtOH) were added to the protein solution and the mixtures were stirred briefly. Spectra were recorded at *ca.* 1 min intervals until no further change was observed (typically  $\leq 3$  min). This process was continued until apparent saturation was reached.

CHAPTER 4  
CHARACTERIZATION OF *Lactococcus lactis* CV56 DIHYDROOROTATE  
DEHYDROGENASES IA AND IB

**Introduction and Rationale**

The previous chapters have discussed the applicability of OYEs as biocatalysts in asymmetric reductions. More specifically, the focus has been on the enantioselectivity of these enzymes and we have described our efforts towards understanding the factors that control substrate stereoselectivity. Since gaining access to stereocomplementary products could open many doors to the application of alkene reductases in synthetic processes, this has been an area of great interest in our group.

Another factor that can limit the suitability of OYEs, and other enzymes, for biocatalysis is the rather narrow substrate range usually displayed. Generally speaking, an enzyme evolves to catalyze one particular chemical reaction and it is, therefore, expected that a high preference for a single substrate or substrate class is displayed. A direct consequence of this is that many chemists will part ways with success as they attempt to increase the value and complexity of the substrates being pursued.

One possible way to address this particular limitation is through the use of protein engineering employing mutagenesis and directed evolution. While these approaches can certainly prove successful, it is virtually impossible to predict the precise impact, if any, that each modification will have on an enzyme. Another point of concern is the fact that abundant effort can be devoted to a particular project without any guarantee that results will be satisfactory. In light of these potential challenges associated with protein engineering, one may consider alternative approaches and rely on natural evolution to provide us with enzymes that have already evolved to accept different substrates while catalyzing equivalent chemical transformations.

In the case of alkene reductases in the OYE family the substrate range is generally narrow due to the small active site coupled to the geometric restraints imposed by the bound flavin mononucleotide and the side chain involved in protonation (usually a Tyr residue). Two particular classes of substrates are generally poorly accepted by OYEs, namely  $\alpha,\beta$ -unsaturated carboxylic acids and  $\beta$ -substituted  $\alpha$ -enones. As has been extensively discussed in chapters 1 and 2, OYE family members are able to catalyze the net *trans*-hydrogenation of activated alkenes and, to a fair approximation, the reactivity of these enzymes is dictated by the highly conserved three-dimensional arrangement of the hydrogen bond donors His and Asn/His, the proton donor Tyr196 and the hydride donor N5 of flavin.

Given the importance and lack of plasticity of the spatial arrangement in the active sites of OYEs', we hypothesized that if we could find other enzymes that shared some of the same structural features perhaps they could catalyze the same chemical reaction irrespective of any overall sequence similarity or substrate specificity. In other words, what other enzymes possess a bound FMN as well as amino acid side chains equivalent to those of OYE1's His191, Asn194 and Tyr196 having similar spatial arrangements relative to one another? Searches through the structural data bank utility PDBeFold<sup>65</sup> led us to the enzyme dihydroorotate dehydrogenase (DHODase or simply DHOD). Like OYE1, DHODase belongs to the TIM phosphate binding family and has a tightly non-covalently associated FMN in the center of its eight-stranded parallel  $\beta$ -barrel domain. While countless enzymes share these same features, deeper examination of the DHODase active site structure led us to believe it could work as an alkene reductase complementing OYEs.

## Background and Experimental Design

### DHODase Function

Dihydroorotate dehydrogenases catalyze the two-electron oxidation of L-dihydroorotate to orotate. This conversion is the only redox step in the universal pyrimidine *de novo* biosynthesis. The formation of orotate is the fourth overall step in the biosynthetic pathway and precedes the formation of orotidine 5'-monophosphate (OMP) (Figure 4-1). Although all DHODS are flavoproteins, the properties of enzymes from different organisms vary considerably<sup>66</sup>. The enzymes from Gram-positive bacteria, archaea, and some lower eukaryotes, e.g., *Saccharomyces cerevisiae*, are soluble proteins, which use soluble substances as electron acceptors. These are members of family 1. The DHODs belonging to family 2 are found mainly in eukaryotic organism and Gram-negative bacteria. Family 2 enzymes, such as human DHOD, are attached to membranes and use respiratory quinones as final electron acceptors<sup>67</sup>. Soluble and membrane-associated DHODs usually have less than 20% sequence identity and the membrane bound enzymes usually display an additional 40 amino acid domain which forms the binding site for quinones in their N-termini and which have no counterpart in soluble DHODs. Soluble DHODs also diverge significantly from each other and have been further divided into two subgroups, family 1A and 1B which show ca. 30% sequence identity<sup>68, 69,69b</sup>.

Family 1A enzymes are found in anaerobic yeasts, some protozoa and in milk-fermenting bacteria such as *Lactococcus lactis*<sup>69b,70</sup> and *Enterococcus faecalis*<sup>71, 72</sup>. A notable remark is that these two bacteria possess both family 1A and 1B DHODs. Family 1A DHODs are soluble homodimeric proteins with one FMN molecule bound to each subunit and use fumarate as an electron acceptor and are sometimes termed

fumarate reductases. In contrast, DHODs of family 1B, predominant in Gram-positive bacteria, form  $\alpha_2\beta_2$  heterotetramers and are able to use  $\text{NAD}^+$  as an electron acceptor<sup>73</sup>. Independent of their family or subfamily, all DHODs are closely related mechanistically in particular with respect to their first half-reaction.

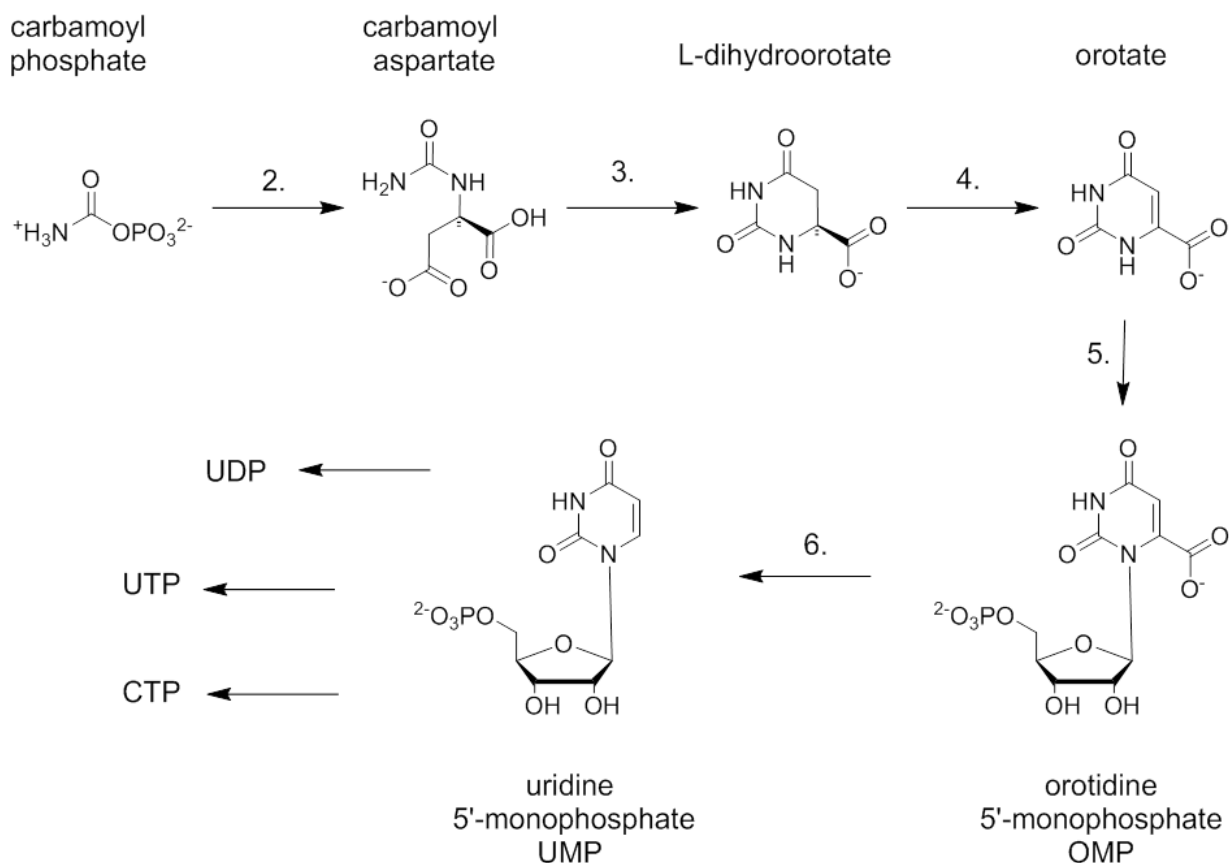


Figure 4-1. The pyrimidine *de novo* biosynthesis. Step four is an oxidation catalyzed by the enzyme dihydroorotate dehydrogenase (DHODase).

### Catalytic Cycle and Electron Acceptors

Similar to OYEs, the catalytic cycle of DHODs can be divided into two separate half-reactions in which the FMN is first reduced to  $\text{FMNH}_2$  and subsequently reoxidized to FMN (Figure 4-2). In the first half reaction, the substrate L-5,6-dihydroorotate binds to

the active site of the FMN containing subunit where a Cys residue is ideally oriented to abstract a proton from C5 of dihydroorotate. This polarization leads to a concomitant transfer of hydride to the FMN resulting in the formation of orotate and FMNH<sub>2</sub>. The first half-reaction appears to be conserved in all DHODs<sup>17b, 74, 75</sup>. Conversely, the mechanism for the second half-reaction depends on the identity of each DHOD.

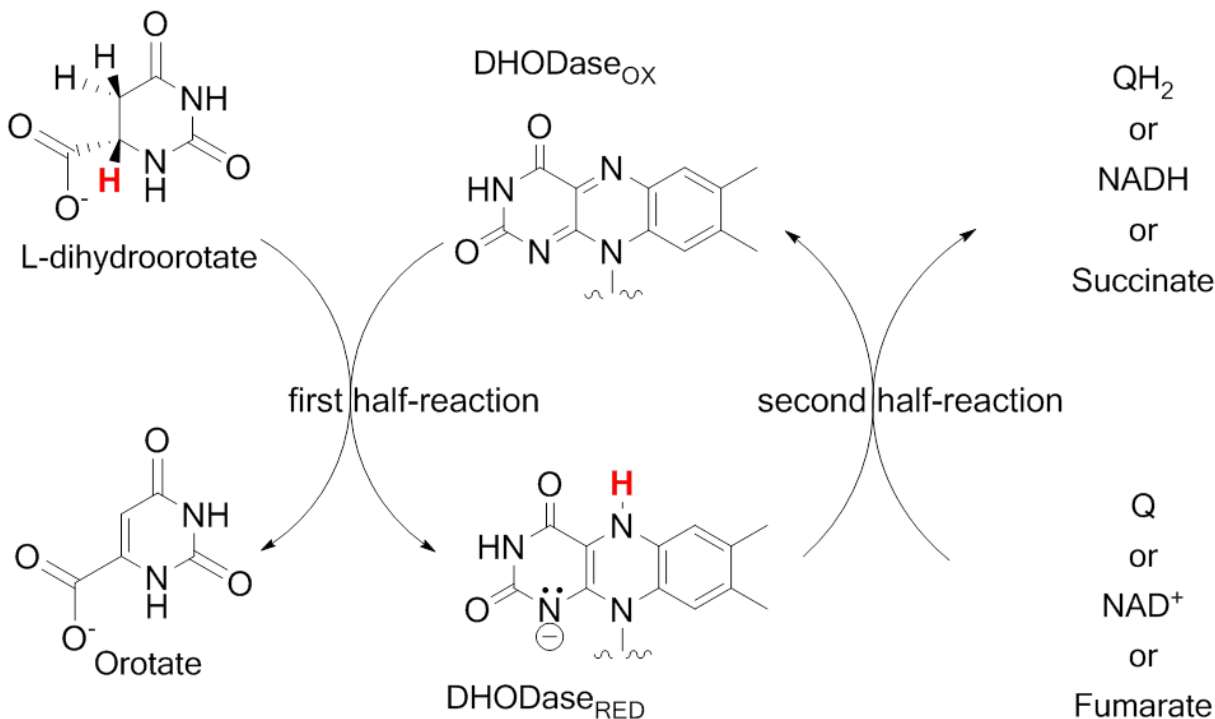


Figure 4-2. The catalytic cycle of DHOD. In the first half-reaction, electrons abstracted from dihydroorotate reduce FMN; in the second half-reaction, FMNH<sub>2</sub> is reoxidized by a variety of electron acceptors.

In summary, the second half-reaction of DHODs regenerates oxidized FMN via different electron acceptors in order to prepare the enzyme for the next catalytic turnover. The identity of the electron acceptor differs in the many DHODs and different classes utilize different classes of molecules. Family 2 enzymes use membrane associated respiratory quinones and their mechanism has been less extensively studied although several inhibitors have been successfully designed<sup>76</sup>. Family 1 DHODs are

soluble proteins and use soluble electron acceptors such as fumarate (DHOD 1A) and NAD<sup>+</sup> (DHOD 1B).

One of the main differences between 1A and 1B enzymes is found in their quaternary structures and this is directly related to their mechanism and substrate specificity. Family 1A enzymes are homodimeric and both first and second half-reactions take place in the same subunit. After oxidation of dihydroorotate, electrons from the reduced flavin are then transferred to the second substrate, fumarate, leading to the formation of succinate in the second half-reaction. The overall process constitutes a one-site ping-pong Bi-Bi kinetic mechanism. DHODs of family 1B are heterotetrameric with two  $\alpha$  and two  $\beta$ -subunits. As in type 1A enzymes, the  $\alpha$ -subunits are the site of the first half-reaction and contain an FMN cofactor. Type 1B enzymes generally cannot use fumarate as an acceptor<sup>73</sup> and electrons are transferred to a bound FAD via an iron sulfur (2Fe-2S) cluster in the  $\beta$ -subunit. In this subunit, NAD<sup>+</sup> binds and electrons are transferred from the FADH<sub>2</sub> completing the cycle. Other molecules such as ferricyanide, the dye DCIP, and oxygen can also serve as electron acceptors for all DHODs. However with the exception of oxygen, these are thought to be gratuitous acceptors and likely have no physiological role.

### **Structural Similarities and Potential as an Alkene Reductase**

As mentioned above, we looked for enzymes that exhibited a scaffold similar to that of OYE1. More specifically we looked for similarities in the three dimensional structure with respect to catalytically relevant amino acid residues hoping the enzyme would be able to catalyze chemical conversions that were equivalent to those of OYE1 while accepting different classes of substrates. The first enzyme we turned our attention to was *L. lactis* DHOD 1A.

Like many OYEs, this enzyme is a cytosolic homodimer and each monomer folds into a single domain ( $\alpha/\beta$ )<sub>8</sub>-barrel with a tightly bound FMN cofactor and it is classified as FMN-linked oxidoreductase. Despite these obvious similarities, sequence alignment of DHOD 1A and OYE1 suggests that these enzymes are not related and a mere 11.2% (45/400) sequence identity is observed. However, structural alignment with respect to the bound flavin mononucleotide group reveals some interesting similarities.

In OYE1, the most catalytically important features of the active site are residues 191, 194, 196 and 37. His191 and Asn194 are responsible for properly orienting the substrate as well increasing its reactivity through stabilization of an enol intermediate. Tyr196 is directly involved in protonation of the substrate to complete the net hydrogenation of the C-C double bond while Thr37 is crucial for regulating the reactivity of the FMN <sup>17c</sup>. Interestingly, DHOD 1A seems to possess residues in similar locations that are, at least in principle, capable of serving the same functions as those in OYE1 (Figure 4-3). The crystal structure of DHOD 1A in complex with orotic acid <sup>77</sup> reveals that a carbonyl oxygen of the pyrimidine ring is hydrogen bonded to Asn127 and Asn193 which placing Sy of Cys130 is 3.3 Å from the carbon  $\alpha$  to the carbonyl, and a  $\beta$ -carbon is 3.5 Å from the N5 of flavin. These values are in close agreement with those seen in structures of OYE1/substrate complexes and seem to describe a favorable geometry for hydride transfer.

Another aspect of DHOD 1A that sparked our interest is related to the substrate of its second half-reaction, fumarate. In the second half-reaction, DHOD 1A catalyzes the reduction of fumarate to succinate and some DHODs have been classified as fumarate reductases in *T. cruzi* <sup>78</sup>. This observation was of particular importance to us

since OYE1 and our library of alkene reductases consistently failed to reduce unsaturated acids and this could further diversify our biocatalytic toolbox. The fact that DHOD 1A is able to convert fumaric acid into succinate indicates that its bound FMN cofactor has a redox potential that is suitable for reduction of alkenes conjugated to carboxylic acids. Since we deduced that a change in substrate selectivity would be more easily achievable than tuning the FMN redox potential, we cloned DHOD.

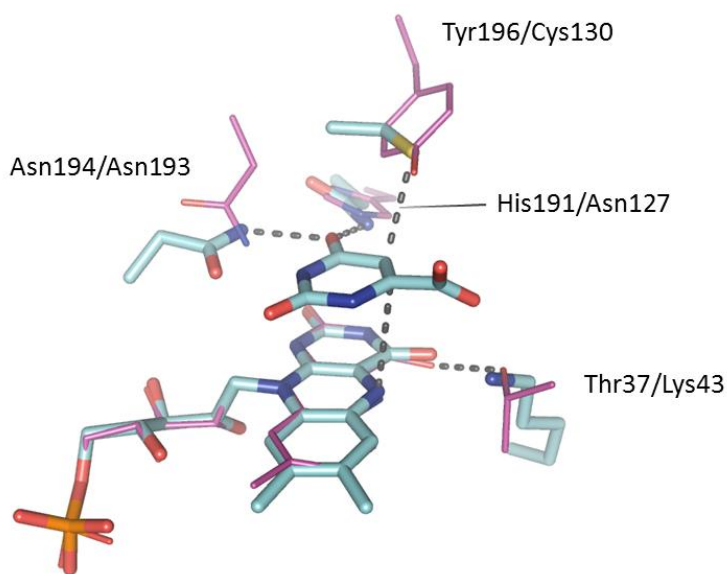


Figure 4-3. Active site alignment of OYE1 and DHOD 1A. The residues are labeled as (OYE1/DHOD) numbers. DHOD 1A residues are shown in thick cyan sticks and OYE1 in thin magenta lines.

## Results and Discussion

### ***Lactococcus lactis* CV56 DHODase 1A Cloning, Expression and Purification**

DHOD 1A was cloned from the purified genomic DNA of *L. lactis* CV56 using primers designed to amplify the *pydA* gene using PCR while inserting *NdeI* and *XhoI* recognition sites (Figure 4-4 A). These restriction sites allowed for direct ligation of the *pydA* gene into the vector pET-22(b)+ (Novagen ®). After ligation, *E. coli* JM109 cells were transformed using the construct and four random colonies were picked for plasmid

extraction. DNA sequencing results showed that the resulting plasmid (pYAP-3) contained the *pydA* gene encoding DHOD 1A (Figure 4-4 B).

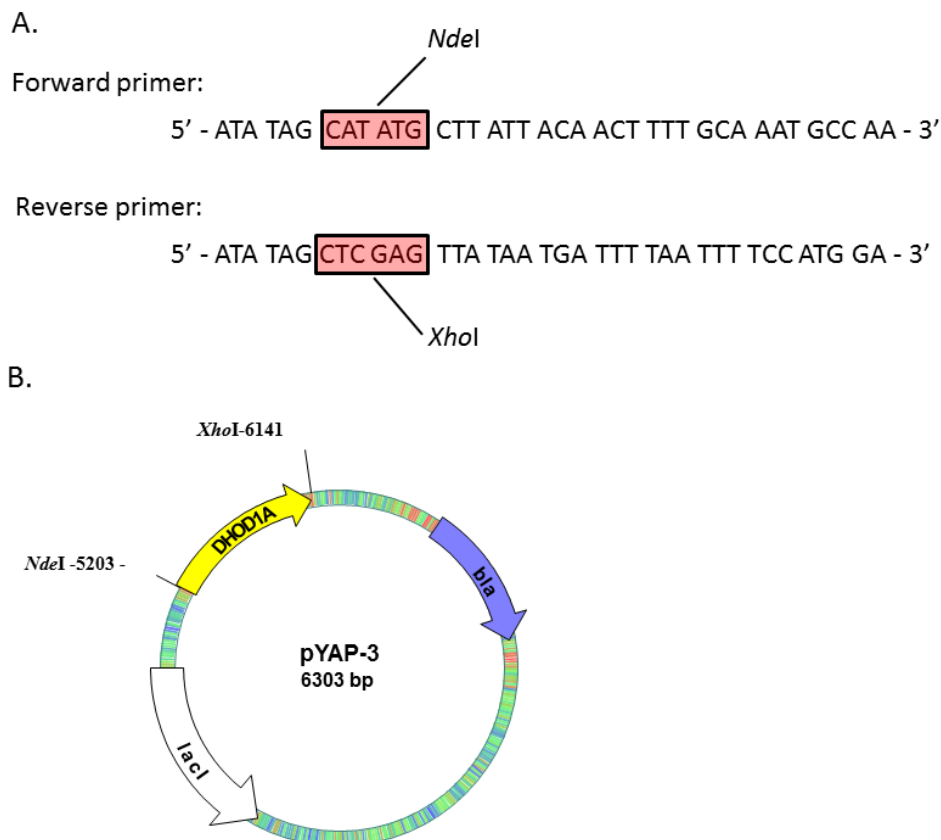


Figure 4-4. A- The primers utilized to clone the *pydA* gene from *L. lactis* CV56. B- The final construct of the plasmid pYAP-3. The *bla* gene encodes  $\beta$ -lactamase and confers ampicillin resistance.

The pYAP-3 plasmid was transformed into *E. coli* BL21-Gold (DE3) and protein overexpression was initiated by addition of 0.5 mM IPTG. Cells were harvested after 8 hrs and the dihydroorotate dehydrogenase activity was assayed using lysate from cells that had been disrupted via sonication. At this stage, the lysate exhibited the characteristic yellow color of flavins suggesting that DHOD 1A was in fact being overexpressed. The lysate total activity was  $2.25 \mu\text{M s}^{-1}\mu\text{L}^{-1}$ . To determine whether the

dehydrogenase activity observed was due to DHOD1A or other contaminants in the lysate, the assay was run using the same cell line lacking plasmid DNA. These cells had a measured dihydroorotate dehydrogenase activity of  $< 0.2 \mu\text{M s}^{-1}\mu\text{L}^{-1}$ . Analysis of the cells using SDS-PAGE further validated the overexpression of DHOD 1A as a strong band consistent with the theoretical molecular weight of 33kDa (Figure 4-5).

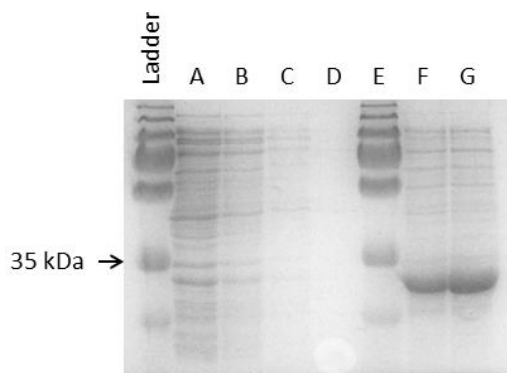


Figure 4-5. SDS-PAGE analysis of *E. coli* cells carrying pYAP-3. Lane A, B and C contain different amounts of boiled cells harvested prior to induction. Lanes F and G contain samples of boiled cells 8 hrs after induction.

In order to carry out more studies of the enzyme we pursued a purification route that could yield large amounts of high purity enzyme. The parent vector of plasmid pYAP-3, pET-22(b)+, is designed to express a C-terminal hexa-histidyl fragment ideal for metal affinity chromatography. In order to express this portion, a stop codon naturally present in the pydA gene needed to be removed. Using a modified procedure of Zheng *et al.*<sup>41</sup>, we designed mutagenic primers that would change the original TAA codon to a GCT codon which encodes an Ala residue. This resulted in a construct, pYAP-7, that carries the gene for DHOD 1A containing a C-terminal His<sub>6</sub>-tag named. Using the plasmid pYAP-7 (appendix E, Figure E-1), DHOD 1A could be successfully

overexpressed and purified by nickel affinity chromatography which was also catalytically active.

Our initial motivation for cloning DHOD 1A was the possibility of using this enzyme as a biocatalyst that could complement the substrate panel for alkene reductases in the OYE family. While DHOD 1A can successfully reduce fumarate and possibly other unsaturated carboxylic acids, this enzyme had one particular limitation that makes it non-ideal for transformations of preparative scale. In a biocatalytic process, often times, the amount of starting material to be converted can range from a couple of milligrams to near a gram. In the case of asymmetric reductions using alkene reductases, such large scale operation can become costly as the price of the electron donor NADPH fluctuates around US\$600-US\$1000 dollars/gram. One way to circumvent the prohibitive prices is to couple a cofactor regeneration system to the biocatalytic process. A widely used method for the regeneration of NADPH is the glucose/glucose dehydrogenase system<sup>79</sup>, which is compatible with most OYE enzymes. In the case of DHOD 1A, this system cannot be used and an analogous reducing equivalents regeneration route is not readily accessible. This enzyme's ultimate electron source is 5,6-dihydroorotate and - since we could not find a feasible way regenerate this molecule - if DHOD 1A were to be employed in a preparative scale process an equimolar amount of L-5,6-dihydroorotate would be needed. Even though the price of US\$ 200 dollars/gram for this compound may not seem as overwhelming as that of nicotinamide cofactors, it is far from insignificant and this prompted us to pursue a different enzyme in DHOD 1B.

## Lactococcus lactis CV56 DHOD 1B

### Introduction

In light of DHOD 1A's deficiencies with respect to the regeneration of electron donors, we turned our attention to a different dihydroorotate dehydrogenase present in *L. lactis*, DHOD 1B. This enzyme differs from DHOD 1A in several aspects that make it a more promising target in expanding the substrate panel for OYE-like alkene reductases.

In contrast to the homodimeric forms of type 1A enzymes, DHOD 1B is a soluble heterotetramer composed of two  $\alpha$ - and two  $\beta$ -subunits. The  $\alpha$ -subunits are closely related in both sequence and structure to the family 1A homodimers. They are the site of dihydroorotate dehydrogenation and consist primarily of an  $(\alpha/\beta)_8$ -barrel (TIM barrel) domain which contain the FMN cofactors. The  $\beta$ -subunit in DHOD 1B is the site of electron-transfer and adopts a conformation similar to that seen in proteins belonging to the NADPH ferredoxin reductase superfamily<sup>80</sup>. It is subdivided into two domains. The N-terminal domain, consisting of the first 100 amino acids serves as the binding site for an FAD molecule. The C-terminal domain comprises an open  $\alpha/\beta$ -structure. It resembles the NAD binding domains of the ferredoxin reductase family and is the putative NAD<sup>+</sup> binding site in DHOD 1B. This structural feature offers a logical explanation for why ability to use NAD<sup>+</sup> as an electron acceptor is unique to family 1B enzymes.

In 1996, Nielsen *et al.*<sup>73</sup> unambiguously identified the genes encoding both the  $\alpha$ -subunit (*pyrDb*) and  $\beta$ -subunit (*pyrK*) in *Lactococcus lactis*. Furthermore, all of the enzyme's cofactors were identified and it was demonstrated that the  $\beta$ -subunit (*pyrK*) was essential for the reduction of NAD<sup>+</sup> at the expense of dihydroorotate. It was also shown that, under acidic conditions, the enzyme could catalyze the reverse of the

physiological reaction, namely the reduction of orotate to dihydroorotate in the presence of NADH.

Even though the physiological relevance of this result was uncertain at the time, it made DHOD 1B an attractive target for our studies. Much like in OYE1 catalyzed alkene reductions, the conversion of orotate to 5,6-dihydroorotate involves the net *trans*-hydrogenation of a C-C double bond at the expense of NADH electrons. Additionally, since a variety of NADH cofactor regeneration systems have been described with success, this enzyme could be, at least in principle, a useful biocatalyst at a reasonable cost.

### **Cloning, expression and purification**

*Lactococcus lactis* is one of the few organisms that carries the genes for both class 1A and 1B DHODs allowing us to clone the 1B enzyme from the same genomic DNA preparation used for DHOD 1A. In the 1,360 to 1,370 kilobase region of the *L. lactis* CV56 genome, the *pyrZ* gene is located directly upstream from the *pyrD* gene. Therefore we designed a forward primer for the 5' end of the *pyrZ* gene and a reverse primer for the 3' end of the *pyrD* gene (Figure 4-6). The primers inserted restriction sites for the endonucleases *NdeI* and *XhoI* which allowed the ligation of the 1796 base pair fragment into pET-22(b)+. The resulting construct was termed pYAP-5 and contained the *pyrZ* gene and the *pyrD* gene expressing a C-terminal His<sub>6</sub>-tag. (appendix B, Figure B-2).

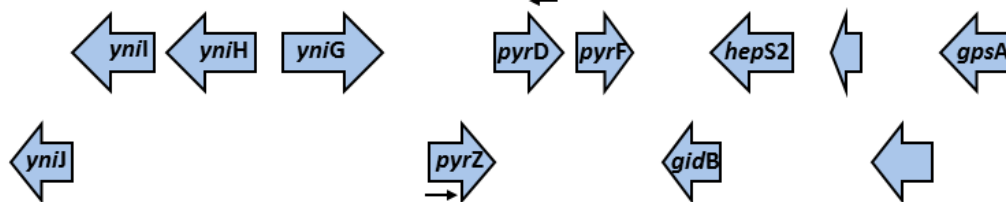
Initially, the protein was overexpressed in *E. coli* BL21-Gold (DE3) cells that were grown in LB broth supplemented with ampicillin utilizing standard protocols and the protein could be successfully purified using nickel affinity chromatography. However this proved unsuccessful and the purified enzyme had low catalytic activity, it had a

molecular weight much lower than that of the tetramer (65kDa versus 125kDa) and exhibited a UV-Vis spectrum that was not consistent with the homotetrameric form (Figure 4-7). In particular, the “yellowish-green” appearance was corroborated by the lack of a broad absorbance band in the range of 520-560 nm which is observed in the heterotetramer. Taken together, these observations suggest that our enzyme preparation failed to produce the correct enzyme form in any appreciable amount and we surmised that either the construct pYAP-5 or the expression protocol, or both needed to be changed in order to achieve more satisfactory results.

Reverse primer:

5' – G CCA **CTC GAG** TGC TTT TTT TGA GTT TTT AAC TTC TTG AAT CAA GTT TTC TAA GCT ATC A – 3'  
*XhoI*

1,374 K | 1,372 K | 1,370 K | 1,368 K | 1,366 K | 1,364 K | 1,362 K | 1,360 K



Forward primer:

5' – TA TCG **CAT ATG** CCT AAG TTA CAA GAG ATG ATG ACG ATT GTC A – 3'  
*NdeI*

Figure 4-6. Region of *L. lactis* CV56 genome containing the *pyrZ* and *pyrD* genes. The black arrows indicate the location of the primers and the primers sequences are shown above and below the gene cluster diagram.

In their original characterization of DHOD 1B, Nielsen *et al.* had described the existence of two forms of the enzyme. One was a “yellowish-green” enzyme, and the other a “brownish-orange” form. The two forms could be separated using anion-

exchange chromatography and it was established that the yellowish green form was a homodimer composed of FMN binding subunits (*pyrD*) while the brownish-orange enzyme was a heterotetramer consisting of two *pyrD* ( $\alpha$ ) and two *pyrZ* ( $\beta$ ) subunits. Based on the published description and the visual appearance of our enzyme solutions, we concluded that the preparation we obtained using cells harboring pYAP-5 grown in LB medium overwhelmingly expressed the *pyrD* protein and nearly undetectable amounts of the  $\beta$ -subunit, *pyrZ*. To repair the inadequacies in expression of the heterotetrameric form of DHOD 1B, changes were made in both the expression protocol and in the construct of the protein.

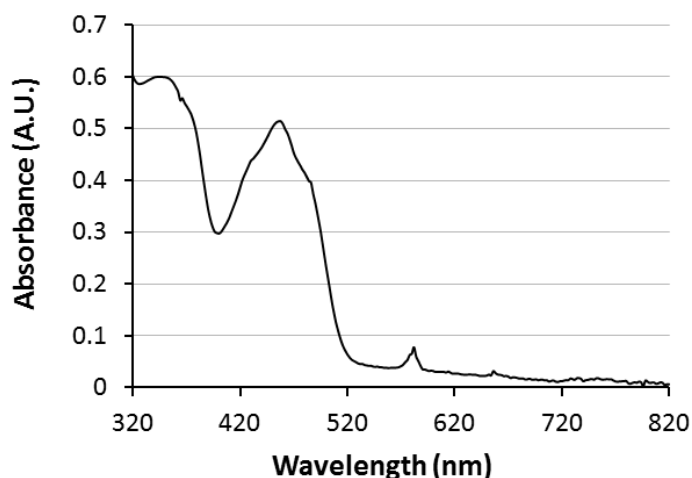


Figure 4-7. Absorption spectrum of DHOD 1A. The lack of a broad absorbance band from 520-560 nm explains the yellow-green appearance of the enzyme solution. The peaks at 360 and 460 nm are typical of FMN cofactors.

*Escherichia coli* is one of the most widely used expression hosts due to its ability to grow rapidly and to high density while generally giving good yields of target proteins. However, expression has been especially troublesome for proteins containing Fe-S clusters<sup>81</sup> and much effort has been devoted toward achieving better results. Ballou and co-workers showed that optimization of growth conditions can lead to high

expression levels of some Fe-S cluster containing proteins without the need for co-expression of genes in the *isc* cluster<sup>82</sup>. Based on these results, we changed the growth medium accordingly and cells were grown in TB (terrific broth) medium instead of LB broth and were supplemented with ferric citrate, ferrous sulfate and cysteine at the time of induction. Another change in the expression protocol was that cells were induced at a late log phase (O.D.<sup>600</sup>  $\approx$  3.0).

To maximize the amount of protein that could be purified we also changed the construct of the plasmid being used. The plasmid pYAP-5 encodes the  $\alpha$ -subunit *pyrZ* protein and the  $\beta$ -subunit *pyrD* protein with an additional hexahistidyl portion in its C-terminus. In a scenario where the expression of the Fe-S cluster containing  $\beta$ -subunit is markedly lower than that of the  $\alpha$ -subunit, this construct will lead to the isolation of homodimeric DHOD almost exclusively. To overcome this deficiency, we used pET-15b (Novagen®) to construct a plasmid, pYAP-6, which encodes *pyrZ*, with an N-terminal His<sub>6</sub>-tag, and *pyrD* in its native state.

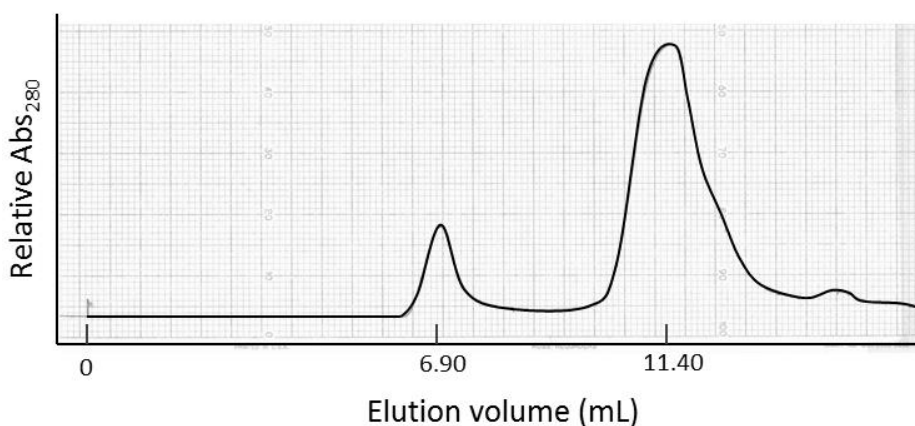


Figure 4-8. Elution profile of the purified DHOD 1B. The enzyme elutes at 11.4 mL primarily.

Cells harboring pYAP-6 were grown in TB and protein expression was carried out based on the results of Ballou and co-workers<sup>82</sup>. Under these conditions the cell lysate displayed a light brown color characteristic of iron-sulfur containing proteins suggesting that the *pyrZ* was being expressed appreciably. The clarified lysate was applied onto a nitrilotriacetic acid agarose resin that had been loaded with Ni<sup>2+</sup> and the resin was quickly “stained” with a dark-brown color indicating that the protein had bound successfully. The protein was eluted and concentrated by ultra-filtration to a concentration of 1.5 mg/mL, and the final yield was approximately 5 mg/L of culture.

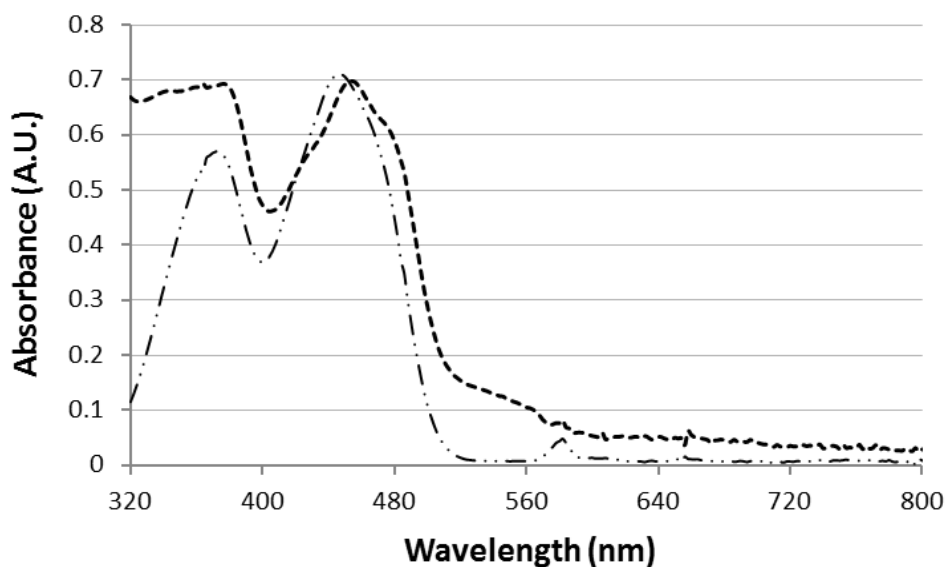


Figure 4-9. The absorption spectrum of the purified DHOD 1B. The enzyme spectrum is shown as a thick dashed line and the spectrum of free FMN is shown in thin dash-dot-dash line.

One interesting observation is that the enzyme was fairly unstable and had the tendency to aggregate in buffer even at low temperatures near 4 °C. However, if cleavage of the N-terminal His6-tag using thrombin was performed, the enzyme exhibited much better stability and could be stored for months with retention of activity.

In order to validate that the protein purified was the desired  $\alpha_2\beta_2$  heterotetramer, we carried out native gel filtration experiments. Under the experimental conditions, the elution volume for the protein was 11.40 mL (Figure 4-8) and a calculated molecular weight of 115 kDa (appendix D) which is in good agreement with the theoretical molecular weight for DHOD 1B of 126 kDa. The absorption spectrum of the purified enzyme showed a broad absorbance band in the 520-560 nm region also suggesting that it contained both FMN containing  $\alpha$ -subunits and Fe-S cluster containing  $\beta$ -subunits (Figure 4-9).

### **Crystallization and Structure of *L. lactis* CV56 DHOD 1B**

In anticipation to future protein engineering projects involving DHOD 1B we decided to crystallize the wild type enzyme. In 2000, Rowland *et al.* published the structure of the first family 1B enzyme<sup>83</sup>, however the source of the protein they crystallized was different than the one we used in this study and the differences in sequence were 18 amino acids and 29 amino acids for the  $\alpha$ - and  $\beta$ -subunits respectively. Furthermore, if we could find conditions that yield diffraction quality crystals they could be used for gaining structural information about different variants we may construct as well as different enzyme substrate complexes.

To screen crystallization conditions, enzyme was concentrated to *ca.* 22 mg/mL in 50 mM NaP<sub>i</sub>, pH 6.0, 10% v/v glycerol solutions. Crystallization drops were set up with either free enzyme or with the ligand orotate in addition to enzyme. After screening 192 conditions, the most promising crystallization results were obtained using PEG of different molecular weights as a precipitant in buffers of acidic pH (3.5-5.0). Unfortunately, the crystals originally formed as thin plates with several layers and diffracted X-rays poorly yielding no interpretable data (Figure 4-10 A). Crystals could be

obtained reproducibly from 0.1 M sodium acetate pH 4.0, PEG 4,000 8% w/v solutions, therefore this buffer was further optimized. In general, the addition of several polyols improved crystal morphology. In particular, the addition of 3% glycerol resulted in crystals appeared singular and possessed nicely defined faces (4-10 B).

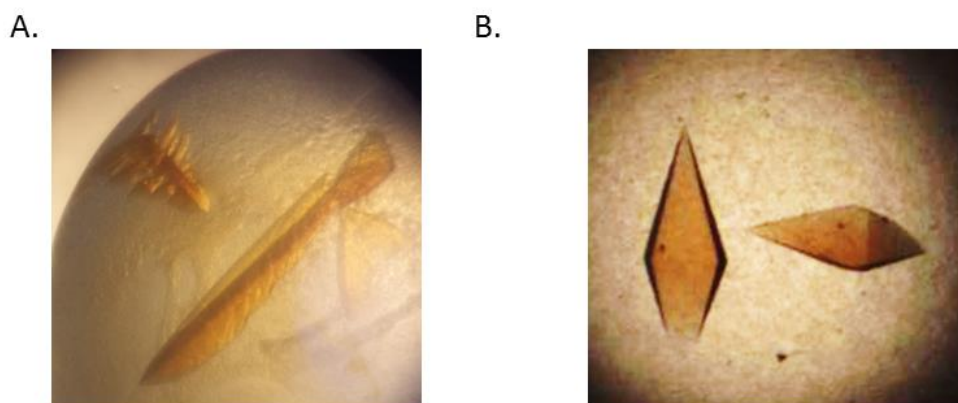


Figure 4-10. Wild-type DHOD 1B crystal optimization. A- Initial crystals obtained in sodium acetate pH 4.0, 8% w/v PEG 4,000. B- Crystals after addition of 3% v/v glycerol.

One puzzling observation was the fact that, despite the significant improvement in their morphology, these crystals failed to yield satisfactory X-ray diffraction data. After several attempts at collecting data under cryogenic temperatures (100 K), we decided to test the diffraction of these crystals at room temperature. One notable difference between these two collection protocols is the fact that, in room temperature collection, there is no need to treat the crystals with a cryoprotecting buffer such as 30% glycerol. While cryoprotection is a necessary step prior to cooling the crystals, it can sometimes be detrimental to X-ray diffraction. Many crystals exhibit extreme sensitivity to the composition of their mother liquor and the slightest changes in osmolality and ionic strength of this solution can lead to a decreased diffraction resolution or even complete dissolution of the crystal. In the case of our DHOD 1B, the crystals diffracted to a

maximum resolution of 2.4 Å at room temperature, while the crystals that had been cryoprotected and frozen in liquid nitrogen usually gave diffraction patterns that were hardly usable. One limitation associated with data collection at room temperature, and also one of the main motivations for the development of cryocrystallography, is the high susceptibility to radiation damage causing loss of diffraction. This was unfortunately the case for us and a full data set could not be collected at room temperature even though the crystals diffracted well enough.

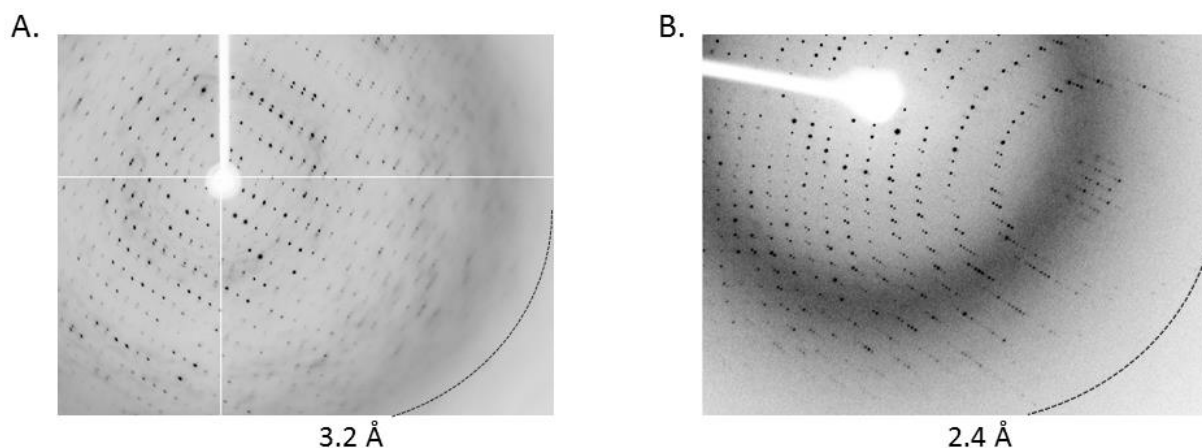


Figure 4-11. X-ray diffraction pattern at different temperatures. A- Typical diffraction pattern of “cryoprotected” crystals. B- Diffraction pattern of crystal at room temperature.

Despite difficulties with finding an appropriate cryoprotection protocol, one full data set was collected on a single crystal. This crystal exhibited high anisotropy, which causes the diffraction pattern to be highly variable depending on the crystal orientation relative to the X-ray beam. By utilizing select X-ray images from different sections of the crystal, diffraction data up to 2.7 Å could be integrated and scaled with an overall completeness of 96.5%. The structure was solved by molecular replacement using the structure of the closely related protein published by Rowland *et al.* (PDB code 1EP2).

The crystals belonged to the orthorhombic space group  $C 2 2 2_1$  with a solvent content of 54.2% and a Matthews coefficient of  $2.68 \text{ \AA}^3/\text{Da}$ . The asymmetric unit contained two  $\alpha\beta$  heterodimers with unit cell dimensions of  $80.2 \times 151.9 \times 214.8 \text{ \AA}$ . Interestingly, the contacts and the surface area of the interface between the two heterodimers in the asymmetric unit suggest this is not the heterotetrameric biological assembly. Rather a neighboring heterodimer, related by a crystallographic 2-fold symmetry operator appears to form heterotetramer that is stable in solution and not a crystallographic artifact. This proposed heterotetramer assembly buries 37% of the total protein surface area, which is almost three times as much as any of the other protein interfaces and has the same overall arrangement as reported by Rowland *et al.* (Figure 4-12). The final model was refined to residuals error values  $R_{\text{work}}$  and  $R_{\text{free}}$  of 0.22 and 0.26, respectively. The complete crystallographic parameters, data collection and refinement statistics can be found in Table 4-1.

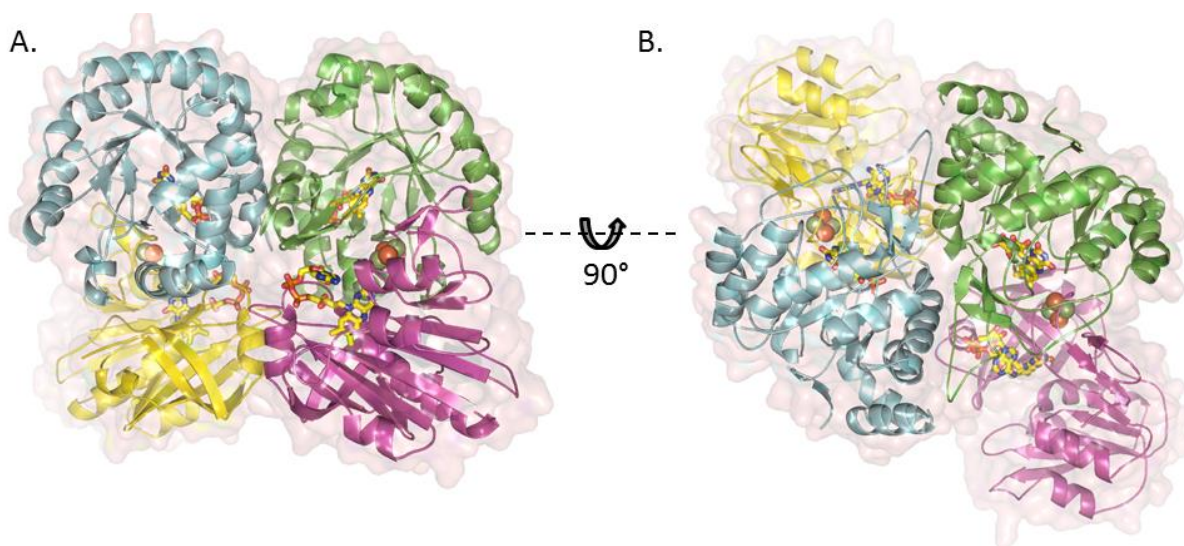


Figure 4-12. The biological heterotetramer of DHOD 1B. The protein backbone is shown as cartoon representation, the FMN and FAD cofactors are shown as sticks, the 2Fe-2S clusters are shown as spheres.

As expected, the overall structure is very closely related to that of *L. lactis* DHOD 1B reported by Rowland, however, one striking difference is observed. In our structure of *L. lactis* CV56 DHOD 1B, a loop region that covers the active site of the  $\alpha$ -subunit is shifted by as much as 12 Å. This loop carries the catalytic Cys135 residue and its movement is directly linked to substrate binding and reactivity<sup>83-84</sup>. It has been suggested that the loop would close upon substrate binding to adopt a catalytically active conformation. The open conformation seen in our structure of DHOD 1B in complex with orotate contradicts this notion and it is likely not the catalytically active conformation. In the open loop form, the catalytic acid/base S $\gamma$  of Cys135 is located almost 7 Å away from the substrate which contrasts a distance of 3.6 Å in the closed form.

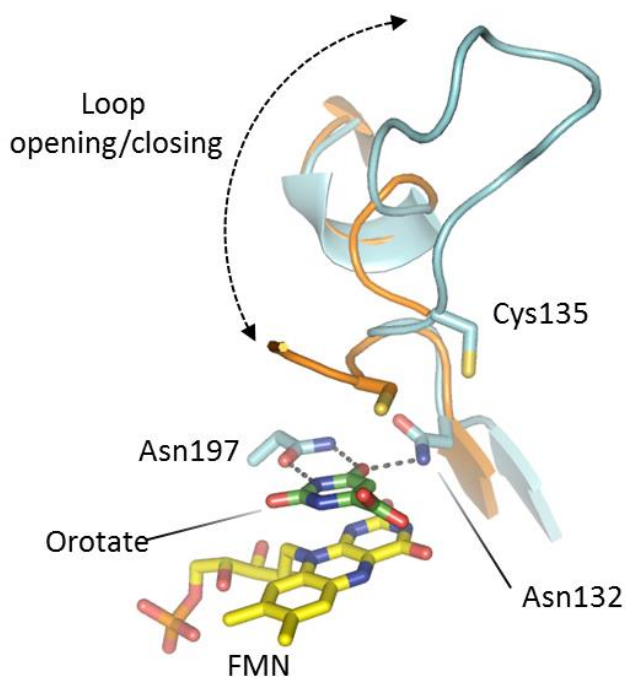


Figure 4-13. The conformational changes in the active site loop. The structure solved in this work has an “open” loop and is shown in cyan carbons. The previously reported structure showed a “closed” loop and is shown in orange carbons.

Table 4-1. X-ray Crystallographic Data Collection and Refinement Statistics

Structure name	Orotate-DHOD 1B
Observed active site ligand	orotate
X-ray source	Rigaku CuK $\alpha$ Rotating Anode
Space group	C 2 2 2 <sub>1</sub>
Unit cell dimensions	
a,b, c (Å)	80.20, 151.91, 214.79
$\alpha,\beta,\gamma$ (°)	90, 90, 90
Resolution (Å)	50.39 - 2.72 (2.817 - 2.72)
Unique reflections	34552 (3497)
Completeness (%)	96.82 (99.57)
Multiplicity	5.1 (5.2)
R <sub>sym</sub> <sup>[b]</sup>	0.13 (0.63)
I/ $\sigma$ (I)	7.34 (1.69)
R <sub>work</sub> <sup>[c]</sup>	0.22 (0.30)
R <sub>free</sub> <sup>[d]</sup>	0.26 (0.37)
Ramachandran statistics <sup>[e]</sup>	
Favored (%)	96
Allowed (%)	3.9
Outliers (%)	0.1
Number of atoms	
Protein	8451
solvent	307
ligand	211
Average B factors (Å <sup>2</sup> )	
Protein	36.6
Solvent	32.8
Ligands	32.4

<sup>[a]</sup>Values in parentheses denote data for the highest resolution bin.

<sup>[b]</sup>R<sub>merge</sub> =  $\sum hkl \sum i |I_i(hkl) - [I(hkl)]| / \sum hkl \sum i I_i(hkl)$ , where  $I_i(hkl)$  is the intensity of the  $i$ th observation of unique reflection  $hkl$ .

<sup>[c]</sup>R<sub>work</sub> =  $\sum | |F_o(hkl)| - |F_c(hkl)| | / \sum |F_o(hkl)|$ .

<sup>[d]</sup>R<sub>free</sub> is calculated in the same manner as R<sub>work</sub> using 10% of the reflection data not included during the refinement.

<sup>[e]</sup>Statistics generated using MOLPROBITY<sup>39</sup>

## Substrate Specificity and Mutagenesis Targets

One property of DHOD 1B that was particularly attractive to us was its ability to catalyze the two-electron reduction of orotic acid to yield dihydroorotic acid. Our wild-type enzyme preparation catalyzed this conversion with a specific activity of  $45.7 \mu\text{mole min}^{-1}\text{mg}^{-1}$  in the presence of 1 mM orotate and 0.18 mM NADH. We wanted, therefore, to explore this property of the enzyme and use it as a more general “alkene reductase” that could offer a substrate panel that was complementary to that of our OYE-type enzymes (Figure 4-14). More specifically we envisioned a possible route for the generation of novel  $\alpha$ -  $\beta$ - and  $\gamma$ -amino acids which can be used in many applications. Furthermore, if we could manipulate the substrate enantioselectivity in DHOD 1B, as we have done with OYE1 and OYE2.6, the synthesis of both D- and L-amino acids would be a possibility.

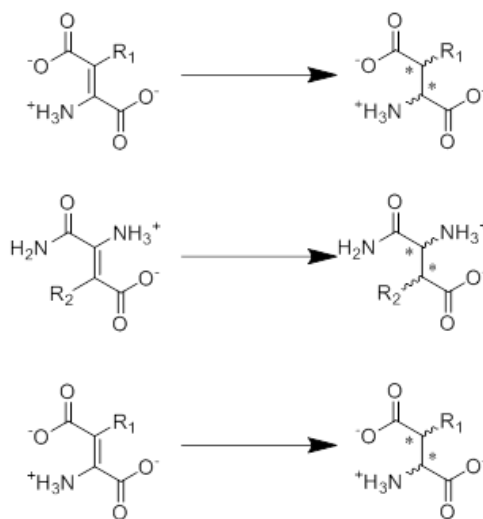


Figure 4-14. Potential substrates for DHOD 1B that would complement the substrate range in our existing library of OYE-like alkene reductases.

The natural substrate for all DHODs is 5,6-dihydroorotate and the fact that these enzymes do not accept 5,6-dihydrouracil or other pyrimidines suggests that the 6-

carboxyl substituent plays a major role in substrate specificity. To achieve our goal of using DHOD as an alkene reductase to convert a variety of non-natural substrates we needed to uncover which active site residues could impact substrate promiscuity and tolerance in DHOD 1B. Additionally, since mutations near the substrate binding site had already proven successful in uncovering enantiocomplementary OYE1 variants, we optimistically decided to employ the same strategy for DHOD 1B. Given the importance of the carboxyl substituent in the substrate for DHODs, we chose the initial target for protein mutagenesis to be a residue that would directly impact the enzyme's interaction with this particular moiety.

We rationalized that enzymes capable of reducing uracil and other pyrimidines could provide some guidance for choosing an amino acid target. We compared the active site of DHOD 1B with that of pig dihydropyrimidine dehydrogenase (DPD), an enzyme that catalyzes the two-electron reduction of uracil to yield 5,6-dihydrouracil. Like DHOD 1B, DPD uses an FMN cofactor for catalysis and the ultimate electron source is reduced nicotinamide. DPD is a large multi-domain protein with two subunits of 1025 amino acids each but, despite these disparities, the architecture of the FMN domain and the pyrimidine binding site is surprisingly close to that of DHOD 1B. In fact, structural alignment of the two proteins using the FMN as reference reveals that many of the residues that define the active site are conserved. Among the subtle differences one amino acid position is particularly interesting, namely Ile74. In DPD the equivalent position is occupied by Glu611 and despite the obvious differences in the physical properties of the two residues, some of the interactions in which Glu611 participates make it a highly interesting residue. In the crystal structure, Glu611 is well positioned to

participate in hydrogen bonding and to form a salt bridge with Lys574 (Figure 4-15 A). The equivalent lysine in DHOD 1B, Lys48 has been shown to undergo large conformational changes upon substrate binding and is important for its orientation as well as controlling the reactivity of the FMN<sup>77, 85</sup>. In order to probe the effect of these interactions in DHOD 1B, we constructed two mutant enzymes, Ile74Glu and Ile74Asp.

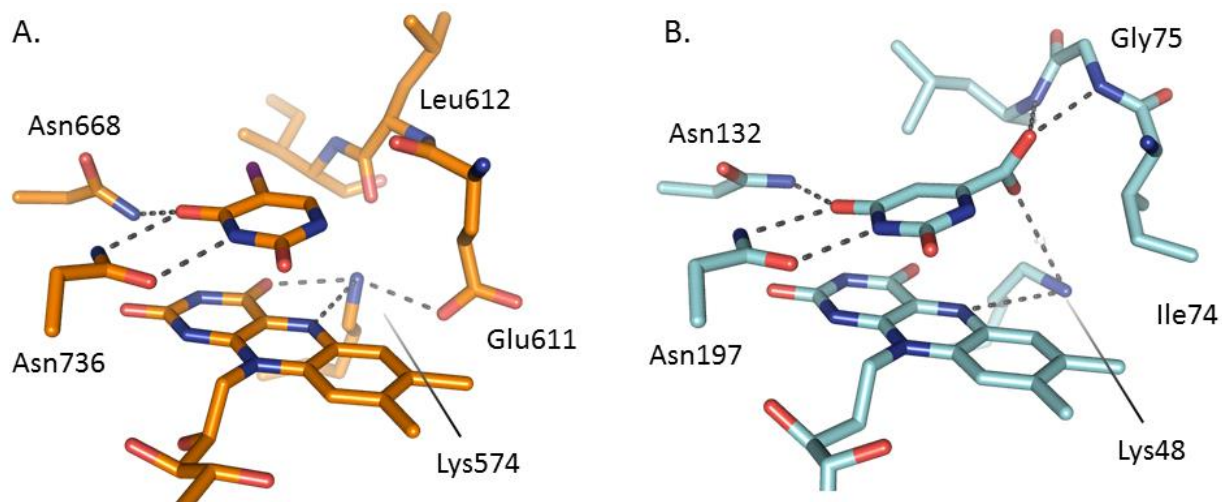


Figure 4-15. Active site comparison of DPD and DHOD 1B. A- The crystal structure of 5-iodouracil bound to pig DPD. B- The crystal structure of orotate bound to *L. lactis* CV56 DHOD 1B. The dashed lines indicate hydrogen bonds and salt bridges.

### Characterization of Ile74Glu and Ile74Asp

The Ile74Glu and Ile74 Asp mutants were constructed with mutagenic primers using the plasmid pYAP-6 as template (Appendix B Figure B-5). Both mutants were expressed and purified as described for the wild-type enzyme. The final protein yield was 3 mg/L for I74D-DHOD 1B and 12 mg/L for the I74E variant.

We wanted to test the hypothesis that by inserting a negative charge in the proximity of Lys48 we would alter the substrate preference of DHOD 1B with the goal of allowing the enzyme to accept uracil and 5,6-dihydrouracil as substrates. In addition to

this direct interaction with Lys48, we hypothesized that the simple repulsion between the carboxyl of orotate and the side-chain of Asp/Glu could be sufficient to cause the enzyme to accept pyrimidines that lack a carboxyl moiety. Unfortunately this was not the case and, like the wild type enzyme, both I74E and I74D mutants failed to catalyze the reduction of uracil (up to 10 mM) in the presence of 0.2 mM NADH in acidic conditions. We also tested the dihydrouracil dehydrogenase activity of both mutants in the presence of up to 0.2 mM NAD<sup>+</sup> in basic conditions but could not detect any rates.

### **Characterization of the G75N and I74E/G75N Mutants**

Since our supposition that introducing a salt bridge interaction between Lys48 and a negatively charged residue would make uracil a substrate failed, we examined other interactions between substrate and protein. Besides being stabilized by the side chain of Lys48, the carboxylate group of orotate appears to be hydrogen bonded to two main chain nitrogen atoms in an “oxyanion hole-like” interaction. The main chain *N* of residues Gly75 and Leu76 are properly oriented to provide stabilization for a negatively charged oxygen (Figure 4-15 B). Curiously, this interaction is not possible in dihydropyrimidine dehydrogenase since two main chain carbonyl oxygens point towards the substrate binding site (Figure 4-15 A). Further examination of the amino acid conformations suggest that this major back bone rearrangement is accomplished by a near 180°  $\psi$  rotation of Ile74 and Gly75. To study this hypothesis, we constructed two additional mutants, Gly75Asn and the double mutant Ile74Glu/Gly75Asn.

The mutants were expressed using plasmids pYAP-12 and pYAP-13 (appendix B, Figure B-5), and both proteins could be purified as described in the previous sections. Both of these mutants were expressed at much lower levels compared to the wild type enzyme. As before, these mutants failed to catalyze the reduction of uracil (up

to 10 mM) in the presence of 0.2 mM NADH in acidic conditions. We also tested the dihydrouracil dehydrogenase activity of both mutants in the presence of up to 0.2 mM NAD<sup>+</sup> in basic conditions but could not detect any rates.

### Steady-state Kinetics and Catalytic Efficiency

Given the lack of success in our attempts to modify the active site of DHOD 1B in order to change its substrate preferences, we decided to characterize the catalytic efficiency of each of the five proteins we had successfully purified. We chose to test each enzyme's dihydroorotate dehydrogenase activity using NAD<sup>+</sup> as the electron acceptor, simulating the physiologically relevant reaction. The assays were carried out in hypoxic conditions by using the oxygen scavenging system GODCAT<sup>86</sup>. This system consumes dissolved oxygen via the oxidation of glucose, catalyzed by glucose oxidase (GOD), to yield gluconic acid and hydrogen peroxide. The hydrogen peroxide is further degraded by catalase (CAT). The initial concentration of NAD<sup>+</sup> was 110 μM for all measurements and its consumption was monitored by changes in absorption at 340 nm over 120 seconds. All assays were performed at 23 °C. Table 4-2 summarizes the results.

Table 4-2. Steady-state parameters of wild-type and mutant DHOD 1B enzymes

Enzyme	Apparent $K_m$	Apparent $k_{cat}$	$k_{cat}/K_m$
	μM	s <sup>-1</sup>	M <sup>-1</sup> s <sup>-1</sup>
Wild-type	18.1±2.3	350±14	1.9x10 <sup>7</sup>
I74D	1561±442	5.70±0.70	3.6x10 <sup>3</sup>
I74E	no reaction <sup>a</sup>	no reaction	-
G75N	429±93	8.66±0.56	2.0x10 <sup>4</sup>
I74E/G75N	ND <sup>b</sup>	-	-

<sup>[a]</sup> No reaction was detected for this enzyme.

<sup>[b]</sup> Parameters could not be determined accurately.

## Wild-type

The wild-type enzyme was clearly the most efficient catalyst with a  $k_{\text{cat}}/K_m$  value of  $1.9 \times 10^7$ . Its apparent  $K_m$  value of  $18.1 \mu\text{M}$  was the lowest measured in this study (Figure 4-16).

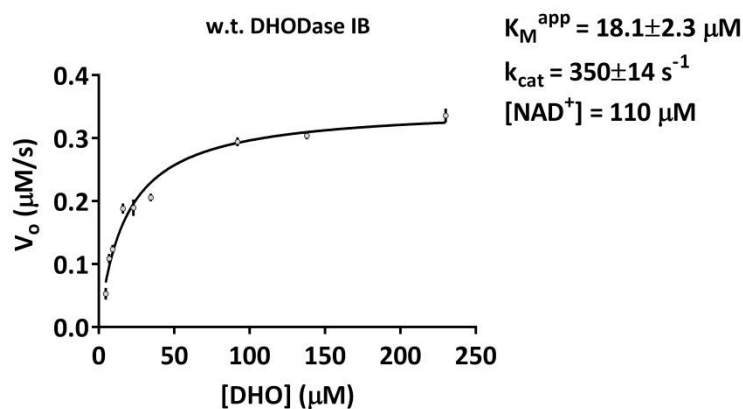


Figure 4-16. Concentration dependence of measured initial velocities  $V_o$  for w.t.

## Ile74Asp mutant

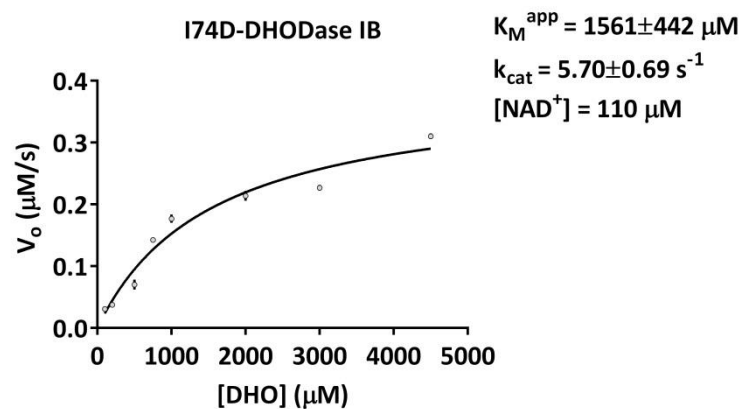


Figure 4-17. Concentration dependence of measured initial velocities  $V_o$  for the I74D mutant

Based on the results obtained, changing position 74 from Ile to Asp was very detrimental to the enzyme's overall efficiency. The  $k_{\text{cat}}/K_m$  value was decreased by a

factor of 5300. Both substrate binding ( $K_m$ ) and catalytic turnover ( $k_{cat}$ ) seemed to have been equally affected negatively by factors of 86 and 61 respectively.

### Ile74Glu mutant

This enzyme variant showed no detectable DHODase activity under the experimental conditions.

### Gly75Asn mutant

This particular mutation was originally intended to cause a shift in the enzyme's back bone in order to destabilize the binding of orotate. Accordingly, it decreased the enzyme's efficiency by a factor of 1000 which still made it the best catalyst besides the wild-type enzyme.

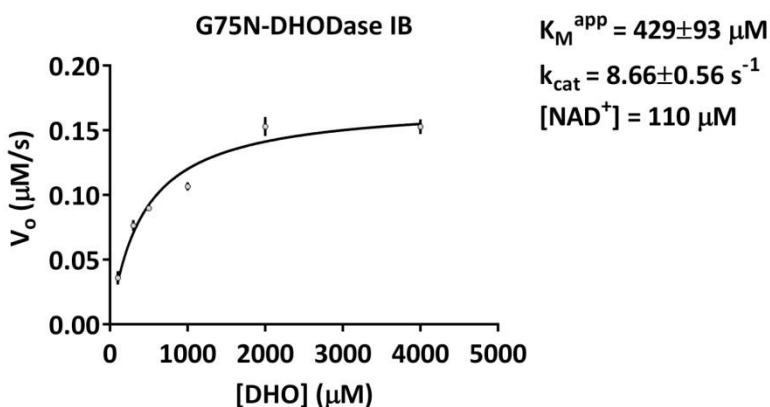


Figure 4-18. Concentration dependence of measured initial velocities  $V_o$  for the G75N mutant.

### Ile74Glu/Gly75Asn mutant

This double mutant displayed interesting behavior in that its velocity decreased with addition of substrate before saturation levels could be reached. The data obtained could not be fit confidently using classic Michaelis-Menten kinetics. The best model to explain the data, albeit a relatively poor one was that of substrate inhibition with a  $K_i$  value of ca. 207  $\mu\text{M}$ . Using a direct fit approach (GraphPad®), acceptable curve fits

could only be found if certain kinetic parameters were constrained and, while a solution was found, it was statistically no better than a mere approximation.

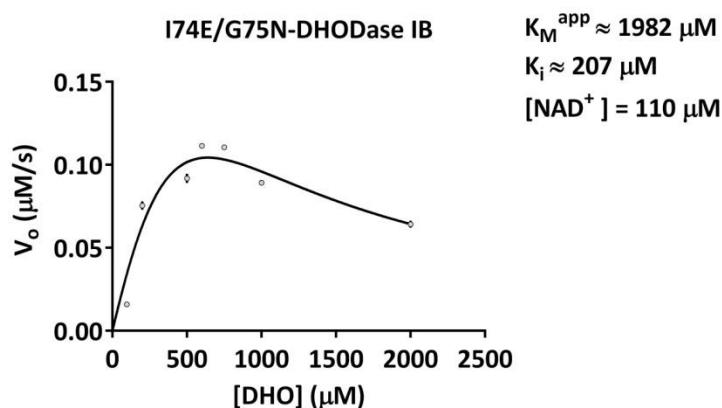


Figure 4-19. Concentration dependence of measured initial velocities  $V_o$  for the I74E/G75N double mutant.

## Residues 74 and 75 can Disrupt Electron Transfer to the $\beta$ -subunit

### Kinetic studies of oxidase reactions

From our kinetic studies it was clear that the amino acid substitutions had negative impacts on the catalytic efficiency of the enzyme. More specifically, they were detrimental to the dihydroorotate dehydrogenase of DHOD1B. One of the limitations of steady-state kinetics is the fact that the overall rate that can be measured will most closely reflect the slowest step in the mechanism. In the case of DHOD 1B the complete catalytic cycle involves several individual steps, however its activity was measured based solely on the formation of NADH, the last step of the second half-reaction (Figure 4-2).

Like many flavin-dependent enzymes, DHOD 1B can use molecular oxygen as the electron acceptor and catalyze oxidase reactions. In the case of DHOD 1B, this property of the flavin opens the possibility for alternate paths to accomplish the second

(or oxidative) half-reaction in the catalytic cycle (Figure 4-20). After completion of the first half-reaction wherein electrons are abstracted from L-dihydroorotate, electrons in the reduced FMN cofactor have two fates. They can be transferred to the FAD molecule in the  $\beta$ -subunit through the Fe-S cluster to ultimately reduce  $\text{NAD}^+$  which would constitute its dehydrogenase activity (Figure 4-20, 2a). Alternatively, electrons can be transferred directly to oxygen in an oxidase reaction.

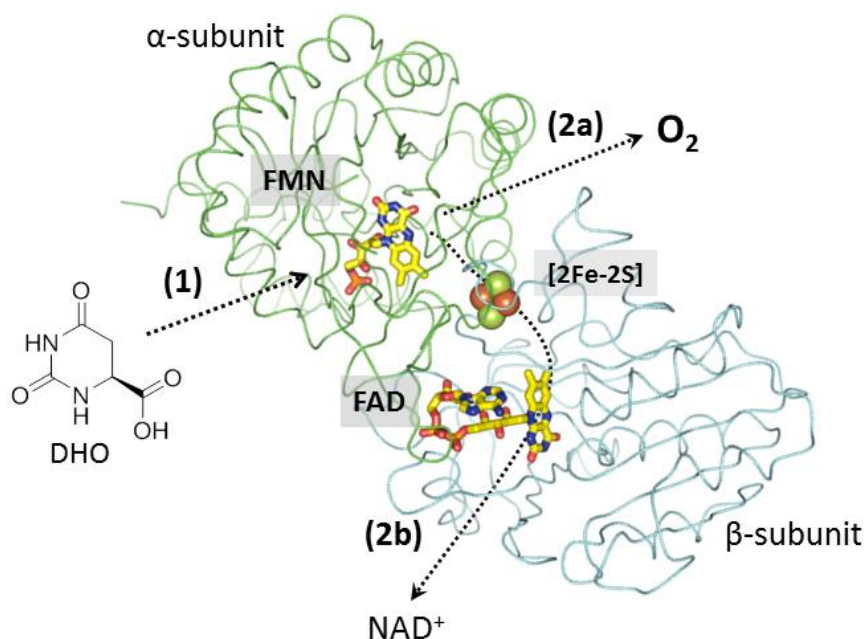


Figure 4-20. The possible fates of electrons in DHOD 1B. In the first half-reaction (1), electrons are transferred from dihydroorotate to the FMN. In the second half-reaction electrons can be accepted by molecular oxygen (2a) or by  $\text{NAD}^+$  via [2Fe-2S]-FAD (2b).

We decide to assay the oxidase activity of all the DHOD variants we generated in order to gain a better understanding of the exact role played by these amino acids. Each enzyme was allowed to react with dihydroorotate in the presence of oxygen. The reaction buffer contained no  $\text{NAD}^+$  or any other electron acceptor and reaction progress

was monitored by following the formation of orotate 278 nm. The kinetic parameters for each enzyme are summarized in Table 4-3.

Table 4-3. Steady-state parameters of wild-type and mutant DHOD 1B enzymes

Enzyme	Apparent $K_m$	Apparent $k_{cat}$	$k_{cat}/K_m$
	$\mu\text{M}$	$\text{s}^{-1}$	$\text{M}^{-1}\text{s}^{-1}$
Wild-type	$5.93 \pm 0.61$	$35.45 \pm 0.83$	$5.9 \times 10^6$
I74D	$981 \pm 123$	$42.80 \pm 2.1$	$4.3 \times 10^4$
I74E	$1793 \pm 246$	$15.7 \pm 1.1$	$8.7 \times 10^3$
G75N	$153 \pm 17$	$12.3 \pm 0.28$	$8.0 \times 10^4$
I74E/G75N	$>2000^a$	-	-

<sup>[a]</sup> This variant failed to display any saturation behavior in substrate concentrations up to 10 mM.

The wild-type enzyme is able catalyze the oxidation of dihydroorotate less efficiently in the absence of  $\text{NAD}^+$ . While the apparent  $K_m$  value was little lower, the enzyme's turnover number decrease by an order of magnitude (Figure 4-21).

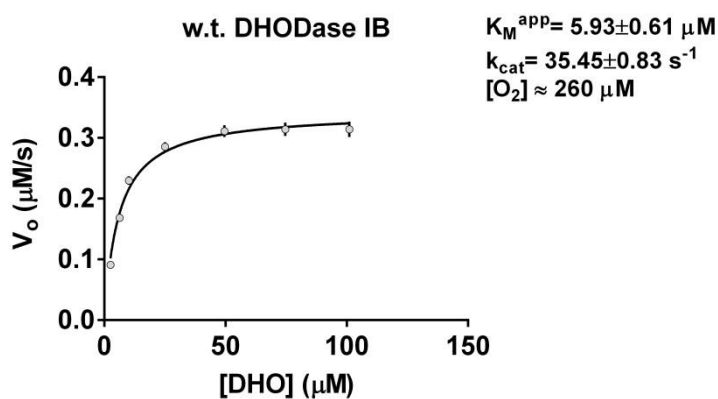


Figure 4-21. Concentration dependence of measured initial velocities  $V_o$  for wild-type DHOD1B.

The Ile74Asp mutant provided us with a surprising result. Whereas this mutation had significantly impaired its dehydrogenase activity, this was not the case for its

oxidase reaction. While the  $K_m$  value was significantly higher than the wild type enzyme, the turnover number is slightly higher at  $42.8 \text{ s}^{-1}$  (Figure 4-22).

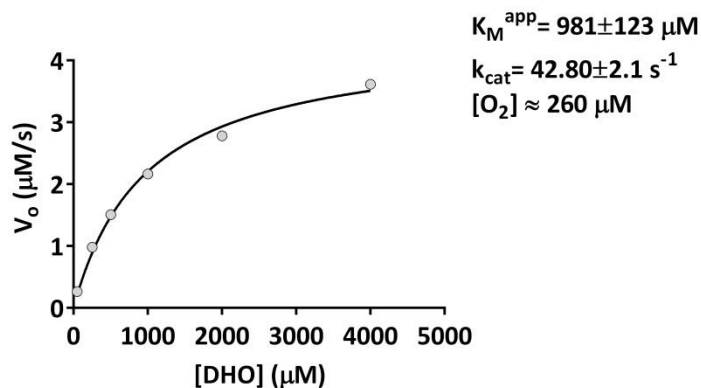


Figure 4-22. Concentration dependence of measured initial velocities  $V_o$  for the I74D mutant.

The Ile74Glu yielded an even more interesting result since it had failed to show any dehydrogenase activity but it was successful in catalyzing the oxidation of dihydroorotate in the presence of oxygen (Figure 4-23).

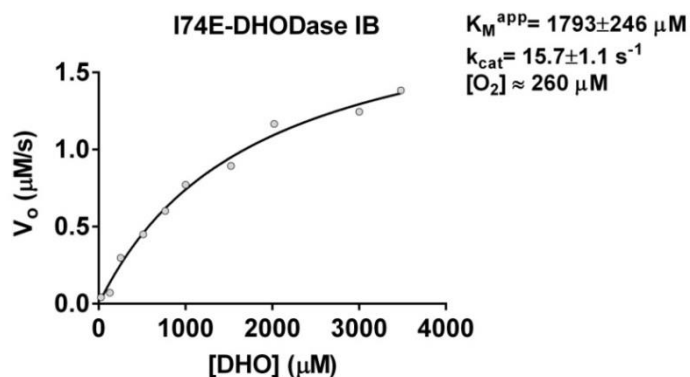


Figure 4-23. Concentration dependence of measured initial velocities  $V_o$  for the I74E mutant.

Consistent with the previous observations, the G75N variant had its apparent  $K_m$  value affected the least and was the most efficient enzyme after the wild-type. Its  $k_{\text{cat}}/K_m$  value has decreased by a factor of 7.3 which suggests that this mutation does not affect the

enzyme's oxidase activity to the same extent as seen in the dehydrogenase reaction.

(Figure 4-24)

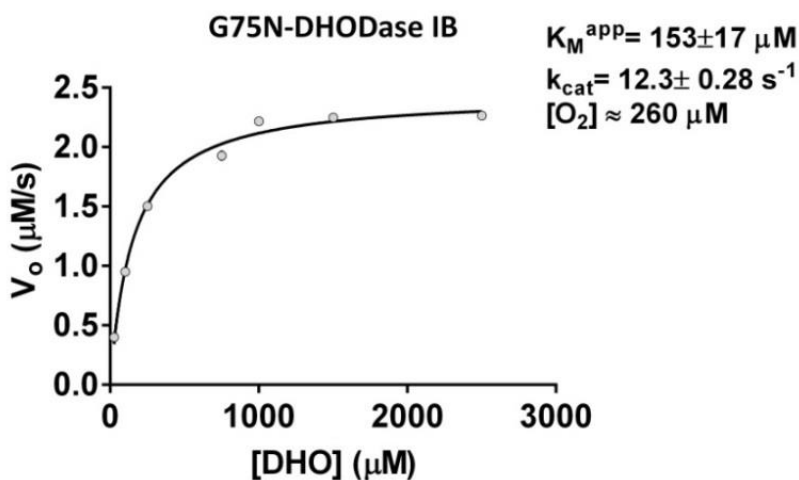


Figure 4-24. Concentration dependence of measured initial velocities  $V_o$  for the G75N mutant.

### Choosing between $\text{NAD}^+$ and oxygen: studies of uncoupling

Our kinetic investigations strongly suggest that mutations to positions 74 and 75 affect not only substrate binding but also the preference for different electron transfer pathways. It seems clear that alteration at these two residues cause the transfer of electron to  $\text{NAD}^+$  to be much less favorable while retaining its oxidase activity. In order to consolidate this notion we carried out experiments that present the enzymes with the choice of which electron acceptor they will utilize for catalysis. In other words, under strictly anaerobic conditions, for every molecule of dihydroorotate that is oxidized there will be a molecule of  $\text{NAD}^+$  that becomes reduced. However, if oxygen is allowed to enter the system this no longer must hold true. If the enzyme utilizes both oxygen and  $\text{NAD}^+$  to oxidize dihydroorotate the mole amounts of  $\text{NADH}$  and orotate will not be equal and an “uncoupling” effect will be observed.

To measure the uncoupling ability of each enzyme, we carried out two sets of experiments. First, each enzyme was forced to catalyze the oxidation of dihydroorotate in the presence of NAD<sup>+</sup> and the absence of oxygen and the formation of both products were monitored. We refer to this set-up as the “hypoxic run”. In a subsequent experiment, the same enzyme variant is mixed with the substrates NAD<sup>+</sup> and dihydroorotate, in similar fashion, but in the presence of oxygen, in the aerobic run. The formation of the products orotate and NADH is monitored and the results from the hypoxic and aerobic runs are compared.

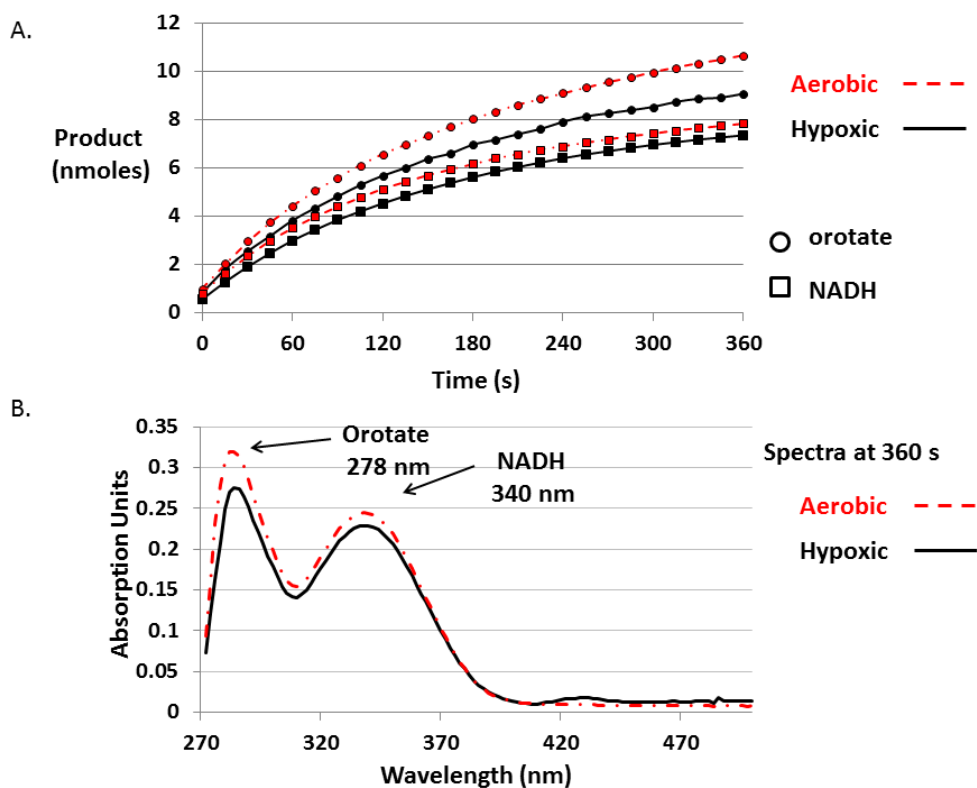


Figure 4-25. Uncoupling by wild-type DHOD 1B. A- Product formation for reaction under hypoxic (red dashed lines) and aerobic conditions (black solid lines). The formation of product is shown as circles (orotate) and squares (NADH). B- UV-Vis spectra taken at the final reaction time under hypoxic (red dashed lines) and aerobic conditions (black solid lines).

The first enzyme that we examined was wild-type DHOD 1B. As we had previously observed, this enzyme was very efficient in catalyzing the anaerobic dehydrogenation of dihydroorotate in the presence of  $\text{NAD}^+$  and, as expected, the formation of orotate and NADH were tightly coupled. They differed by only 1.7 nmoles under hypoxic conditions and the enzyme kept the tight coupling even under aerobic conditions where the difference in moles was only slightly higher, 2.6 nmoles (Figure 4-25 A). The UV-Vis spectra of the reactions taken at the final time point of 360 s further corroborated these results. The relative peak heights for orotate (278 nm) and NADH (340 nm) remained relative unchanged (Figure 4-25 B).

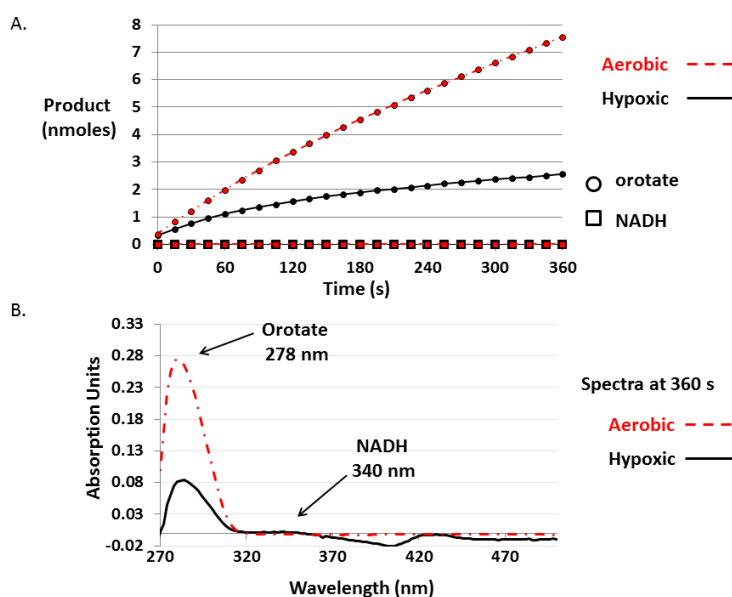


Figure 4-26. Uncoupling by I74E DHOD 1B. A-.Product formation for reaction under hypoxic (red dashed lines) and aerobic conditions (black solid lines). The formation of product is shown as circles (orotate) and squares (NADH). B- UV-Vis spectra taken at the final reaction time under hypoxic (red dashed lines) and aerobic conditions (black solid lines).

As we had seen during our steady-state studies, the Ile74Glu mutant showed no dehydrogenase activity but was fairly efficient in catalyzing the aerobic oxidation of dihydroorotate. These results were certainly validated by the nearly complete

uncoupling of orotate and NADH formation. Virtually no NADH formation could be detected under either the aerobic or hypoxic reaction conditions. The formation of approximately 2.5 nmoles of orotate was observed under hypoxic conditions and probably reflected the fact that the reaction mixture was not strictly anaerobic. Conversely, the enzyme was able to convert dihydroorotate to orotate much more efficiently in the presence of oxygen (Figure 4-26).

The two enzymes discussed so far are very different in behavior and can be thought of as polar opposites. The wild-type enzyme showed little to no tendency of utilizing oxygen as the electron acceptor, while the Ile74Glu variant used oxygen as the sole electron acceptor. The other variants exhibited behaviors that were not so binary in nature. Rather, their activities constituted a continuum that ranged from the wild-type to the Ile74Glu enzyme and are summarized in figures 4-27 through 4-29.

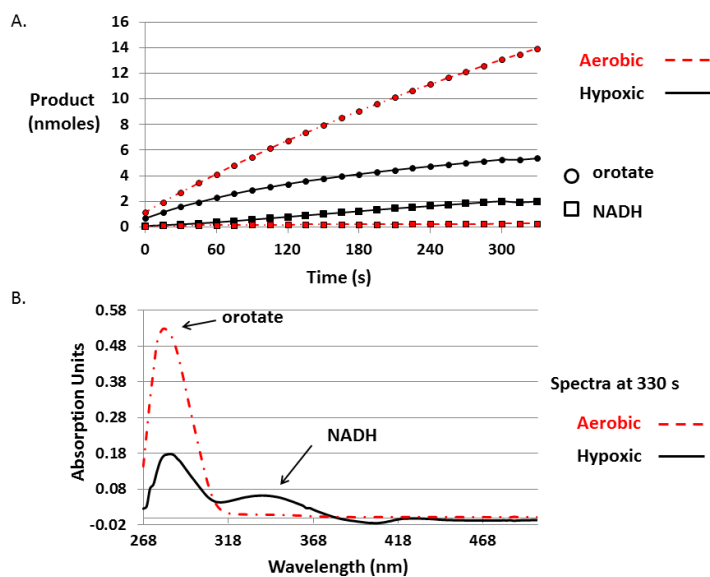


Figure 4-27. Uncoupling by I74D DHOD 1B. A-.Product formation for reaction under hypoxic (red dashed lines) and aerobic conditions (black solid lines). The formation of product is shown as circles (orotate) and squares (NADH). B-UV-Vis spectra taken at the final reaction time under hypoxic (red dashed lines) and aerobic conditions (black solid lines).

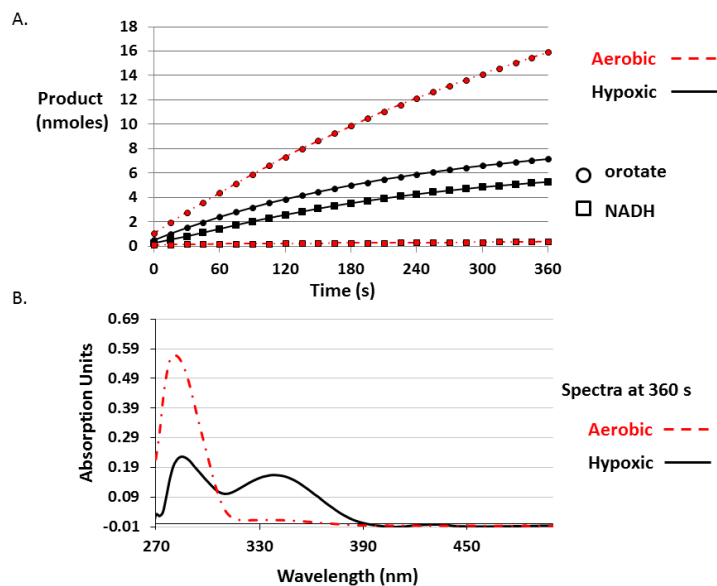


Figure 4-28. Uncoupling by G75N DHOD 1B. A-.Product formation for reaction under hypoxic (red dashed lines) and aerobic conditions (black solid lines). The formation of product is shown as circles (orotate) and squares (NADH). B- UV-Vis spectra taken at the final reaction time under hypoxic (red dashed lines) and aerobic conditions (black solid lines).

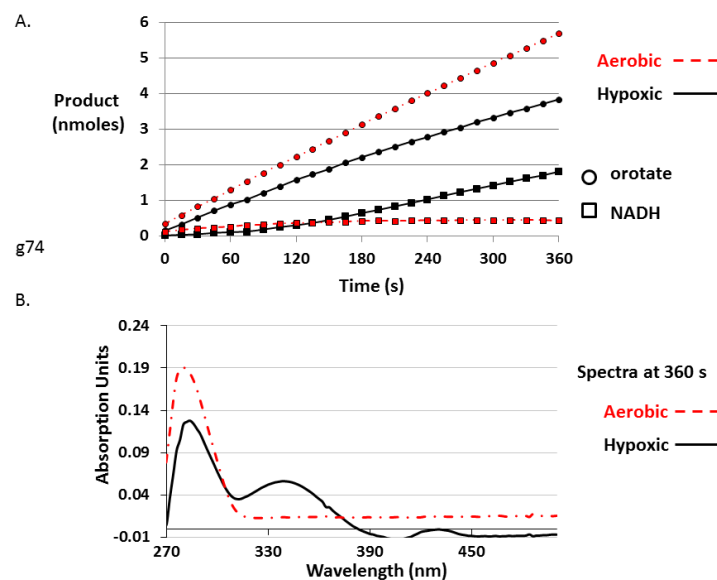


Figure 4-29. Uncoupling by I74E/G75N DHOD 1B. A-.Product formation for reaction under hypoxic (red dashed lines) and aerobic conditions (black solid lines). The formation of product is shown as circles (orotate) and squares (NADH). B- UV-Vis spectra taken at the final reaction time under hypoxic (red dashed lines) and aerobic conditions (black solid lines).

## Conclusion and Future Directions

In our search for enzymes that could function as alkene reductases and expand our collection of biocatalysts and their substrate panel, we cloned and over-expressed two dihydroorotate dehydrogenases from *Lactococcus lactis* CV56. The type 1B enzyme seemed to be the more suitable candidate due to its ability to accept electrons directly from NADH to carry out the reduction of the C-C double of orotate. We therefore purified it to homogeneity and solved its crystal structure in complex with orotate. In an attempt to change the enzyme's substrate specificity we designed four mutants, I74D, I74E, G75N and a double mutant I74D/G75N. These variants showed no tolerance towards the substrate uracil which lacks a carboxyl group present in orotate. Next we used steady state kinetics to characterize the catalytic efficiency of each DHOD 1B variant. Since all of the mutations seemed to have largely detrimental effects on the dehydrogenase activity of the enzyme, we took on the investigation of the "dihydroorotate oxidase" activity of these proteins. Interestingly, while binding of the substrate was largely affected as well, the mutations did not show the same negative effect on the enzyme's catalytic efficiency and all turnover numbers were close in magnitude. Additionally, we showed that these mutations largely impacted the electron-transfer rates to NAD<sup>+</sup>. Rather, under aerobic conditions, most of the electrons are transferred to oxygen.

Since the  $\beta$ -subunit, or *pyrZ* protein, contains the [2Fe-2S] cluster and its structure is closely related to other NAD binding enzymes, formation of NADH is most likely to happen through this subunit. Furthermore, Nielsen *et al.* had showed that the absence of the  $\beta$ -subunit did not affect electron transfer to oxygen but was necessary for the formation of NADH<sup>73</sup>. Based on these observations and the results we obtained

in this study, we suggest that residues Ile74 and Gly75 are important not only for substrate binding, but are crucial for electron transfer from the  $\alpha$ -subunit (*pyrD*) to the  $\beta$ -subunit (*pyrZ*). In fact, the Ile74Glu mutant seems to completely block electrons from reaching the  $\beta$ -subunit which results in loss of its dehydrogenase activity while retaining most of its oxidase activity. Each of the five DHOD 1B proteins we investigated had slightly different catalytic properties. In addition, each mutation had effects on the efficiency of the enzyme's dehydrogenase activity which were not the same for the oxidase activity. Table 4-4 summarizes the catalytic properties of each of the mutants.

Table 4-4. Catalytic Properties of WT and DHOD 1B mutants.

Enzyme	Dehydrogenase $k_{cat}$ $s^{-1}$	Oxidase $k_{cat}$ $s^{-1}$	Coupling Efficiency
Wild-type	350±14	35.45±0.83	0.91
I74D	5.70±0.70	42.80±2.1	0.05
I74E	-	15.7±1.1	0
G75N	8.66±0.56	12.3±0.28	0.03
I74E/G75N	-	-	0.16

Using the data from our “uncoupling” studies, we determined the preference of each enzyme for  $NAD^+$  over oxygen as the electron acceptor, termed “coupling efficiency” C.E. This term was calculated using the following equation:

$$C.E. = \frac{Orot/NADH}{Orot'/NADH'}$$

Where  $Orot$  and  $NADH$  are the number of moles formed, under hypoxic conditions, of orotate and NADH respectively.  $Orot'$  and  $NADH'$  are the number of moles formed, under aerobic conditions, of orotate and NADH respectively.

Our results show that mutations of positions 74 and 75 can decrease the “coupling efficiency” of DHOD1B from 0.91 in wild-type to zero in the Ile74Glu mutant. Put differently, the wild-type enzyme strongly prefers to utilize  $NAD^+$  as the electron acceptor while the Ile74Glu mutant could only use oxygen. This striking result prompted us to rationalize the possible mechanism by which this change was taking place.

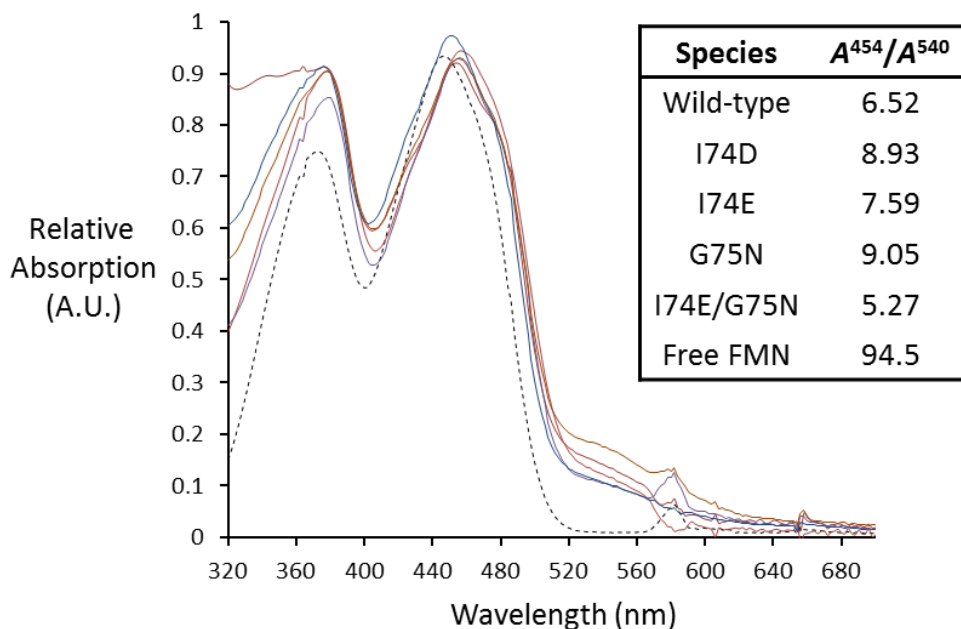


Figure 4-30. Absorption spectra of the five DHOD 1B enzymes studied. Solid lines represent the enzymes and the dashed line shows the spectrum of free FMN. The inset shows the ratio of absorbance at 454/540 nm.

The simplest explanation for the poor ability of some mutants to transfer electrons to the NAD binding domain could be that mutants failed to express this

domain altogether. However based on the physical properties of the mutants and their size according to gel filtration experiments, we have no reason to believe that this is an important factor. Additionally, because of how the proteins were constructed for purification, if the  $\beta$ -subunit had not been expressed, the protein could not have been purified successfully using metal affinity chromatography and this theory is supported by SDS-PAGE experiment (see experimental procedures). Another plausible explanation is that the mutant enzymes do not form/bind the iron sulfur cluster which is essential for inter-subunit electron transfer. To test this, we collected UV-Vis absorption spectra of all enzymes since each cofactor has characteristic peaks. The FMN and FAD cofactor have strong peaks *ca.* 450 nm while the Fe-S cluster shows a broad band near 540 nm. The spectra suggest that all of the enzymes have successfully complexed the iron-sulfur cluster, at least to an appreciable extent as shown by the ratio  $Abs^{454}/Abs^{540}$  (Figure 4-30).

Since all of the enzymes appeared to be structurally sound, we focused our attention on the structure of the active site of DHOD 1B in order to rationalize the results obtained. In our crystal structure, Ile74 is positioned close to both the dimethyl benzene moiety of the FMN cofactor and the bound orotate (Figure 4-15 B). Initially we had focused our attention on the possible interactions between this residue, Lys48 and the substrate. One important detail that was overlooked is the fact that this Ile 74 is also in close proximity of the Fe-S cluster in the neighboring  $\beta$ -subunit.

Several factors suggest that the exact position of this residue seem critical in regulating the reactivity of the FMN and the redox center. First Ile74 is positioned right

in between the FMN and Fe-S cluster, at the interface of the  $\alpha$ - and the  $\beta$ -subunit (Figure 4-31 A).

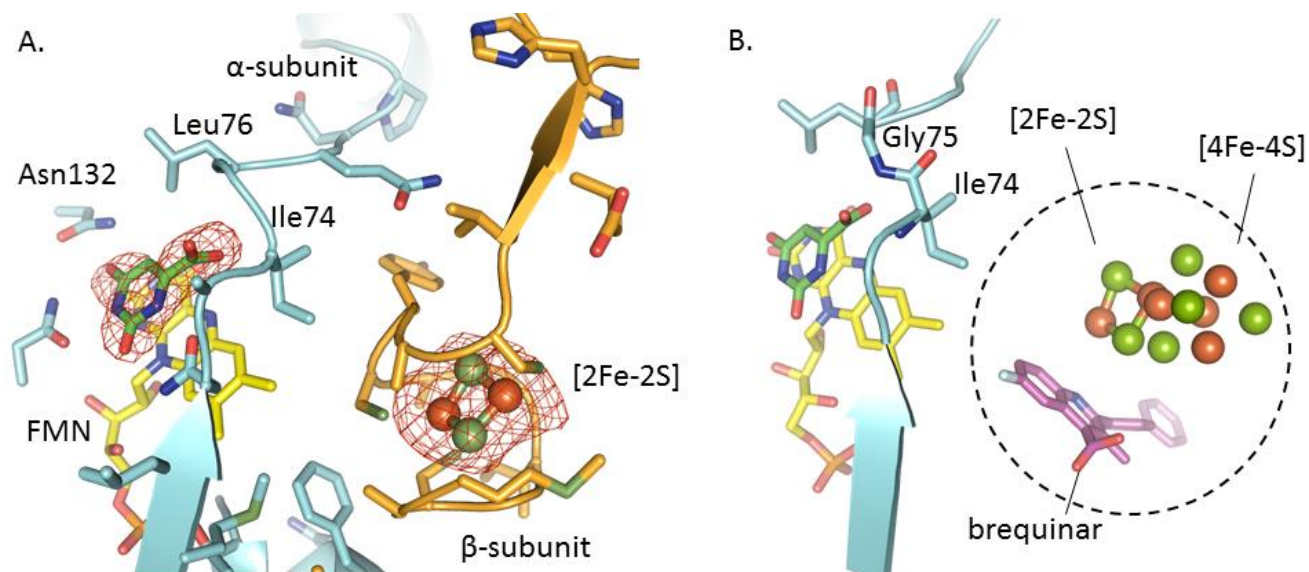


Figure 4-31. A- The subunit interface region in DHOD 1B. Residues in the  $\alpha$ -subunit are shown in cyan carbons while those in the  $\beta$ -subunit are in orange carbons. The red mesh shows the omit  $mF_o-DF_c$  electron density map contoured at  $3\sigma$  around orotate and the  $2Fe-2S$  cluster. B- The preferred region (dashed circle) for electron transfer from the FMN in DPD, DHOD 1B and DHOD 2.

Although this residue is not strictly conserved across DHOD enzymes, it is almost always a hydrophobic residue. It is conserved in the DHOD B subgroup; it is a methionine DHOD A subgroup, and it is generally tyrosine, methionine, or cysteine in family 2 enzymes. It had been previously hypothesized that the nature of this side chain is probably important in defining the environment of the dimethylbenzene part of the flavin isoalloxazine ring, rather than in binding the substrate<sup>77</sup>. Our results suggest otherwise and the nature of this residue can impact not only substrate binding but also electron transfer. One curious observation is the fact that there seems to be a geometric preference for electron transfer reactions between the FMN and other electron acceptors.

In the case of DHOD 1B, the 2Fe-2S redox center is held by the  $\beta$ -subunit directly behind the dimethylbenzene ring of the FMN. In DPD, the [4Fe-4S] is held in place by an adjacent monomer, nonetheless, it is located in a very similar position relative to the FMN cofactor. In the membrane associated family 2 enzyme, such as humanDHOD, there is no external redox center. Rather, this enzyme utilizes membrane bound quinone as the electron acceptor. Curiously, in the crystal structure of human DHOD in complex with the immunosuppressant/anticancer drug brequinar, the drug binds in a long cleft formed by two N-terminal  $\alpha$ -helices that are unique to family 2 enzymes. Here again the position of the drug is very close to those observed in the enzymes that contain other electron transfer cofactor (figure 4-31 B). This “conserved” arrangement suggests the existence of an optimal location for electron transfer to and from the FMN. We hypothesize that our mutations to positions 74 and 75 could cause disturbances to this spatial arrangement which would lead to poor electron transfer efficiencies across the  $\alpha$ - and  $\beta$ -subunits.

Our hypothesis seems to offer an explanation for how the mutations could impair electron transfer. The decreased dehydrogenase activity is likely due to mutations making electron-transfer to the  $\beta$ -subunit less favorable, and since electrons can be transferred to oxygen within the  $\alpha$ -subunit oxidase activity was retained. However, one question remains unanswered. How can the wild type so efficiently transfer electrons to NAD<sup>+</sup> even in the presence of oxygen? The I74D mutant seems to have slightly higher oxidase activity suggesting that not only does the wild type enzyme prefer NAD<sup>+</sup> but also curbs oxidase activity. The answer to this question is not trivial, unfortunately. The exact factors that regulate flavin reactivity towards oxygen and other reactive oxygen

species (ROS) is still not fully understood. It seems that different enzymes can tune the flavin reactivity in different manners and no real consensus is observed. Despite the apparent complexity of the flavin reactivity control, some factors seem to be more recurrent. Mattevi suggests that the polarity and solvation of the flavin binding site environment can largely affect its reactivity through stabilization of the superoxide anion<sup>87</sup>. It seems therefore possible that a mutation such as Ile74Asp can exert its effect through a change in active site polarity.

Future work should focus towards obtaining crystal structures of each mutant in order to evaluate how the substitutions can perturb the environment around the enzymes redox centers. Also more systematic mutagenesis studies are likely to shed light onto electron transfer mechanism not only in DHOD 1B but in a general sense.

## Experimental Procedures

### Site-Directed Mutagenesis

All mutants used for were generated by PCR using primers with the desired mutation at position 74 or 75 in a modification of the method published by Zheng *et al.*<sup>41</sup>. Table 4-5 lists the primers used in this study. G75N\* indicates that the template used was pYAP-9 which already contained the I74E mutation.

Table 4-5. Mutagenic primers utilized for constructing the mutant enzymes.

Mutation	Primer Sequence
I74E <i>fwd</i>	5'-TGC TTA ATG CA GAA G GAC TAC AAA ATC CAG GAT TAG AAG T-3'
I74E <i>rev</i>	5'-TTT TGT AGT CC TTC T GCA TTA AGC ATG CCG CTC GCT VTT T-3'
I74D <i>fwd</i>	5'-TGC TTA ATG CA GAT G GAC TAC AAA ATC CAG GAT TAG AAG T -3'
I74D <i>rev</i>	5'- TTT TGT AGT CC ATC T GCA TTA AGC ATG CCG CTC GCT VTT T -3'
G75N <i>fwd</i>	5'- TT AAT GCA ATT AAT CTA CAA AAT CCA GGA TTA GAA GTT AT-3'
G75N <i>rev</i>	5'-GG ATT TTG TAG ATT AAT TGC ATT AAG CAT GCC GCT CGC TG-3'
G75N* <i>fwd</i>	5'- TT AAT GCA GAA AAT CTA CAA AAT CCA GGA TTA GAA GTT AT -3'
G75N* <i>rev</i>	5'- GG ATT TTG TAG ATT TTC TGC ATT AAG CAT GCC GCT CGC TG -3'

The shaded letters indicate the mutagenic codons.

Each PCR reaction (total volume 100  $\mu$ L) containing 5  $\times$  Phusion HF Buffer (20  $\mu$ L), pYAP-6 (Appendix B Figure B-4) (20 ng), forward and reverse primers (0.5  $\mu$ M each), dNTPs (200  $\mu$ M each), and Phusion Hot Start II High-Fidelity DNA Polymerase (1 U) was subjected to an initial denaturation step of 98  $^{\circ}$ C (30 s) followed by 25 cycles of 98  $^{\circ}$ C (10 s) and 72  $^{\circ}$ C (4 min) followed by a final incubation at 72 $^{\circ}$ C (7 min). Amplicons were purified by DNA spin columns, digested with *DpnI* at 37 $^{\circ}$ C (10 U for 4 h followed by an additional 10 U for 4 h) then purified by an additional DNA spin column. Aliquots (5  $\mu$ L) were used to transform *E. coli* JM109 (75  $\mu$ L) by electroporation. SOC medium was added (600  $\mu$ L), then the samples were incubated for 1 h at 37  $^{\circ}$ C prior to selection on LB medium supplemented with ampicillin. Plasmid DNA purified (spin columns) from randomly-chosen colonies was analyzed by DNA sequencing to identify the desired DHOD 1B variants.

### **Protein Expression and Purification**

Plasmids were transformed into *E. coli* BL21-Gold (DE3) cells and grown in TB broth supplemented with and 200  $\mu$ g/mL ampicillin. Cultures were induced by addition of 0.4 mM isopropyl- $\beta$ - thiogalactoside (IPTG) when the optical density Abs600 reached 2.0. At this point, the growth was supplemented with 1mM cysteine, 0.1 mg/mL ferrous sulfate and 0.1 mg/mL ferric citrate. The temperature was decreased to 30 $^{\circ}$ C during protein expression. Cells were harvested after 16 hours at a density of approximately 12 g/L. Cells were then pelleted by centrifugation at 5350 x g for 10 minutes and pellet resuspended to a density of 1g/mL in 50 mM NaP<sub>i</sub> pH 6.0, 10% glycerol containing 10 $\mu$ M phenylmethanesulfonyl fluoride (PMSF). All of the subsequent steps were performed at 4  $^{\circ}$ C. The resuspended cells were lysed at 15,000 psi using a Carver

laboratory press. Lysed cells had debris removed by centrifugation at 20,000 x g for 1 hour. Protamine sulfate (1 mg/mL) was added and nucleic acids were removed by centrifugation at 10,000 x g for 15 min. For the purification step an NTA-resin that had been pre-loaded with 100 mM nickel sulfate and equilibrated with 50 mM NaP<sub>i</sub> pH 6.0, 10% glycerol, 40 mM imidazole using a Pharmacia® FPLC system. Cell extract was loaded onto the column and it was washed with buffer until the absorbance at 280 nm became stable at approximately 0.1 A.U. For elution, the column was washed with 3 column-volumes of the same buffer supplemented with 500 mM imidazole. Enzyme was collected in approximately 10 mL. Fractions were pooled and concentrated by centrifugation using a 10,000 MWCO membrane. For regeneration of the affinity matrix, the column was washed with 3 volumes of buffer containing 50 mM. To remove the His-tag, protein was incubated with thrombin (1:1000 mass ratio) after all imidazole had been removed by dialysis. The protein mixture was then centrifuged again and reapplied onto the nickel chelating resin and the flow through contained DHOD 1B. Figure 4-30 shows SDS-PAGE analysis of all of the DHOD proteins purified in this study. For crystallography, the flow-through was concentrated and the purified protein was then loaded onto a Superdex 200 HR 10-30 (Pharmacia) for further purification. The column was equilibrated with low ionic strength buffer, 50 mM NaP<sub>i</sub>, 10% glycerol pH 6.0. Only the major peak at 280 nm was collected. Proteins were concentrated to >2 mg/mL and could be stored in 50% glycerol at -20 °C. For crystallization trials the wild-type protein was concentrated to 22 mg/mL and utilized without freezing.

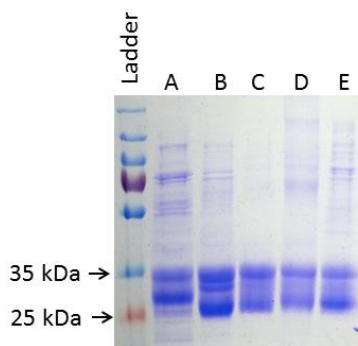


Figure 4-32. SDS-PAGE analysis of all DHOD 1B enzymes purified in this study. Lane A, wild-type; lane B, I74E; lane C, I74D; lane D, G75N; lane E, I74E/G75N mutant. The theoretical molecular weight is 32.2 kDa for the  $\alpha$ -subunit and 28.8 kDa for the  $\beta$ -subunit.

### Crystallographic Studies

A protein solution of ca. 22 mg/mL DHOD 1B in 50 mM NaP<sub>i</sub> pH 6.0, 10% v/v glycerol was used in screening for crystallization conditions. In 96 well crystallization plates, 1  $\mu$ L of protein solution was mixed with an equal volume of 96 unique crystallization buffers (Classics II Suite, Qiagen). This procedure was repeated using a different set of crystallization conditions (PEGRx, Hampton). The most promising results appeared in low pH buffers with low-to-medium molecular weight PEGs as precipitant with the most promising condition being 0.1 M sodium acetate pH 4.0, PEG 4,000 12% w/v. Crystals appeared very quickly (<1 hr) and seemed to be made of various thin layers. Unfortunately these crystals could not be utilized for structure solution as they were highly mosaic and appeared to contain multiple poorly define lattices that could not be indexed. As this condition proved recalcitrant to optimization, a screening kit containing 96 unique additives was used in combination with the original crystallization buffer. Finally, the best crystals were grown using the hanging drop vapor diffusion method on silanized glass covers from 0.1 M sodium acetate pH 4.0, PEG 4,000 12% w/v supplemented with 3% v/v glycerol. These crystallization conditions were not ideal

for cryo-crystallography and data collected at 100 K varied significantly in quality and an ideal cryo-protection protocol could not be readily indentified. A more systematic investigation showed that the best diffraction data were obtained when crystals were mounted for data collection in the mother liquor at room temperature (figures 4-10 and 4-11).

### **Structure Solution**

X-ray data were processed using and iMOSFLM<sup>42-43</sup>. The structure of *L. lactis* CV56 DHOD 1B was solved by molecular replacement using AUTOMR in the PHENIX suite<sup>44</sup>. The search used a high resolution model of *L. lactis* DHOD 1B (PDB code 1EP3). The initial search model was devoid of water molecules and any ligands. Inspection of the electron density maps was followed by manual rebuilding, addition of ordered waters and refinement of each model's coordinates and temperature factors against the X-ray data. During refinement, inspection of the calculated 2mFo-DFc and mFo-DFc difference maps showed clear positive electron density for the ligand orotate as well as the cofactors FMN, FAD and 2Fe-2S. This allowed for building of the missing side chains and unambiguous placement of all ligands. This process was performed iteratively until residuals errors  $R_{\text{work}}$  and  $R_{\text{free}}$  converged. The complete crystallographic parameters, data collection and refinement statistics can be found in Results and Discussion.

### **Steady-State Kinetics**

Enzyme solutions were quantified using a specific absorption coefficient  $A^{452}$  of  $0.6 \text{ mg}^{-1} \text{ mL}^{-1}$ <sup>73</sup>. Enzyme concentrations were 1 nM for wild-type, 20 nM for G75N, 65 nM for I74E, 68 nM for I74D and 125 nM for the I74E/G75N variant. Reactions were assayed using a 1 cm quartz cuvette at 23 °C in 100 mM  $\text{KP}_i$  pH 7.5, 2 mM L-cysteine,

10 mM glucose, glucose oxidase 5 U/mL, catalase 2 U/mL and the total reaction volume was 1 mL. Reactions were pre-incubated for 2 min and initiated by addition of dihydroorotate. The initial concentration of NAD<sup>+</sup> was 110 μM and initial velocities were measured for 60-120 seconds by monitoring the formation of NADH at 340 nm. The data were fitted using the software GraphPad ®. For oxidase activity measurements, the buffer was vigorously stirred prior to data collection to ensure oxygen concentration reached the atmospheric concentration of 260 μM. The total reaction volume was 200 μL and initial velocities were measured for 60-120 seconds by monitoring the formation of orotate at 278 nm.

## APPENDIX A SELECTED GC-MS DATA

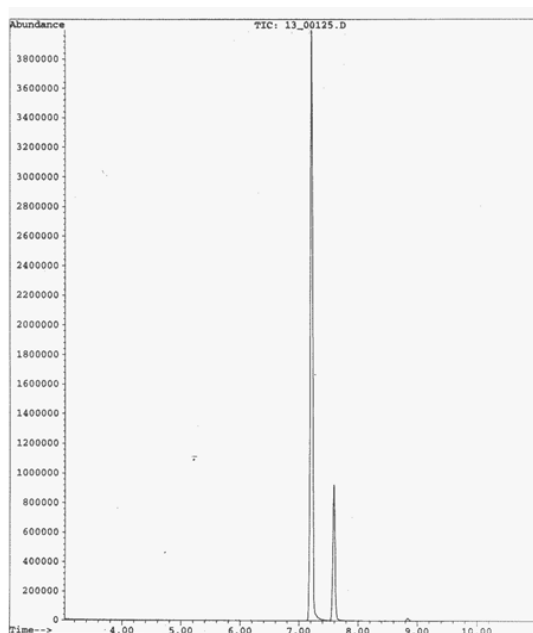


Figure A-1. Authentic standard (Acros) of (+)-dihydrocarvone containing a mixture of isomers. The peak at 7.2 min is *trans*-(2*R*,5*R*)-dihydrocarvone present at 80%. The peak at 7.6 min is *cis*-(2*S*,5*R*)-dihydrocarvone present at 20%.

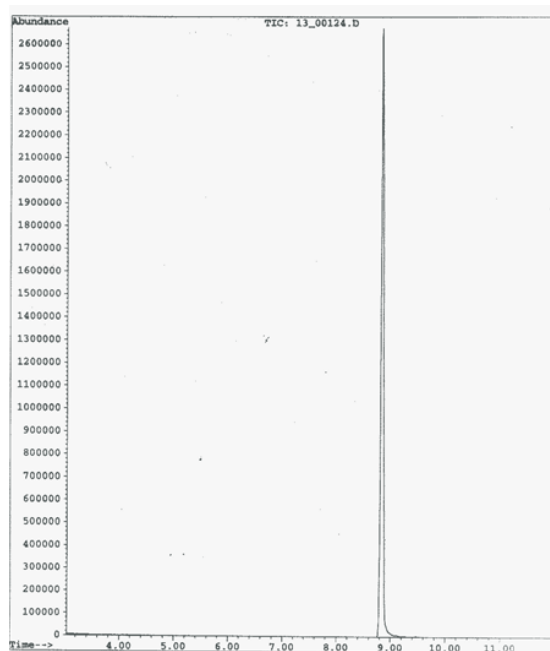


Figure A-2. Chromatogram of authentic sample of (*R*)-carvone (Acros Organics). The peak has retention time of 8.8 min. Because of the non-chiral nature of the stationary phase, (*S*)-carvone had the same retention time.

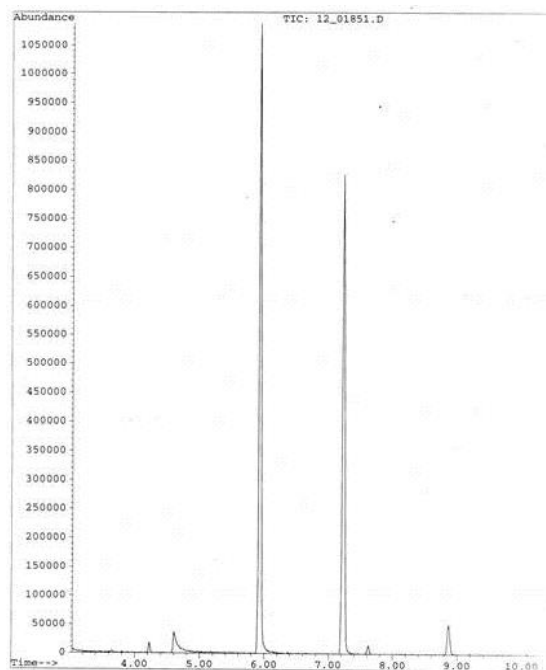


Figure A-3. GC-MS analysis of OYE1 catalyzed (*R*)-carvone reduction. Peak identities: 6.0 min, methyl benzoate (standard); 7.2 min, *trans*-(2*R*,5*R*)-dihydrocarvone; 7.6 min *cis*-(2*S*,5*R*)-dihydrocarvone; 8.8 min, (*R*)-carvone.

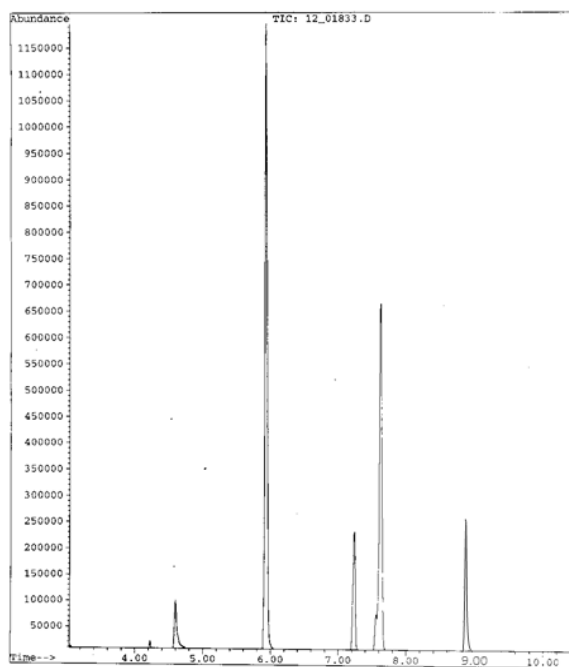


Figure A-4. GC-MS analysis of W116A-OYE1 catalyzed (*R*)-carvone reduction. Peak identity: 6.0 min, methyl benzoate (standard); 7.2 min, *trans*-(2*R*,5*R*)-dihydrocarvone; 7.6 min *cis*-(2*S*,5*R*)-dihydrocarvone; 8.8 min, (*R*)-carvone.

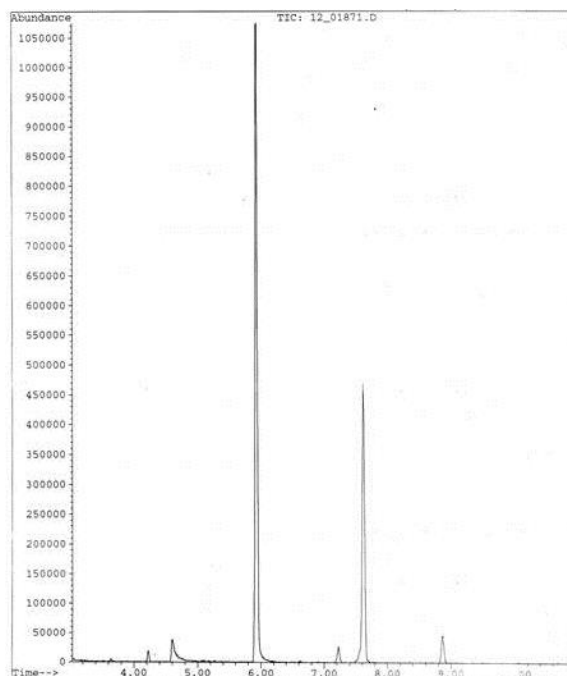


Figure A-5. GC-MS analysis of OYE1 catalyzed (*S*)-carvone reduction. Peak identity: 6.0 min, methyl benzoate (standard); 7.2 min, trans-(2*S*,5*S*)-dihydrocarvone; 7.6 min cis-(2*R*,5*S*)dihydrocarvone; 8.8 min, (*S*)-carvone.

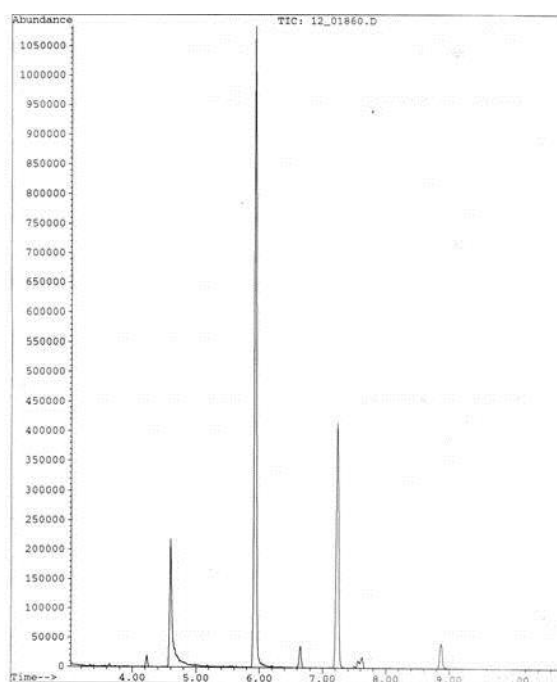


Figure A-6. GC-MS analysis of W116I- OYE1 catalyzed (*S*)-carvone reduction. Peak identity: 6.0 min, methyl benzoate (standard); 7.2 min, trans-(2*S*,5*S*)-dihydrocarvone; 7.6 min cis-(2*R*,5*S*)dihydrocarvone; 8.8 min, (*S*)-carvone.

APPENDIX B  
PLASMID CONSTRUCTS USED

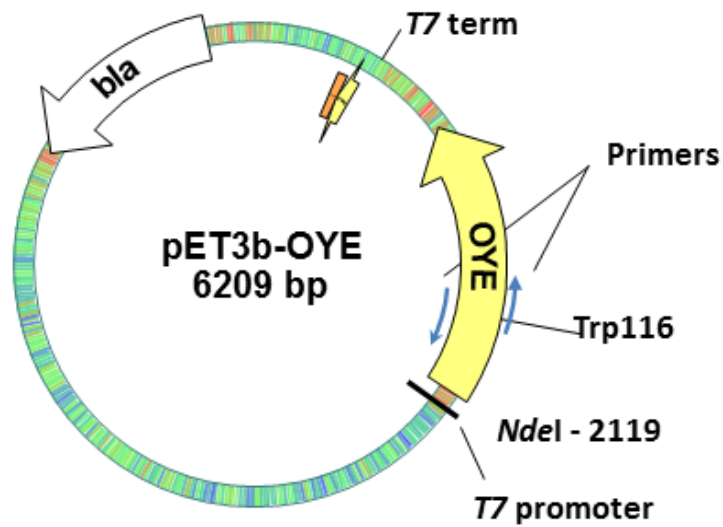


Figure B-1. Plasmid map of all pET-OYE-W116X used for structural studies. Small arrows indicate location of the mutagenic primers used.

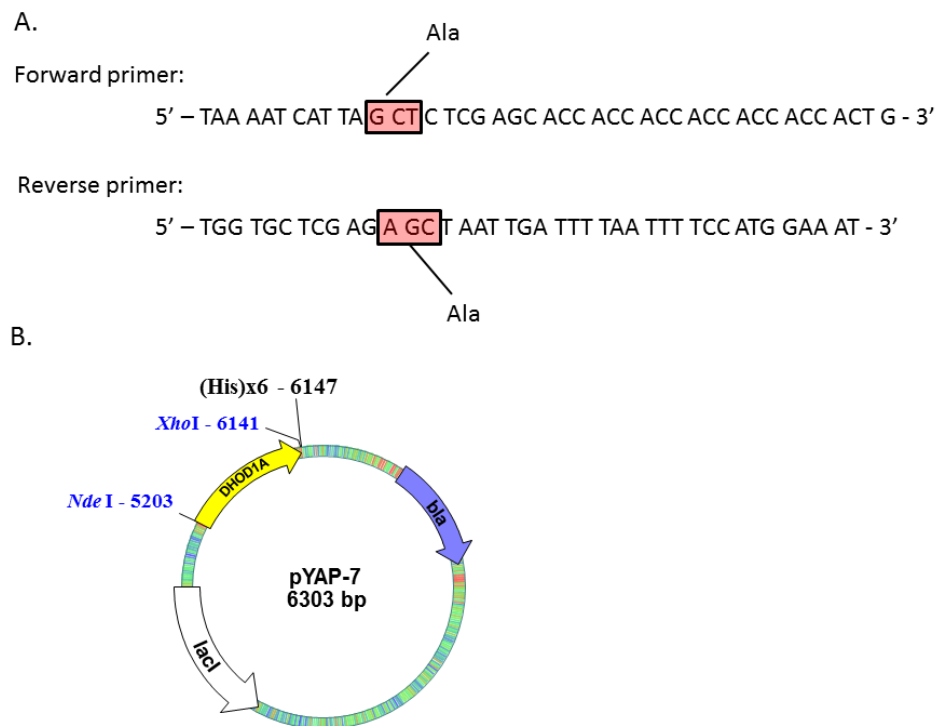


Figure B-2. Plasmid construct of pYAP-7. DHOD 1A with C-terminal His-tag.

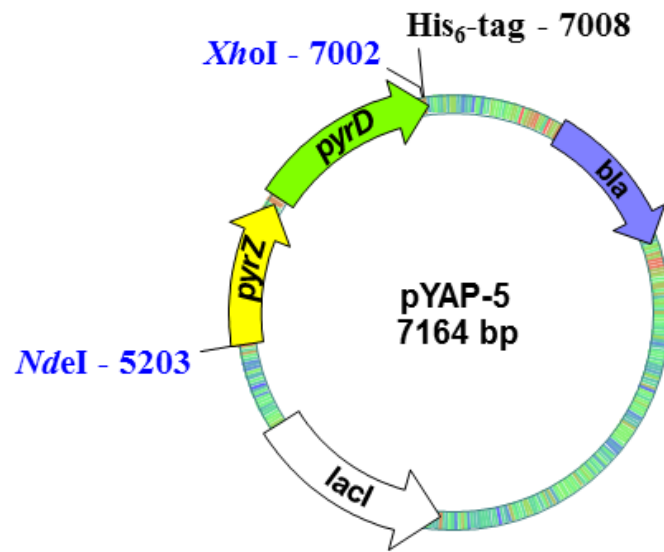


Figure B-3. pYAP-5 encodes pyrD with C-terminal His-tag.

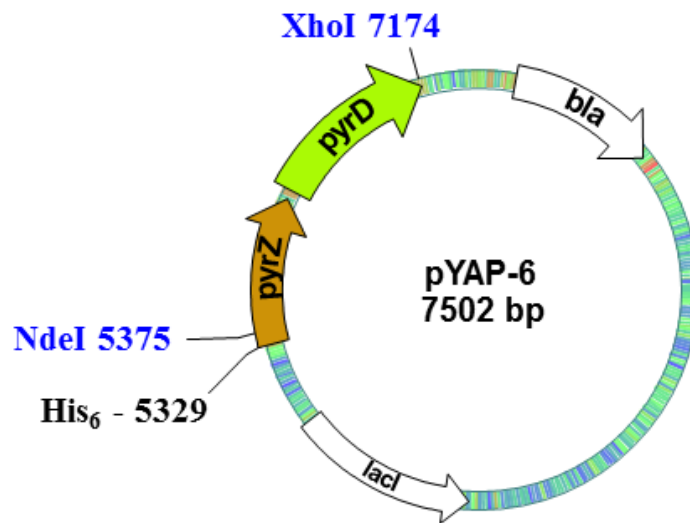


Figure B-4. pYAP-6 encodes pyrZ with N-terminal His-tag.

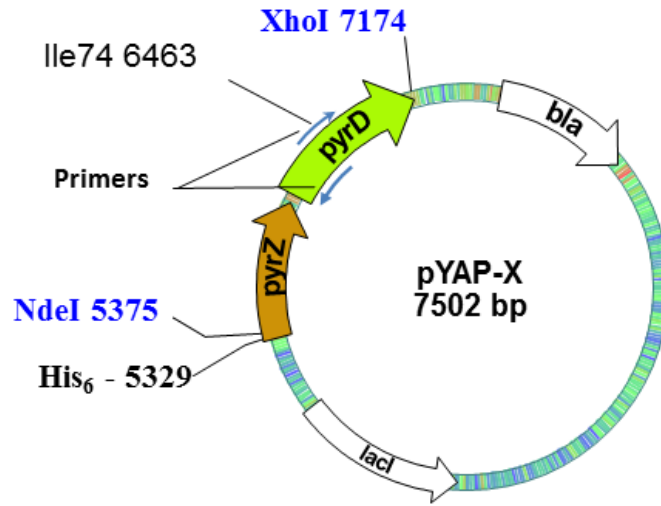


Figure B-5. Basic plasmid construct for pYAP-8, pYAP-9, pYAP-12 and pYAP-13. Each mutant was created using primers listed in Table 4-4.

APPENDIX C  
PURIFIED OYE1 SDS-PAGE ANALYSIS

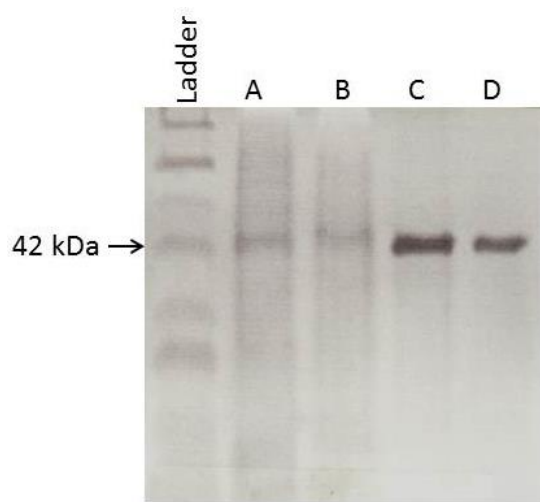


Figure C-1. Typical purity of OYE1 enzymes used for X-ray crystallography. Lanes A,B- Samples after affinity chromatography. Lanes C,D- Samples after following size exclusion chromatography with Superdex 200.

APPENDIX D  
GEL FILTRATION OF PROTEIN LADDER AND LINEAR REGRESSION

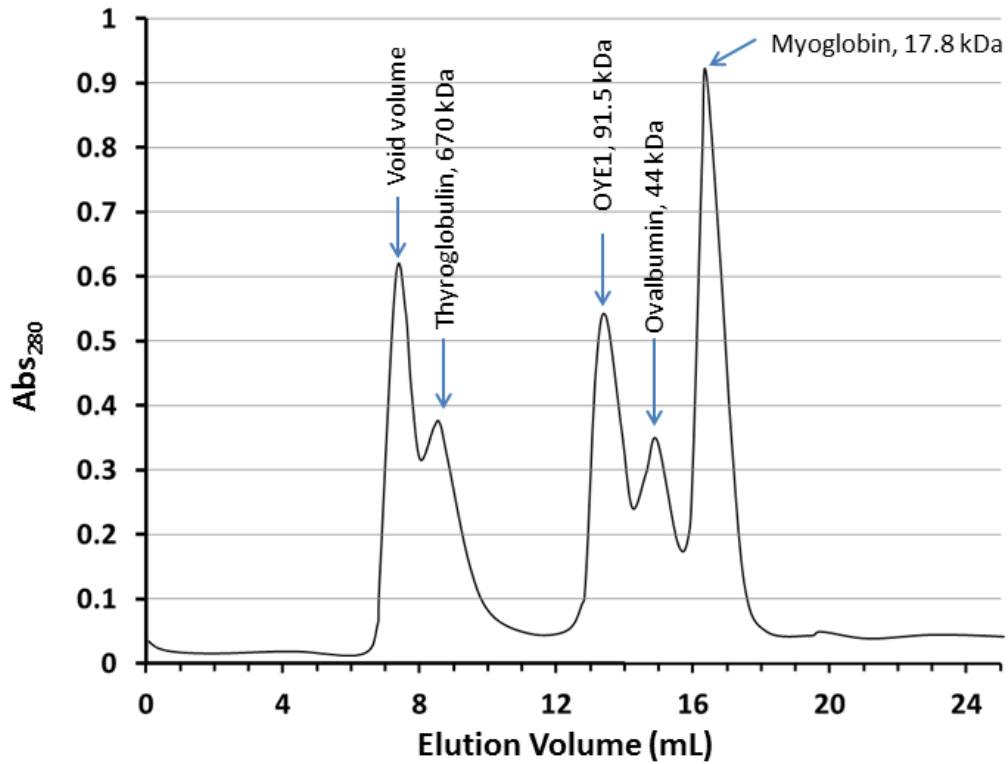


Figure D-1. Elution profile of the protein standards used for calibration.

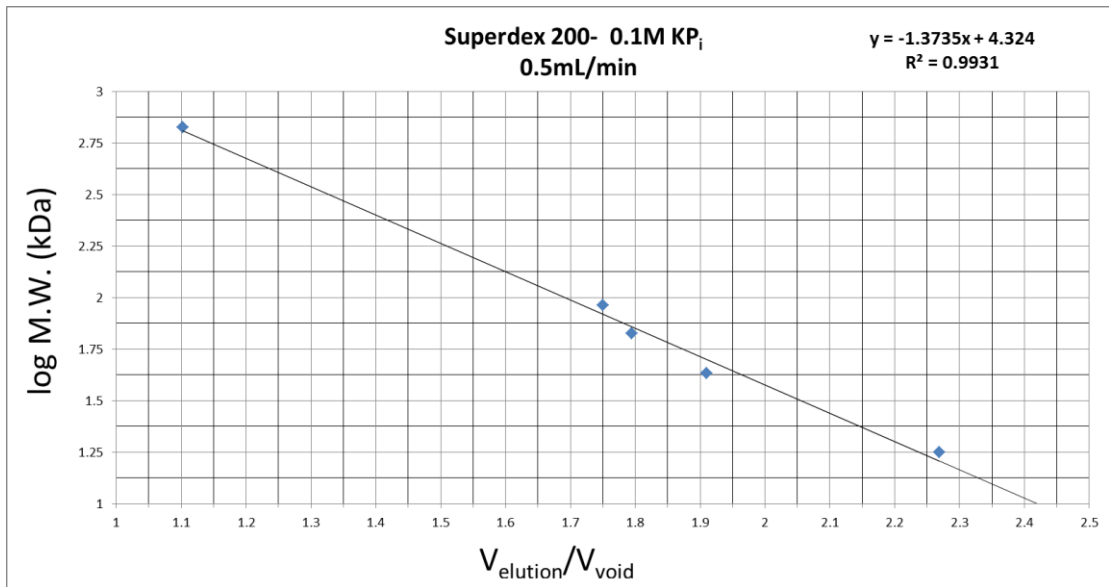


Figure D-2. The linear fit of the molecular weight (log M.W.) versus the relative elution volumes plot.

## LIST OF REFERENCES

1. Toogood, H. S.; Gardiner, J. M.; Scrutton, N. S., Biocatalytic Reductions and Chemical Versatility of the Old Yellow Enzyme Family of Flavoprotein Oxidoreductases. *Chemcatchem* **2010**, 2 (8), 892-914.
2. Warburg, O.; Christian, W., On a new oxidation enzyme. *Naturwissenschaften* **1932**, 20, 980-981.
3. Haas, E., Isolation of a new yellow enzyme. *Biochem Z* **1938**, 298 (5/6), 378-390.
4. Theorell, H.; Akeson, A., Molecular Weight and Fmn Content of Crystalline Old Yellow Enzyme. *Arch Biochem Biophys* **1956**, 65 (1), 439-448.
5. Matthews, R. G.; Massey, V., Isolation of Old Yellow Enzyme in Free and Complexed Forms. *J Biol Chem* **1969**, 244 (7), 1779-&.
6. Massey, V.; Palmer, G., Charge-Transfer Complexes of Lipoyl Dehydrogenase. *Biochem J* **1961**, 81 (1), P22-&.
7. Matthews, R. G.; Massey, V.; Sweeley, C. C., Identification of Para-Hydroxybenzaldehyde as Ligand in Green Form of Old Yellow Enzyme. *J Biol Chem* **1975**, 250 (24), 9294-9298.
8. Abramovitz, A. S.; Massey, V., Interaction of Phenols with Old Yellow Enzyme - Physical Evidence for Charge-Transfer Complexes. *J Biol Chem* **1976**, 251 (17), 5327-5336.
9. Abramovitz, A. S.; Massey, V., Purification of Intact Old Yellow Enzyme Using an Affinity Matrix Fo Sole Chromatographic Step. *J Biol Chem* **1976**, 251 (17), 5321-5326.
10. Saito, K.; Thiele, D. J.; Davio, M.; Lockridge, O.; Massey, V., The Cloning and Expression of a Gene Encoding Old Yellow Enzyme from *Saccharomyces-Carlbergensis*. *J Biol Chem* **1991**, 266 (31), 20720-20724.
11. Stott, K.; Saito, K.; Thiele, D. J.; Massey, V., Old Yellow Enzyme - the Discovery of Multiple Isozymes and a Family of Related Proteins. *J Biol Chem* **1993**, 268 (9), 6097-6106.
12. Macheroux, P.; Massey, V., 8-Thiocyanatoflavins as Active-Site Probes for Flavoproteins. *Biochemistry-Us* **1991**, 30 (2), 456-464.
13. Fox, K. M.; Karplus, P. A., Crystallization of Old Yellow Enzyme Illustrates an Effective Strategy for Increasing Protein Crystal Size. *J Mol Biol* **1993**, 234 (2), 502-507.

14. Fox, K. M.; Karplus, P. A., Old Yellow Enzyme at 2-Angstrom Resolution - Overall Structure, Ligand-Binding, and Comparison with Related Flavoproteins. *Structure* **1994**, *2* (11), 1089-1105.
15. Banner, D. W.; Bloomer, A. C.; Petsko, G. A.; Phillips, D. C.; Pogson, C. I.; Wilson, I. A.; Corran, P. H.; Furth, A. J.; Milman, J. D.; Offord, R. E.; Priddle, J. D.; Waley, S. G., Structure of Chicken Muscle Triose Phosphate Isomerase Determined Crystallographically at 2.5 Å Resolution Using Amino-Acid Sequence Data. *Nature* **1975**, *255* (5510), 609-614.
16. (a) Abendroth, J.; Niefind, K.; May, O.; Siemann, M.; Syltatk, C.; Schomburg, D., The structure of L-hydantoinase from *Arthobacter aurescens* leads to an understanding of dihydropyrimidinase substrate and enantio specificity. *Biochemistry-Us* **2002**, *41* (27), 8589-8597; (b) Barna, T.; Messiha, H. L.; Petosa, C.; Bruce, N. C.; Scrutton, N. S.; Moody, P. C. E., Crystal structure of bacterial morphinone reductase and properties of the C191A mutant enzyme. *J Biol Chem* **2002**, *277* (34), 30976-30983; (c) Barna, T. M.; Khan, H.; Bruce, N. C.; Barsukov, I.; Scrutton, N. S.; Moody, P. C. E., Crystal structure of pentaerythritol tetranitrate reductase: "Flipped" binding geometries for steroid substrates in different redox states of the enzyme. *J Mol Biol* **2001**, *310* (2), 433-447; (d) Kitzing, K.; Fitzpatrick, T. B.; Wilken, C.; Sawa, J.; Bourenkov, G. P.; Macheroux, P.; Clausen, T., The 1.3 Å crystal structure of the flavoprotein YqjM reveals a novel class of Old Yellow Enzymes. *J Biol Chem* **2005**, *280* (30), 27904-27913.
17. (a) Brown, B. J.; Hyun, J. W.; Duvvuri, S.; Karplus, P. A.; Massey, V., The role of glutamine 114 in Old Yellow Enzyme. *J Biol Chem* **2002**, *277* (3), 2138-2145; (b) Inaoka, D. K.; Sakamoto, K.; Shimizu, H.; Shiba, T.; Kurisu, G.; Nara, T.; Aoki, T.; Kita, K.; Harada, S., Structures of *Trypanosoma cruzi* dihydroorotate dehydrogenase complexed with substrates and products: Atomic resolution insights into mechanisms of dihydroorotate oxidation and fumarate reduction. *Biochemistry-Us* **2008**, *47* (41), 10881-10891; (c) Xu, D.; Kohli, R. M.; Massey, V., The role of threonine 37 in flavin reactivity of the old yellow enzyme. *P Natl Acad Sci USA* **1999**, *96* (7), 3556-3561.
18. Dundas, J.; Ouyang, Z.; Tseng, J.; Binkowski, A.; Turpaz, Y.; Liang, J., CASTp: computed atlas of surface topography of proteins with structural and topographical mapping of functionally annotated residues. *Nucleic Acids Res* **2006**, *34*, W116-W118.
19. Vaz, A. D. N.; Chakraborty, S.; Massey, V., Old Yellow Enzyme - Aromatization of Cyclic Enones and the Mechanism of a Novel Dismutation Reaction. *Biochemistry-Us* **1995**, *34* (13), 4246-4256.
20. Kohli, R. M.; Massey, V., The oxidative half-reaction of old yellow enzyme - The role of tyrosine 196. *J Biol Chem* **1998**, *273* (49), 32763-32770.

21. Toscano, M. D.; Woycechowsky, K. J.; Hilvert, D., Minimalist active-site redesign: Teaching old enzymes new tricks. *Angew Chem Int Edit* **2007**, *46* (18), 3212-3236.
22. Schmid, A.; Dordick, J. S.; Hauer, B.; Kiener, A.; Wubbolts, M.; Witholt, B., Industrial biocatalysis today and tomorrow. *Nature* **2001**, *409* (6817), 258-268.
23. Panke, S.; Held, M.; Wubbolts, M., Trends and innovations in industrial biocatalysis for the production of fine chemicals. *Curr Opin Biotech* **2004**, *15* (4), 272-279.
24. (a) Dougherty, M. J.; Arnold, F. H., Directed evolution: new parts and optimized function. *Curr Opin Biotech* **2009**, *20* (4), 486-491; (b) Romero, P. A.; Arnold, F. H., Exploring protein fitness landscapes by directed evolution. *Nat Rev Mol Cell Bio* **2009**, *10* (12), 866-876.
25. (a) Tuttle, J. B.; Ouellet, S. G.; MacMillan, D. W. C., Organocatalytic transfer hydrogenation of cyclic enones. *J Am Chem Soc* **2006**, *128* (39), 12662-12663; (b) Ouellet, S. G.; Tuttle, J. B.; MacMillan, D. W. C., Enantioselective organocatalytic hydride reduction. *J Am Chem Soc* **2005**, *127* (1), 32-33.
26. Toogood, H. S.; Fryszkowska, A.; Hare, V.; Fisher, K.; Roujeinikova, A.; Leys, D.; Gardiner, J. M.; Stephens, G. M.; Scrutton, N. S., Structure-Based Insight into the Asymmetric Bioreduction of the C=C Double Bond of alpha,beta-Unsaturated Nitroalkenes by Pentaerythritol Tetranitrate Reductase. *Adv Synth Catal* **2008**, *350* (17), 2789-2803.
27. Chaparro-Riggers, J. F.; Rogers, T. A.; Vazquez-Figueroa, E.; Polizzi, K. M.; Bommarius, A. S., Comparison of three enoate reductases and their potential use for biotransformations. *Adv Synth Catal* **2007**, *349* (8-9), 1521-1531.
28. Swiderska, M. A.; Stewart, J. D., Stereoselective enone reductions by *Saccharomyces carlsbergensis* old yellow enzyme. *J Mol Catal B-Enzym* **2006**, *42* (1-2), 52-54.
29. Hall, M.; Stueckler, C.; Hauer, B.; Stuermer, R.; Friedrich, T.; Breuer, M.; Kroutil, W.; Faber, K., Asymmetric bioreduction of activated C = C bonds using *Zymomonas mobilis* NCR enoate reductase and old yellow enzymes OYE 1-3 from yeasts. *Eur J Org Chem* **2008**, (9), 1511-1516.
30. Swiderska, M. A.; Stewart, J. D., Asymmetric bioreductions of beta-nitro acrylates as a route to chiral beta(2)-Amino acids. *Org Lett* **2006**, *8* (26), 6131-6133.
31. Opperman, D. J.; Piater, L. A.; van Heerden, E., A novel chromate reductase from *Thermus scotoductus* SA-01 related to old yellow enzyme. *J Bacteriol* **2008**, *190* (8), 3076-3082.

32. Adalbjornsson, B. V.; Toogood, H. S.; Fryszkowska, A.; Pudney, C. R.; Jowitt, T. A.; Leys, D.; Scrutton, N. S., Biocatalysis with Thermostable Enzymes: Structure and Properties of a Thermophilic 'ene'-Reductase related to Old Yellow Enzyme. *ChemBiochem* **2010**, *11* (2), 197-207.
33. Meah, Y.; Massey, V., Old Yellow Enzyme: Stepwise reduction of nitro-olefins and catalysis of aci-nitro tautomerization. *P Natl Acad Sci USA* **2000**, *97* (20), 10733-10738.
34. Kosjek, B.; Fleitz, F. J.; Dormer, P. G.; Kuethe, J. T.; Devine, P. N., Asymmetric bioreduction of alpha,beta-unsaturated nitriles and ketones. *Tetrahedron-Asymmetr* **2008**, *19* (12), 1403-1406.
35. Padhi, S. K.; Bougioukou, D. J.; Stewart, J. D., Site-Saturation Mutagenesis of Tryptophan 116 of *Saccharomyces pastorianus* Old Yellow Enzyme Uncovers Stereocomplementary Variants. *J Am Chem Soc* **2009**, *131* (9), 3271-3280.
36. Zamyatnin, A. A., Amino-Acid, Peptide, and Protein Volume in Solution. *Annu Rev Biophys Bio* **1984**, *13*, 145-165.
37. Fraaije, M. W.; Mattevi, A., Flavoenzymes: diverse catalysts with recurrent features. *Trends Biochem Sci* **2000**, *25* (3), 126-132.
38. Massey, V.; Schopfer, L. M., Reactivity of Old Yellow Enzyme with Alpha-Nadph and Other Pyridine-Nucleotide Derivatives. *J Biol Chem* **1986**, *261* (3), 1215-1222.
39. Chen, V. B.; Arendall, W. B.; Headd, J. J.; Keedy, D. A.; Immormino, R. M.; Kapral, G. J.; Murray, L. W.; Richardson, J. S.; Richardson, D. C., MolProbity: all-atom structure validation for macromolecular crystallography. *Acta Crystallogr D* **2010**, *66*, 12-21.
40. Brown, B. J.; Deng, Z.; Karplus, P. A.; Massey, V., On the active site of old yellow enzyme - Role of histidine 191 and asparagine 194. *J Biol Chem* **1998**, *273* (49), 32753-32762.
41. Zheng, L.; Baumann, U.; Reymond, J. L., An efficient one-step site-directed and site-saturation mutagenesis protocol. *Nucleic Acids Res* **2004**, *32* (14).
42. Otwinowski, Z.; Minor, W., Processing of X-ray diffraction data collected in oscillation mode. *Method Enzymol* **1997**, *276*, 307-326.
43. Battye, T. G. G.; Kontogiannis, L.; Johnson, O.; Powell, H. R.; Leslie, A. G. W., iMOSFLM: a new graphical interface for diffraction-image processing with MOSFLM. *Acta Crystallogr D* **2011**, *67*, 271-281.

44. Adams, P. D.; Afonine, P. V.; Bunkoczi, G.; Chen, V. B.; Davis, I. W.; Echols, N.; Headd, J. J.; Hung, L. W.; Kapral, G. J.; Grosse-Kunstleve, R. W.; McCoy, A. J.; Moriarty, N. W.; Oeffner, R.; Read, R. J.; Richardson, D. C.; Richardson, J. S.; Terwilliger, T. C.; Zwart, P. H., PHENIX: a comprehensive Python-based system for macromolecular structure solution. *Acta Crystallogr D* **2010**, *66*, 213-221.
45. Emsley, P.; Lohkamp, B.; Scott, W. G.; Cowtan, K., Features and development of Coot. *Acta Crystallogr D* **2010**, *66*, 486-501.
46. Murshudov, G. N.; Vagin, A. A.; Dodson, E. J., Refinement of macromolecular structures by the maximum-likelihood method. *Acta Crystallogr D* **1997**, *53*, 240-255.
47. Walton, A. Z.; Conerly, W. C.; Pompeu, Y.; Sullivan, B.; Stewart, J. D., Biocatalytic Reductions of Baylis-Hillman Adducts. *Acs Catal* **2011**, *1* (9), 989-993.
48. Stueckler, C.; Winkler, C. K.; Bonnekessel, M.; Faber, K., Asymmetric Synthesis of (R)-3-Hydroxy-2-methylpropanoate ('Roche Ester') and Derivatives via Biocatalytic C=C-Bond Reduction. *Adv Synth Catal* **2010**, *352* (14-15), 2663-2666.
49. Chen, A. Q.; Xu, J.; Chiang, W.; Chai, C. L. L., L-Threonine-catalysed asymmetric alpha-hydroxymethylation of cyclohexanone: application to the synthesis of pharmaceutical compounds and natural products. *Tetrahedron* **2010**, *66* (7), 1489-1495.
50. Mase, N.; Inoue, A.; Nishio, M.; Takabe, K., Organocatalytic alpha-hydroxymethylation of cyclopentanone with aqueous formaldehyde: Easy access to chiral delta-lactones. *Bioorg Med Chem Lett* **2009**, *19* (14), 3955-3958.
51. Bougioukou, D. J.; Walton, A. Z.; Stewart, J. D., Towards preparative-scale, biocatalytic alkene reductions. *Chem Commun* **2010**, *46* (45), 8558-8560.
52. Matthews, B. W., Solvent Content of Protein Crystals. *J Mol Biol* **1968**, *33* (2), 491-&.
53. Nagano, N.; Orengo, C. A.; Thornton, J. M., One fold with many functions: The evolutionary relationships between TIM barrel families based on their sequences, structures and functions. *J Mol Biol* **2002**, *321* (5), 741-765.
54. Schaller, F.; Weiler, E. W., Molecular cloning and characterization of 12-oxophytodienoate reductase, an enzyme of the octadecanoid signaling pathway from *Arabidopsis thaliana* - Structural and functional relationship to yeast old yellow enzyme. *J Biol Chem* **1997**, *272* (44), 28066-28072.
55. Miller, S.; Lesk, A. M.; Janin, J.; Chothia, C., The Accessible Surface-Area and Stability of Oligomeric Proteins. *Nature* **1987**, *328* (6133), 834-836.

56. Krissinel, E.; Henrick, K., Inference of macromolecular assemblies from crystalline state. *J Mol Biol* **2007**, *372* (3), 774-797.
57. Stewart, R. C.; Massey, V., Potentiometric Studies of Native and Flavin-Substituted Old Yellow Enzyme. *J Biol Chem* **1985**, *260* (25), 3639-3647.
58. Karplus, P. A.; Fox, K. M.; Massey, V., Flavoprotein structure and mechanism .8. Structure-function relations for old yellow enzyme. *Faseb J* **1995**, *9* (15), 1518-1526.
59. Pudney, C. R.; Hay, S.; Pang, J. Y.; Costello, C.; Leys, D.; Sutcliffe, M. J.; Scrutton, N. S., Mutagenesis of morphinone reductase induces multiple reactive configurations and identifies potential ambiguity in kinetic analysis of enzyme tunneling mechanisms. *J Am Chem Soc* **2007**, *129* (45), 13949-13956.
60. (a) Etayo, P.; Nunez-Rico, J. L.; Vidal-Ferran, A., Chiral Rhodium Complexes Derived From Electron-Rich Phosphine-Phosphites as Asymmetric Hydrogenation Catalysts. *Organometallics* **2011**, *30* (24), 6718-6725; (b) Pautigny, C.; Jeulin, S.; Ayad, T.; Zhang, Z. G.; Genet, J. P.; Ratovelomanana-Vidal, V., Convenient General Asymmetric Synthesis of Roche Ester Derivatives through Catalytic Asymmetric Hydrogenation: Steric and Electronic Effects of Ligands. *Adv Synth Catal* **2008**, *350* (16), 2525-2532; (c) Wassenaar, J.; Kuil, M.; Lutz, M.; Spek, A. L.; Reek, J. N. H., Asymmetric Hydrogenation with Highly Active IndolPhos-Rh Catalysts: Kinetics and Reaction Mechanism. *Chem-Eur J* **2010**, *16* (22), 6509-6517.
61. Yep, A.; Kenyon, G. L.; McLeish, M. J., Saturation mutagenesis of putative catalytic residues of benzoylformate decarboxylase provides a challenge to the accepted mechanism. *P Natl Acad Sci USA* **2008**, *105* (15), 5733-5738.
62. Hulley, M. E.; Toogood, H. S.; Fryszkowska, A.; Mansell, D.; Stephens, G. M.; Gardiner, J. M.; Scrutton, N. S., Focused Directed Evolution of Pentaerythritol Tetranitrate Reductase by Using Automated Anaerobic Kinetic Screening of Site-Saturated Libraries. *Chembiochem* **2010**, *11* (17), 2433-2447.
63. Toogood, H. S.; Fryszkowska, A.; Hulley, M.; Sakuma, M.; Mansell, D.; Stephens, G. M.; Gardiner, J. M.; Scrutton, N. S., A Site-Saturated Mutagenesis Study of Pentaerythritol Tetranitrate Reductase Reveals that Residues 181 and 184 Influence Ligand Binding, Stereochemistry and Reactivity. *Chembiochem* **2011**, *12* (5), 738-749.
64. Bougioukou, D. J.; Kille, S.; Taglieber, A.; Reetz, M. T., Directed Evolution of an Enantioselective Enoate-Reductase: Testing the Utility of Iterative Saturation Mutagenesis. *Adv Synth Catal* **2009**, *351* (18), 3287-3305.
65. Krissinel, E.; Henrick, K., Multiple alignment of protein structures in three dimensions. *Computational Life Sciences, Proceedings* **2005**, 3695, 67-78.

66. Bjornberg, O.; Gruner, A. C.; Roepstorff, P.; Jensen, K. F., The activity of *Escherichia coli* dihydroorotate dehydrogenase is dependent on a conserved loop identified by sequence homology, mutagenesis, and limited proteolysis. *Biochemistry-Us* **1999**, *38* (10), 2899-2908.
67. Rawls, J.; Knecht, W.; Diekert, K.; Lill, R.; Loffler, M., Requirements for the mitochondrial import and localization of dihydroorotate dehydrogenase. *Eur J Biochem* **2000**, *267* (7), 2079-2087.
68. Andersen, P. S.; Jansen, P. J. G.; Hammer, K., 2 Different Dihydroorotate Dehydrogenases in *Lactococcus-Lactis*. *J Bacteriol* **1994**, *176* (13), 3975-3982.
69. (a) Rowland, P.; Nielsen, F. S.; Jensen, K. F.; Larsen, S., The crystal structure of the flavin containing enzyme dihydroorotate dehydrogenase A from *Lactococcus lactis*. *Structure* **1997**, *5* (2), 239-252; (b) Andersen, P. S.; Martinussen, J.; Hammer, K., Sequence analysis and identification of the pyrKDbF operon from *Lactococcus lactis* including a novel gene, pyrK, involved in pyrimidine biosynthesis. *J Bacteriol* **1996**, *178* (16), 5005-5012.
70. Nielsen, F. S.; Rowland, P.; Larsen, S.; Jensen, K. F., Purification and characterization of dihydroorotate dehydrogenase A from *Lactococcus lactis*, crystallization and preliminary X-ray diffraction studies of the enzyme. *Protein Sci* **1996**, *5* (5), 852-856.
71. Li, X. T.; Weinstock, G. M.; Murray, B. E., Generation of Auxotrophic Mutants of *Enterococcus-Faecalis*. *J Bacteriol* **1995**, *177* (23), 6866-6873.
72. Marcinkeviciene, J.; Jiang, W. J.; Locke, G.; Kopcho, L. M.; Rogers, M. J.; Copeland, R. A., A second dihydroorotate dehydrogenase (type A) of the human pathogen *Enterococcus faecalis*: Expression, purification, and steady-state kinetic mechanism. *Arch Biochem Biophys* **2000**, *377* (1), 178-186.
73. Nielsen, F. S.; Andersen, P. S.; Jensen, K. F., The B form of dihydroorotate dehydrogenase from *Lactococcus lactis* consists of two different subunits, encoded by the pyrDb and pyrK genes, and contains FMN, FAD, and [FeS] redox centers. *J Biol Chem* **1996**, *271* (46), 29359-29365.
74. Bjornberg, O.; Rowland, P.; Larsen, S.; Jensen, K. F., Active site of dihydroorotate dehydrogenase A from *Lactococcus lactis* investigated by chemical modification and mutagenesis. *Biochemistry-Us* **1997**, *36* (51), 16197-16205.
75. Fagan, R. L.; Nelson, M. N.; Pagano, P. M.; Palfey, B. A., Mechanism of flavin reduction in class 2 dihydroorotate dehydrogenases. *Biochemistry-Us* **2006**, *45* (50), 14926-14932.

76. Hurt, D. E.; Sutton, A. E.; Clardy, J., Brequinar derivatives and species-specific drug design for dihydroorotate dehydrogenase. *Bioorg Med Chem Lett* **2006**, *16* (6), 1610-1615.
77. Rowland, P.; Bjornberg, O.; Nielsen, F. S.; Jensen, K. F.; Larsen, S., The crystal structure of *Lactococcus lactis* dihydroorotate dehydrogenase A complexed with the enzyme reaction product throws light on its enzymatic function. *Protein Sci* **1998**, *7* (6), 1269-1279.
78. Takashima, E.; Inaoka, D. K.; Osanai, A.; Nara, T.; Odaka, M.; Aoki, T.; Inaka, K.; Harada, S.; Kita, K., Characterization of the dihydroorotate dehydrogenase as a soluble fumarate reductase in *Trypanosoma cruzi*. *Mol Biochem Parasit* **2002**, *122* (2), 189-200.
79. Weckbecker, A.; Groger, H.; Hummel, W., Regeneration of Nicotinamide Coenzymes: Principles and Applications for the Synthesis of Chiral Compounds. *Adv Biochem Eng Biot* **2010**, *120*, 195-242.
80. Ingelman, M.; Bianchi, V.; Eklund, H., The three-dimensional structure of flavodoxin reductase from *Escherichia coli* at 1.7 angstrom resolution. *J Mol Biol* **1997**, *268* (1), 147-157.
81. Beinert, H.; Holm, R. H.; Munck, E., Iron-sulfur clusters: Nature's modular, multipurpose structures. *Science* **1997**, *277* (5326), 653-659.
82. Jaganaman, S.; Pinto, A.; Tarasev, M.; Ballou, D. P., High levels of expression of the iron-sulfur proteins phthalate dioxygenase and phthalate dioxygenase reductase in *Escherichia coli*. *Protein Express Purif* **2007**, *52* (2), 273-279.
83. Rowland, P.; Norager, S.; Jensen, K. F.; Larsen, S., Structure of dihydroorotate dehydrogenase B: Electron transfer between two flavin groups bridged by an iron-sulphur cluster. *Structure* **2000**, *8* (12), 1227-1238.
84. Norager, S.; Arent, S.; Bjornberg, O.; Ottosen, M.; Lo Leggio, L.; Jensen, K. F.; Larsen, S., *Lactococcus lactis* dihydroorotate dehydrogenase A mutants reveal important facets of the enzymatic function. *J Biol Chem* **2003**, *278* (31), 28812-28822.
85. Combe, J. P.; Basran, J.; Hothi, P.; Leys, D.; Rigby, S. E. J.; Munro, A. W.; Scrutton, N. S., Lys-D48 is required for charge stabilization, rapid flavin reduction, and internal electron transfer in the catalytic cycle of dihydroorotate dehydrogenase B of *Lactococcus lactis*. *J Biol Chem* **2006**, *281* (26), 17977-17988.
86. Aitken, C. E.; Marshall, R. A.; Puglisi, J. D., An oxygen scavenging system for improvement of dye stability in single-molecule fluorescence experiments. *Biophys J* **2008**, *94* (5), 1826-1835.

87. Mattevi, A., To be or not to be an oxidase: challenging the oxygen reactivity of flavoenzymes. *Trends Biochem Sci* **2006**, 31 (5), 276-283.

## BIOGRAPHICAL SKETCH

Yuri A. A. Pompeu was born in Tubarão, Santa Catarina, Brazil. He was raised in Sorocaba, São Paulo and after graduating from high school in 2003 he moved to the US to accept a scholarship as a student-athlete at Murray State University. Yuri played varsity tennis for all four years and graduated with a B.S. degree in chemistry. He performed undergraduate research in the laboratory of Professor Kevin Revell. In 2008, Yuri started his graduate studies at the University of Florida under the supervision of Professor Jon Stewart. His initial research focused on electrochemical reductions mediated by OYE1 but by his second year the focused had completely shifted towards X-ray crystallography and structure guided protein engineering. Largely influenced by Professor Steve Bruner, X-ray crystallography became his true passion. Towards the end of his graduate career, Yuri became involved in a project that studied the genetic association between the protein HLA-B57:01 and abacavir hypersensitivity syndrome (AHS). Along with Professor David Ostrov, Yuri was able to solve the crystal structure of a ternary complex composed of HLA, abacavir and a “non-natural” peptide ligand. This structure provided the structural basis for (AHS), and has been of significant impact in the field of immunology and has led to the search for other diseases that are now believed to occur through a similar mechanism. In the future Yuri will focus his studies on human immunology, with a particular interest in disease related structural immunology.